Department of Mechanical & Aerospace Engineering

University of Strathclyde

Numerical Modelling of Rubber Hyperelasticity: Parameter Identification and Finite Element Implementations

Stephen John Connolly

Submitted in fulfilment of the requirements for the degree of

Doctor of Philosophy

2020

Declaration of Authenticity and Author's Rights

This thesis is the result of the author's original research. It has been composed by the author and has not been previously submitted for examination which has led to the award of a degree.

Signed:
Stephen John Connolly

Date:
19th June 2020

Previously published work

Some of the content within this thesis has been published in whole or in part for conference proceedings and journal publications listed in the List of Publications. The extent of the author's contribution to these works was 100% and as such no further clarification on the author's contributions to these works is necessary.

Signed:
Stephen John Connolly

Date:
19th June 2020

Abstract

The aim of the presented research is to investigate and develop methods to model rubber hyperelasticity. Accurate numerical modelling of the hyperelastic behaviour of rubber requires a capable constitutive model and experimental data from the material or component of interest. This research focuses on three areas: hyperelastic constitutive modelling with homogeneous experimental parameter identification, implementing hyperelasticity in the Finite Element Method and simulating the hyperelastic behaviour of industrial rubber components.

Postulated conditions are proposed to ensure the physical plausibility of hyperelastic homogeneous experimental data. Using experimental data from literature deemed to meet these conditions, the connection between constitutive model, the extent of experimental data and the ability to predict the complete hyperelastic behaviour is investigated. A more efficient means of experimental parameter identification is suggested, which uses only "sufficient" experimental data. This data encompasses the expected range of deformations for a material or component. To develop this method for industrial rubber components, the Finite Element Method is used.

Open-source user subroutines are developed to enable the implementation of hyperelastic constitutive models in the Finite Element Method. Analytical implementations are developed for hyperelastic constitutive models defined by two common strain measures, Cauchy-Green invariants and principal stretches. Implementations are also developed for two complimentary real-domain approximation methods. All implementations are validated in terms of their numerical accuracy and computation time. The implementations are accurate to double precision and analytical methods are more computationally efficient than approximation methods.

A methodology for simulating rubber components using sufficient experimental data is developed. The approach uses prototype simulations to identify the strain region of the component under operating conditions. A modification is proposed for simulating strain-loaded and stress-loaded components, as the latter affects the strain region. The method is demonstrated by simulating two industrial components, one for each loading type.

List of Publications

Journal publications

S. J. Connolly, D. Mackenzie, and Y. Gorash. **Isotropic hyperelasticity in principal stretches: explicit elasticity tensors and numerical implementation**. *Computational Mechanics*, **64**(5):1273-1288, 2019.

S. J. Connolly, D. Mackenzie, and Y. Gorash. **Higher-order and higher floating-point precision numerical approximations of finite strain elasticity moduli**. *International Journal for Numerical Methods in Engineering*, **120**(10):1184-1201, 2019.

Conference proceedings

S. J. Connolly, D. Mackenzie, and T. Comlekci. **Multi-objective optimization of hyperelastic material constants**. *In Constitutive Models for Rubber X*, pages 273–278. CRC Press, 2017.

S. J. Connolly, D. Mackenzie, and Y. Gorash. **The implications of constitutive model selection in hyperelastic parameter identification**. *In Constitutive Models for Rubber XI*, pages 329–334. CRC Press, 2019.

Acknowledgements

I would like to express my gratitude to my academic supervisors, Donald Mackenzie and Yevgen Gorash. I am very grateful to Donald for providing me with this opportunity. I feel very lucky to have been allowed the freedom to discover this PhD and for your confidence in my ability throughout. To Yevgen, I know that I would not have gotten here without you. At the beginning of this journey, almost five years ago during my undergraduate project, your enthusiasm for research inspired me to pursue a PhD. For this, I also extend my gratitude to Bobby Hamilton in particular and the other academics who inspired my appreciation for research.

Above all, I thank my family and friends for their ongoing love and support.

To my parents,

Ruth, Peter, Dave and Sandy

Contents

List of Figures

List of Tables

List of Symbols and Acronyms

$\boldsymbol{\sigma}$	Cauchy stress tensor
$\boldsymbol{\tau}$	Kirchhoff stress tensor
$\boldsymbol{\chi}$	Motion from reference to spatial
δ_{ij}	Kronecker delta
ϵ_i	Principal nominal strains, $i = 1, 2, 3$
η	Perturbation magnitude
κ	Dimensionless shear measurement
λ_a	Principal stretches, $a = 1, 2, 3$
$\mathbb{1}$	Fourth-order identity tensor
$\mathbb{A}$	Generic fourth-order material tensors
$\mathbb{C}$	Material elasticity tensor
$\mathbb{c}$	Spatial elasticity tensor
$\mathbf{1}$	Second-order identity tensor
$\mathbf{A}$	Generic second-order material tensors
$\mathbf{a}$	Generic second-order spatial tensors
$\mathbf{b}$	Left Cauchy-Green deformation Tensor
$\mathbf{C}$	Right Cauchy-Green deformation Tensor
$\mathbf{F}$	Deformation gradient
$\mathbf{P}$	First Piola-Kirchhoff stress tensor
$\mathbf{R}$	Rotation Tensor
$\mathbf{S}$	Second Piola-Kirchhoff stress tensor
$\mathbf{U}$	Right Stretch Tensor
$\mathbf{v}$	Left Stretch Tensor
$\mathcal{O}$	Big $\mathcal{O}$ Landau symbol
ν	Poisson's ratio

$\overline{\mathbb{P}}$	Material projection tensor
$\overline{\mathbb{p}}$	Spatial projection tensor
ψ	Strain energy density
$\mathbf{N}_a$	Principal directions in reference configuration, $a = 1, 2, 3$
$\mathbf{n}_a$	Principal directions in spatial configuration, $a = 1, 2, 3$
$\mathbf{X}$	Material point
$\mathbf{x}$	Spatial point
`macheps`	Machine epsilon
ε_{ijk}	Levi-Civita symbol
a_0	Generic quantity in undeformed configuration
A_{ij}	Component form of generic second-order tensors, $i, j = 1, 2, 3$
A_i	Principal components of generic second-order tensor, $i = 1, 2, 3$
c_m	Finite difference coefficient
D	Diameter
F	Force
G	Shear Modulus
H	Height
I_1	First Cauchy-Green invariant
I_2	Second Cauchy-Green invariant
I_3	Third Cauchy-Green invariant
J	Volume ratio
K	Bulk Modulus
L	Length
p	Pressure
PCC	Pearson's Correlation Coefficient
r	Radius
t	Thickness
t	Time
U	Volumetric strain energy density
V	Volume
W	Isochoric strain energy density

w	Width
$\boldsymbol{\Omega}$	Spatial configuration
$\boldsymbol{\Omega}_0$	Reference configuration
$\mathbb{R}^3$	Three-dimensional real coordinate space
DIC	Digital Image Correlation
E	Error
EC	Equibiaxial Compression
ET	Equibiaxial Tension
FE	Finite Element
FEA	Finite Element Analysis
FEM	Finite Element Method
GB	General Biaxial
MPa	Megapascal
PC	Planar Compression
PT	Planar Tension
SS	Simple Shear
UC	Uniaxial Compression
UT	Uniaxial Tension

Chapter 1

Introduction

From the discovery of natural rubber and the realisation of the vulcanisation process, natural and synthetic rubber compounds have found use in many engineering applications due to their unique mechanical properties. Applying relatively small applied mechanical loads, compared with other engineering materials, rubbers are low cost materials capable of sustaining large elastic deformations without damage. Deformations of over 800% are known to be possible for some technical rubber compounds. As a compounded material, the ingredients of a rubber enable a wide variety of mechanical and chemical properties. The compounding recipe and process affects a rubber's stiffness, maximum elongation, damping properties, operating temperatures, chemical compatibilities, frictional behaviour, density and cost, to name but a few (1, 2). This flexibility of material properties enables the use of rubbers across a broad range of applications, including critical sealing components in pressurised systems, tyres for automobiles and aircraft, and the soles of shoes. Some of these properties are also shared by soft biological tissues. "Rubber" may therefore be applied to any material that shares similar mechanical properties and fits the description of a rubber-like material.

Prior to the employment of a product within an engineering application, it is beneficial to gain prior knowledge of how it will respond to service conditions. This is a key aspect of a modern design process and has led to the development of analytical and numerical modelling methods. To describe the mechanical response of a material to a prescribed loading, a constitutive model is required. For components with simple geometries and boundary conditions, analytical equations may be derived from a constitutive model describing the material. However, for more complex components and boundary conditions, a numerical method is likely to be required. For the modelling of solids, the Finite Element Method (FEM) is a commonly applied numerical simulation method. Accurate prediction of a component by either numerical method requires constitutive model parameters that are fitted to experimental data from the

physical component. An accurate insight of component performance and behaviour through Finite Element Analysis (FEA) enables engineering design capabilities, such as: identifying design weaknesses, computing fatigue life or geometric optimisation.

In the presented work, numerical modelling of rubber was investigated in terms of analytical solutions for simple homogeneous experiments and by FEA of industrial rubber components. These investigations were restricted to the isothermal equilibrium behaviour of rubber in the time-domain, for which hyperelasticity theory may be applied. Homogeneous experimental data from literature was studied, motivated by its use in parameter identification of hyperelastic constitutive models. Using hyperelastic constitutive models fitted to experimental data from a component, the isothermal equilibrium behaviour of a rubber component may be predicted using FEA. By way of literature review, it was found that the extent of experimental data and the choice of constitutive model to accurately simulate a rubber component was not well understood. An investigation into both factors was carried out, with consideration of how they relate to one another. There was indication that certain constitutive models may be generally more capable than others and that some may even accurately predict the complete hyperelastic behaviour of rubber using minimal experimental data.

The commercial FEM software Abaqus (3) was used to study the extent of experimental data required and the choice of constitutive model to simulate industrial rubber components. As the wealth of published constitutive models were not available in the FEM software, numerical implementations were developed. The aim of these was to allow the implementation of most known hyperelastic constitutive models in the FEM. This was enabled through the development of open-source subroutines, which aimed to minimise user input with acceptable computational costs. The ambiguous nature of certain hyperelastic constitutive model definitions led to an investigation of numerically approximated implementations. Using the developed user subroutines, two industrial rubber components were studied. A methodology was proposed for the simulation of the hyperelastic behaviour of industrial rubber components using only "sufficient" experimental data.

This thesis consists of seven chapters. The topics of each chapter are described as follows. All data associated with this thesis and the developed programs and subroutines are available in the dataset (4).

Chapter 2 introduces and reviews the isothermal behaviour of rubber. The general isothermal behaviour is discussed to justify the focus on only the equilibrium hyperelastic behaviour. The complete hyperelastic behaviour and the complex behaviours of rubber are introduced. The approaches to hyperelastic constitutive modelling, experimental parameter identification and the FE (Finite Element) implementation of

hyperelasticity are then reviewed.

Chapter 3 investigates hyperelastic constitutive modelling and parameter identification using homogeneous experiments. This aims to reveal the relationship between the choice of constitutive model, the extent of experimental data and the ability to predict the complete hyperelastic behaviour. Interpolated behaviours are compared to investigate the validity of assuming the complete behaviour may be predicted by single loading experimental data. The prediction of smaller interpolated regions by lesser extents of experimental data is also investigated by interpolated predictions.

Chapters 4 and **5** discuss the developed FE implementations of hyperelasticity by user subroutines. In Chapter 4, implementations by numerically approximated tangent moduli are investigated using Cauchy-Green invariant constitutive models. Initially, two user subroutine interfaces of Abaqus are studied, UMAT and UHYPER. For this, analytical implementations of Cauchy-Green invariant constitutive models are developed and validated. Using the validated implementations, two complimentary methods of numerical implementation by real-domain numerical approximation of tangent moduli are investigated. Chapter 5 develops a FE implementation for hyperelastic constitutive models defined in terms of principal stretches. The principal stretches are a strain measure affected by numerical instabilities. The developed implementation uses an explicitly derived analytical elasticity tensor, which is numerically stable. For all developed implementations throughout Chapters 4 and 5, the numerical accuracy and computational efficiencies are assessed, with consideration of built-in constitutive models from Abaqus.

Chapter 6 focuses on developing a methodology for the simulation of the hyperelastic behaviour of industrial rubber components in the FEM. The proposed method is based on the use of only sufficient experimental data to identify constitutive model parameters. The sufficient experimental data is that which encompasses the expected strain range of the component. Predicting the expected strain range requires a different approach depending on the nature of the applied loading, whether it is strain-loaded or stress-loaded. The former can be predicted without material insights, but the strain range of a component exposed to stress-loading is dependent on the material properties. Either approach provides a more efficient experimental procedure to simulate industrial rubber components. Two components are investigated, one is strain-loaded and the other features stress-loading.

Chapter 7 summarises the conclusions from each of these chapters and proposes the next steps in further developing this research.

Chapter 2

Numerical Modelling and Parameter Identification of Hyperelasticity

A review of the literature is presented for the isothermal behaviour of rubber with a focus on constitutive modelling, parameter identification and numerical implementation of the equilibrium behaviour of rubber in the Finite Element Method. Prior to discussing the isothermal rubber behaviour, the finite elasticity framework is defined with reference to Holzapfel (5).

2.1 Finite Elasticity Framework

In three-dimensional real coordinate space $\mathbb{R}^3$, a Lagrangian or reference undeformed configuration $\mathbf{\Omega}_0$ and an Eulerian or current deformed configuration $\mathbf{\Omega}$ are defined for a body of interest. A material point $\mathbf{X}$ in the reference configuration $\mathbf{X}\in\mathbf{\Omega}_0$ at time $t = 0$, is mapped to its current position $\mathbf{x}$ in the current configuration $\mathbf{x}\in\Omega$ at time $t = t$, by χ. The motion $\chi : \Omega_0 \rightarrow \mathbb{R}^3$ and therefore $\mathbf{x}=\chi(\mathbf{X}, t)$. Arguments are subsequently neglected for clarity. The motion χ describes the deformation and the rigid body motions (translation and rotation). To remove translation, the two-point deformation gradient tensor, defined by $\mathbf{F}=\partial\chi/\partial\mathbf{X}$ is used. The change in volume, in terms of the volume ratio $J=V/V_0$, is calculated from this deformation tensor by its determinant using

$$J = \det(\mathbf{F}) \tag{2.1}$$

The polar decomposition of the deformation gradient splits $\mathbf{F}$ into pure stretch and pure rotation tensors by $\mathbf{F}=\mathbf{RU}$ and $\mathbf{F}=\mathbf{vR}$. Here, $\mathbf{U}$ and $\mathbf{v}$ are respectively the symmetric positive definite right and left stretch tensors in the material and spatial con-

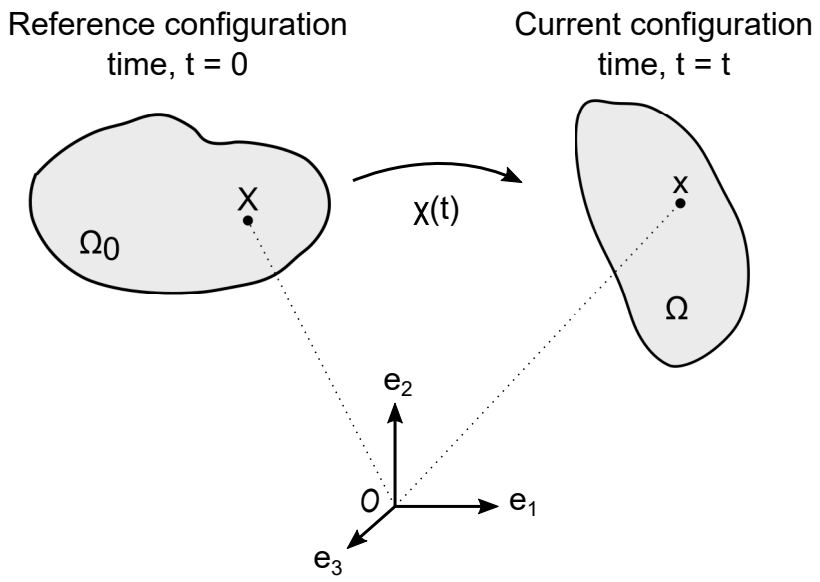

Figure 2.1: Motion between a body's reference and current configurations

figurations. Tensor $\mathbf{R}$ defines the rigid body rotation and is a proper orthogonal tensor, which implies the relations $\mathbf{R}^{\mathrm{T}}\mathbf{R}=\mathbf{R}\mathbf{R}^{\mathrm{T}}=\mathbf{1}$, where $\mathbf{1}$ is the second-order identity tensor. The superscripted notation $\mathbf{A}^{\mathrm{T}}$ indicates the transpose of a tensor $\mathbf{A}$. With these relations, two further symmetric pure stretch tensors in the material and spatial descriptions may be defined in terms of $\mathbf{F}$. These are, respectively, the right and left Cauchy-Green deformation tensors $\mathbf{C}$ and $\mathbf{b}$

$$\mathbf{C} = \mathbf{F}^{\mathrm{T}}\mathbf{F} = \left(\mathbf{U}\mathbf{R}^{\mathrm{T}}\right)(\mathbf{R}\mathbf{U}) = \mathbf{U}^2 \tag{2.2}$$

$$\mathbf{b} = \mathbf{F}\mathbf{F}^{\mathrm{T}} = (\mathbf{v}\mathbf{R})\left(\mathbf{R}^{\mathrm{T}}\mathbf{v}\right) = \mathbf{v}^2 \tag{2.3}$$

Due to the symmetry of the Cauchy-Green deformation tensors, the spectral decomposition may be used to represent these tensors in terms of real eigenvalues ${\lambda_a}^2$ and sets of mutually orthogonal eigenvectors $\mathbf{N}_a$ and $\mathbf{n}_a$

$$\mathbf{C} = \sum_{a=1}^{3} {\lambda_a}^2 \left(\mathbf{N}_a \otimes \mathbf{N}_a\right) \tag{2.4}$$

$$\mathbf{b} = \sum_{a=1}^{3} {\lambda_a}^2 \left(\mathbf{n}_a \otimes \mathbf{n}_a\right) \tag{2.5}$$

The eigenvalues of both Cauchy-Green deformation tensors ${\lambda_a}^2$ are the squared principal stretches. The eigenvectors $\mathbf{N}_a$ and $\mathbf{n}_a$ are the principal directions in the material and spatial configurations. When summation symbols are present the principal stretches are defined as λ_a, other principal values are defined using λ_i. When the principal stretches are uniform and aligned with the principal directions, which is often assumed for experimental convenience, each may be defined in terms of an

arbitrary initial length L_0 and their current length L in the principal direction i as

$$\lambda_i = \frac{L}{L_0} \quad i = 1,2,3 \tag{2.6}$$

This is related to another useful experimental measure, the principal nominal strain, which is defined by ϵ_i by $\epsilon_i = \lambda_i - 1$ where $i = 1,2,3$.

The Cauchy-Green deformation tensors and principal stretches are also related in terms of three scalar invariants I_1, I_2 and I_3. These are referred to throughout as the Cauchy-Green invariants. As they are "invariant", this implies that they are objective and do not change with a transformation of basis or a change of observer. They are therefore defined equivalently in terms of the tensors $\mathbf{C}$ and $\mathbf{b}$ and can be expressed in terms of the principal stretches by

$$I_1 = \text{tr}\mathbf{C} = \text{tr}\mathbf{b} = {\lambda_1}^2 + {\lambda_2}^2 + {\lambda_3}^2 \tag{2.7}$$

$$I_2 = \frac{1}{2}\left[(\text{tr}\mathbf{C})^2 - \text{tr}\left(\mathbf{C}^2\right)\right] = \frac{1}{2}\left[(\text{tr}\mathbf{b})^2 - \text{tr}\left(\mathbf{b}^2\right)\right] = {\lambda_1}^2{\lambda_2}^2 + {\lambda_1}^2{\lambda_3}^2 + {\lambda_2}^2{\lambda_3}^2 \tag{2.8}$$

$$I_3 = \det\mathbf{C} = \det\mathbf{b} = {\lambda_1}^2{\lambda_2}^2{\lambda_3}^2 = J^2 \tag{2.9}$$

These use the definition of the trace of a tensor $\mathbf{A}$ as $\text{tr}\mathbf{A} = A_{ii}$ and the determinant of $\mathbf{A}$ is defined using the Levi-Civita symbol ε_{ijk} as $\det\mathbf{A} = \varepsilon_{ijk}A_{1i}A_{2j}A_{3k}$.

As originally proposed by Flory (6), the nearly incompressible nature of rubber necessitates a split of the deformation into deviatoric and dilatational contributions. Bar notation is used to indicate an isochoric, constant volume quantity. Starting with the deformation gradient $\mathbf{F}$, the multiplicative split is defined as

$$\mathbf{F} = \left(J^{\frac{1}{3}}\mathbf{1}\right)\overline{\mathbf{F}} = J^{\frac{1}{3}}\overline{\mathbf{F}} \tag{2.10}$$

The volumetric deformation is therefore a ratio of the original volume defined as $J^{\frac{1}{3}}\mathbf{1}$. The isochoric part is $\overline{\mathbf{F}}$, which is computed by $\overline{\mathbf{F}} = J^{-\frac{1}{3}}\mathbf{F}$. Other isochoric strain measures are defined implicitly from this, such that

$$\overline{\mathbf{C}} = J^{-\frac{2}{3}}\mathbf{C} \tag{2.11}$$

$$\overline{\mathbf{b}} = J^{-\frac{2}{3}}\mathbf{b} \tag{2.12}$$

$$\overline{\lambda}_a = J^{-\frac{1}{3}}\lambda_a \tag{2.13}$$

The isochoric Cauchy-Green invariants may then be defined equivalently to equations (2.7), (2.8) and (2.9) by these isochoric components. Alternatively they are defined $\overline{I}_1 = J^{-\frac{2}{3}}I_1$, $\overline{I}_2 = J^{-\frac{4}{3}}I_2$ and $\overline{I}_3 = 1$. In the case of incompressibility, the volume is constant such that $\overline{I}_3 = I_3 = J = 1$, which implies $\overline{I}_1 = I_1$, $\overline{I}_2 = I_2$ and $\overline{\lambda}_a = \lambda_a$. A multiplicative split of the deformation allows near and full incompressibility and was used throughout, unless otherwise stated.

2.2 Isothermal Behaviour of Rubber

The widespread use of rubber as an engineering material is primarily due to its ability to stretch up to several hundred times its length elastically, without damage. Its stiffness is also significantly lower than other engineering materials, meaning that these large deformations are induced by much smaller applied stresses. For most materials, an applied stress is equilibrated by internal stress of a material due to intermolecular forces. However, these forces only support internal strains to around 10% (7). The ability of rubber materials to undergo large deformations and produce an equilibrating stress without damage therefore requires additional theories.

The finite strain equilibrium behaviour of rubber is typically defined by hyperelasticity. Though this behaviour is the focus of the presented work, an overview of complex isothermal behaviours for rubber in the time-domain is also presented. These theories are discussed for the isothermal behaviour of rubber with reference to stress-strain plots and the underlying hyperelastic equilibrium response. The experimental methods to characterise the hyperelastic behaviour are discussed in greater detail in Section 2.4. The discussion of rubber's behaviour is categorised into equilibrium elasticity and complex behaviours.

2.2.1 Rubber Elasticity

Rubbers are a network of molecules primarily consisting of a "backbone" of long-chain monomers with cross-links (2). The backbone material is typically what the rubber material is referred to as. Common examples include polyisoprene (natural rubber), silicone and ethylene propylene diene. The mechanical properties of vulcanized rubbers are dependent on the properties of the backbone monomer and the degree of cross-linking induced during vulcanization (8). Additives included in the compounding of rubber also strongly influence its mechanical properties. The most pronounced effect is due to the inclusion of reinforcing filler particles, which are most commonly carbon-black or silica (2, 9). The internal forces of rubber are due to interactions within and between the long chain molecules and the other compounding constituents.

The typical hyperelastic behaviour of rubber is shown in Figure 2.2 for three stress-strain curves with different applied modes of deformation. The complete stress response for a typical rubber material may be described in terms of three characteristic features (10, 11, 12, 13, 14). The first two features describe the S-shaped (15, 16) stress response in each deformation mode. At low to moderate strains the initial stiffness decreases gradually but remains positive. This is then followed by a stiffening positive asymptotic stress response at high strains. The third feature is that there is a

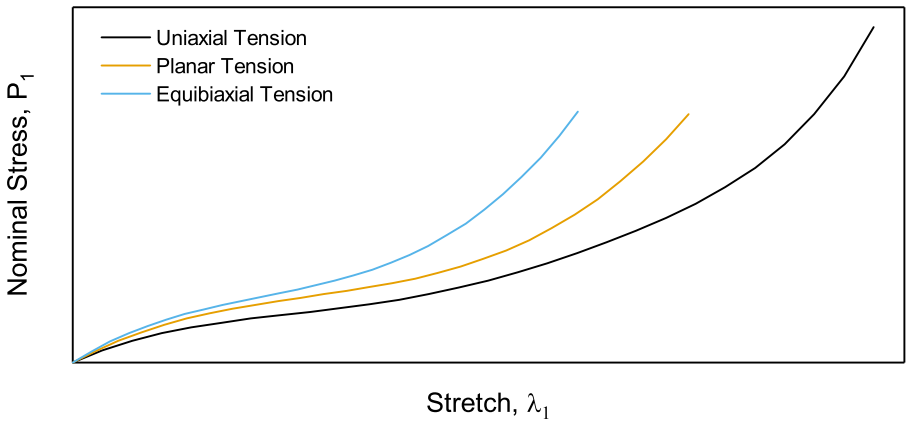

Figure 2.2: Dimensionless plot of typical stress-strain elastic behaviour of rubber in different deformation modes

distinct difference in stress at the same stretch value for different deformation states. The asymptotic behaviour in any deformation mode will cause the rubber to fail. The deformation state dependence means that the asymptote, and therefore material failure, occurs at different stretch magnitudes depending on the mode of deformation (11).

The seminal paper by Flory (17) outlines the historical development of the accepted theory of rubber elasticity. The three stated features may be described in terms of the molecular theory of rubber and were developed in respective historical order. The decreasing stiffness at low strains was initially explained by a Gaussian distribution of the long-chain monomer network (2, 7, 17). The long-chain molecules are assumed to have an end-to-end length related to a Gaussian distribution, which is much shorter than the total length of each molecule. When stretched to low and moderate strains, the network is initially stiff due to the orientation of the molecules. As the molecules align, the stiffness decreases. The network is assumed to be affine such that the stiffness decrease at the molecular level explains the macroscopic softening response. However, as the strain increases, the Gaussian network chains do not have a limited extensibility (7, 15), which fails to produce an asymptotic rise in the stiffness at higher strains.

The asymptotic behaviour of rubber may be described by considering the finite extensibility of the chains (10, 15, 18, 19). This may be modelled by a non-Gaussian distribution of molecular chain lengths, for example an inverse Langevin distribution was shown by Arruda and Boyce (15) to be suitable. The inverse Langevin distribution was also assumed to be non-affine to account for the deformation state dependence. However, this theory does not adequately characterise the distinction, additional theory is required (20). The distinction is explained by topological tube-like constraints (11, 21, 22, 23). In the tube theory, as described by McCleish (23), the chains are

contained within tubes of constant diameter, which may entangle with other chains and tubes during deformation. In uniaxial deformation, the tubes are deformed in the same direction and so the least amount of entanglement occurs. In equibiaxial tension, where the material is deformed by equal amounts in two perpendicular directions, the maximum amount of tube entanglement occurs. This phenomena explains the magnification of stress from the conforming uniaxial tensile deformation to the more constrained equibiaxial tensile deformation.

Prior to vulcanization, rubber materials are typically in a fluid-like state at room temperature (7). The ratio of the shear and bulk modulus for a fluid is very low. This implies that applied stress will cause the fluid to distort but its volume will not change unless the fluid is highly confined. When rubber is vulcanized, the low ratio of shear to bulk moduli is retained. The linear equation relating the bulk modulus K, the shear modulus G and the Poisson's ratio ν is given by

$$\nu = \frac{(3K - 2G)}{(6K + 2G)} \tag{2.14}$$

If the ratio of G/K tends towards zero, the Poisson's ratio tends towards 0.5. In this case, a simple tensile deformation causes enough hydrostatic compression in the transverse direction to preserved volume. Therefore, unless the rubber material or component is highly confined, loads applied to rubbers cause only isochoric deformations.

Vulcanized rubber ideally behaves as an incompressible elastic solid, in that it returns to its original configuration upon removal of stress. The described elastic behaviours of rubber are defined by hyperelasticity. This is discussed in greater detail in Section 2.3. However, rubber is affected by rate-dependence, inelastic effects and other phenomena. Rubbers used in industry are often highly filled, due to the stiffness reinforcement effect of filler particles. An increased content of filler particles is known to intensify some of these effects (24, 25). When more complex behaviours are modelled, the hyperelastic behaviour represents their equilibrium behaviour (26, 27, 28, 29, 30).

2.2.2 Complex Rubber Behaviours

This discussion of complex behaviours is not considered to be a comprehensive description of all rubber phenomena. For example, the complex behaviour of rubber friction and temperature effects (31, 32) were omitted. As the presented work focuses on the equilibrium hyperelastic behaviour, the prominent complex behaviours for rubber in the time-domain are briefly discussed. The complex behaviours included are hysteresis, viscoelasticity, the Mullins effect and strain crystallisation.

Rubber hysteresis is an elastic phenomenon that appears in cyclic loading. During loading, the stress required to reach a certain strain value is higher than if the same value of strain was measured through unloading. The effect is illustrated in Figure 2.3a. Hysteresis in rubber is often assumed to be a time-dependent viscoelastic effect (2, 33, 34). This is due to its pronounced magnitude at higher strain-rates (24, 26, 35). Bergström and Boyce (26, 35) observed a specimen held at same value of strain reached by loading and unloading over a long relaxation time. They assumed that an infinitely large relaxation time would eventually achieve the same equilibrium stress value. Due to the experimental infeasibility to allow long relaxation times without material degradation, some authors (24, 36) propose that hysteresis may be considered as a time-independent effect. In either case, the equilibrium hyperelastic behaviour may be measured between the loading and unloading responses. The hysteretic response may then be modelled as a scaling of the hyperelastic behaviour with dependence on the nature of the applied loading (35, 36, 37).

The viscoelastic behaviour of rubber is explained in part as time-dependent hysteresis and the description of the remaining behaviour depends on whether the component is strain-loaded or stress-loaded (2, 33, 34). For strain-loading, time dependence is considered in terms of the strain-rate in applying or removing a load and the duration of strain-loading if the load is held constant. In strain-loaded experiments with linearly scaled strain-rates, the measured stress responses are amplified for higher strain-rates, as shown in Figure 2.3b. This amplification is nonlinearly related to the strain-rates (29, 35, 38). If strain-loads are applied and held constant, stress relaxation will occur at a higher rate for larger strains, shown in Figure 2.3c. Due to nonlinear viscoelasticity, the rate of relaxation is nonlinearly related to the magnitude of the applied strain. With constant stress-loading, the strain will increase over time during loading and decrease during unloading, both tending towards equilibrium, shown in Figure 2.3d. This creep behaviour is nonlinearly related to the amplitude of the applied stress. These effects may also be modelled as a scaling of the equilibrium hyperelastic behaviour (29, 35, 37), but the scaling should account for nonlinear time-dependence. For an application without dynamic effects or rubbers with very short relaxation times (39), the viscoelastic effects may be neglected.

When rubber is cycled to the same magnitude of stress or strain, a stress softening (35) or cyclic creep (40) response occurs between each subsequent load cycle during the first number of cycles. The largest softening occurs after the first cycle (41) and the effect has been found for up to ten cycles (42). This softening is known as the Mullins effect (43). An idealised depiction of the Mullins effect, which removes the hysteretic behaviour, is shown in Figure 2.3e. In this idealised Mullins effect behaviour, the first loading to any strain magnitude that exceeds the maximum of the material's loading history has an amplified stiffness during loading. The unloading path is then at a

lower stress than the unloading for any previous maximum. All subsequent loadings lie on the unloading path of the historical maximum load (44). The effect may also be coupled with residual strains, which are known as permanent set for rubber (45). The amount of permanent set increases with strain magnitude and the percentage filler content (25). Without hysteresis, the Mullins effect and permanent set may be modelled by a hyperelastic constitutive model with a damage parameter (25, 30, 44). More complex models account for the induced anisotropy of the Mullins effect. These models also use the hyperelastic behaviour as the equilibrium response but, as the historical maximum loading and softening occurs in the direction of the applied load, a directional history is required (37, 46, 47).

Strain crystallisation is another cyclical behaviour. It affects the stress-strain response similarly to the Mullins effect, as shown in Figure 2.3f. During loading, rubber may begin to crystallise once the strain exceeds a critical strain threshold (48), which increases the stiffness. Upon unloading, the crystallites begin to melt, lowering the stiffness, and the stress-strain path reunites the loading curve at approximately the point of the critical strain threshold. The capability of a rubber to crystallise depends on its backbone monomer (2). For crystallising rubbers, the strain at which crystallisation occurs is dependent on the compounding recipe and it ranges from a lower limit of around 200% up to 450% (7) at room temperature. The onset of crystallisation is delayed by higher strain-rates and at higher temperatures (49). Loos et al (48) recently demonstrated a thermodynamically consistent constitutive model to predict the stress-strain behaviour and a measure of the crystallinity content of a crystallising rubber in a uniaxial tension test. This model is based on the assumption that a hyperelastic constitutive model represents the equilibrium behaviour of the material.

2.2.3 Complete Behaviour of Rubber

From the literature, it is clear that the molecular theory of the rubber elasticity is well understood and there is significant progress in understanding and modelling the discussed complex effects. There are several models that take into account two or more of these behaviours. Hysteresis, viscoelasticity and the Mullins effect have been modelled successfully (30, 50, 51). Models are also available for complex processes such as rubber curing (52, 53, 54) and the thermal recovery of the Mullins effect (55). The common goal of research into these complex behaviours and processes seems to be to achieve a complete model for rubber. In state of the art research, hyperelasticity is used to model part of the equilibrium behaviour of rubber, often as the foundation of a complex model. This highlights the importance and relevance of further study into accurate numerical modelling of rubber hyperelasticity.

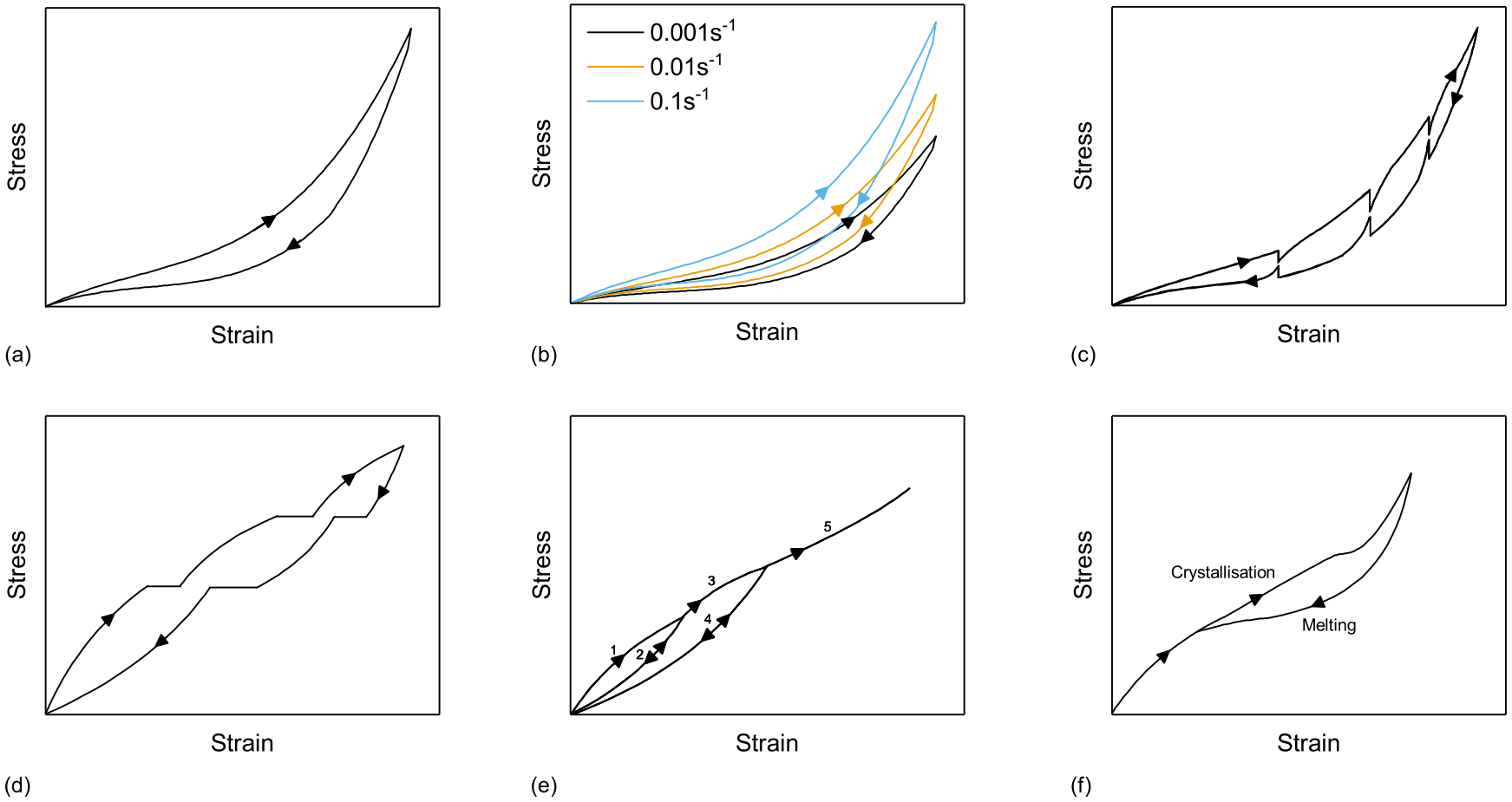

Figure 2.3: Stress-strain plots of complex rubber behaviours in uniaxial tension (a) elastic hysteresis, (b) strain-rate dependence, (c) viscoelastic stress relaxation, (d) viscoelastic creep, (e) idealised Mullins effect, (f) strain crystallisation

2.3 Isochoric Hyperelastic Constitutive Modelling

Based on the framework defined in Section 2.1, a hyperelastic material is an idealised constitutive theory for largely deforming elastic behaviour. The theory assumes that a Helmholtz strain energy function ψ exists (5). Assuming isothermal and isotropic behaviour, the function is objective and fully defined by a strain measure in terms of unit volume, $\psi = \psi(\mathbf{F}) = \psi(\mathbf{QF})$, where $\mathbf{Q}$ is an orthogonal rotation tensor. These functions are often referred to as strain energy density functions or hyperelastic constitutive models. The practical use of strain energy density functions is that they may be used to compute the stress and stiffness of a material. In finite elasticity definitions, these quantities are fully defined by a second-order stress tensor and a fourth-order elasticity tensor. Variations of these tensors exist for reference and current configurations. For demonstration, the material second Piola-Kirchhoff stress $\mathbf{S}$ and the material elasticity tensor $\mathbb{C}$ are defined in terms of the derivative of the strain energy density ψ and the right Cauchy-Green tensor $\mathbf{C}$ by

$$\mathbf{S} = 2\frac{\partial \psi}{\partial \mathbf{C}} \tag{2.15}$$

$$\mathbb{C} = 2\frac{\partial \mathbf{S}}{\partial \mathbf{C}} = 4\frac{\partial^2 \psi}{\partial \mathbf{C} \partial \mathbf{C}} \tag{2.16}$$

As the stress is defined as a derivative of the strain energy density with respect to strain, hyperelastic constitutive models may be formulated from stress-strain behaviour then integrated to determine the strain energy density function (56). Due to the near incompressibility of rubber, the stress-strain behaviour may be assumed to be purely isochoric. Otherwise, the strain energy is split additively into isochoric W and volumetric U components (6) as

$$\psi = W\left(\overline{\mathbf{F}}\right) + U(J) \tag{2.17}$$

The stress and stiffness are also assumed to be additively split into isochoric and volumetric contributions and are computed or measured as such. Both quantities may require definition for numerical methods, however, the subsequent discussion focuses on isochoric hyperelastic constitutive models. It is assumed that rubber is fully incompressible and the discussion of hyperelastic constitutive models is therefore related only to the isochoric behaviour.

The isochoric hyperelastic behaviours, discussed in Section 2.2.1, should be captured by the constitutive model. The constitutive models should be capable of fitting the decreasing stiffness at low strains, the asymptotic finite extensibility and the deformation mode dependence. Many constitutive models have been proposed to predict some or all of these behaviours. The constitutive models may be categorised in two

ways. The first is due to the nature of their constants, which may be either micro-mechanical or phenomenological (11, 57, 58). This means, respectively, that they are defined in relation to physical characteristics of the rubber's microstructure or are purely numerical constants for the purpose of curve-fitting the mechanical response. Alternatively, constitutive models may be categorised on how they define strain (59). The modelling approaches discussed here are categorised as Cauchy-Green invariant constitutive models, principal stretch constitutive models and network constitutive models. Data-driven approaches, which are free of a specific constitutive model formulation, are mentioned for completeness. Prior to these descriptions, postulates and conditions to ensure the physical plausibility of hyperelastic constitutive models are discussed.

2.3.1 Hyperelastic Constitutive Modelling Postulates

To ensure the physical plausibility of a constitutive model, regardless of its phenomenological or micro-mechanical nature, a number of postulates and conditions have been proposed. Postulates were proposed by Treloar (7) and Ogden (19). Attard (60) compiled these with additional postulates related to compressibility. Darijani and Naghdabadi (61) presented postulates based on these for only isochoric behaviour, which are as follows

1. *"The strain energy density function must be non-negative for all deformations."*
2. *"The strain energy density function must be invariant under coordinate transformations."*
3. *"The strain energy density must be a function of either the stretch or strain invariants. Also, because of isotropy, the strain energy density is symmetrical with respect to the principal stretches λ_1, λ_2 and λ_3."*
4. *"The strain energy density must have a zero value at the undeformed state ($\lambda_1 = 1$, $\lambda_2 = 1$ and $\lambda_3 = 1$)"*
5. *"The strain energy density must be a minimum at the undeformed state. This guarantees that the material is stress free at the undeformed state." Hence*

$$\left(\frac{\partial W}{\partial \lambda_a}\right) = 0, \quad a = 1, 2, 3 \tag{2.18}$$

$$\left(\frac{\partial^2 W}{\partial {\lambda_a}^2}\right) > 0, \quad a = 1, 2, 3 \tag{2.19}$$

6. *"The strain energy density must approach positive infinity at the singularity case ($\lambda_1 = 0$, $\lambda_2 = 0$ or $\lambda_3 = 0$) and for very large deformations ($\lambda_1 = \infty$, $\lambda_2 = \infty$ or $\lambda_3 = \infty$)."*

A constitutive model obeying these conditions would have an initial positive stiffness and an asymptotic response. To ensure positive stiffness until finite extensibility, the Drucker stability inequality (62), $\left[\sum_{i=1}^{3} \mathrm{d}\sigma_i \mathrm{d}\epsilon_i > 0\right]$ where σ is the Cauchy stress, should be satisfied. These would ensure only that the finite extensibility was modelled and the decreasing stiffness at low strains could be modelled. The Baker-Ericksen inequality (63), $\left[\left(\sigma_i - \sigma_j\right)\left(\lambda_i - \lambda_j\right) > 0 \text{ if } \lambda_i \neq \lambda_j\right]$, should also be obeyed. This ensures that the direction of the largest principal stress is in the direction of the largest principal stretch. However, no postulate or inequality is known to define the deformation state dependence of the stress response and its physical nature.

Few constitutive models are known to have been developed on the basis of physically plausible postulated behaviour (16, 18, 61). Models developed on the basis of stress-strain relationships require a correction factor after integration to ensure zero energy in the undeformed state (56, 64). The more common approach taken to achieve this is through constrained parameter identification (22, 63, 65). Constitutive models, whether described phenomenologically or micro-mechanically, are typically developed with the aim of describing experimental data. For use in analytical or numerical predictive methods, hyperelastic constitutive models are fully defined in terms of common strain measures, their derivatives and numerically fitted parameters.

2.3.2 Cauchy-Green Invariant Constitutive Models

Many constitutive models are defined in terms of the first and second isochoric Cauchy-Green invariants, $\overline{I}_1$ and $\overline{I}_2$. One of the earliest models was proposed by Mooney (66). This was expressed in terms of Cauchy-Green invariants by Rivlin (67) and is commonly known as the Mooney-Rivlin model. Rivlin (68) later derived a general expression, from which the Mooney-Rivlin model is a specific form of, it is defined as

$$W_R = \sum_{i,j=0}^{n} C_{ij} \left(\overline{I}_1 - 3\right)^i \left(\overline{I}_2 - 3\right)^j \tag{2.20}$$

This constitutive model is often referred to as the generalised Rivlin model or the polynomial model (63). The Mooney-Rivlin model is described as the case where $i = j = 1$ and $C_{00} = C_{11} = 0$ leaving the two coefficient model with parameters C_{10} and C_{01}. Simplifying to one parameter C_{10}, so that $C_{01} = 0$, leaves the neo-Hookean model (69). This simple one parameter model defined only by $\overline{I}_1$ is said to represent the Gaussian network (7). To model the complete hyperelastic response, many other models are derived from the generalised Rivlin form using the infinite combinations of whole integer values for i and j. As reviewed by Hartmann (63), models are less numerically stable when a greater number of higher-order terms are included. The

stability of models fitted to experimental data is also dependent on the extent of experimental data available (70).

Modifications of the generalised Rivlin model form the basis of many other constitutive models. The reduction to only terms using the first invariant $\bar{I}_1$ is said to improve stability (70). Non-integer powers may be used (71, 72) to improve the mathematical range of fitted behaviour. Many of the proposed models based on the generalised Rivlin model have been derived from a model building approach. Model building approaches using Cauchy-Green invariants were reviewed by Beda (73) and Darijani and Naghdabadi (61). Their approaches consider paired combinations of the invariants using polynomial, power law, exponential and logarithmic terms. These models can be created in terms of the strain energy density functions or as a stress function by the derivatives of W with respect to $\bar{I}_1$ and $\bar{I}_2$ (56, 74, 75, 76). These approaches demonstrate the infinite possibilities of modelling hyperelasticity by Cauchy-Green invariants.

An alternative approach to constitutive modelling with Cauchy-Green invariants is to fit the three characteristic features of a typical rubber material. As mentioned, the low strain behaviour can be predicted by a simple one term neo-Hookean model (7) defined in terms of the first invariant $\bar{I}_1$. Models of the finite extensibility behaviour build upon this by including an additional parameter to define the location of the asymptotic behaviour, also in terms of only $\bar{I}_1$. The inverse Langevin function was shown to be approximated by Arruda and Boyce (15) in their eight-chain model. Following this, a simpler phenomenological model using a logarithmic term to predict the finite extensibility was proposed by Gent (18). These models, and similar terms within more complex models (22, 77), were shown to be equivalent by Chagnon et al (78) as they all use two parameters with the same purpose of providing an initial stiffness and an asymptotic response at finite chain extensibility.

The low strain and finite extensibility behaviours, whether described phenomenologically or micro-mechanically, are modelled capably by the first Cauchy-Green invariant $\bar{I}_1$. Models of the tube-like phenomena, responsible for the deformation state dependence, are often defined with two additive contributions, one part defines the energy of the chains and the other part defines the tube constraints (12, 14, 22, 59, 79). Khiêm and Itskov (59) approximate the tube behaviour using a one parameter additive contribution in terms of the second invariant $\bar{I}_2$. The second Cauchy-Green invariant is significantly higher for the same value of stretch in equibiaxial tension compared with uniaxial tension. It is therefore a useful term in predicting the distinction between deformation states (80). The extension of a two parameter finite extensibility model to consider this behaviour by an additional $\bar{I}_2$ term is common

(10, 77, 81, 82). Of the known tube models, the tube component is more commonly modelled in terms of principal stretches (12, 14, 22, 79).

2.3.3 Principal Stretch Constitutive Models

Hyperelastic constitutive models defined in terms of principal stretches were originally based on the Valanis-Landel hypothesis (83). The "model" proposed by Valanis and Landel (83) assumes the strain energy is a separable function of the three principal stretches such that the total strain energy density function is defined by

$$W_{VL} = f(\lambda_1) + f(\lambda_2) + f(\lambda_3) \tag{2.21}$$

The model is unlike other constitutive models as it does not have adjustable parameters. Each function of energy is to be determined from experimental data in which one stretch is held constant as another is applied. On its own, the model is more frequently referred to as a hypothesis. From this hypothesis, Ogden (84) developed a purely phenomenological constitutive model in terms of principal stretches with a wide fitting capability (85)

$$W_{Og} = \sum_{i=1}^{N} \frac{2\mu_i}{{\alpha_i}^2} \left({\overline{\lambda}_1}^{\alpha_i} + {\overline{\lambda}_2}^{\alpha_i} + {\overline{\lambda}_3}^{\alpha_i} - 3 \right) \tag{2.22}$$

The Ogden model may be viewed as a phenomenological power law model in terms of principal stretches (86). Attard (60) proposed a similar model where each power of N has two component terms, though this model can be derived from the Ogden model. Phenomenological models in terms of principal stretches may also be derived or constructed from exponential and logarithmic terms, or combinations of any of these (13, 64, 87). As with Cauchy-Green invariant models, the number of terms and the use of higher-order terms in a model increases the likelihood of numerical instabilities (62, 88).

Principal stretch constitutive models may also be derived with a view of fitting the complete hyperelastic behaviour. The Gaussian response is modelled by a single term Ogden model with $N = 1$ and $\alpha_1 = 2$. Using equation (2.7), this model is equivalent to the neo-Hookean model (69). A finite chain extensibility model in terms of logarithmic principal stretches was proposed by Horgan and Murphy (89). The model of Davidson and Goulbourne (12) uses principal stretches to define the finite extensibility and the tube constraints. However, as the first invariant adequately models the chain contribution, other tube models use the first invariant for this and the tube contribution is predicted with one or two additional parameters in an additive contribution defined in terms of principal stretches (12, 14, 22, 79). Though there are a greater number of micro-mechanical tube-like models defined in terms of principal

stretches, in general, fewer models are known to have been derived with this strain measure. It is supposed (40) that this is due to the difficulties associated with their implementation in a numerical method. These difficulties are discussed in further detail in Section 2.5.2.

2.3.4 Molecular Network Constitutive Models

The molecular phenomena of rubber hyperelasticity may be approximated in some cases by Cauchy-Green invariants and principal stretches. However, a closer physical definition is possible through the use of network models. In these models, the behaviour of rubber molecules are approximated by a simplified unit-cell microstructure (90). If the assumed chain model is of simple enough geometry, the deformation may be scaled up to macroscopic strain measures, as is the case for the three-chain (91) and eight-chain (15) models. It was shown in a review by Boyce and Arruda (90) that the eight-chain model shows a greater deformation state dependence than the three-chain model, but is still lacking in this area (10, 92). The difference is due to the eight-chain model modelling non-affine chain deformation. Affine network models assume that the stretch of a chain is equal to the macroscopic stretch. In a real polymer network, a chain approaching its finite extensibility limit will oppose further stretch and surrounding chains will therefore stretch more to account for further increases in macroscopic deformation (7). An improvement on the eight-chain model is the non-affine micro-sphere model proposed by Miehe et al (11). This model considers both the finite extensibility of chains and the tube-like constraints using an integration of a unit-sphere by 42 chains, 21 chains with symmetry.

2.3.5 Data-driven Approaches

Although data-driven approaches were not explored, an overview is presented for completeness. These methods require a wealth of experimental data and may even require specially developed simulation tools (93). The first and simplest data-driven method was the general first-invariant hyperelastic constitutive model by Marlow (94). This model uses a single set of experimental data to obtain the derivative of the measured strain energy density with respect to the first invariant. The stress and stiffness are computed by interpolated experimental values. As only one experiment may be used, the deformation state dependence is not predicted accurately by this approach. Marlow (95) later extended this to include the second invariant and incorporate uniaxial tension and equibiaxial tension, or equivalent data. Deformation states lying between these are interpolated by an energy contribution from each of the measured experimental data sets.

An alternative approach was presented by Sussmann and Bathe (96) using spline interpolations of the strain energy defined in terms of principal logarithmic strains. This method allows any number of data points obtained from conventional homogeneous experiments to be used. Latorre and colleagues (97, 98, 99, 100) further developed these models referring to them as WYPIWYG ("what you prescribe is what you get") models. The WYPIWYG models have been extended to include transverse isotropic hyperelasticity, orthotropic hyperelasticity and compressibility. A development of data-driven isotropic hyperelasticity models by Dalemat et al (93) enables the use of inhomogeneous experimental methods. This is achieved by matching experimentally measured digital image correlation (DIC) quantities to their equivalent simulated values by FEA.

2.4 Experimental Parameter Identification

The review of hyperelastic constitutive modelling revealed that regardless of the approach taken, models are constructed and chosen based on their ability to fit stress-strain experimental data from the material of interest. Experimental test specimens should be extracted from the component itself or manufactured similarly to the component (62, 101, 102). A hyperelastic constitutive model is fitted to experimental data by the adjustment of its parameters. This is achieved by comparing the experimental and model predicted values graphically or more accurately by the use of an error function. The error is minimised by adjustment of the constitutive model parameters manually or by an optimisation algorithm.

Parameter identification by conventional homogeneous experimental methods is a focus of the presented work. These methods are outlined with reference to their experimental procedure and measurements. Inhomogeneous parameter identification methods are mentioned for completeness. Following this, two particular aspects of experimental parameter identification are discussed: the extent of experimental data required to model the complete hyperelastic behaviour and the selection of constitutive models. The ideal hyperelastic constitutive model would be that which could predict the complete behaviour using the least amount of experimental data.

For an incompressible material, the entire range of deformations may be represented by the region of attainable deformations (103) on a plot of the isochoric invariant plane, as shown in Figure 2.4. Each point in the region of attainable deformations is defined in terms of the first and second Cauchy-Green invariants $\bar{I}_1$ and $\bar{I}_2$. The isochoric invariants were computed in terms of the experimental principal stretches, as defined in equations (2.6) and (2.9). Evaluating the ability to fit or predict the complete hyperelastic behaviour therefore requires experimental data across this region.

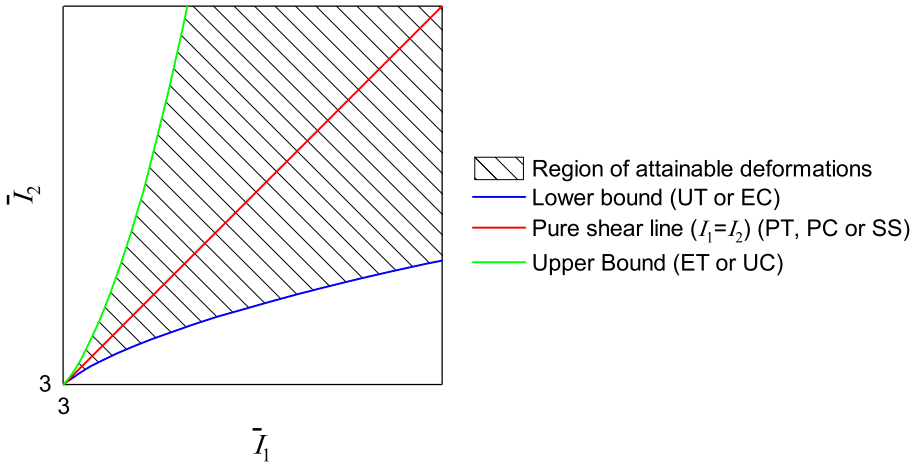

Figure 2.4: Dimensionless plot of the isochoric invariant plane

2.4.1 Homogeneous Experiments for Parameter Identification

Homogeneous experiments are assumed to be those in which the strain may be reduced to a single scalar quantity. The stress and stiffness tensors may therefore also be reduced to scalar functions. Based on this assumption, two further restrictions are placed on the definition of a homogeneous experimental method. A homogeneous experiment requires that the stress and strain is assumed to be constant in a measurable region of the specimen. The other is that the stress should be computed as a function of a measured strain quantity directly, such that an iterative solution is not required. These restrictions mean that only a limited number of experiments are referred to throughout. In terms of the invariant plane, the strain range of an experiment loaded monotonically in one state of deformation is restricted to the upper and lower bounds and the pure shear line. These are referred to throughout as single loading experiments. To obtain additional data by a homogeneous experiment, a general biaxial experiment is used, which consists of multiple loadings in tension.

Due to the high bulk modulus of rubber, homogeneous experiments are assumed to be approximated by fully incompressible behaviour. Symbolic distinctions are therefore not made for isochoric quantities.

Uniaxial Tension and Equibiaxial Compression The lower bound of the region of attainable deformations is achieved experimentally by uniaxial tension (UT) or equibiaxial compression (EC). The uniaxial tension experiment is common as it is simple to perform and does not require bespoke equipment. Testing procedures are well-defined for rubber by the international standards BS ISO 37 (104) and ASTM D412 (105). Alternatively, the equivalent equibiaxial compression experiment is not

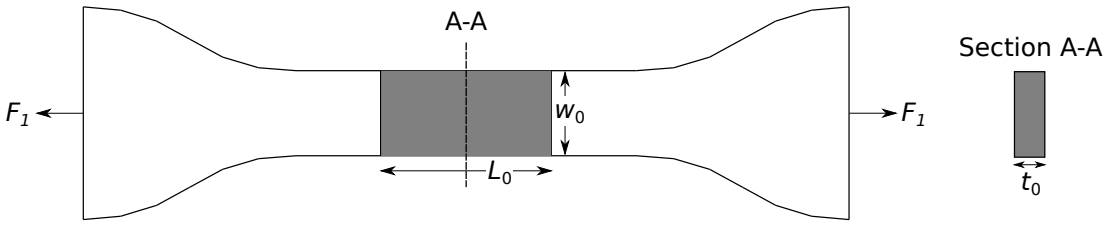

Figure 2.5: Uniaxial tension "dogbone" specimen with highlighted gauge length

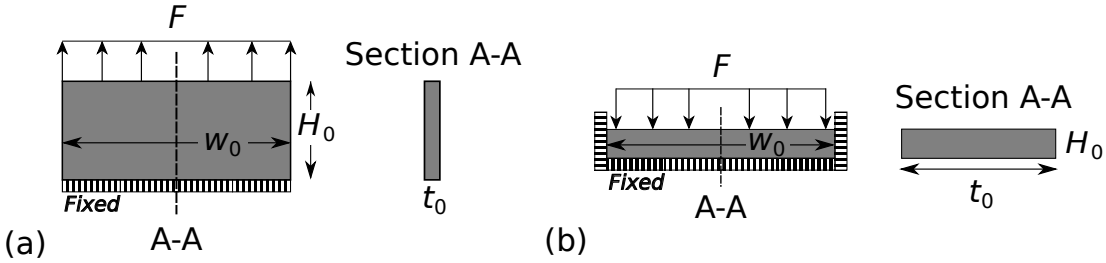

Figure 2.6: Planar experimental specimens: (a) planar tension, (b) planar compression

known to have been realised experimentally. Therefore, only the uniaxial tension experiment was considered.

In a standardised uniaxial tension experiment, a "dogbone" shaped specimen of constant thickness is loaded in the direction of its longest dimension, as shown in Figure 2.5. The loading may be applied by a force or displacement, which are equivalent for a time-independent material. The strain is measured by observation of two or more points in the gauge length of the specimen where the deformation is assumed to be homogeneous. The measured nominal strain ϵ_1 is the ratio of the change in length ΔL to the original length L_0 of two observed points, defined as $\epsilon_1 = \Delta L / L_0$. The first principal Piola-Kirchhoff, or nominal, stress P_1 is found from the measured longitudinal force F_1 divided by the undeformed cross-sectional area of the gauge length $A_0 = w_0 t_0$, in terms of its undeformed width w_0 and thickness t_0, as $P_1 = F_1 / w_0 t_0$.

Planar Tension and Planar Compression International standards are not known for either planar tension or planar compression experiments. The planar tension experiment is more common but requires a bespoke wide grip fixture (106, 107). The specimen should be wide enough that thinning in its width direction may be treated as negligible. The planar compression experiment also requires bespoke equipment in the form of a wide bounded compression channel (26, 35). Furthermore, it is required that friction is negligible. The lateral constraints of the channel ensure the specimen remains constant in this direction. Diagrams of these experiments are shown in Figures 2.6a and 2.6b.

Ensuring that the undeformed width $w_0 = w$ and therefore the strain in one dimension is kept constant, $\epsilon_2 = 0$ or $\lambda_2 = 1$, the applied stretch λ_1 is inversely proportional

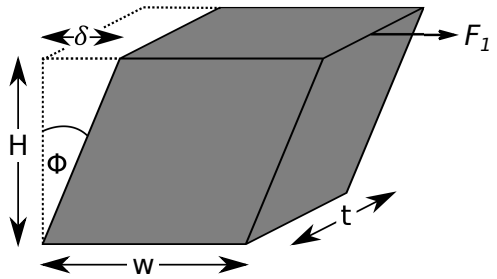

Figure 2.7: Idealised deforming homogeneous simple shear specimen

to the remaining free stretch λ_3, whether loaded in tension or compression, such that $\lambda_1 = 1/\lambda_3$. This leads to a deformation where the first and second strain invariants are equal $I_1 = I_2$ and the deformations are therefore equivalent to pure shear. The measured nominal strain ϵ_1 is the ratio of the change in height ΔH to the original height of the specimen H_0, defined by $\epsilon_1 = \Delta H / H_0$. The first Piola-Kirchhoff stress P_1 is calculated by the same method as the uniaxial tension experiment, $P_1 = F_1 / w_0 t_0$.

Simple Shear An alternative method of attaining experimental data for the pure shear line of the invariant plane is by a simple shear experiment, shown in Figure 2.7. This experiment is described for rubber in the testing standards BS ISO 1827 (108) and ASTM D429 (109). With the exception of Method A in BS ISO 1827 where a 25% shear modulus is found, the primary focus of these standards is related to the adhesion behaviour of rubber. However, the procedure to obtain stress-strain data from this test may otherwise be found in the literature (7, 110, 111, 112).

In this experiment, one or four rubber cubic specimens are bonded to metal plates that are assumed to be rigid. The rigid plates are then displaced with constant separation to maintain the specimen height. Throughout their deformation it is assumed that the specimen maintains a constant parallelogram cross-section and constant thickness. The strain measure for this test is unlike the others in that a dimensionless quantity κ is used, known as the amount of shear. κ is related to the ratio of the displaced distance δ and the fixed specimen height H, through $\kappa = \delta / H$. It is therefore equivalent to $\tan \phi$, where ϕ is the angle of the shear deflection as annotated in Figure 2.7. The stress measure used for simple shear is the first Piola-Kirchhoff shear stress P_{12}. This is obtained experimentally from the applied force F_1 divided by the constant area $A = wt$ of the top face of the specimen by $P_{12} = F_1 / A$. Though it is known that a physical specimen will deviate from this idealised deformation (113, 114), if the bulk of the material follows the assumed behaviour then the deviation is assumed to be negligible.

Equibiaxial Tension and Uniaxial Compression Equibiaxial tension and uniaxial compression are equivalent experimental means of attaining data for the upper

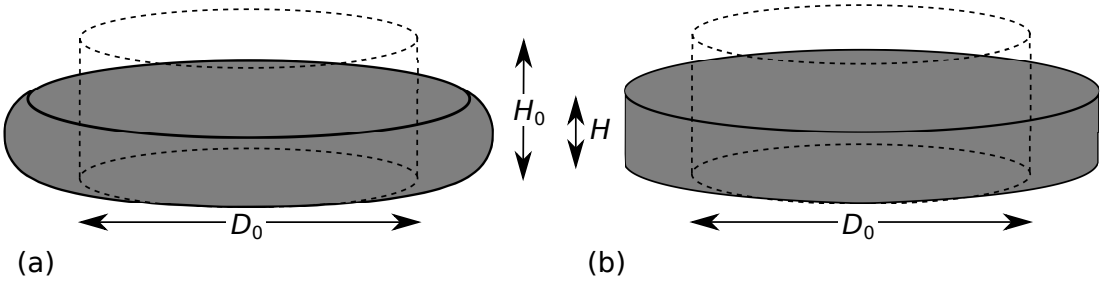

Figure 2.8: Uniaxial compression specimens (a) bonded compression, (b) frictionless compression

bound of the region of attainable deformations. While there are no known industry standards for the testing procedure of equibiaxial tension experiments on rubber, uniaxial compression experiments are described in ASTM D575 (115) and BS ISO 7743 (116).

In the testing procedure of ASTM D575 (115), a cylindrical specimen is compressed between rigid platens with either a bonded or high friction interface to prevent slip. This results in an inhomogeneous deformation, as shown in Figure 2.8a. As a result of the bulging behaviour, the force and displacement data cannot be interpreted in terms of stress and strain. To achieve the desired homogeneous deformation state by a uniaxial compression test, a frictionless interface is required, shown in Figure 2.8b. In BS ISO 7743 (116), it is recommended that the test specimen is suitably lubricated and has a slenderness ratio (height to diameter) greater than one. In an idealised frictionless uniaxial compression experiment, identical stress-strain results would be found regardless of specimen geometry. This is not possible in practice and negligible friction should be sought. A high slenderness ratio is known to reduce the effect of friction (116, 117, 118) but is limited by buckling effects when the slenderness ratio > 1. The compressive strain is found from $\epsilon_1 = \Delta H / H_0$ and the compressive first Piola-Kirchhoff stress is computed by $P_1 = F_1 / A_0$, where the undeformed area A_0 is defined in terms of the undeformed diameter D_0 as $A_0 = \left(\pi {D_0}^2\right)/4$ and the other symbols have their usual definitions.

In an equibiaxial tension test, bespoke testing equipment is required in order to apply equal perpendicular stretches to a region of a rubber specimen (119, 120, 121). This can be achieved using a cruciform specimen, as shown in Figure 2.9a. By application of equal and perpendicular forces or displacements, the centre of the specimen is deformed homogeneously in a state of equibiaxial tension. Alternatively, but with greater complexity, square or circular specimens may be used with circumferentially symmetric tensile loading. The use of advanced optical methods, e.g. DIC (122), and an optimised specimen geometry is recommended (39, 123, 124). Tensile equibiaxial loading is difficult to attain high strains due to stress concentrations occurring around where the specimen is gripped. Alternatively, a thin circular specimen may be

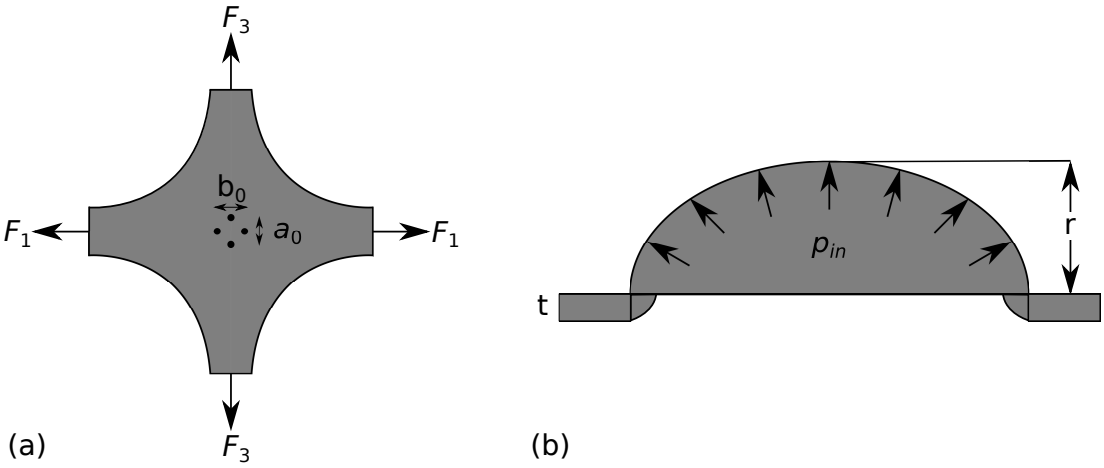

Figure 2.9: Equibiaxial tension specimens (a) (equi)biaxial cruciform, (b) membrane inflation

inflated to produce an equivalent deformation at the apex of the inflated membrane (106, 125, 126, 127), as shown in Figure 2.9b.

By either variation of tensile loading, the nominal strain ϵ_1 may be measured by continuous observation of two points, or a shape, within a central region of the specimen. In terms of an initial distance between two points a_0 and the change in distance Δa, the nominal strain is therefore defined as $\epsilon_1 = \Delta a / a_0$. For planar equibiaxial experiments, the first Piola-Kirchhoff stress is defined by $P_1 = F_1 / A_0$, using the measured or applied force in either direction $F_1 = F_3$ and the undeformed cross-sectional area A_0 of the region of interest. The undeformed area is defined as $A_0 = b_0 t_0$, where the distance $b_0 = a_0$ due to the equal perpendicular loading and t_0 is the thickness of the undeformed specimen. In the inflation experiment, the first Piola-Kirchhoff stress is defined by the membrane stress $P_1 = p_{in} r / 2 t_0$ (106). Here p_{in} is the applied pressure, r is the radius of curvature of the membrane and t_0 is the initial thickness of the membrane, as annotated in Figure 2.9b.

General Biaxial Strain Using a cruciform or square specimen, the general biaxial experiment is measured by the same method as the equibiaxial experiment shown in Figure 2.9a but requires independent actuation of the perpendicularly applied loading. This allows measurement of strains in both ϵ_1 and ϵ_3 directions. The measured forces F_1 and F_3 are then used with their undeformed perpendicular areas to compute P_1 and P_3. A typical testing method (128, 129) is to initially load the cruciform specimen in the λ_1 direction, creating an initial uniaxial tension deformation state. The perpendicular load λ_3 is then applied from its contracted state until the equibiaxial tension state, $\lambda_3 = \lambda_1$, with stress and strain measured throughout.

2.4.2 Inhomogeneous Experimental Parameter Identification

To reduce the time and difficulty of obtaining the experimental specimens and performing the conventional homogeneous experiments, alternative means of parameter identification have been developed using inhomogeneous experiments. In an inhomogeneous experiment, a specimen may be deformed in multiple deformation states simultaneously (130). A numerical method may then be used to simulate the inhomogeneous specimen and compare its results to multiple experimentally measured quantities. The experimental quantities may consider only macroscopic behaviour, the force and displacement of an indentation test (131, 132) for example, or a full-field measurement, such as a three-dimensional strain field (125). These experimental measurements may be compared to FEA results by the inverse Finite Element Method (133, 134). As with homogenous experiments, the error between experimental and numerical quantities is minimised by optimisation of constitutive model parameters.

An approach developed with a focus on industrial rubber components is component-oriented parameter identification (102, 135). In this method, the specimen geometry and boundary conditions are chosen to be similar to the component and its operating conditions. The deformation state and strain range of the simplified component is therefore similar to that of the component during operation. Another advantage is that the differences in material properties due to the production between the experimental specimen and the component are reduced. This method provides an alternative viewpoint for parameter identification where only sufficient experimental data of the component is collected, rather than experimental data for the complete behaviour of the material. Though the computational nature of this method, and inverse FE methods in general, is more complex and more time consuming, the extent of experimentation is more efficient.

2.4.3 Selection of Experimental Methods and Constitutive Models

Numerically predicting the complete hyperelastic behaviour of a rubber material or component is important in engineering design (136, 137). It is apparent that a model's ability to predict general hyperelastic behaviour would be related to how well it can fit or predict general biaxial experimental data (128, 129). Though the complete hyperelastic behaviour is also assumed to be consistently predicted by a constitutive model capable of fitting or predicting a complete set of single loading homogeneous experiments (7, 84, 127, 138). A complete set of single loading homogeneous experiments is therefore assumed to consist of uniaxial, planar and equibiaxial tension experimental data, or data from equivalent experiments.

It has been suggested that parameters identified to uniaxial and equibiaxial tension, or both uniaxial states, can also predict the complete hyperelastic response (117, 139, 140). If both variations of complete data are equivalent, they will return the same parameters. Other combinations of data, or the use of one single loading experiment, to identify parameters are generally considered as being incapable of accurately predicting the complete behaviour (11, 39, 141, 142). It has also been shown for fits to single experiments that extrapolating beyond the experimentally measured strain range has high variation for different models (143, 144). However, it is not known if models fitted or predicting the complete behaviour also have high variation beyond the fitted strain range. Furthermore, this ability and more generally the extent of experimental data required may be dependent on the chosen constitutive model.

A vast number of hyperelastic constitutive models are available. To predict the behaviour of a material, the models' parameters are identified by fitting prescribed experimental data. In an ideal scenario, for any constitutive model and any experimental method, unique parameters would be found. As a minimisation problem, a unique global minimum, which gives unique parameters, is known to be dependent on both the choice of constitutive model and experimental method (145). A simple one parameter model may have a unique minimum when identified to a single experiment (146). If the parameters are suitably constrained (141), the same can be shown for models with a greater number of parameters fitted to a single experiment. However, complete hyperelastic behaviour requires a prediction of deformation state dependence, found using multiple experiments.

A one parameter model fitted to data from one single loading experiment requires a different magnitude when fitted to a different experiment (57). A constitutive model capable of predicting the complete hyperelastic behaviour of rubber that returns the same parameters regardless of experimental input is not known. However, it has been shown that the use of a physically defined constitutive model may return similar parameters and therefore predict similar behaviour when fitted to data from different deformation states (57, 58, 132). Of particular interest is the extended-tube model, which was shown by Hossain and Steinmann (58) to accurately predict unfitted experimental data. Parameters were identified using each of the single loading experiments from the complete data set of Treloar (127), and its predictions of the unfitted deformation states were shown to be accurate.

Another approach to constitutive model selection is to refer to studies where models are ranked against one another. In Marckmann and Verron (138), twenty constitutive models are compared and their ranking is based on several factors: the ability to fit the complete strain range, the number of parameters (lower being better) and the

same parameter set being able to simultaneously predict the data of Treloar (127) and Kawabata et al (129). If models remain alike after those three criteria then a micro-mechanically defined model is given preference of a higher ranking. Given that the experimental materials and procedures of Treloar (127) and Kawabata et al (129) are not identical, this associated criterion is considered to be unsubstantiated.

The ranking study by Dal et al (147) compares forty models and considers only the ability of the model to fit the prescribed data, with modification of the strain range if an adequate fit cannot be found. As these ranking studies focus on the fitting of the data of Treloar (127), it is unknown if the rankings are generally applicable to complete hyperelastic material data. A more appropriate method of constitutive model selection may be to repeat the procedures of these ranking studies and use the model with the lowest error when fitting the prescribed data.

2.5 Finite Element Implementation of Hyperelastic Constitutive Models

The geometry and loading conditions of industrial rubber components means that simple analytical solutions, as used for homogeneous deformations, are rarely applicable to predict their behaviour. The complex nonlinear behaviour of rubber may be modelled by a numerical method, such as the FEM. The FEM software used throughout the presented work was Abaqus (3). Within this package, the implicit solver Abaqus/Standard was preferred over the explicit solver Abaqus/Explicit. This was due to the Abaqus/Standard better modelling static simulations and approximating incompressibility, whereas Abaqus/Explicit is better suited to transient analyses. The elements and formulations in Abaqus/Standard are capable of accurately modelling the near or fully incompressible behaviour of rubber. For an overview of how numerical incompressibility is computed, see Kadapa and Hossain (148).

The associated modelling interface software, Abaqus/CAE, contains a library of hyperelastic constitutive models. This consists of generally understood and well documented models. Many of the highly ranked constitutive models of interest (138, 147) were not available. However, the user subroutine interfaces of Abaqus allow the implementation of any user-defined constitutive behaviour. The FE implementation of hyperelastic constitutive models was therefore investigated, with a focus on Abaqus/Standard user subroutines. In an implicit FEM, like Abaqus/Standard, both the stress tensor and consistent tangent moduli require computation. While stress computations determine the physical nature of the simulated component, the tangent moduli are used in the iterative solution of the stiffness matrices to ensure

convergence and detect stiffness instabilities (149). For hyperelasticity, the consistent tangent moduli are identical to the components of the fourth-order elasticity tensor. As defined in equation (2.16), the elasticity tensor is the derivative of the stress tensor with respect to the strain tensor (5). These derivatives may therefore be found analytically or by alternative differentiation methods. The discussion of the implementation of hyperelastic constitutive models in the FEM is presented in terms of analytical implementations of Cauchy-Green invariant constitutive models, principal stretch constitutive models and implementations by numerical differentiation methods.

2.5.1 Implementation of Hyperelasticity in terms of Cauchy-Green Invariants

For hyperelastic constitutive models defined in terms of Cauchy-Green invariants, two user subroutine interfaces are relevant, UHYPER and UMAT. In both cases, the subroutines are written in fixed format Fortran 77 code and require the user to define a number of predefined variables. These required variables are defined in terms of additional predefined variables, which are read at every iteration of the simulation at each integration point.

UHYPER provides a specialised interface for the implementation of user-defined hyperelastic constitutive behaviour. However, it is restricted to isotropic hyperelastic constitutive models defined in terms of the isochoric Cauchy-Green invariants, $\overline{I}_1$ and $\overline{I}_2$, and optionally the volumetric behaviour may be defined in terms of the volume ratio J. The simulation outputs the magnitudes of these variables to the subroutine. The user is required to define the strain energy density function and its derivatives in terms of these variables. The stress and elasticity tensors are then computed by Abaqus. UHYPER cannot therefore be used for the implementation of constitutive models defined in terms of isochoric principal stretches $\overline{\lambda}_i$, or fictitious tensors, as in the micro-sphere model (11).

The UMAT subroutine interface may be used to define any mechanical constitutive behaviour. The benefit of developing implementations of hyperelastic constitutive models in the UMAT environment is the ability to extend the code to consider more the complex behaviours for which hyperelasticity is the equilibrium response, see Section 2.2.2. As in the UHYPER interface, predefined variables are output by the simulation. In UMAT, these variables are then used to compute the stress and tangent moduli tensors used by Abaqus/Standard. These tensors are defined as the Cauchy stress and the Jaumann-rate of the Cauchy stress, respectively. The elastic strain energy must also be defined if it is to be output by the simulation. For hyperelastic constitutive models, due to their rate-independence, only the deformation

gradient is required to compute the strain energy density, stress tensor and tangent moduli. There are several approaches to obtain stress and elasticity tensors for hyperelasticity in terms of the Cauchy-Green invariants (5, 150, 151, 152). These have some minor differences, primarily in terms of their depth of derivation. One method uses fictitious stress and elasticity tensors and matrix operations (151). The alternative method fully expands and groups terms and may therefore be obtained by any derivation (5, 150, 151, 152). Numerical implementation of hyperelasticity in terms of Cauchy-Green invariants is therefore well understood, though a comparison of these different implementations is not known.

2.5.2 Implementation of Hyperelasticity in terms of Principal Stretches

The current UHYPER interface in Abaqus enables only the implementation of user-defined hyperelastic constitutive models in terms of Cauchy-Green invariants. To implement principal stretch hyperelasticity, the UMAT interface must be used. For the implementation of these constitutive models, various forms of the elasticity tensor were found in literature. The ambiguity of their elasticity tensor transpires as a consequence of how the principal stretches are computed. As the eigenvalues of the Cauchy-Green strain tensors, these may be computed by direct or explicit methods, along with their associated eigenvectors.

The original analytical derivation of elasticity tensors for principal stretch hyperelasticity relied on explicit calculation of these eigenvalues and eigenvectors (19, 153, 154). Though the seminal numerical implementation in the FEM by Simo and Taylor (155) used direct methods to compute the principal stretches. The computation of the principal directions was avoided entirely by the use of eigenvalue bases. This was justified by the aim to reduce computational effort. However, due to technological advances, Simo (156) later stated that explicit calculation should be preferred due to the instabilities associated with the direct methods when the principal stretches are equal or numerically similar (156, 157, 158). Despite this, the direct methods and associated tensors find continued use (22, 132, 158, 159, 160, 161, 162, 163). A detailed numerical implementation for explicitly defined principal stretch hyperelasticity was not found in the literature.

2.5.3 Implementation by Numerical Approximation

In the UMAT interface, an alternative to analytical implementations is to use a differentiation method. Alternative differentiation methods previously applied to obtain tangent moduli can be categorised into symbolic, automatic and numerical methods. In a symbolic differentiation method (164), algebraic mathematics software is used,

or developed, such that the stress equations are differentiated symbolically to give the analytical expressions. Following this, the program codifies these expressions for numerical usage in the form required by the FE solver. In automatic differentiation methods (165, 166, 167, 168), the derivative is obtained numerically by algorithmic accumulation of "elementary operations with known derivatives, thus allowing evaluation of exact derivatives". Perhaps due to the additional programming required, these methods are generally less common. A more prevalent approach applies numerical differentiation methods to obtain approximated tangent moduli, as first proposed by Miehe (169).

For both material and spatial finite strain configurations, Miehe (169) applied a perturbation technique wherein the stress components are perturbed in the six unique directions and orientations of the symmetric stress tensor. The tangent moduli are subsequently found by connection of the perturbed and stationary (unperturbed) stress components by the well-known forward difference formula. This method was further developed by Sun et al (170), adapting the expressions to the Jaumann-rate of the Cauchy stress, for implementation in Abaqus/Standard. In these methods, the accuracy of the numerically approximated tangent moduli is dependent on the magnitude of the applied perturbation. Ideally, as the perturbation tends towards zero, the truncation error would also tend towards zero. However, due to finite floating-point precision in these computational problems, the accuracy is limited due to a conflicting source of error: subtractive round-off error. For an overview of these error descriptions, see the references (171, 172, 173, 174).

The forward difference formula is a first-order approximation but higher-order approximations may also be utilised in this context. The central difference method is a second-order approximation that has been investigated in several studies (173, 174, 175, 176, 177). In (173, 175, 176, 177), it is shown that second-order approximations give more accurate tangent moduli; but their optimal perturbation magnitude is larger due to the influence of the subtractive round-off error. Kiran and Khandelwal (176) use numerical approximations of tangent moduli up to the eighth-order. They found that the computational cost increases (176) as the order of approximation increases. However, the optimal perturbation magnitude and the numerical accuracy of higher-order approximation methods beyond second-order were not investigated.

Approximation methods utilising complex numbers allow for smaller perturbation magnitudes and reduce truncation error, as they are not subjected to subtractive round-off error. Complex approximation methods were first implemented for small strain problems by Pérez-Foguet et al (173, 174), using the complex step derivative approximation (178). This method has also been applied to finite strain problems (149, 175). The numerically approximated Cauchy integral, implemented by Kiran

and Khandelwal (176), is a further example of a complex numerical differentiation method used to compute tangent moduli. Another complex numerical differentiation method uses hyper-dual numbers (179), applied in the context of finite elasticity, by Tanaka et al (180), for first and second derivatives of hyperelastic strain energy functions. The complex approximation methods allow for tangent moduli closer to the analytical solutions. However, their implementation is more difficult than real domain approximations. Complex methods require redefinition of pre-programmed mathematical functions to allow for complex variables, otherwise its benefits are limited (173). Such a change is not possible in older programming languages such as Fortran 77 used by Abaqus/Standard.

Improvements to numerically approximated tangent moduli in the real domain were therefore of interest. Higher-orders of approximation were found to have been applied previously (176), but their numerical accuracy, computational costs and limitations were not known to have been investigated. Additionally, it has been shown in other applications that round-off error may be reduced by the use of increased floating-point precision (181). However, these have also not been investigated in the context of approximating finite elasticity moduli for the FEM.

2.5.4 A Note on Work Conjugacy Errors

The spatial elasticity tensor exists in several other forms due to the requirement of fulfilling objectivity, which is not inherent as in the reference configuration (182). The spatial tensors used throughout were known to be objective. However, a possible concern is that they may not satisfy work-conjugacy (87, 183, 184, 185, 186). These may be missing a volumetric term in their objective rates. The error is therefore insignificant for near and full incompressibility. If compressive behaviour requires consideration, Bazant et al (184) provide a modification for commercial FEM software. This was not needed due to the assumption of near and fully incompressibility.

2.6 Research Aims

Based on the reviewed literature, three key areas were identified for the research conducted and presented in this thesis.

The first area concerned parameter identification of hyperelastic constitutive models by homogeneous experiments. This work is presented in Chapter 3. Many constitutive models appear to be capable of predicting the identified complete hyperelastic response, which consists of a reducing stiffness at low strains, an asymptotic finite extensibility and distinct deformation state dependence. Predicting this behaviour

uses hyperelastic constitutive models that either fit or predict experimental data for these phenomena by optimisation of their parameters. Various postulates and criteria ensure the behaviour of optimised hyperelastic constitutive models is physically plausible. However, similar postulates or criteria are not known for ensuring that homogeneous experimental data is physically plausible. It was determined that a set of postulates to ensure the physical plausibility of experimental data would be proposed and assessed. Data that fulfills these proposed postulated conditions may be assumed to be physically plausible, but the extent of experimental data required to predict the complete hyperelastic behaviour required investigation.

The extent of experimental data was suggested to be dependent on the chosen constitutive model. Whether certain constitutive models are capable of predicting unfitted hyperelastic behaviours would be investigated. Additionally, the applicability of constitutive model rankings would be investigated by the same method. The studies from literature often use only data from single loading experiments. The error when fitting or predicting complete data is often assumed to be an indication of a model's ability to predict the general hyperelastic behaviour. This assumption was studied by comparing their interpolated predictions in terms of the invariant plane. Inspired by component oriented parameter identification, interpolations between strain ranges from lesser amounts of experimental data were investigated. These determined whether the use of only sufficient experimental data was valid for homogeneous experiments.

The second area, presented in Chapters 4 and 5 aimed to develop numerical implementations of hyperelastic constitutive models for the FEM such that any constitutive model could be implemented. These UMAT subroutines aimed to require minimal user input and be made available open-source. Firstly, UMAT subroutines for the two different implementations of Cauchy-Green invariant constitutive models were created. These were compared to equivalent built-in and UHYPER models for validation and to assess their computation time. Implementations using real-domain numerically approximated elasticity moduli were developed. These implementations would investigate the use of higher floating-point precision and higher-order approximations in terms of their numerical accuracy and computation time. Then validated analytical implementations for principal stretch constitutive models were developed using explicitly derived terms and current eigenvalue and eigenvector algorithms.

With the ability to implement hyperelastic constitutive models in the FEM, the third key area, presented in Chapter 6, investigated methodologies for the efficient simulation of industrial rubber components. These methodologies would apply the findings of the study into hyperelastic parameter identification. An approach for gaining only sufficient experimental data, identifying parameters of the constitutive model and

simulating industrial rubber components was proposed. This investigation would validate the proposed methodologies by FEA studies involving real industrial rubber components. The aim being to ensure that hyperelastic constitutive models with parameters identified using sufficient data would give as consistent, or more consistent, predictions of the behaviour of industrial rubber components when compared with predictions by models with parameters identified using complete data.

Chapter 3

Homogeneous Parameter Identification of Hyperelastic Constitutive Models

The prediction of the hyperelastic behaviour of a rubber component requires adequate experimental data. A "complete" set of experimental data is considered to be that which, when accurately fitted, enables consistent predictions of a material or component's general mechanical behaviour throughout the range of attainable deformations. The aim of the following investigations was to determine the extent of experimental data required, or at least recommended, to accurately predict hyperelastic behaviour. Within this, it was considered whether certain hyperelastic constitutive models have the capability to accurately predict a material's response beyond the experimentally measured strain range. The applicability of constitutive model rankings across different materials was also investigated.

Studies of homogeneous experimental data from literature are presented with a focus on parameter identification of hyperelastic constitutive models. The numerical solutions for these experimental methods are described. A set of criteria is proposed to ensure that gathered hyperelastic experimental data is physically plausible. A parameter identification method was developed for investigations into the sufficiency of homogeneous experimental data. Using single loading experimental data, case studies are presented wherein constitutive model parameters were identified using varying extents of experimental data. The final investigation of the chapter assessed the assumption of single loading experiments as a complete experimental data set by comparing predictions of interpolated behaviour. The interpolated data was then used to propose and investigate a more efficient means of parameter identification where only sufficient experimental data is acquired.

3.1 Numerical Solutions for Homogeneous Experiments

In the parameter identification of a hyperelastic constitutive model, experimentally measured data is compared to equivalent numerical predictions made by a constitutive model. Throughout this chapter, it was assumed that the experimented materials are fully incompressible. In the following, the analytical solutions for homogeneous experimental methods are described.

As discussed in Section 2.3, the isochoric contribution W to the strain energy density ψ of hyperelastic constitutive models is generally defined as a function in terms of either the first and second invariants of the isochoric Cauchy-Green strain tensors or the isochoric principal stretches. For hyperelastic constitutive models defined by these strain measures, the analytical solutions to homogeneous deformations are subsequently defined. Analytical solutions for constitutive models defined by alternative means are detailed where required. Simple shear solutions are omitted due to the ability to convert their experimental data to equivalent planar tension data, as later defined in Section 3.2.3.

It was assumed that boundary conditions are applied in the direction of the principal axes for the homogeneous experimental data sets. The analytical solutions were therefore defined in terms of the principal components of the first Piola-Kirchhoff stresses P_i and the principal stretches λ_i, where $i = 1, 2, 3$ each representing a direction of the reference Cartesian coordinate system. The principal first Piola-Kirchhoff stresses are defined for an incompressible material in terms of the partial derivative of the isochoric strain energy density function W by the principal stretches λ_i and the hydrostatic pressure p as

$$P_i = \frac{\partial W}{\partial \lambda_i} + \frac{p}{\lambda_i} \tag{3.1}$$

For convenience, it was assumed throughout that the boundary conditions were applied to the λ_1 and λ_3 directions only, such that the material is free to expand or contract in the λ_2 direction. This implies that the stress in the λ_2 direction is zero, $P_2 = 0$. With the assumption of incompressibility, the unloaded λ_2 direction is therefore used in determining the hydrostatic pressure as follows

$$p = -\lambda_2 \frac{\partial W}{\partial \lambda_2} \tag{3.2}$$

Hence, the applied stress in the λ_1 direction is computed by

$$P_1 = \frac{\partial W}{\partial \lambda_1} - \frac{\partial W}{\partial \lambda_2} \frac{\lambda_2}{\lambda_1} \tag{3.3}$$

The Cauchy-Green invariants may be expressed in terms of the principal stretches, and therefore the first Piola-Kirchhoff stresses are also calculable from equation (3.3).

However, due to the abridged derivatives, it is more convenient to define the first Piola-Kirchhoff stresses in terms of the derivatives of the isochoric energy function W by the first and second invariants I_1 and I_2 as

$$P_1 = 2\left[\left(\lambda_1 - \frac{{\lambda_2}^2}{\lambda_1}\right)\frac{\partial W}{\partial I_1} - \left({\lambda_1}^{-3} - \frac{{\lambda_2}^{-2}}{\lambda_1}\right)\frac{\partial W}{\partial I_2}\right] \tag{3.4}$$

The assumption of incompressibility also permits the relationships between the principal stretches to be defined such that the solutions for homogeneous planar deformations aligned with the principal axes are calculable as follows

$$\text{Uniaxial} \quad \lambda_1 = \lambda_{UT}; \quad \lambda_2 = {\lambda_{UT}}^{-\frac{1}{2}}; \quad \lambda_3 = {\lambda_{UT}}^{-\frac{1}{2}} \tag{3.5}$$

$$\text{Planar} \quad \lambda_1 = \lambda_{PT}; \quad \lambda_2 = {\lambda_{PT}}^{-1}; \quad \lambda_3 = 1 \tag{3.6}$$

$$\text{Equibiaxial} \quad \lambda_1 = \lambda_{ET}; \quad \lambda_2 = {\lambda_{ET}}^{-2}; \quad \lambda_3 = \lambda_{ET} \tag{3.7}$$

These relationships are applicable to uniaxial, planar and equibiaxial deformations in both tension and compression. The first Piola-Kirchhoff stresses in the direction of the applied loads for these single loading deformation states in tension may be defined by $P_{1,UT}$, $P_{1,PT}$ and $P_{1,ET}$, or equivalently $P_{1,UC}$, $P_{1,PC}$ and $P_{1,EC}$ in compression.

For a general biaxial experiment, $\lambda_2 = {\lambda_1}^{-1}{\lambda_3}^{-1}$ and both λ_1 and λ_3 are applied or measured experimentally. The first Piola-Kirchhoff stresses $P_{1,GB}$ and $P_{3,GB}$ are therefore also calculated using either equation (3.3) or (3.4).

3.2 Plausibility of Homogeneous Hyperelastic Experimental Data

As discussed in Section 2.3.1, a number of postulates and conditions have been proposed to ensure constitutive models are physically plausible. Similar considerations are not known for assessing the physical plausibility of hyperelastic experimental data. Based on homogeneous parameter identification experiments and the known postulates, general criteria for assessing plausible hyperelastic experimental data in multiple deformation modes are proposed. In addition, a novel criterion is proposed. An explicit proof of the proposed criterion was not realised, however its prevalence is demonstrable with physically constrained constitutive models. The simple means of assessing the plausibility of hyperelastic experimental data is aided by utilising the equivalence of homogeneous deformation modes for an incompressible material. Case studies on the plausibility of published experimental data sets are then considered, in which plausible experimental data sets were identified for later parameter identification and constitutive modelling studies.

3.2.1 Criteria for Plausible Hyperelastic Experimental Data

The postulates discussed in Section 2.3.1 for a physically realistic strain energy density function were modified here, where applicable, to define criteria for physically realistic experimental data. From an experimental perspective, the following criteria are proposed

1. *Stress magnitude must be zero and at a minimum in the undeformed state*
2. *Stress magnitude must be greater than zero for any non-zero strain*
3. *Stress components should be equal if obtained for applied strains that are equivalent to a coordination transformation, ensuring material isotropy*
4. *Stress should tend towards a positive or negative singular value (until material failure) in the application of a maximum tensile or compressive strain, respectively*

In addition to these criteria, a simple and novel criterion for physically plausible experimental data is proposed. Considering a general biaxial experiment for an incompressible material where strain is applied and varied in the λ_1 and λ_3 directions, leaving the λ_2 direction to deform freely, the fifth criterion is proposed as follows

5. *For a constant applied principal stretch λ_1, where $\lambda_1 > 1$, the first Piola-Kirchhoff stress P_1 increases monotonically as λ_3 increases from $\lambda_3 = \lambda_1^{-1/2}$ to $\lambda_3 = \lambda_1$*

To elaborate, it is considered in this hypothetical general biaxial experiment that the principal stretch in the λ_1 direction is initially loaded while the λ_3 direction is allowed to deform freely, resulting in uniaxial tension. If the principal stretch in the λ_3 direction is then loaded through $\lambda_3 = \lambda_1^{-1/2}$ to $\lambda_3 = \lambda_1$, from uniaxial tension to equibiaxial tension, then P_1 increases as $\lambda_3 \to \lambda_1$, due to the increasing constraint and resulting additional hydrostatic pressure. The prominence of this proposed criterion in physically constrained constitutive models is demonstrated in Section 3.2.2.

This chapter investigates parameter identification of hyperelastic constitutive modelling mainly using single loading experimental data. By applying conversions of equivalent deformation modes, the criterion is more easily assessed in terms of a hierarchical order of the three homogeneous single loaded experiments in the tensile domain. These are uniaxial tension (UT), planar tension (PT) and equibiaxial tension (ET) experiments. The criterion is therefore simplified for an equal stretch λ to

$$\text{For all } \lambda_1 > 1: \quad P_{1,ET}(\lambda_1) > P_{1,PT}(\lambda_1) > P_{1,UT}(\lambda_1) \tag{3.8}$$

3.2.2 Demonstration of Proposed Plausibility Criterion

The proposed criterion is based on an observed outcome when constitutive models are restricted to physically realistic behaviour (62, 63, 65). One aspect of guaranteeing a physically realistic response of a constitutive model requires that a material stability criterion is met. This criterion states that a positive incremental increase in strain induces a positive increase in stress, for which the reverse should also be true for negative increments of strain. Additionally, polyconvexity is said to ensure a physically realistic response (65, 187). For Rivlin-type constitutive models, Hartmann and Neff (65) state that polyconvexity is ensured unconditionally by constraining model parameters to positive values. Constitutive models with parameters constrained to physically realistic responses are used to demonstrate the proposed plausibility criterion.

Simple Constitutive Models For a simple constitutive model with linear shear modulus, the hierarchical response may be shown from the analytical solutions to the homogeneous deformations. The analytical solutions for constitutive models derived in terms of the Cauchy-Green invariants are defined for uniaxial tension (UT), planar tension (PT) and equibiaxial tension (ET) in terms of the first Piola-Kirchhoff stress in the loaded λ_1 direction P_1 as follows

$$P_{1,UT} = 2\left[\left(\lambda - \lambda^{-2}\right)\frac{\partial W}{\partial I_1} + \left(1 - \lambda^{-3}\right)\frac{\partial W}{\partial I_2}\right] \tag{3.9}$$

$$P_{1,PT} = 2\left[\left(\lambda - \lambda^{-3}\right)\frac{\partial W}{\partial I_1} + \left(\lambda - \lambda^{-3}\right)\frac{\partial W}{\partial I_2}\right] \tag{3.10}$$

$$P_{1,ET} = 2\left[\left(\lambda - \lambda^{-5}\right)\frac{\partial W}{\partial I_1} + \left(\lambda^3 - \lambda^{-3}\right)\frac{\partial W}{\partial I_2}\right] \tag{3.11}$$

The simplest constitutive model defined by both strain invariants is the Mooney-Rivlin model (66). It may be derived from the generalised Rivlin model defined in equation (2.20) as

$$W_{M-R} = C_{10}\left(I_1 - 3\right) + C_{01}\left(I_2 - 3\right) \tag{3.12}$$

The derivatives of the Mooney-Rivlin model are simply $\partial W_{M-R}/\partial I_1 = C_{10}$ and $\partial W_{M-R}/\partial I_2 = C_{01}$. With the parameters constrained to positive values for a physically realistic constitutive model , $C_{10} > 0$ and $C_{01} > 0$, the behaviour $P_{1,ET} > P_{1,PT} > P_{1,UT}$ is apparent since $\left(\lambda - \lambda^{-5}\right) > \left(\lambda - \lambda^{-3}\right) > \left(\lambda - \lambda^{-2}\right)$ and $\left(\lambda^3 - \lambda^{-3}\right) > \left(\lambda - \lambda^{-3}\right) > \left(1 - \lambda^{-3}\right)$ for all $\lambda > 1$.

The neo-Hookean model (69), which may be seen as a simplification of the Mooney-Rivlin model, is represented in terms of only the I_1 term as

$$W_{nH} = C_{10}\left(I_1 - 3\right) \tag{3.13}$$

Implicitly, the proposed criterion $P_{1,ET} > P_{1,PT} > P_{1,UT}$ also holds true for this model for all $C_{10} > 0$ and $\lambda > 1$.

Finite Extensibility Constitutive Models Another type of constitutive model for which the proposed criterion may be demonstrated are those that model the finite extensibility response of rubber. A phenomenological model of this type is the Gent model (18). The model consists of only two parameters and represents the finite extensibility behaviour of rubber in a convenient form (82, 188). Its strain energy density is defined as

$$W_G = -\frac{\mu J_m}{2} \ln\left(1 - \frac{I_1 - 3}{J_m}\right) \tag{3.14}$$

The parameter μ is the shear modulus, and therefore $\mu > 0$ for a physically realistic response. The other parameter J_m is the limit of the first invariant defined by $J_m = I_{1,max} - 3$. Its first derivative is fully defined as

$$\frac{\partial W_G}{\partial I_1} = \frac{\mu}{2\left(1 - \frac{I_1 - 3}{J_m}\right)} \tag{3.15}$$

From this equation it can be seen that $\lim_{(I_1-3)\to J_m} (\partial W_G / \partial I_1) \to \infty$ and hence the stress tends towards a singular value in the same limit. The relationships for the first invariant for uniaxial tension, planar tension and equibiaxial tension deformations are then considered, respectively given by

$$I_{1,UT} = \lambda^2 + 2\lambda^{-1} \tag{3.16}$$

$$I_{1,PT} = \lambda^2 + \lambda^{-2} + 1 \tag{3.17}$$

$$I_{1,ET} = 2\lambda^2 + \lambda^{-4} \tag{3.18}$$

From these, it can be shown that $I_{1,ET} > I_{1,PT} > I_{1,UT}$ for all $\lambda > 1$. This establishes that the stress response always obeys $P_{1,ET} > P_{1,PT} > P_{1,UT}$ for the realistic strain range $(I_1 - 3) < J_m$ for all $\lambda > 1$, further demonstrating the proposed criterion's appearance in physically constrained constitutive models.

The 8-chain network model by Arruda and Boyce (15) is based on an inverse Langevin distribution of network chains to model the finite extensibility of rubber. Its strain energy density function may be described by an approximation in terms of I_1 as

$$\begin{aligned} W_{8c} = \mu \Bigg[& \frac{1}{2}(I_1 - 3) + \frac{1}{20N}\left(I_1^2 - 9\right) + \frac{11}{1050N^2}\left(I_1^3 - 27\right) \\ & + \frac{19}{7000N^3}\left(I_1^4 - 81\right) + \frac{519}{673750N^4}\left(I_1^5 - 243\right) \Bigg] \end{aligned} \tag{3.19}$$

Similar to the Gent model, μ is the shear modulus, with $\mu > 0$ for a physically realistic response, and N is a positive parameter that dictates the asymptotic response of the

model. It is therefore observed that the same behaviour as in the Gent model occurs for the 8-chain model. The Hart-Smith model (77) was shown by Chagnon et al (78) to be equivalent to the Gent and 8-Chain models in that it models the finite extensibility response but through a different mathematical means. Regardless of the functions used to approximate the finite extensibility of rubber, physically constrained finite extensibility models are found to exhibit the behaviour of the proposed criterion as they tend towards an asymptotic limit.

Polyconvex Rivlin-type Polynomial Models For more complex hyperelastic constitutive models, analytical means of demonstrating the proposed criterion were not realised. Graphical methods were therefore used to investigate the proposed criterion within physically constrained constitutive models. Following the procedure by Hartmann and Neff (65), two Rivlin-type polynomial models are investigated with parameters constrained to positive values to ensure polyconvexity and hence a physical response. For both models, the analytical solutions for the first Piola-Kirchhoff stress P_1 in the λ_1 direction of a general biaxial experiment were computed using equation (3.5). The computed values were investigated for a fixed range of values for λ_1, where $\lambda_1 > 1$, while λ_3 was varied from $\lambda_3 = \lambda_1^{-\frac{1}{2}}$ to $\lambda_3 = \lambda_1$. The results are presented over two scales: at a small scale (from $\lambda_3 = 1.1$ to $\lambda_3 = 1.5$) and a large scale (from $\lambda_3 = 2$ to $\lambda_3 = 6$).

The first investigated constitutive model is the model proposed by Yeoh (189) with strain energy density function

$$W_Y = C_{10}\left(I_1 - 3\right) + C_{20}\left(I_1 - 3\right)^2 + C_{30}\left(I_1 - 3\right)^3 \tag{3.20}$$

Arbitrary positive values for the parameters were defined ($C_{10} = 1$MPa, $C_{20} = 0.01$MPa and $C_{30} = 0.001$MPa). The results are plotted in Figures 3.1a and 3.1b. These show that for all fixed values of λ_1 the first Piola-Kirchhoff stress increases as λ_3 is varied from $\lambda_3 = \lambda_1^{-1/2}$ to $\lambda_3 = \lambda_1$.

The same procedure was repeated for the constitutive model proposed by Haines and Wilson (190), henceforth referred to as the Haines-Wilson model. Its strain energy density function is defined as

$$\begin{aligned} W_{HW} = {} & C_{10}\left(I_1 - 3\right) + C_{01}\left(I_2 - 3\right) + C_{11}\left(I_1 - 3\right)\left(I_2 - 3\right) \\ & + C_{02}\left(I_2 - 3\right)^2 + C_{20}\left(I_1 - 3\right)^2 + C_{30}\left(I_1 - 3\right)^3 \end{aligned} \tag{3.21}$$

As previous, arbitrary positive values are assigned to each of the parameters of the model ($C_{10} = 0.1$MPa, $C_{01} = 0.01$MPa, $C_{11} = 1\text{E}{-4}$MPa, $C_{02} = 1\text{E}{-6}$MPa, $C_{20} = 1\text{E}{-5}$MPa, $C_{30} = 1\text{E}{-6}$MPa). The results are plotted in Figures 3.2a and 3.2b demonstrating the same results as the Yeoh model in that the proposed criterion exists for a physically constrained constitutive model.

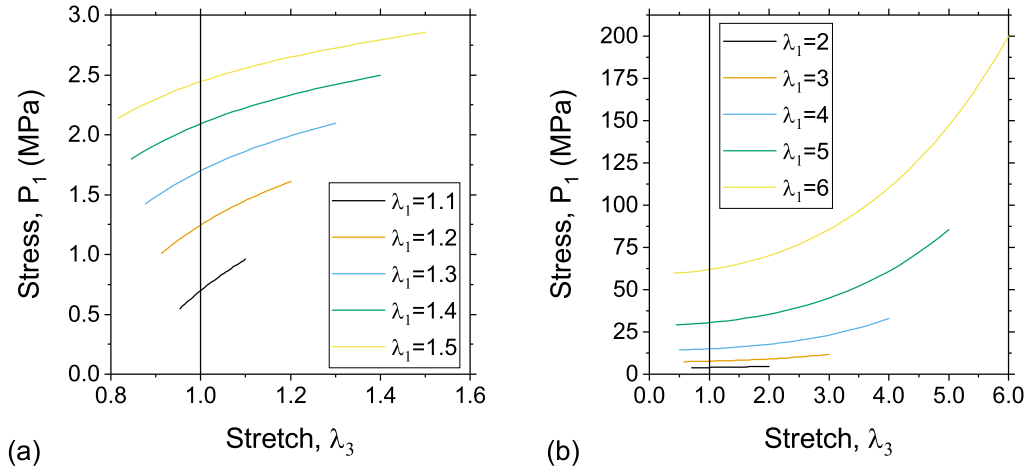

Figure 3.1: General biaxial analytical solutions for a Yeoh model with physically constrained parameters (a) small scale, (b) large scale

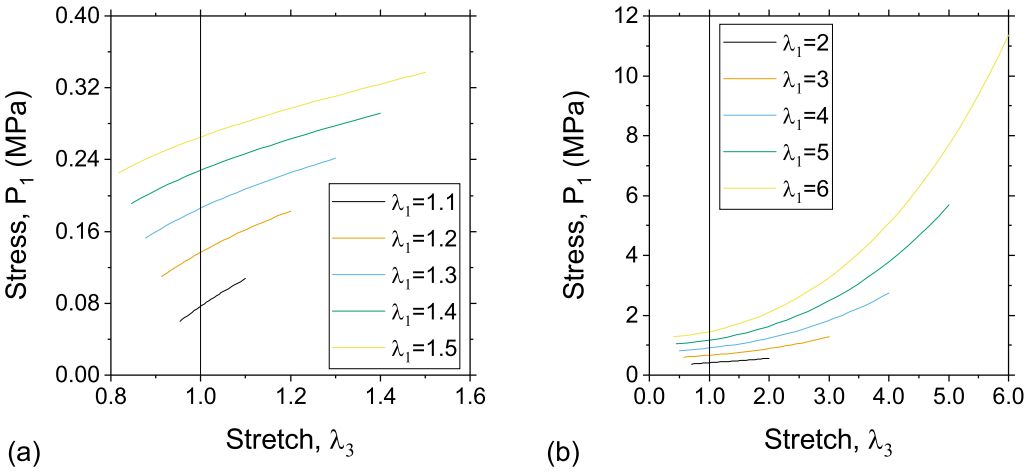

Figure 3.2: General biaxial analytical solutions for a Haines-Wilson model with physically constrained parameters (a) small scale, (b) large scale

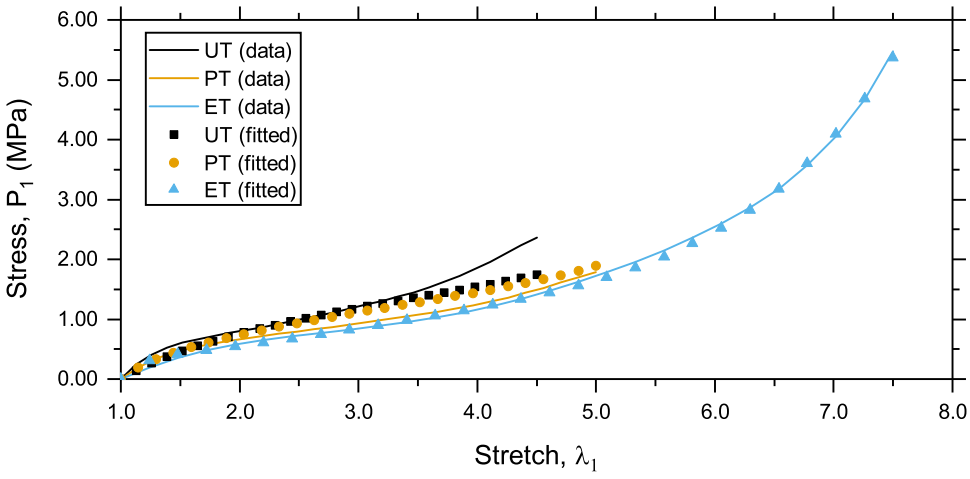

Figure 3.3: Unconstrained three-term Ogden model fitted to non-physical synthetic data where $P_{1,ET} < P_{1,PT} < P_{1,UT}$

Further Observations An additional method of demonstrating the proposed criterion is by attempting parameter identification of a synthetic data set in which the reverse of the proposed criterion occurs such that $P_{1,ET} < P_{1,PT} < P_{1,UT}$. As would be suggested by the earlier demonstrations, a constitutive model restricted to physically constrained parameters is unable to accurately fit such behaviour with any accuracy. However, using a phenomenological model with unconstrained parameters, fitting this unrealistic data is still possible. The Ogden model (84) is known to accurately fit prescribed data but not necessarily with a physically realistic outcome (191). Its strain energy density function was defined previously in equation (2.22). Using the parameter identification method, discussed later in Section 3.3, an Ogden model with $N = 3$ is fitted to synthetic data where $P_{1,ET} < P_{1,PT} < P_{1,UT}$. The result, which is shown in Figure 3.3, shows that it is possible for non-physical data to be fitted by an unconstrained constitutive model. Whereas previous studies (63, 143, 187) restrict constitutive models to physically realistic behaviour, this observation highlights the importance of ensuring physically plausible experimental data.

3.2.3 Conversion of Equivalent Homogeneous Experimental Data

To assess the plausibility of single loading homogeneous experimental data in terms of the criterion proposed in equation (3.8), equations were derived for the conversion of experimental data to the tensile domain. By consideration of the invariant plane, any coordinate (I_1,I_2) that lies on the upper and lower bounds and the pure shear line has a unique deformation gradient. For a point on either the upper or lower bound, its unique deformation gradient may be attained by either tensile or compressive loading. A coordinate on the pure shear line may be obtained by pla-

nar tension, planar compression or simple shear deformations. It is apparent that a unique coordinate (I_1,I_2) has equal derivatives $\partial W/\partial I_1$ and $\partial W/\partial I_2$. This is central in the conversion of equivalent experimental data. In the following, conversions to the tensile domain are defined for uniaxial compression, planar compression and simple shear experimental data.

Uniaxial Compression to Equibiaxial Tension A point (I_1,I_2) on the upper bound of the invariant plane corresponds to a deformation gradient obtained by either uniaxial compression or equibiaxial tension. The applied principal stretches for these deformations, λ_{UC} and λ_{ET}, are related by considering that their applied stresses and hydrostatic pressures are opposite but equivalent. Based on equations (3.5) and (3.7), the relationship between λ_{UC} and λ_{ET} is defined as

$$\lambda_{UC} = {\lambda_{ET}}^{-2} \tag{3.22}$$

The above is then substituted into the analytical solution for the first Piola-Kirchhoff stress in uniaxial compression $P_{1,UC}$, which is equivalent to equation (3.9). This gives $P_{1,UC}$ in terms of the converted equibiaxial tension stretch λ_{ET} as

$$P_{1,UC} = 2\left[\left({\lambda_{ET}}^{-2} - {\lambda_{ET}}^{4}\right)\frac{\partial W}{\partial I_1} + \left(1 - {\lambda_{ET}}^{6}\right)\frac{\partial W}{\partial I_2}\right] \tag{3.23}$$

By comparison of equation (3.23) to the analytical solution for the first Piola-Kirchhoff stress in equibiaxial tension $P_{1,ET}$, defined in equation (3.11), and given that the derivatives $\partial W/\partial I_1$ and $\partial W/\partial I_2$ are equal, the conversion is defined by

$$P_{1,ET} = -{\lambda_{ET}}^{-3} P_{1,UC} \tag{3.24}$$

Planar Compression to Planar Tension Applying the same arguments, a point that lies on the pure shear line of the invariant plane may correspond to a planar tension or a planar compression deformation. The relationship between principal stretches for planar compression λ_{PC} and planar tension λ_{PT} is defined as

$$\lambda_{PC} = {\lambda_{PT}}^{-1} \tag{3.25}$$

Then by equivalent substitutions as those previous, the first Piola-Kirchhoff stresses are related by

$$P_{1,PT} = -{\lambda_{PT}}^{2} P_{1,PC} \tag{3.26}$$

Simple Shear to Planar Tension Simple shear experiments also produce deformation states that lie on the pure shear line of the invariant plane. Though the homogeneous simple shear experiment is not characterised by a deformation applied in a perpendicular system, its measurements may still be converted by the equivalence of the derivatives $\partial W/\partial I_1$ and $\partial W/\partial I_2$ for simple shear and planar tension (or compression).

The analytical solution for planar tension is further derived from equation (3.10) to

$$P_{1,PT} = 2\left(\lambda_{PT} - {\lambda_{PT}}^{-3}\right)\left(\frac{\partial W}{\partial I_1} + \frac{\partial W}{\partial I_2}\right) \tag{3.27}$$

For a simple shear experiment, the analytical solution for the first Piola-Kirchhoff shear stress P_{12} was defined by Rivlin (192) as

$$P_{12} = 2\kappa\left(\frac{\partial W}{\partial I_1} + \frac{\partial W}{\partial I_2}\right) \tag{3.28}$$

These stresses may be simply related as the derivatives $\left(\frac{\partial W}{\partial I_1} + \frac{\partial W}{\partial I_2}\right)$ are equal in both cases. The relationship between planar tension and simple shear first Piola-Kirchhoff stresses is therefore derived as

$$P_{1,PT} = \frac{P_{12}}{\kappa}\left(\lambda_{PT} - {\lambda_{PT}}^{-3}\right) \tag{3.29}$$

An additional relationship is required to convert the experimental strain measures. The amount of shear κ is related to the corresponding planar tension stretch λ_{PT}, as derived by Horgan and Murphy (114), by the following

$$\lambda_{PT} = \frac{\kappa + \sqrt{4 + \kappa^2}}{2} \tag{3.30}$$

3.2.4 Case Studies of Published Experimental Data Sets

The method for assessing the plausibility of homogeneous experimental data for hyperelastic parameter identification was established as follows. First, experimental data sets are converted into equivalent data in the tensile domain where required. The data is then plotted in the tensile domain and the criteria for physically plausible experimental data are assessed. In the case where deformation modes are repeated upon conversion, the tensile and converted data are superimposed and compared. This provides further insights into the accuracy of the experimental data and the validity of experimental assumptions. In the following, experimental data sets from literature are described and assessed. Plausible sets of experimental data were identified for later use in hyperelastic parameter identification studies.

Treloar (1944) The first set of experimental data defined is the classical experimental data set of Treloar (127). The data was digitised by Lopez-Pamies (71) and this was used in the present work. It consists of uniaxial tension, planar tension and membrane inflation experiments. This data is widely considered as a benchmark in the proposal and comparison of hyperelastic constitutive models due to its high strain range and classical S-shaped softening-stiffening response in each of the three deformation modes (22, 57, 58, 59, 84, 138, 147). Since the three deformation modes are tensile and unique, no conversion or superposition is required to establish the physical plausibility of the data. Upon observation of the digitised data, as shown in Figure 3.3a, the data satisfies the criteria.

Jones and Treloar (1975) The experimental data of Jones and Treloar (128) is taken from a general biaxial experiment. The data used here was taken from the tabulated form by Haines and Wilson (190). The equibiaxial tension data points are only approximately equal in terms of the applied stretches, such that $\lambda_1 \approx \lambda_3$. There is no duplication of experimental methods and no conversion is required. Despite a lack of equibiaxial tension data points and some scatter of the uniaxial tension data points, the experimental data is physically plausible, as observed in Figure 3.3b.

Kawabata et al (1981) A general biaxial experiment was used in Kawabata et al (129) with the experimental data presented in tabulated form. For each fixed value of stretch in the general biaxial experimental data, the stress generally increases as the other stretch is varied from uniaxial to equibiaxial tension as required for physical plausibility. However, as can be seen in Figure 3.3c when the uniaxial and planar tension stresses are plotted together, the stresses overlap at higher strain magnitudes. This suggests that the data is mostly physically plausible but is affected by experimental errors or imperfect elasticity at high strain.

Heuillet and Dugautier (1997) The experimental data of Heuillet and Dugautier (193) is referenced within several studies involving constitutive modelling of hyperelasticity (16, 56, 61, 194). However, the original data could not be found. The data was therefore obtained by digitisation of figures from two sources: Attard and Hunt (16) and Darijani and Naghdabadi (61). The data consists of uniaxial, planar and equibiaxial tension experiments as well as a uniaxial compression experiment. The uniaxial compression experiment was converted and superimposed in the tensile domain. Upon observation of the combined data, as shown in Figure 3.3d, it was deemed to be physically plausible. The converted uniaxial compression data is seen to be affected by noise, this is primarily due to errors in digitisation related to the scaling of the published figures. Despite this, it can be seen that the converted uniaxial

compression data corresponds well with the equibiaxial tension data, which suggests that the experimental assumptions are valid and that the experimental methods were accurate.

Yeoh and Fleming (1997) Yeoh and Fleming (70) performed uniaxial tension, simple shear and uniaxial compression tests on specimens made from four rubber compounds. Each compound is of the same backbone material (2), natural rubber, but has different amounts of sulphur in its compounding recipe, labelled A, B, C and D. The simple shear and uniaxial compression data are converted to planar tension and equibiaxial tension data, respectively. The combined data for each compound is plotted in Figures 3.5a-d, with respect to their compound label names. For all other than specimen B, the simple shear data has lower stress than uniaxial tension. For all specimens, the stiffness of the uniaxial compression converted data begins to decrease below that of uniaxial tension. It is therefore determined that the four sets of experimental data are not considered to be physically plausible by the proposed criteria.

Bradley et al (2001) Bradley et al (117) investigate whether uniaxial data alone, considering both tension and compression, is sufficient for the prediction of the general mechanical response. For validation, a planar tension experiment was also performed. Bradley et al (117) converted uniaxial compression data to equibiaxial tension data. They then used a constitutive model with parameters identified to the uniaxial compression data to predict the converted equibiaxial tension data. The prediction of the converted data is identical to the fit to the original compression data, however, making the comparison redundant. If the converted data was compared in the tensile domain, as shown in Figure 3.6a, the non-physical nature of the data may have been observed. The data used in the present plausibility assessment is subjected to digitisation errors due to the scale of the published graphs (117). As such, the original experimental data may be plausible but cannot be stated conclusively here.

Meunier et al (2008) The experimental data of Meunier et al (88) is of particular interest due to the inclusion of equivalent deformation modes. The data consists of five homogeneous experiments: uniaxial tension, planar tension, uniaxial compression, planar compression and membrane inflation. The experimental data was extracted by digitisation. Due to the high quality of the published figures (88) the plotted data was assumed to be an accurate reproduction of the original data. The planar compression data and uniaxial compression data were both converted and combined with

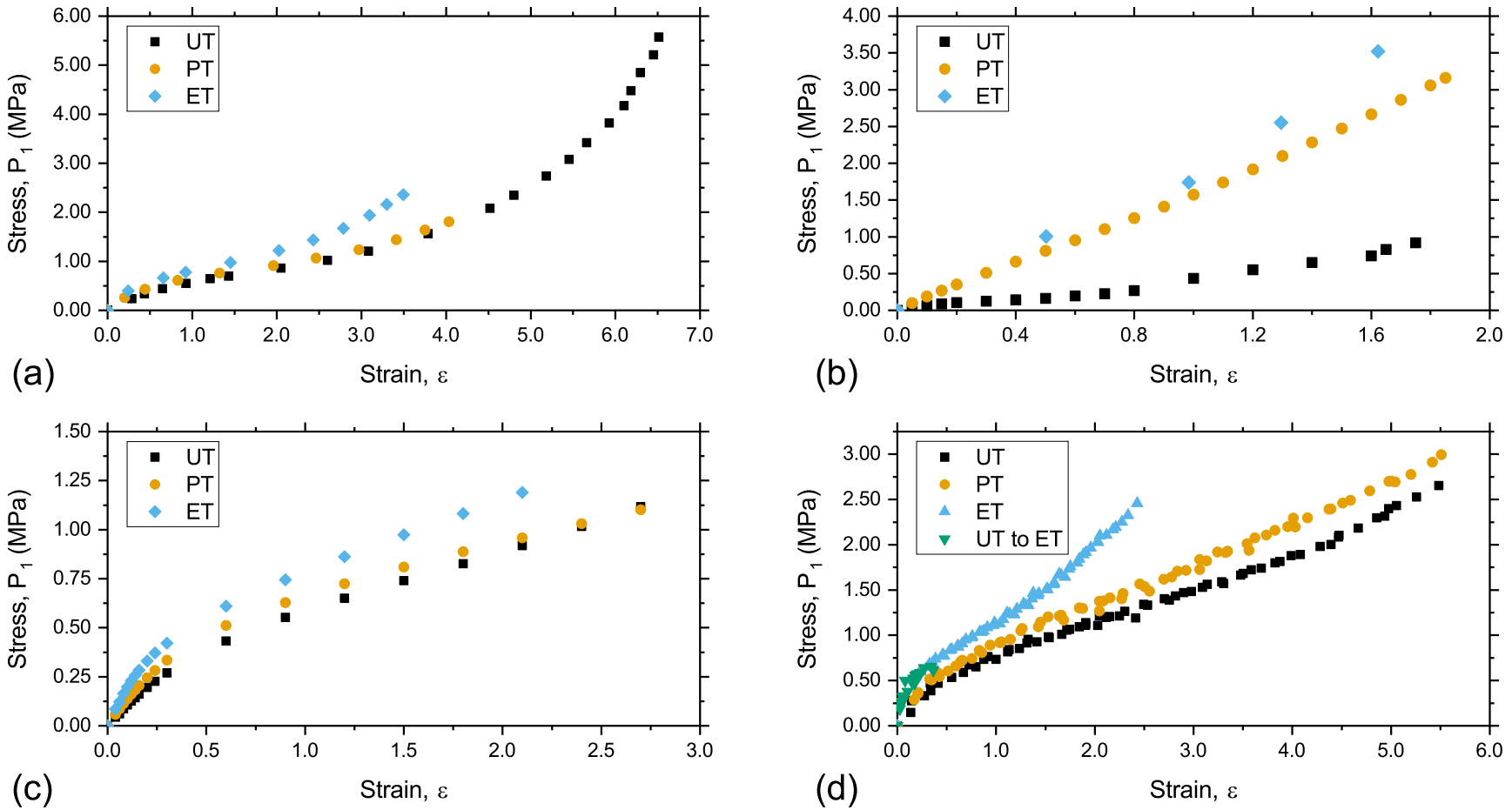

Figure 3.4: Experimental data from literature in the tensile domain: (a) Treloar (1944) - **Plausible**, (b) Jones & Treloar (1975) - **Plausible**, (c) Kawabata et al (1981) - **Not plausible**, (d) Heuillet & Dugautier (1997) - **Plausible**

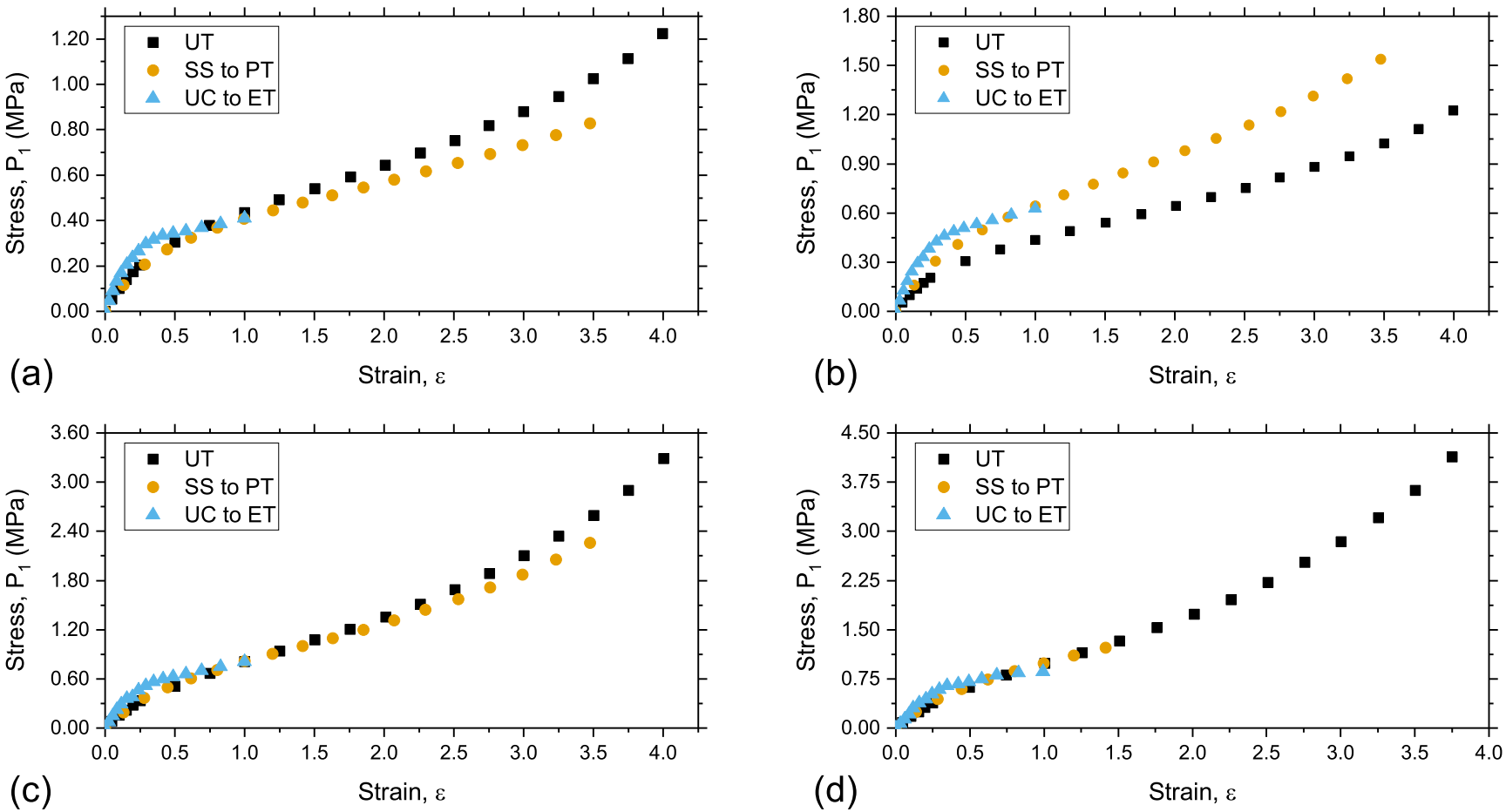

Figure 3.5: Experimental data from Yeoh & Fleming (1997) in the tensile domain: (a) Specimen A - **Not plausible**, (b) Specimen B - **Not plausible**, (c) Specimen C - **Not plausible**, (d) Specimen D - **Not plausible**

their equivalent tensile data. The combined data of the five experiments is plotted in Figure 3.6b and was found to be physically plausible.

The comparison of the superimposed membrane inflation and converted uniaxial compression data shows that both experiments produce consistent results. This suggests that the assumptions of incompressibility and negligible friction are valid for the selected material and experimental procedures. Upon comparing the planar tension data and converted planar compression data, it is found that the results are similar but with some deviation. The larger specimen size of the planar compression specimen increases both the frictional effects and hydrostatic pressure, which are likely to affect the frictionless and incompressible assumptions, respectively.

Le Saux et al (2011) In Le Saux et al (132), uniaxial tension, planar tension and uniaxial compression tests are performed. The uniaxial compression test data is converted to equibiaxial tension and the data from the three tests is plotted, as shown in Figure 3.6c. The data is found to be physically plausible in terms of the proposed criteria. Converting the uniaxial compression data to the tensile domain highlights the distinct difference in the strain ranges of the three tests. This is another insight allowed by converting and comparing experimental data in the tensile domain.

Moreira and Nunes (2013) The experiments of Moreira and Nunes (195) focused on the comparison of simple shear and planar tension. The data is of interest as the two pure shear experimental data sets were compared by parameter identification. Each of the shear experiments was used to identify the parameters of an Ogden model (84) and used to predict the other shear experiment. As derived in Section 3.2.3, the data may simply have been converted for comparison without the influence of error induced by parameter identification and prediction by the constitutive model. The simple shear data is converted and compared to the planar tension in Figure 3.6d, which reveals the same divergence discussed in Moreira and Nunes (195).

3.2.5 Observations

Assessing the physical plausibility of experimental data is not known to have been previously proposed. By converting data into the tensile domain, an insight into the validity of the experimental methods and data and their associated assumptions is enabled. It may be demonstrated, as shown in Bradley et al (117), that parameter identification to equivalent deformation modes will produce the same parameters, provided that the constitutive model parameters are obtained from the global minimum and are suitably unique (145). Therefore, it is recommended that repeated experiments should be converted to the tensile domain and used to assess experimental

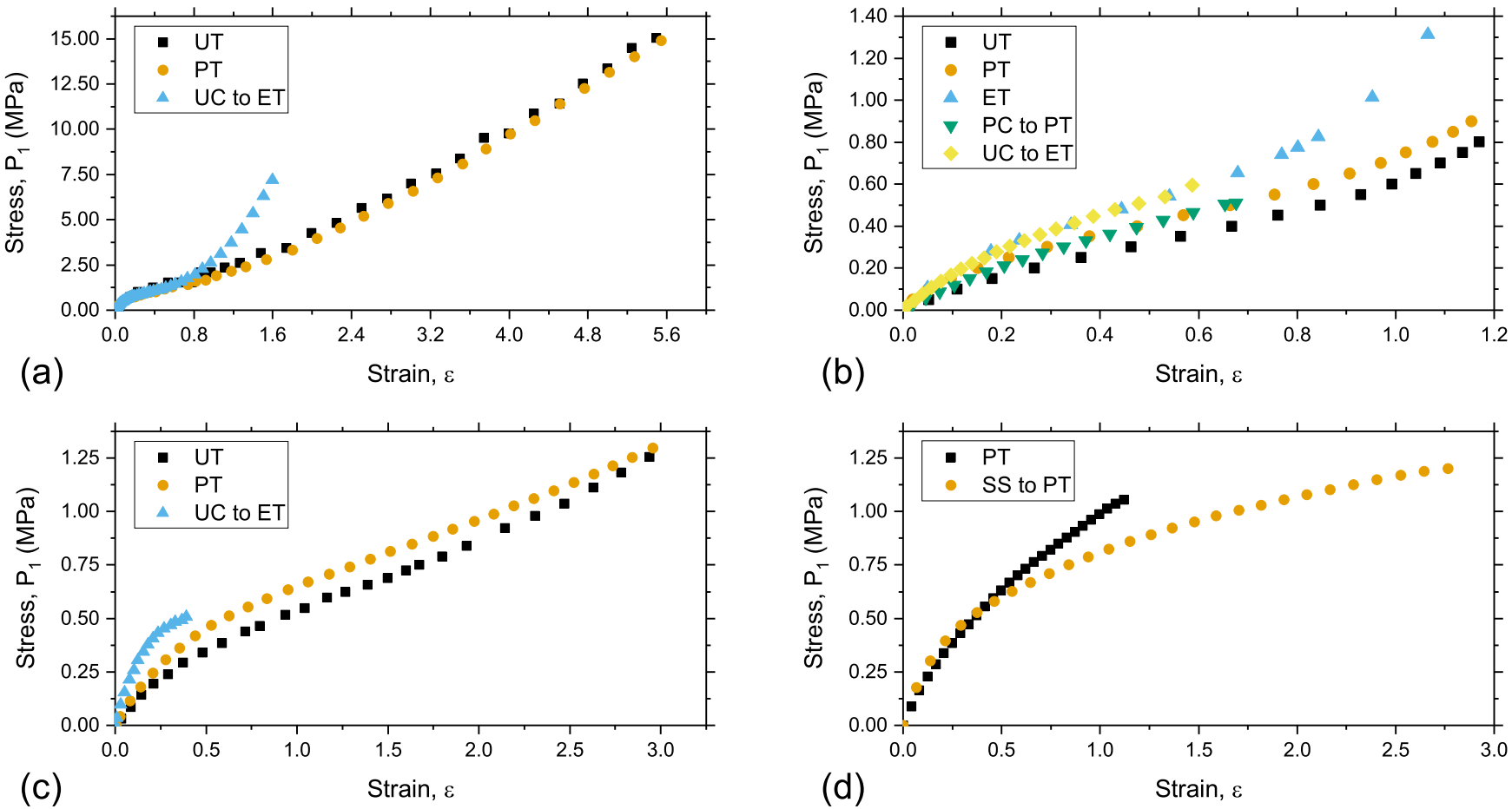

Figure 3.6: Experimental data from literature in the tensile domain: (a) Bradley et al (2001) - **Not plausible**, (b) Meunier et al (2008) - **Not plausible**, (c) Le Saux et al (2011) - **Plausible**, (d) Moreira & Nunes (2013) - **Not plausible**

validity and physical plausibility prior to parameter identification. The converted and combined physically plausible data may then be used in parameter identification.

The case studies reveal some additional insights into homogeneous experimental methods. It was found that uniaxial compression tests can be problematic for obtaining equibiaxial data. This is due to the experimental difficulty in achieving negligible friction as well as the effect of hydrostatic pressures affecting the compressibility of the specimen at higher strains. In practice, neither the effects of friction or compressibility can truly be zero (89). It was also found that planar tension data generally tends towards the uniaxial result. The divergence from ideal pure shear behaviour in a planar tension test was demonstrated by FEA of this experiment by Chevalier and Marco (196). Similarly, the simple shear test is known to have an ambiguous nature in terms of its produced stress field (113). Simple shear measurements are based on the assumption that the bulk of the material is deforming homogeneously. The indeterminate normal stress distributions are then assumed to have negligible effect on the measured shear stress and strain quantities (113, 114). For pure shear experimental methods, measurements are improved by the use of optical methods such as digital image correlation (107, 197). These problems highlight the importance of assessing the physical plausibility of gathered experimental data.

3.3 Parameter Identification Methodology

The investigations of hyperelastic constitutive models require plausible hyperelastic experimental data and a reliable parameter identification method. The parameter identification method was developed to fit experimental data from multiple single loading experiments. The obtained experimental data was optimised with the aim of removing statistical bias towards a particular experiment or strain range. An error function was defined to quantitatively compare predictions of the constitutive models to the experimental data. An optimisation method was selected to compute and minimise the difference between the numerical solutions and the experimental data by way of an error function and an optimisation algorithm.

3.3.1 Homogeneous Experimental Data

Based on the previously defined plausibility criteria, the data of Treloar (127), Heuillet and Dugautier (193) and Meunier et al (88) were chosen for use in the subsequent parameter identification studies. These data sets consist of uniaxial, planar and equibiaxial tension, or equivalent, experimental data. The combination of these experiments was assumed to be sufficient for the prediction of the general hyperelastic behaviour, such that it may be described as a complete set of experimental data.

To ensure that constitutive model parameters were fitted with a view of accurately predicting the complete isochoric deformation range, it was necessary to minimise any statistical bias evident in the experimental data. The source of statistical bias was identified to be due to two factors, strain range distribution and stress magnitude. While the latter is accounted for in the definition of the error function, discussed in Section 3.3.3, the former may be minimised by modification of the experimental data.

To ensure that the optimisation was evenly weighted across the measured experimental strain range, the proposed approach ensures that the data for each deformation mode consists of an equal number of evenly distributed data points along their strain axes. For this purpose, Dal et al (147) used the micro-sphere model of Miehe et al (11) to fit the data for each deformation mode independently then applied the fitted constitutive model to predict an equal number of extrapolated data points for each deformation mode. However, given that the ability of various constitutive models to fit experimental data was being investigated, this method seems problematic as there will naturally be bias towards the constitutive model used to create the extrapolated data. To avoid this, the method of Dal et al (147) was modified.

A sixth-order polynomial function was fitted to each deformation mode within Microsoft Excel. To ensure physical behaviour, the polynomial functions were constrained to fit data with an intercept of zero stress ($P_1 = 0$) in the undeformed state, $\epsilon = 0$). The average percentage error was compared with the experimental data to ensure that the error from modifying the data was assumed to be within an acceptable range, similar to that of experimental measurement errors. The fitted polynomial functions were then used to extrapolate 28 evenly spaced data points for each deformation mode.

As shown in Figure 3.7, the fit of the independent polynomial functions to each set of experimental data is visually accurate. The average absolute percentage errors are computed for each of the data sets and presented in Table 3.1. The largest errors, from the Heuillet and Dugautier (193) equibiaxial tension data and Meunier et al (88) planar tension data, are due to the scatter caused by digitisation errors at low strain of the converted uniaxial compression and planar compression data sets, respectively. The polynomials functions are determined to be accurate for use in extrapolating the experimental data.

3.3.2 Chosen Constitutive Models

Eight hyperelastic constitutive models were chosen for subsequent investigation. They were selected as the top models from two different papers in which hyperelastic constitutive models are ranked. This included the top five ranked models from Marckmann and Verron (138) which, in ranked order, are: extended-tube (22), Shariff

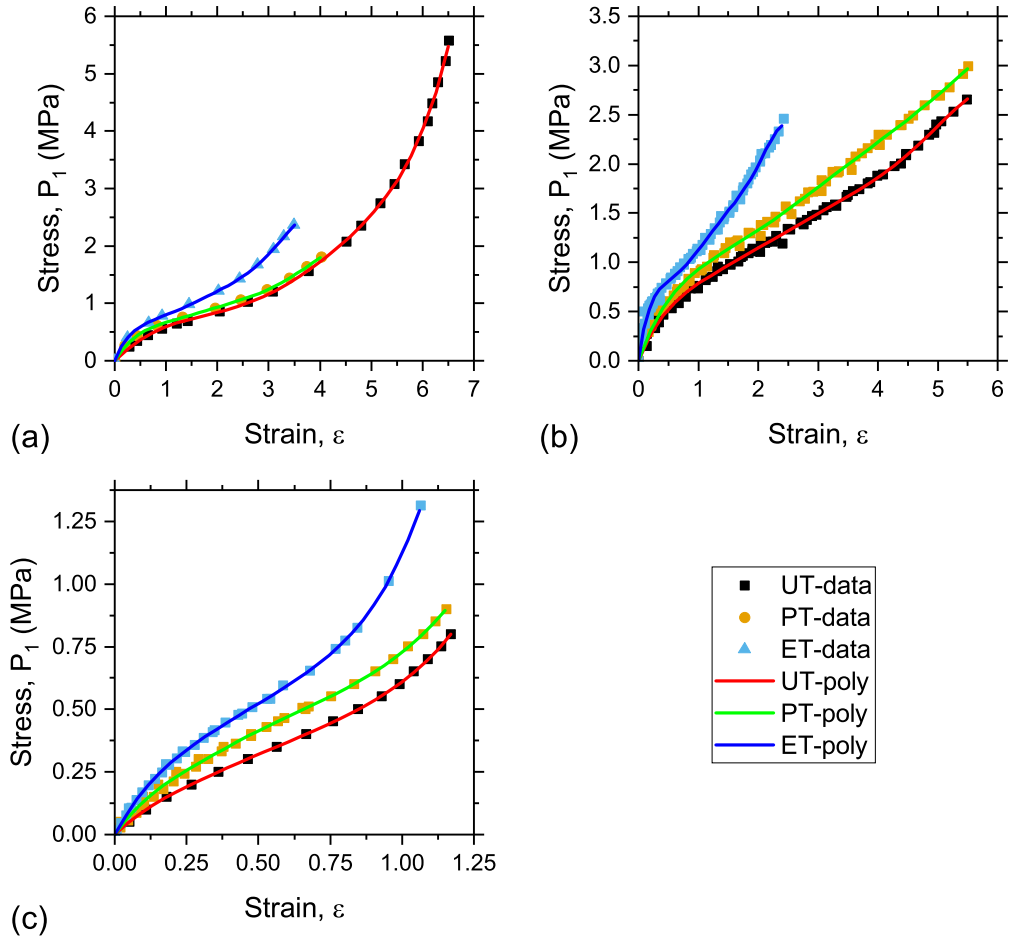

Figure 3.7: Polynomial fits to experimental data: (a) Treloar (1944), (b) Heuillet & Dugautier (1997), (c) Meunier et al (2008)

Table 3.1: Average absolute percentage error for sixth-order polynomials independently fitted to experimental data

	UT error	PT error	ET error
Treloar	1.43%	0.84%	0.49%
Heuillet & Dugautier	2.62%	2.62%	5.51%
Meunier et al	0.45%	6.00%	1.68%

(64), non-affine micro-sphere (11), three-term Ogden (84) and Haines-Wilson (190). Also, the top six ranked models from Dal et al (147) which, in ranked order, are: non-affine micro-sphere (11), Alexander (74), Diani-Rey (56), extended-tube (22), Shariff (64) and Carroll (76) models. The Carroll (76) model was of particular interest due to its high ranking (147) with only three parameters. The parameters and the specific forms of the strain energy density functions W, where applicable, for the chosen constitutive models are defined in Table A.1. The strain energy density functions for some models are obtained by integration. For the Alexander (74), Diani-Rey (56) and Carroll (76) models, this is because they are derived based on the derivatives $\partial W/\partial I_1$ and $\partial W/\partial I_2$. The Shariff (64) model is similar in that it is derived as a function of the principal Cauchy stresses σ_i where $i = 1, 2, 3$. However, for parameter identification, only the derivatives with respect to the relevant strain measures are required.

In the subsequently described studies in Section 3.4, it was investigated as to whether the performance of the chosen constitutive models, implied by their ranking, is broadly applicable. This was assessed by determining their relative performances and rankings when different materials' hyperelastic experimental data is included. The analytical solutions for all models other than the micro-sphere (11) are defined using the previous analytical solutions, equations (3.3) and (3.4). The extended-tube (22) and three-term Ogden (84) models require definition of their derivatives with respect to the isochoric principal stretches, as defined in Table A.2, and are then solved using equation (3.3). The Haines-Wilson (190), Alexander (74), Diani-Rey (56) and Carroll (76) models require definition of their derivatives with respect to the first and second isochoric Cauchy-Green invariants, defined in Table A.3, and are solved using equation (3.4).

The Shariff (64) model is defined in terms of the principal Cauchy stresses σ_i where $i = 1, 2, 3$. For an isochoric material, the principal Cauchy stresses σ_i are identical to the principal Kirchhoff stresses τ_i and are therefore related to the derivative of the strain energy density in terms of principal stretches λ_i by (5)

$$\frac{\partial W}{\partial \lambda_i} = \frac{1}{\lambda_i}\sigma_i \tag{3.31}$$

The derivative of the Shariff model may therefore be defined as in Table A.2, and solved using the analytical solution for the principal stretches, from equation (3.3).

For the non-affine micro-sphere model (11), the analytical solutions to homogeneous deformations were computed using the fictitious Kirchhoff stress tensor $\overline{\boldsymbol{\tau}}$ defined in Table 4 of Miehe et al (11). As the homogeneous deformations are aligned with the principal axes, the components of the fictitious Kirchhoff stress tensor $\overline{\tau}_{ii}$ are equal to the principal components $\overline{\tau}_i$, where $i = 1, 2, 3$. All other shear tensor components are equal to zero. Due to incompressibility, the hydrostatic pressure is equal to the fictitious Kirchhoff stress $\overline{\tau}_2$ such that the first Piola-Kirchhoff stress P_1 is given by

$$P_1 = \frac{1}{\lambda_1} \left(\overline{\tau}_1 - \overline{\tau}_2 \right) \tag{3.32}$$

With the plausible experimental data determined and analytical solutions defined for the chosen constitutive models, a robust optimisation method was developed to identify constitutive model parameters.

3.3.3 Optimisation Method

The optimisation of hyperelastic constitutive model parameters revolves around the automated adjustment of parameters to minimise the difference between the numerical analytical solutions and the prescribed experimental data. An error function is defined to quantify the difference between experimental and analytically computed data sets. An optimisation algorithm is chosen to adjust the parameters and minimise the error function for all models and each variation of input experimental data. To constrain the problem to a finite number of solutions, the parameters' upper and lower bounding values were defined for all constitutive models. For most micromechanically defined parameters, the bounds may be constrained to physically plausible values. However, the values for phenomenological parameters were arbitrarily defined then expanded if a probable global minimum was not found.

In an ideal optimisation method, a low number of iterations would locate a unique set of parameters that attain the global minimum error for all constitutive models. However, in the case of hyperelastic constitutive models when multiple experimental data sets are used, a unique global minimum error may not exist (145, 146). The optimisation method was therefore developed to locate a probable global minimum with acceptable computation time.

The optimisation procedures were carried out using the Solver module in Microsoft Excel and automated by macros. The chosen algorithm was a nonlinear Generalised Reduced Gradient algorithm combined with a multi-start method, limited to 10,000 randomly seeded initial parameters. A benefit of this method is that it significantly

reduces any dependence on initial parameters, which would otherwise find only local minima. The developed macros minimised the need for user input by allowing the Solver module to run automatically and sequentially for all optimised quantities.

The minimised error function was a summed absolute relative error function, which can be expressed as a percentage. By summing the absolute values, it is ensured that the weighting of an over or under prediction contribute equally to the total error. The relative component of the error function ensures that the weighting of any given point is independent of its stress magnitude. This error function was chosen over a least squares error function as the latter is affected by outliers in the data, which was not required as the fitted experimental data was smooth. The summed absolute relative error function E_{RE} is defined in terms of the analytical and experimentally measured first Piola-Kirchhoff stresses in the λ_1 direction P_{1a_i} and P_{1d_i}, respectively, for the number of deformation modes D and the number of data points N as

$$E_{RE} = \sum_{i=1}^{D} \left(\sum_{j=1}^{N} \left| \frac{P_{1a_j} - P_{1d_j}}{P_{1d_j}} \right| \right)_i \tag{3.33}$$

After fitting the parameters to each variation of experimental data, it was assessed for each constitutive model whether the optimised minima were consistent and could be assumed to be global minima. These assessments ensured that the lowest error was found for the minimised quantity across the ten variations of input experimental data. For example, the optimisation where the complete data set was minimised should have a lower error than any prediction of this data set by the same constitutive model. Furthermore, optimising the error of a single experiment should attain lower error than when the experiment was predicted or formed only a part of the minimised error function. If this was found not to be the case, the optimisation was repeated with a wider range of parameter bounds until a more probable global minimum was found.

3.4 Parameter Identification Case Studies

The investigations of hyperelastic constitutive models are organised into four case studies. Within each of the case studies, the parameters of the chosen constitutive models were identified using varying extents of prescribed experimental data. In the first case study the models were compared on their ability to fit the assumed complete sets of experimental data. The second case study identified parameters using experimental data with limited strain ranges; in the third, only two of the three single loaded homogeneous experiments were used; and in the final case study the parameters were identified using the data of only one of the three homogeneous experiments. In all case studies, the models were compared on their ability to fit the

prescribed data. When parameters were identified by lesser extents of experimental data, as in all case studies but the first, it was also investigated how well constitutive models could *predict* the complete data.

The minimised error values were used to quantitatively investigate and compare the ability of the chosen constitutive models to fit the prescribed experimental data and predict the complete experimental data. These errors were converted throughout to the average percentage error of each data point. The averaging considered both the number of deformation modes and the number of data points within each deformation mode. The average percentage error $E_{\%}$ is adapted from equation (3.33) as

$$E_{\%}(\%) = \frac{1}{ND} \sum_{i=1}^{D} \left(\sum_{j=1}^{N} \left| \frac{P_{1a_j} - P_{1d_j}}{P_{1d_j}} \right| \right)_i \times 100 \tag{3.34}$$

This function allows the minimised errors to be compared to one another for different amounts of data points or deformation modes.

The case studies used the assumption that a complete set of hyperelastic experimental data consists of uniaxial, planar and equibiaxial experiments. A constitutive model capable of accurately fitting or predicting these single loading experiments was assumed to imply an ability to predict the complete hyperelastic response of the experimented material. The error in the prediction of complete data was therefore used as a metric of the performance of the constitutive models within each of the case studies. An overall ranking of the constitutive models considering all four case studies was not sought. This was due to inconsistent constitutive model performance when different materials were considered.

Across four case studies there were ten variations of experimental data fitted by each constitutive model. This was repeated for the three chosen materials. With eight constitutive models, this resulted in a total of 240 sets of parameters and predictions of the complete data sets. For this reason, and due to the sensitivity to numerical rounding for some parameters, the optimised parameters sets are not provided here. The parameters and related data are available in the dataset (4).

3.4.1 Case Study 1: Complete Data - Three Single Loading Experiments

The first case study investigated parameter identification with experimental data from a complete set of single loading experiments. The parameters of each constitutive model were identified by minimisation of the summed uniaxial, planar and equibiaxial tension errors. By comparing error values from all case studies, it was assumed that probable global minima were found. The results were tabulated in terms of the average percentage error of each data point $E_{\%}$ and an assigned ranking R for each material. The average error of the eight constitutive models for each

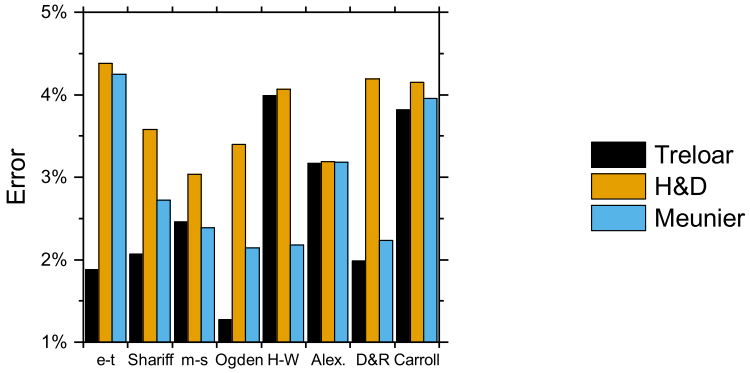

Figure 3.8: Case study 1: Error of models fitted to Treloar, H&D and Meunier complete data sets

material was also calculated. Additionally, an overall ranking based on the totalled rankings from the three experimental data sets was given. The overall ranking was determined by a summation of each model's ranking to the three materials; if equal, the model with the lower average error was given the better ranking. Though the ranking studies of Marckmann and Verron (138) and Dal et al (147) use different parameter identification methods, they provide a useful reference for discussion of the first case study's results.

The following abbreviations are used: the experimental data of Heuillet and Dugautier is abbreviated to H&D, the data of Meunier et al is abbreviated to Meunier, the extended-tube model is abbreviated as e-t, Miehe's non-affine micro-sphere model is given by m-s, the three term Ogden model is referred to as Ogden, Haines and Wilson's model is HW, Lambert-Diani and Rey's is denoted D&R, and the Alexander model is abbreviated to Alex..

The tabulated results for the first case study are given in Table 3.2. Their errors are plotted in Figure 3.8. Plots of the nominal stress and strain for the best and worst fitting models to the complete data for each of the three materials are given in Figure 3.9, where only half of the experimental data points are plotted for clarity. All models fitted the complete data sets with an average error of less than 5% for the three materials. The lowest error achieved was an average error of only 1.27% for the Ogden model fitting the data of Treloar. The highest error remained at only 4.38% of the extended-tube model in fitting the data of Heuillet and Dugautier. In terms of the general ranking of the chosen constitutive models, there is a lack of consistency across the different materials.

For brevity and due to the lack of generality, the discussion is limited to the best and worst performing models of this study and the best performing models of Marckmann and Verron (138) and Dal et al (147). The Ogden model was found in the

Table 3.2: Case study 1 results – minimised error and rankings of the investigated constitutive models

	Treloar		**H&D**		**Meunier**		**Overall**
	$E_{\%}$	R	$E_{\%}$	R	$E_{\%}$	R	R
e-t	1.88%	2	4.38%	8	4.25%	8	7
Shariff	2.07%	4	3.58%	4	2.72%	5	3
m-s	2.46%	5	3.03%	1	2.38%	4	2
Ogden	1.27%	1	3.40%	3	2.14%	1	1
HW	3.99%	8	4.07%	5	2.18%	2	6
Alex.	3.17%	6	3.19%	2	3.18%	6	5
D&R	1.98%	3	4.19%	7	2.24%	3	4
Carroll	3.82%	7	4.15%	6	3.95%	7	8
Average	2.58%		3.75%		2.88%		

present case study to be the best performing model overall, achieving the lowest error for two of the three data sets and the third best fit to the other data set, that of Heuillet and Dugautier. The Carroll model was the least accurate, suggesting that using only three parameters is inadequate to capture the response of different hyperelastic materials. The micro-sphere model, ranked as the best model in Dal et al (147) and third best in Marckmann and Verron (138), provided the second best ranked model overall. The extended-tube model, ranked as the best in Marckmann and Verron (138) and fourth in Dal et al (147) for fits to Treloar's experimental data, achieved the second most accurate fit to the data of Treloar but was the least accurate in fitting the other two materials.

The inconsistency of model rankings highlights the need for a robust parameter identification procedure when a complete set of experimental data is available, such as the method developed in Section 3.3. The procedure should compare multiple constitutive models to the prescribed experimental data. From this the most accurate constitutive model may be identified and selected for numerical predictions of a material's general hyperelastic behaviour. The likelihood of an accurate fit is improved by the inclusion of a wide range of constitutive models.

3.4.2 Case Study 2: Strain Range Reductions

In the second case study, the original sets of experimental data for the three materials were modified in terms of their strain ranges. For each set of complete experimental data, the uniaxial, planar and equibiaxial tension data were each reduced to strain ranges of 75%, 50% and 25% of their maximum values. The parameters of the eight constitutive models were then identified by minimising the error between the modified experimental data and the numerical solutions of this data.

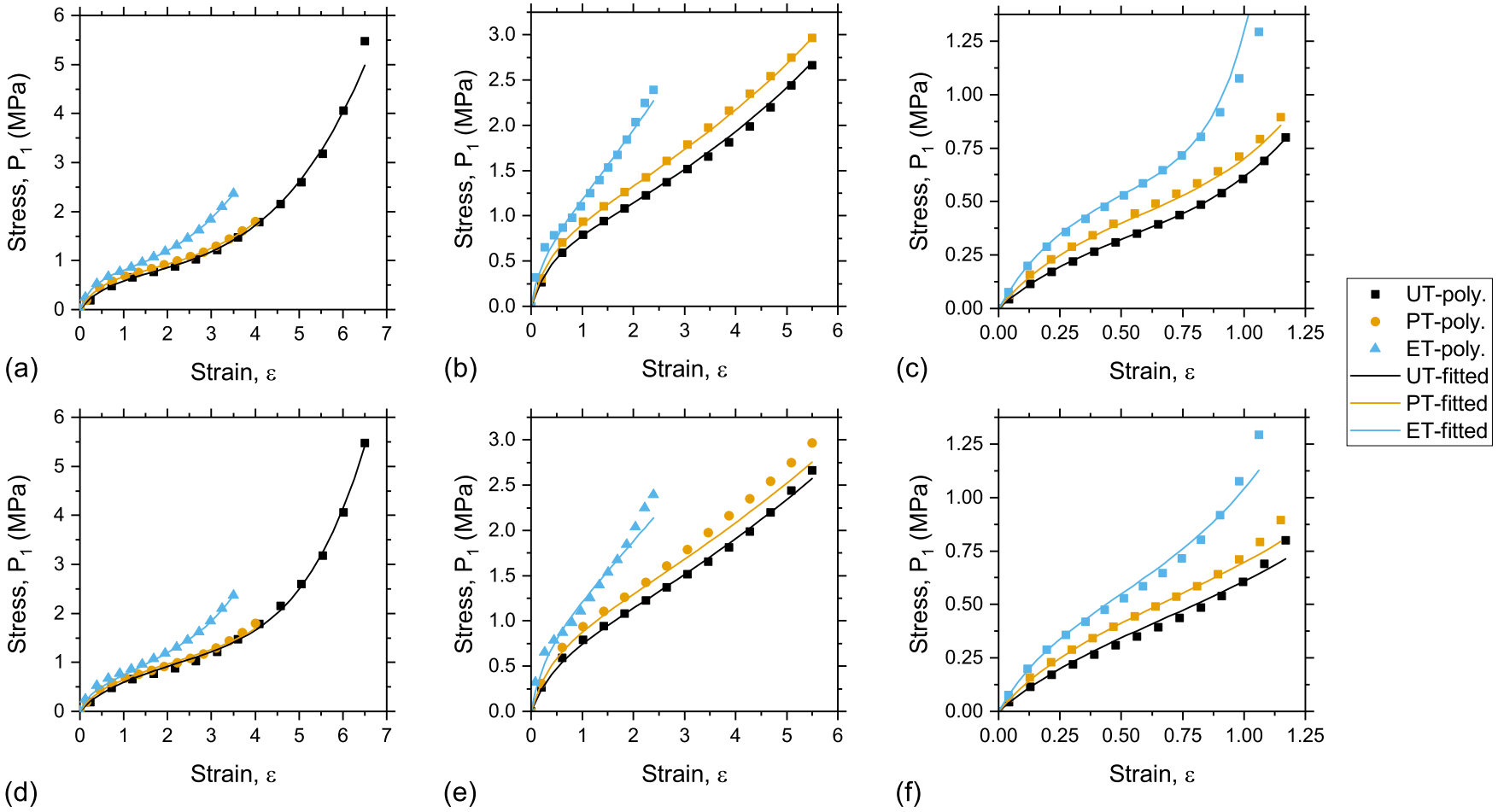

Figure 3.9: Case study 1: Best (a-c) and worst (d-f) fitting models using parameters identified by complete data sets (a) Treloar fitted by Ogden (b) H&D fitted by micro-sphere (c) Meunier fitted by Ogden (d) Treloar fitted by Haines-Wilson (e) H&D fitted by extended-tube (f) Meunier fitted by extended-tube

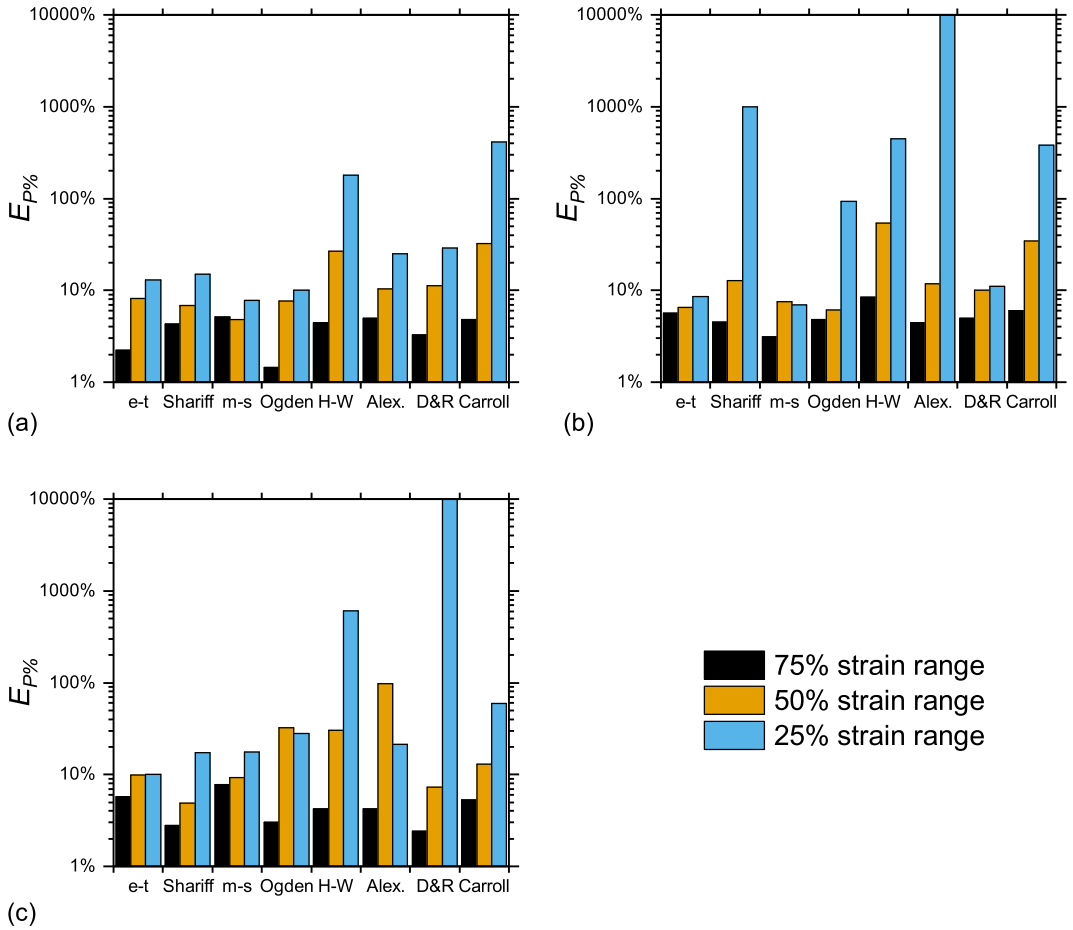

Figure 3.10: Case study 2: Error of complete data prediction by models fitted to (a) Treloar, (b) H&D and (c) Meunier reduced strain range data sets

The results of this case study are tabulated separately for each of the investigated materials in Tables B.1, B.2 and B.3 for Treloar, Heuillet and Dugautier and Meunier data, respectively. The prediction error values for this case study are plotted in Figure 3.10. Within the tables, two error values are given: the error when fitting the prescribed strain range data $E_{F\%}$ and the error of the prediction of the complete data set $E_{P\%}$. The average errors were computed for both. These are given alongside a ranking value to determine the models most capable of fitting the minimised data R_F and those most capable of predicting the complete data R_P based on a fit using a minimised strain range. The difference in error between each model's global minimum error when fitting the complete data to the predicted error was computed, denoted as "Dif." throughout. An overall ranking was given for both the models' ability to fit the prescribed reduced data and their ability to predict the complete data, following the procedure of the first case study.

By observation of the average fitted errors, it was found that the error in fitting the limited strain ranges generally decreases with a smaller strain range. While this

means that low strain ranges are generally modelled more accurately, the error in predicting the complete data increased significantly when smaller strain ranges were used. In some cases this also led to significant instabilities. The worst case was the Diani-Rey model fitted to reduced Meunier data. This model's fit of the 75% data and its prediction of the complete data were the most accurate of the chosen models. However, when fitted to 25% strain range data its prediction resulted in a numerical instability; it was therefore assigned an error value of $E_{P\%} = 1\text{E}99\%$. Stress-strain plots demonstrating this deteriorating accuracy are shown in Figures 3.11a, 3.11b, and 3.11c.

There are only four exceptions where the error difference value was found to improve upon reduction of the strain range: micro-sphere 75% to 50% for Treloar's data, micro-sphere 50% to 25% for Heuillet and Dugautier's data, Ogden 50% to 25% for Meunier et al's data and Alexander 50% to 25% for Meunier et al's data. Even in these exceptional cases, the prediction of the complete error was at least twice as high as their global minimum errors when the complete data was fitted. When fitted using 75% of the strain range, on average, there was only a small increase in error. These results imply that predictions of hyperelastic behaviour are increasingly unreliable as they extend beyond the experimental strain range used in parameter identification. However, if the expected range of deformations was less than the experimental data, fitting a lower strain range is more accurate.

3.4.3 Case Study 3: Two of Three Single Loading Experiments

The third case study investigated the performance of constitutive models when two of the three single loading homogeneous experiments were used in parameter identification. There are therefore three different experimental combinations for each of the three materials: uniaxial and planar tension (UT&PT), planar and equibiaxial tension (PT&ET) and uniaxial and equibiaxial tension (UT&ET). The combination of uniaxial and equibiaxial tension has been hypothesised by some authors (50, 117, 139, 140) to describe the complete behaviour of a material; this combination is therefore of particular interest.

The results for this case study are tabulated with the inclusion of an average difference column for each constitutive model. The results are given in Tables B.4, B.5 and B.6. The prediction errors are shown in Figure 3.12. All models fitted the prescribed data from the two tests with an error of less than 5%. The error in predicting the complete data was found to vary with a general dependence on the chosen experimental combination. The combination of uniaxial and equibiaxial experiments resulted in the lowest average error in the prediction of the complete behaviour. A difference in

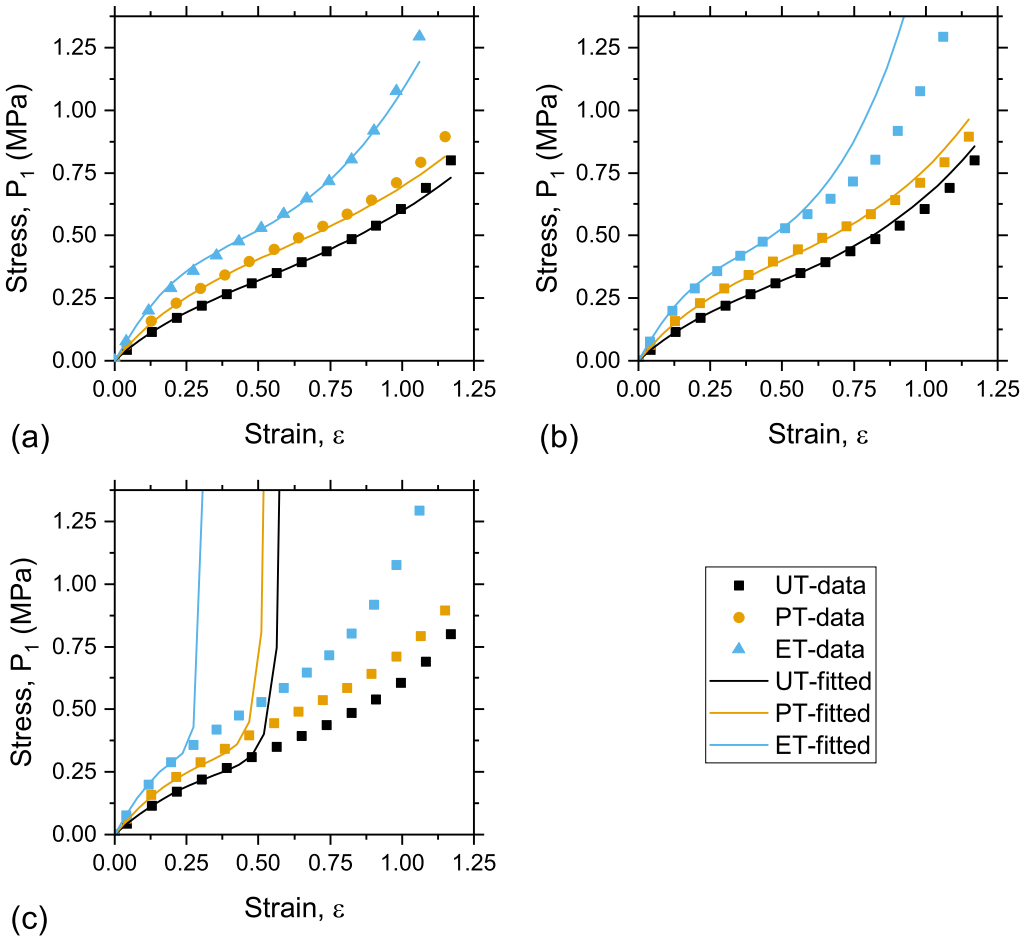

Figure 3.11: Case study 2: Meunier reduced strain range data fitted by D&R model (a) 75% (b) 50% (c) 25%

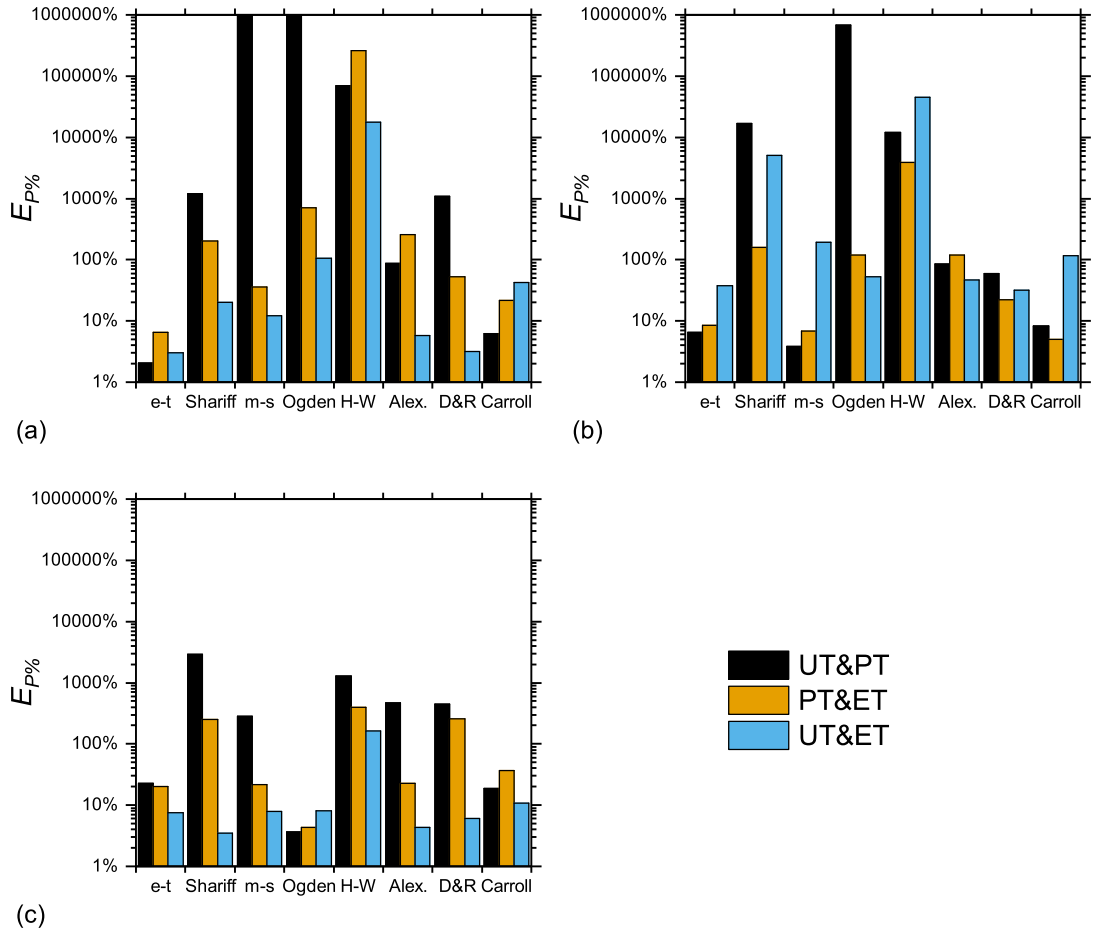

Figure 3.12: Case study 3: Error of complete data prediction by models fitted to two experiment combinations of (a) Treloar, (b) H&D and (c) Meunier experimental data

error of less than 1% for the all constitutive models was found with only one exception in the Haines-Wilson model for Heuillet and Dugautier's data. The remaining two combinations were less consistent. The combination of planar and equibiaxial data in the case of Heuillet and Dugautier's data gave a low average difference comparable to the uniaxial and equibiaxial combination. This is thought to be due to their similar strain ranges and that uniaxial and planar deformations are less distinct than equibiaxial deformations in terms of the invariant plane for this material's data.

From the average difference and overall predictive rankings, some general conclusions can be drawn on the individual predictive performance of the constitutive models. For Treloar's data, three models attained an average difference of less than 1% for all three combinations. The extended-tube model in particular was found to have a very low average difference for this data. However, the extended-tube's average difference to the other material data was considerably higher; both its fit and prediction were generally less accurate than most other models. Regarding the average

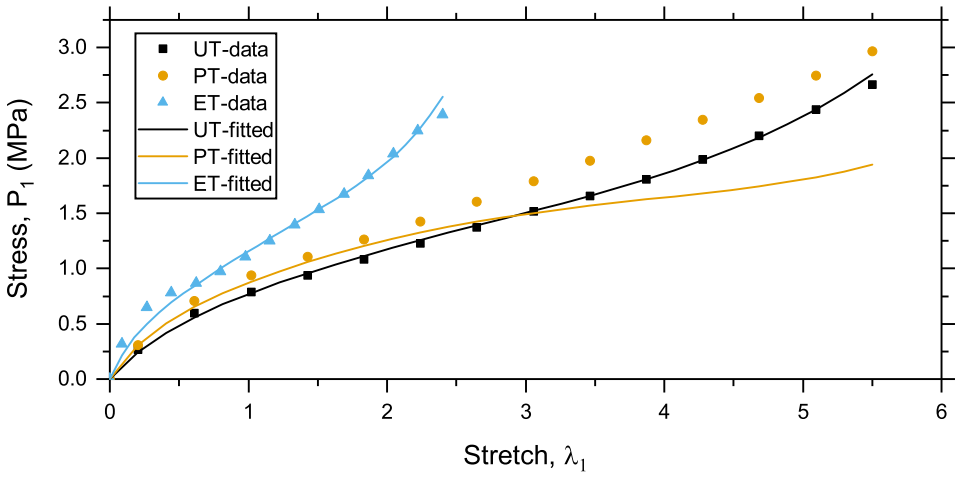

Figure 3.13: Case study 3: H&D UT&ET data fitted by Haines-Wilson

error and overall predictive ranking of the other models, no model was found to be capable of predicting the complete behaviour when fitted to any arbitrary combination of two single loading experiments. In the overall rankings for R_F, the Ogden model was generally the most accurate. However, its predictive performance was less consistent; as with all models, the predictability depends on the chosen experimental combination.

For all models and materials, the parameter set obtained by fitting the complete data was not returned by any combination of two single loading experiments. However, with the assumption that accurate fitting or prediction of complete data enables a consistent prediction of a material's general behaviour, the combination of uniaxial and equibiaxial tension is the most suitable. The effectiveness of this combination is hypothesised to be a result of these deformation modes bounding the attainable deformations, as represented on the invariant plane, see Figure 2.4 for reference. All other attainable deformations may be considered as interpolations between these bounds.

In alignment with the findings of the previous case study, if the expected range of deformations by a component was contained between the bounds of planar tension and either uniaxial or equibiaxial tension, it would be assumed that these interpolations would be more accurate if their associated fitted data was used. In the mentioned atypical result, which would evidence the contrary to this, as shown in Figure 3.13, it can be observed that the predicted planar tension stress does not meet the proposed criterion from Section 3.2.1. It is therefore recommended that predictions of planar tension or other interpolations are assessed in terms of their physical plausibility.

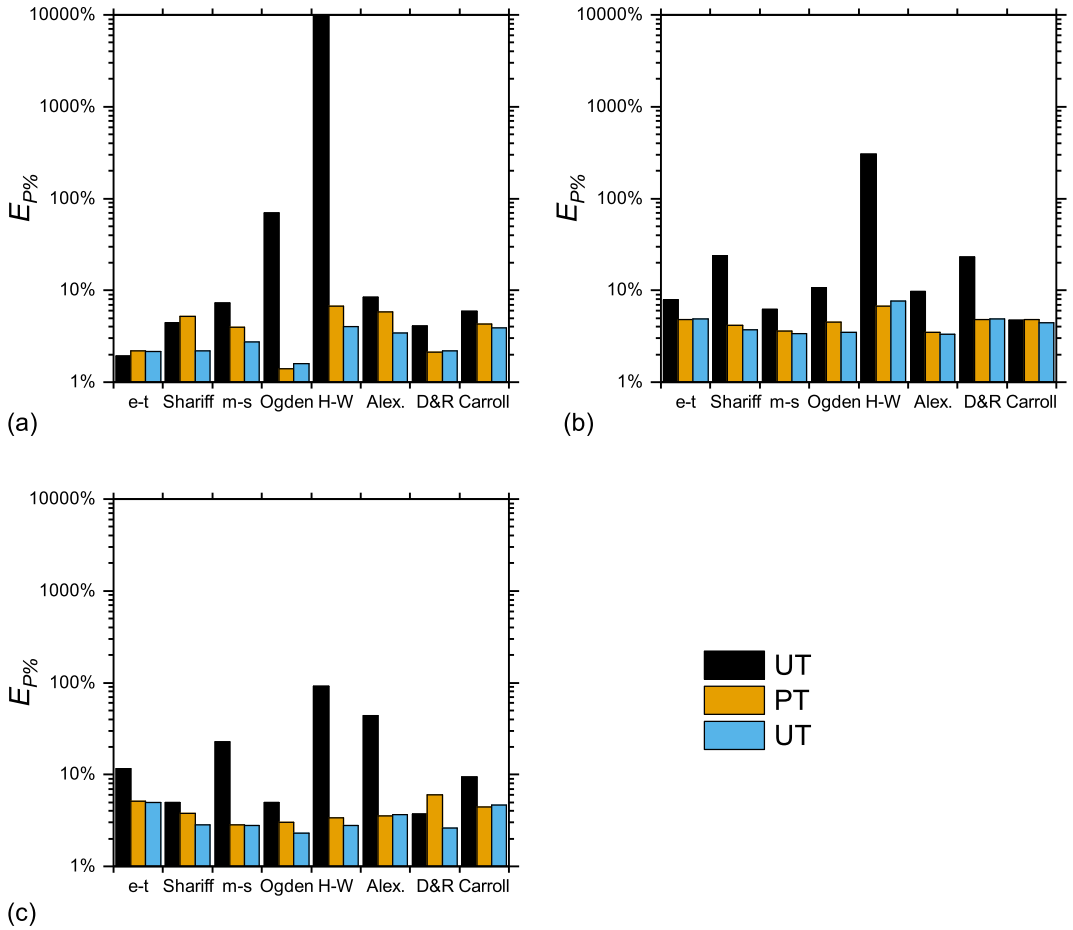

Figure 3.14: Case study 4: Error of complete data prediction by models fitted to a single loading experiment from (a) Treloar, (b) H&D and (c) Meunier experimental data

3.4.4 Case Study 4: One Single Loading Experiment

Based on the results of the second and third case studies, and from literature (57, 58, 139), it was presumed that models with parameters identified to a single deformation mode would not be capable of consistent and accurate prediction of the complete data set. The only exception being the extended-tube model in the case of Treloar's data, as demonstrated by Hossain and Steinmann (58). These hypothesised results were found to hold true. The results are presented in the same method as in the third case study and given in Tables B.7, B.8 and B.9. The prediction errors are plotted in Figure 3.14. The accurate prediction by the extended-tube model was found for uniaxial and equibiaxial tension fitted parameters but was less accurate for planar tension, as shown in Figures 3.15a, 3.15b, and 3.15c.

All models fitted the prescribed data with lower average errors than the other case studies. However, the predictions and differences in error from the complete data were considerably higher. Examples of the accurate fit to the prescribed data and

high error in the prediction of the unfitted deformation modes are shown in Figures 3.15d, 3.15e, and 3.15f. The large deviations in the predicted behaviour suggest that predicting a hyperelastic material's complete behaviour is not recommended when constitutive model parameters are identified from only one single loading experiment. A constitutive model with parameters identified with such data would be recommended only if the material or component was expected to deform with minimal deviation from the fitted mode of deformation with physically constrained parameters.

3.4.5 Summary of Case Studies

The developed parameter identification method was well-suited to this study. A probable global minimum was found for all variations of experimental data and all constitutive models. The requirements of low computation time and robustness in finding the probable global minima were achieved using easily employed and available methods. The use of macros further improved the method by reducing user input. The developed method was employed to reveal insights into parameter identification through the four case studies.

It was found that the ability of constitutive models to fit the prescribed experimental data is dependent on the nature of the data. Opposed to selecting a model based on a general ranking value, it is recommended that parameters for multiple constitutive models are identified and then compared on how well they fit experimental data. However, the accuracy of a model's fit to a prescribed experimental data set does not necessarily indicate how well a material's behaviour is described. To predict the general hyperelastic response throughout the range of attainable deformations, the chosen constitutive model should be that which most accurately fits or predicts a *complete* set of experimental data.

Of the limited and reduced experimental data used in the case studies, it was found that only the combination of uniaxial and equibiaxial tension data may constitute a complete set of experimental data. However, if a material or component's expected range of deformations does not span the region of attainable deformations, it is proposed that parameters may be identified using only "sufficient" experimental data. This was suggested by the consistent lower errors when fitting smaller ranges of experimental data. Sufficient experimental data could therefore include reduced strain ranges and fewer experiments. Validating these findings and the assumption of complete single loading experimental data is the focus of the following section.

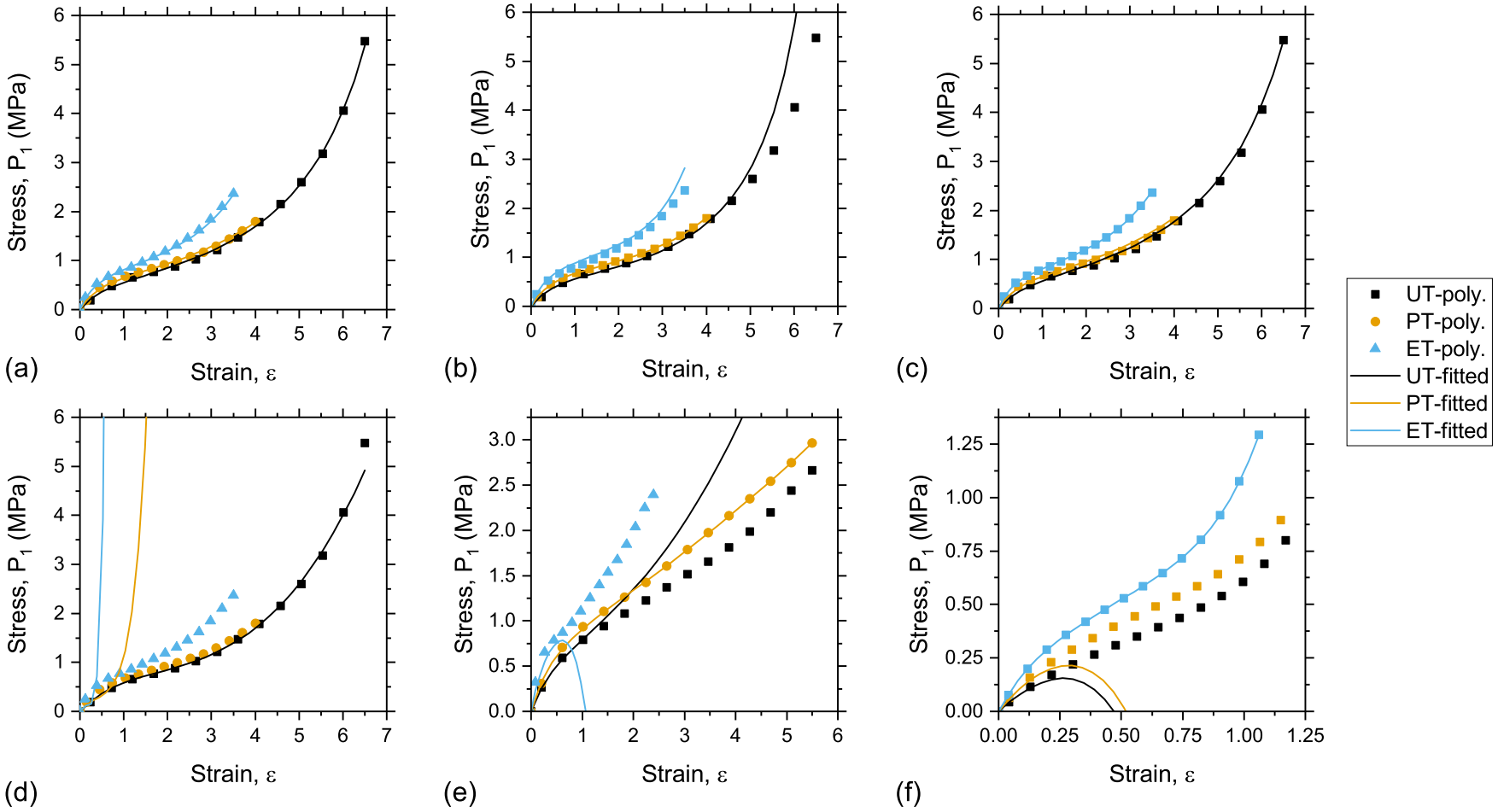

Figure 3.15: Case study 4: (a) Treloar UT fitted by extended-tube (b) Treloar PT fitted by extended-tube (c) Treloar ET fitted by extended-tube (d) Treloar UT fitted by Ogden (e) H&D PT fitted by Shariff (f) Meunier ET fitted by Haines-Wilson

3.5 Complete Hyperelastic Experimental Data

The previous parameter identification case studies investigated the ability of constitutive models to predict the upper and lower bounds and pure shear line of the invariant plane. This assumed that accurately fitting these single loading experiments gives a consistent prediction of the general mechanical behaviour of a hyperelastic material. As well as by fitting the three experiments, the combination of uniaxial and equibiaxial tension, or equivalent, data may also be capable of consistent predictions by the same assumption. A means of evaluating the assumption was developed using predictions of the stress response at interpolated deformation states. Another consideration concerns the range of interpolated values for which the predictions are consistent. Additional studies using the interpolated data were also performed. These investigated: the difference in constitutive models' fitted to interpolated behaviour and their predictions from fits to complete data, predictions of interpolated behaviour by parameters obtained from all data variations, and the difference in predictions by constitutive models fitted to complete and sufficient data.

3.5.1 Synthetic General Biaxial Data

All possible deformation states within the region of attainable deformations can be achieved by a general biaxial experiment. As a homogeneous experiment with simple analytical solutions, the general biaxial experiment is ideal for investigating the predictions of the interpolated behaviour. General biaxial data was not available for any of the three materials investigated previously. The interpolated general biaxial responses were computed using constitutive models with parameters fitted to complete data. This had the advantage of being free from experimental error. Using the generated synthetic general biaxial data, the consistency of interpolated predictions was investigated. Consistent predictions would imply that the assumption of complete hyperelastic experimental data by single loading experiments is valid.

Using the experimental data for the three materials and the concept of the invariant plane, interpolated "paths" were generated in terms of I_1 and I_2 coordinates. As found in Section 3.4.2, extrapolations beyond the fitted strain range are unreliable. The interpolated paths were therefore constrained by the maximum experimental values. Ten paths consisting of 31 points each were generated for the three materials by two methods of linear interpolation. In the first method, I_1 and I_2 coordinates were obtained by linearly interpolating between the uniaxial tension coordinate to the planar tension coordinate, then from the planar tension coordinate to the equibiaxial tension coordinate. The second method interpolated between the uniaxial tension and equibiaxial tension coordinates directly. In both methods the first path was

generated by interpolating between the maximum values for the principal stretch in the λ_1 direction. The remaining nine paths were created using 10% decreasing increments of the maximum principal stretch λ_1. The first interpolated path method is denoted as $UT{\rightarrow}PT{\rightarrow}ET$ and the second is denoted as $UT{\rightarrow}ET$. The ten paths by the first method are shown in Figures 3.16(a), 3.16(c) and 3.16(e) and for the second method in Figures 3.16(b), 3.16(d) and 3.16(f).

The constitutive models' predictions were investigated using the maximum principal Piola-Kirchhoff stress P_1 at each generated point. In order to compute the analytical solutions of the general biaxial tests, the interpolated I_1 and I_2 coordinates were resolved into principal stretches. The principal stretches were obtained by an optimisation problem. The difference between the computed and interpolated I_1 and I_2 coordinates was minimised, obtaining the computed invariants in terms of the principal stretches by equations (2.7) and (2.8) with the constraint $\lambda_1 \geq \lambda_3 \geq \lambda_2$. As previous, this assumed that the biaxial specimen was loaded in the λ_1 and λ_3 directions in tension while the λ_2 direction was free to contract.

To compare the general biaxial predictions quantitatively, the previous error function E_{RE} from equation (3.33) was used. This error function required a value for experimental data which was not available. To resolve this, the most accurate constitutive model to each complete experimental data set was used to create synthetic experimental data. The errors were computed with respect to the synthetic data. The average errors of all paths of the general biaxial predictions were used to determine the consistency of the predictions. Also, the correlation was determined between the closeness of fit to the complete single loading data sets and the error in predicting general biaxial data. Pearson's correlation coefficient (PCC) was used to quantify the correlation. The value of this correlation coefficient ranges between +1 and -1. A correlation of +1 indicates linear correlation, -1 indicates linear inverse correlation and a value of zero means that no correlation exists. Though the magnitude of the PCC is subjective, it provided a useful comparative measure.

The parameter identification studies of Section 3.4 used eight models for succinctness, five additional models were considered here to increase the statistical significance of the results. Additional highly ranked models from Marckmann and Verron (138) and Dal et al (147) were considered: Biderman (Bid.) (from Alexander (74)), Hart-Smith (H-S) (77) and Network-averaging tube (NA-t) (59). The Edwards-Vilgis (E-V) model (79) was not used in either ranking study but was shown to be a capable model by Le Saux et al (132) and was therefore included. Additionally, a novel constitutive model referred to as the eight-chain tube (8c-t) model was included. Based on the discussion by Meissner and Matějka (10), this model combines the eight-chain model (15) with a tube constraint component based on the extended-tube model (22). The

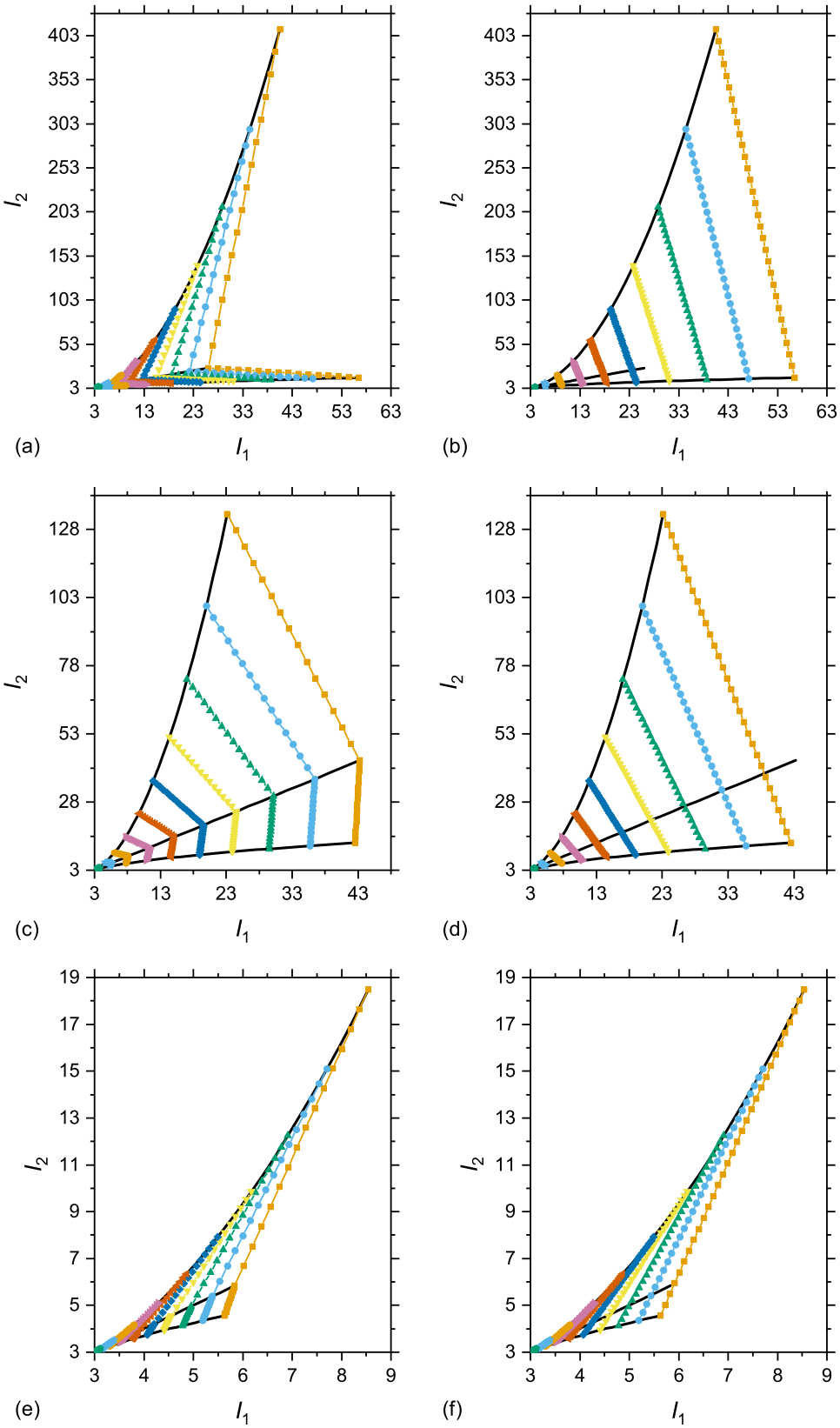

Figure 3.16: Interpolation paths for synthetic general biaxial experiments: Treloar (a) *UT→PT→ET* (b) *UT→ET*; H&D (c) *UT→PT→ET* (d) *UT→ET*; Meunier (e) *UT→PT→ET* (f) *UT→ET*

strain energy density functions for these constitutive models are defined in Table A.4. Using the parameter identification method defined in Section 3.3, two parameter sets for each additional model were identified by fitting uniaxial, planar and equibiaxial tension data and fitting uniaxial and equibiaxial tension data for the three materials. As previous, the parameters are not defined here due to their vastness and numerical sensitivity. These are available with the complete numerical results in the dataset (4).

3.5.2 Consistency of Predicted Synthetic General Biaxial Data

With three materials, two fitted parameter sets for thirteen constitutive models and two sets of ten paths, this resulted in 1560 sets of synthetic biaxial experimental data. The data required reduction in order to be effectively studied. Therefore, only the average errors for the 10 paths were compared. From this, the results were viewed in terms of the three materials, the two interpolation path variations and the two complete data variations. This gave twelve average error values and twelve correlation coefficients such that each variation could be compared. The fitted error $E_{F\%}$ refers to the minimised error function used in parameter identification, from either $UT{+}PT{+}ET$ or $UT{+}ET$ errors. The other error values refer to the values computed with respect to the predicted and synthetic biaxial data averaged over the ten computed paths. The models used to generate the synthetic data are identifiable as they have zero error.

The results for the average biaxial errors and their corresponding parameter identification error are shown for all variations in Table B.10 for Treloar and H&D data and in Table B.11 for Meunier data. The average errors and correlation coefficients for all data in both pairs, data combination and interpolation paths, were computed and shown in Table B.11. The overall average error and overall correlation coefficient computed using all 156 pairs of average biaxial and fitted errors is also given. The two variations of assumed complete experimental data and the interpolation path methods were examined by extracting and rearranging only their average biaxial errors and correlation coefficients for all models in Tables B.12 and B.13, respectively.

It was found that the overall average error is 3.16% and the individual errors of the twelve variations are all generally similar, ranging from 2.51% to 4.57%. This suggests that general biaxial data, and hence implies the general isochoric behaviour also, can be predicted based on fits to single loading homogeneous experiments with similar consistency for the considered data variations. The overall correlation was computed as 0.644, implying that a positive correlation exists between the fitted error to a complete set of single loading experiments and the consistency of predicting the general behaviour.

Comparing the two variations of prescribed experimental data, it was found that the biaxial prediction by three experiments was marginally more consistent, as shown in Table B.12, and had lower total average error, as shown in Table B.11. The correlation coefficients show on average that the use of three tests gave a stronger correlation between biaxial predictions and fitted errors. This difference was primarily due to the atypical result of the combined uniaxial and equibiaxial tension data for the Heuillet and Dugautier synthetic data. This reflects the previous finding in Section 3.4.3 where the Heuillet and Dugautier uniaxial tension and equibiaxial tension experiments could be fitted accurately but the unconstrained parameter fit produced a physically unrealistic result for the planar tension test. Combining all results separately for the three and two experiment generated data, a higher correlation and marginally less variation in biaxial predictions was found when three experiments were used in parameter identification.

The results of the interpolation paths are given in Table B.13 with overall averages referring to the results in Table B.11. The average error for the two path interpolation methods was found to be similar, the first method had generally lower average error. In terms of correlation coefficient, the first method generally had a higher correlation coefficient and an overall higher correlation coefficient in the results combined for all materials. The correlation for the Heuillet and Dugautier data was low for these, which was due to the previous observation for this material when two experiments were used. In the case of three experiments with Heuillet and Dugautier data, the correlation was slightly higher for the second path method. Generally, the first method gave a lower average biaxial prediction error and a better overall correlation and is therefore considered the more reliable method of interpolation.

3.5.3 Additional Investigations of Interpolated Behaviour

To provide further insight into the validity of predicting the interpolated behaviour by parameters identified using single loading experiments, two additional investigations were carried out. In the first, the error was compared between the fitted constitutive models' interpolated predictions and the minimum error attainable when optimised to the synthetic biaxial data. Following this, all constitutive models and all experimental data variations from the case studies of Section 3.4 were used to predict biaxial data. Their error values were computed compared with the generated synthetic data. The final investigation of this chapter assesses the proposed efficient method of parameter identification using only sufficient data.

Comparison to a Fitted Biaxial Response The general biaxial error $E_{GB\%}$ and the fitted biaxial error $E_{FB\%}$ were compared for each material. The parameters of each

constitutive model were identified by minimisation of their average biaxial errors. The average biaxial error was computed as previous, using the most accurate fitting model to create the synthetic data. For the three materials, the first method of interpolation was used, $UT{\rightarrow}PT{\rightarrow}ET$, and synthetic data using both $UT{+}PT{+}ET$ and $UT{+}ET$ data combinations were considered.

The results are shown in Table B.14 for synthetic data generated using the best fit to $UT{+}PT{+}ET$ data. The average biaxial error value represents the error obtained in the previous study from predictions of the biaxial data. The fitted error is the error obtained when parameters are identified using the generated synthetic biaxial data. The constitutive model used in the generation of the data has zero error in the first instance and when parameters are fitted since the same parameters should be re-identified. As expected, the average biaxial error for all models and all three materials decreased when parameters were identified using the synthetic biaxial data. However, the largest average difference was only 1.08% in the case of the Heuillet and Dugautier data. This demonstrated that a significant proportion of the biaxial errors was due to difference in the ability of the constitutive models to fit the interpolated biaxial data.

Using synthetic data generated by the best fit to $UT{+}ET$ data, the results were similar, as shown in Table B.15. The error when the constitutive models were fitted to the synthetic biaxial data was found to be lower than when the synthetic data was predicted. The average difference for the constitutive models was found to be higher than with three single loading experiments. However, the maximum average difference was only 1.61%. This further demonstrates that a significant contribution to the error lies in the ability to fit, rather than predict, the synthetic biaxial data. It may therefore be concluded that the use of sufficient single loading experiments is appropriate in the prediction of general hyperelastic behaviour and that the fitted error value is a good indicator of how well the behaviour is predicted.

Predictions of Biaxial Response from Experimental Data Variations The thirteen constitutive models were used to predict interpolated behaviour using parameters identified from the ten variations of experimental data from Section 3.4. Some further parameter identification was required for the five additional constitutive models. The parameters were obtained using the previous method outlined in Section 3.3. For each variation, the biaxial data was predicted and compared to synthetic biaxial data by way of the error function used throughout, defined in equation (3.33). Based on the previous investigations of the interpolated behaviour, it was determined that the best approximation of the biaxial data was by constitutive models fitted to three single loading experiments and with the interpolation path $UT{\rightarrow}PT{\rightarrow}ET$.

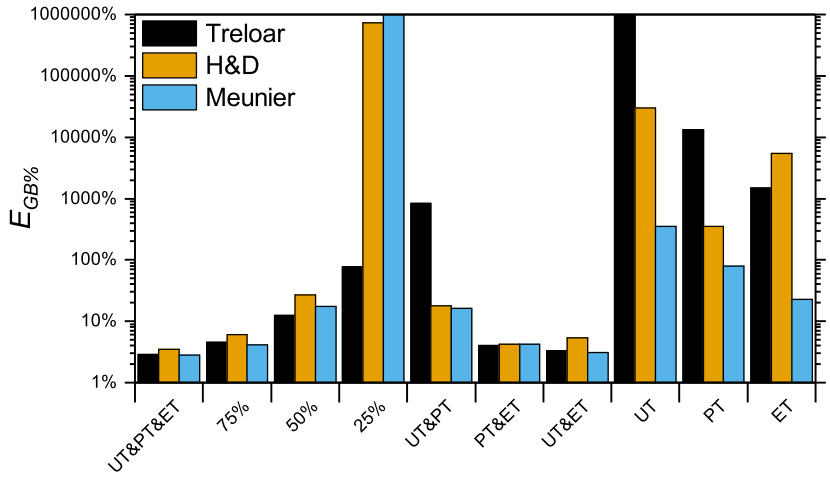

Figure 3.17: Average predicted biaxial errors for all variations of experimental data

The results were viewed in terms of the predicted biaxial errors $E_{GB\%}$ averaged across all constitutive models for the three materials. As shown in Figure 3.17, this provides an insight of the consistency of biaxial predictions with a focus on the experimental data used in parameter identification. The results of these predictions were consistent with the previous conclusions of the case studies in Section 3.4. Parameter identification by three experiments gives the lowest error, followed generally by the combination of uniaxial and equibiaxial tension. The combination of pure shear and equibiaxial tension and a 75% strain range were found to have relatively low errors in their predictions. This was due to a significant number of data points that lie between these strain ranges. Along with the high error of the other results, it becomes clear that complete experimental data should encompass the range of attainable deformations to enable consistent and hence accurate predictions within that strain range.

The results of this investigation also further suggest the use of the more efficient approach of parameter identification when the complete response is not required. It has been shown in the present study that interpolated predictions are consistent. However, predictions of the complete material response are not required if the component is not expected to deform over the entire region of attainable deformations. It would therefore be more efficient to identify parameters using only experimental data that encompasses the expected strain region for the material or component of interest. Based on the case studies for reduced strain ranges and using only two of three experiments in Sections 3.4.2 and 3.4.3, it was hypothesised that the more accurately fitted reduced or limited data would give more consistent predictions of their interpolated regions. The proposed use of only sufficient data was therefore investigated.

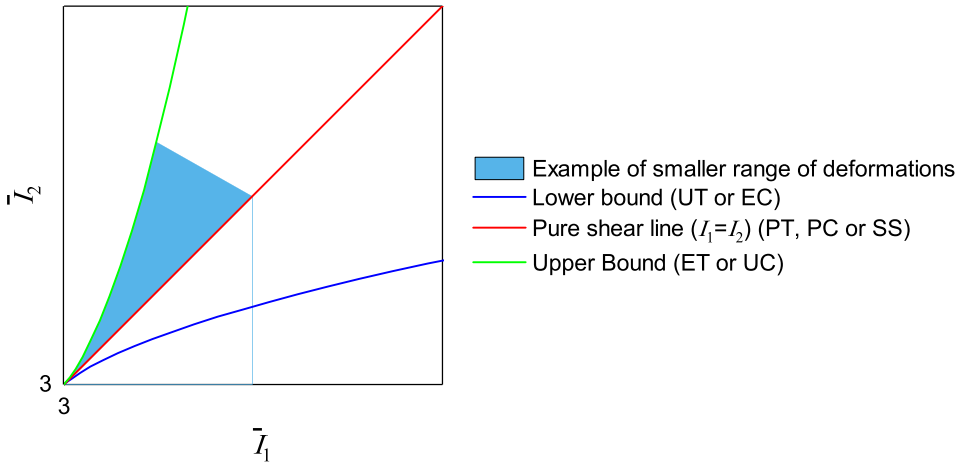

Figure 3.18: Dimensionless plot of the invariant plane with an example of a smaller range of deformations

Sufficient Hyperelastic Experimental Data A final investigation using the interpolated biaxial data was performed to assess the proposed efficient method of parameter identification using sufficient data. To further clarify what is meant by sufficient data an example is shown in Figure 3.18. In this example, the material or component has a reduced strain range and its deformations are bounded by planar and equibiaxial tension, or equivalent, deformations. In the proposed method, it would be beneficial to neglect the uniaxial tension experiment and use a strain range that efficiently encompasses the smaller range of deformations.

A comparison was made between the consistency of the predictions by complete data and sufficient data by constitutive models. As previous, the synthetic biaxial data was generated using the most accurate fit to the prescribed data for the three materials. To compute the consistency for predictions made by models fitted to sufficient data, additional synthetic data was required. This data was generated using the best fitting model to the limited or reduced experimental data set, found from the previous case studies and the inclusion of the additional constitutive models. With the generated synthetic data, the consistency was compared by use of the previous error function $E_{GB\%}$ defined in equation (3.33).

Five variations of sufficient experimental data were used, each taken from the previous case studies. The experimental data sets were: 75% strain range, 50% strain range, 25% strain range, uniaxial and planar tension, and planar tension and equibiaxial tension. The constitutive models used the previously identified parameters for the complete data or the reduced data where relevant. The synthetic biaxial data for these reduced strain regions was obtained simply by modification of the biaxial data with the interpolation path $UT \rightarrow PT \rightarrow ET$ to the smaller ranges required. To gain a general insight into the applicability of the use of complete or sufficient experimental

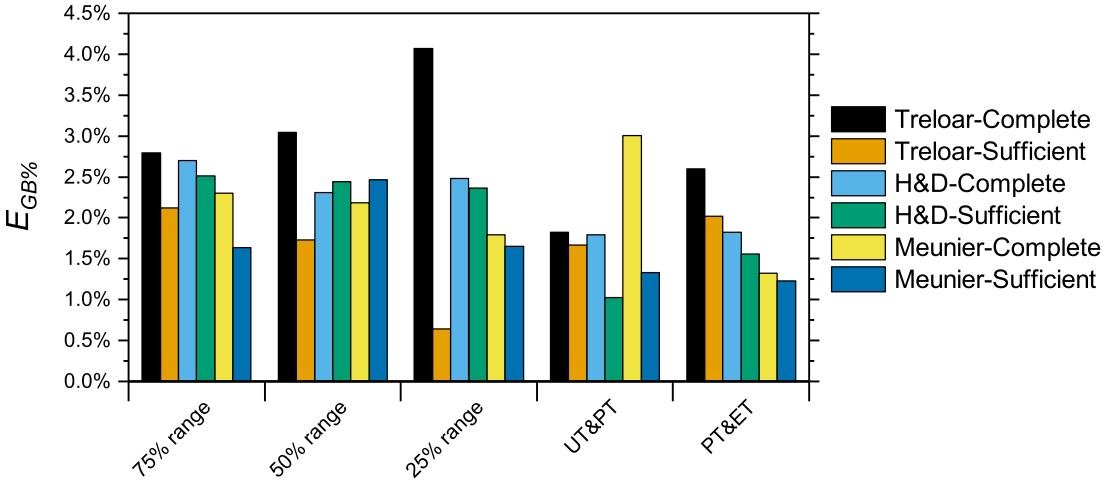

Figure 3.19: Average predicted biaxial errors for constitutive models fitted to complete or sufficient experimental data

data, only the average errors for each material and data variation was observed.

The results of this investigation are shown in Figure 3.19. As hypothesised, it was found that the parameters identified by limited and reduced experimental data generally gave more consistent predictions of interpolated data within these ranges of deformation. Of the thirty averaged errors, there were found to be only two exceptions to this conclusion, for 50% strain in H&D and Meunier data sets. In both of these cases the difference in their average predicted error values was small, within 0.3%. Upon observation of the predictions made by models fitted to the complete data, the consistency was found to often be much lower, with errors of up to 4.5%. It is therefore apparent and quantifiable that predictions of a material or component are more accurate if only sufficient experimental data is used, which encompasses the range of expected deformations. For a component with a well-defined range of deformations, such as one with only displacement loads, use of only the relevant experiments enables a more efficient approach to hyperelastic parameter identification.

3.5.4 Discussion of Biaxial Investigations

Predictions of general biaxial experiments by constitutive models with parameters fitted to data from single loading experiments were found to show a positive correlation between the fitting accuracy and the consistency of biaxial predictions. For the investigated materials it was found that the error when fitting uniaxial, planar and equibiaxial tension data generally gives a better indication of how consistently the interpolated behaviour is predicted when compared with the error when fitting only uniaxial and equibiaxial tension data. However, both data combinations enable consistency of predicted interpolated behaviour with an average of 3.13% and 3.19%

for three and two fitted experiments, respectively. When only uniaxial tension and equibiaxial tension, or equivalent, data is available it should be ensured that the prediction of the planar tension stress obeys the proposed physically realistic criterion. When linearly interpolating the single loading data on the invariant plane, the use of an interpolation path from uniaxial to planar to equibiaxial behaviour was found to be slightly favourable to a linear interpolation from uniaxial to equibiaxial behaviour.

If the complete response is to be predicted, interpolations should be constrained to the maximum experimental strain range for reliability, as initially found in the case study with reduced strain ranges, in Section 3.4.2, and further evidenced in the second investigation of Section 3.5.3. A distinction between complete and sufficient experimental data was also made. A material or component's complete response requires parameters to be identified using a complete set of experimental data covering the region of attainable deformations. However, accurate prediction of a material or component may use experimental data that encompasses its expected strain range. This is particularly useful for strain-loaded materials or components as their expected strain range is expected to be independent of material properties. This therefore permits a more efficient approach to experimentation for hyperelastic parameter identification. With the use of sufficient experimental data, it should still be assessed whether the interpolated behaviour is physically realistic.

3.6 Summary of Homogeneous Parameter Identification Studies

The various studies of this chapter aimed to provide new insights into homogeneous experiments used in hyperelastic parameter identification. A set of criteria to assess the physical plausibility of hyperelastic experimental data was proposed. These were based on previously defined constraints to ensure the physically realistic behaviour of constitutive models. An additional criterion was proposed that provides a simple means of assessing the plausibility of homogeneous experimental data in the tensile domain. A robust parameter identification method for hyperelastic constitutive models was then developed. To fit the complete strain range of the input experimental data with minimised bias, consideration was given to each data set's strain range distribution and stress magnitude.

Using a developed parameter identification method, an investigation of the use of single loading experimental data and the implications of constitutive model selection was carried out. It was found that an accurate fit to prescribed experimental data does not necessarily imply an accurate prediction of a material's general behaviour.

Extrapolations outside of the fitted experimental data range are unreliable; this includes exceeding the experimental strain range or predictions of unfitted deformation modes. The exception of this is when the unfitted deformations are interpolations of the experimental measurements, in terms of their strain ranges when viewed on the invariant plane. The hypothesis of complete data was tested for two experimental data combinations: uniaxial, planar and equibiaxial tension experiments and uniaxial and equibiaxial tension experiments. By comparing predictions of synthetic general biaxial data, it was found that the use of three experiments has more reliable predictions, but either method predicted the synthetic general biaxial data accurately for the chosen constitutive models.

In terms of hyperelastic constitutive model selection, the results of the studies presented in this chapter highlight some key findings. The ability of a specific constitutive model to predict unfitted behaviour was shown to be unreliable when different materials were considered. On the same basis, the ranking of constitutive models based on their fit to a single material was found not to be universally applicable. To predict the hyperelastic response of a material, it is recommended that sufficient experimental data is acquired. It was shown that sufficient experimental data is that which encompasses the expected strain range of the component's deformation, for which the use of the invariant plane is insightful. A more efficient method is to use only relevant experiments bounding the expected range of deformations. A parameter identification method for the sufficient data should then be used with several capable constitutive models. The constitutive model should be chosen on the basis that it most accurately fits the sufficient experimental data and its predicted interpolated values are physically realistic.

The use of experimental data from literature and synthetic general biaxial data allowed an insight into the predictions of the interpolated hyperelastic behaviour. A more efficient approach to hyperelastic parameter identification was proposed and demonstrated to be valid for predictions of interpolated biaxial behaviour. It is also relevant to demonstrate the proposed approach and investigate the implications of parameter identification with complete and sufficient experimental data in the context of predicting the behaviour of an industrial component. The nature of industrial components is often too complex to feasibly construct analytical solutions. A numerical method may therefore be employed. Therefore, the implicit Finite Element Method was used within the commercial solver Abaqus/Standard (3). Some of the investigated constitutive models were not available in Abaqus' constitutive model library. Numerical implementations for user-defined hyperelastic constitutive models were therefore developed. These are discussed subsequently in Chapters 4 and 5. Investigations of hyperelastic parameter identification are then continued in the context of simulating industrial components in Chapter 6.

Chapter 4

Finite Element Implementation of Hyperelasticity by Numerically Approximated Elasticity Moduli

User subroutines for the numerical implementation of hyperelastic constitutive models in the FEM were investigated with a focus on Abaqus/Standard. As discussed in Section 2.5, there are well established derivations for constitutive models defined in terms of Cauchy-Green invariants. However, models defined in terms of isochoric principal stretches are ambiguous in their elasticity tensor's definition and its numerical implementation. This led to the development and investigation of various methods of numerical implementation discussed in this chapter and subsequently in Chapter 5.

The ambiguous nature of the elasticity tensor for principal stretch models, which is obtained by differentiation of the relevant stress tensor, led to an investigation into numerical differentiation methods. Two complimentary real domain approximation methods for accurate computation of finite strain elasticity moduli were developed. As the stress and elasticity tensors for hyperelasticity in terms of Cauchy-Green invariants are well established and numerically stable, these enabled the development and validation of the numerically approximated tangent moduli implementations. The developed methods were also investigated in terms of their computational efficiencies. The methods from this chapter were used in the development of a novel principal stretch implementation, discussed subsequently in Chapter 5.

4.1 Finite Element Implementation of Hyperelasticity in terms of Cauchy-Green Invariants

An initial investigation presented in this chapter compared built-in constitutive models in Abaqus/Standard to UHYPER and UMAT implementations of the same constitutive model. This validated the UMAT implementations developed for hyperelasticity in terms of Cauchy-Green invariants, which were later used for the development of the novel numerical implementations. A UHYPER user subroutine and two variations of UMAT subroutines were investigated using a benchmark FEM simulation in Abaqus/Standard. The criteria for the comparison were their numerical accuracy, computational efficiencies and convergence behaviour. Initially, the stress and elasticity tensors for hyperelasticity in terms of Cauchy-Green invariants are outlined and the developed numerical implementations are discussed.

4.1.1 Hyperelasticity in terms of Cauchy-Green Invariants

Two variations were considered for numerical implementation of isochoric Cauchy-Green invariant constitutive models. The difference between the numerical implementations is their depth of derivation. One method uses the derivation by Miehe (151) with fictitious stress and elasticity tensors. These are required in the implementation of the non-affine micro-sphere model (11). Opposed to deriving these terms further, the developed method performs various tensor operations within matrices to compute the necessary stress and elasticity tensor components directly. The other method further expands the derivation and the resulting variables can therefore be obtained by any known derivation (5, 150, 151, 152). The terms derived by Miehe (151) are therefore applicable for both considered methods. This derivation was used for reference and is outlined here with comment upon where the two numerical implementation methods deviate. For completeness, the variables are defined initially in the reference configuration and their spatial equivalent terms required by Abaqus/Standard are obtained by push-forward operations.

Both methods are defined using the finite elasticity framework described in Section 2.1. An additive split of the isochoric and volumetric contributions of the strain energy density function is used (6). The stress tensor and elasticity moduli are also split into isochoric and volumetric contributions. The total strain energy ψ is split into isochoric W and volumetric U contributions. With symbols defined as previous, this is defined as

$$\psi = W\left(\bar{I}_1, \bar{I}_2\right) + U\left(J\right) \tag{4.1}$$

Material Stress Tensor In the reference configuration, the second Piola-Kirchhoff stress tensor $\mathbf{S}$ defines the material stress. For a hyperelastic constitutive model this is calculated as the derivative of the energy ψ with respect to the right Cauchy-Green deformation tensor $\mathbf{C}$ as

$$\mathbf{S} = 2\frac{\partial \psi}{\partial \mathbf{C}} \tag{4.2}$$

$$\mathbf{S} = \mathbf{S}_{iso} + \mathbf{S}_{vol} = 2\frac{\partial W\left(\overline{I}_1, \overline{I}_2\right)}{\partial \mathbf{C}} + 2\frac{\partial U\left(J\right)}{\partial \mathbf{C}} \tag{4.3}$$

The volumetric stress tensor $\mathbf{S}_{vol}$ is simply defined using a chain rule (5) to give

$$\mathbf{S}_{vol} = 2\frac{\partial U}{\partial J}\frac{\partial J}{\partial \mathbf{C}} = J\frac{\partial U}{\partial J}\mathbf{C}^{-1} \tag{4.4}$$

The isochoric component $\mathbf{S}_{iso}$ is defined (5, 151, 152) in terms of the volume ratio J and the Lagrangian deviator of the fictitious second Piola-Kirchhoff stress tensor $\mathrm{Dev}\left(\overline{\mathbf{S}}\right)$ as

$$\mathbf{S}_{iso} = J^{-\frac{2}{3}}\mathrm{Dev}\left(\overline{\mathbf{S}}\right) \tag{4.5}$$

The fictitious second Piola-Kirchhoff stress tensor $\overline{\mathbf{S}}$ is defined by

$$\overline{\mathbf{S}} = a_1\mathbf{1} - a_2\overline{\mathbf{C}} \tag{4.6}$$

The scalar coefficients a_1 and a_2 are constitutive model dependent and computed by

$$a_1 = 2\left(\frac{\partial W}{\partial \overline{I}_1} + \overline{I}_1\frac{\partial W}{\partial \overline{I}_2}\right) \tag{4.7}$$

$$a_2 = 2\left(\frac{\partial W}{\partial \overline{I}_2}\right) \tag{4.8}$$

The Lagrangian deviatoric operator $\mathrm{Dev}\left(\mathbf{A}\right)$ is defined for a generic second-order material tensor $\mathbf{A}$ by

$$\mathrm{Dev}\left(\mathbf{A}\right) = \left(\mathbf{A}\right) - \frac{1}{3}\left[\left(\mathbf{A}\right) : \mathbf{C}\right]\mathbf{C}^{-1} \tag{4.9}$$

By performing the tensor operations in the subroutine using matrices, the above terms are therefore sufficient to obtain the stress tensor. However, in the further derived implementation the isochoric second Piola-Kirchhoff stress tensor was defined as

$$\mathbf{S}_{iso} = a_1 J^{-\frac{2}{3}}\left(\mathbf{1} - \frac{1}{3}I_1\mathbf{C}^{-1}\right) + a_2 J^{-\frac{4}{3}}\left(\mathbf{C} - \frac{1}{3}\mathrm{tr}\left(\mathbf{C}^2\right)\mathbf{C}^{-1}\right) \tag{4.10}$$

Spatial Stress Tensors The equivalent spatial stress tensors may all be obtained by push-forward operations of the previous variables. Both implementations use the same scalar coefficients a_1 and a_2 for user input. The total spatial stress tensor is

defined in terms of the Kirchhoff stress, $\boldsymbol{\tau}$. This stress tensor is related to the second Piola-Kirchhoff stress tensor by

$$\boldsymbol{\tau} = \mathbf{F}\mathbf{S}\mathbf{F}^{\mathrm{T}} \tag{4.11}$$

The spatial Kirchhoff stress tensor is also split into isochoric $\boldsymbol{\tau}_{iso}$ and volumetric $\boldsymbol{\tau}_{vol}$ components by $\boldsymbol{\tau} = \boldsymbol{\tau}_{iso} + \boldsymbol{\tau}_{vol}$. The volumetric Kirchhoff stress tensor $\boldsymbol{\tau}_{vol}$ is found using equation (4.11) to give

$$\boldsymbol{\tau}_{vol} = J\frac{\partial U}{\partial J}\mathbf{1} \tag{4.12}$$

For the implementation with matrix operations, the isochoric Kirchhoff stress tensor $\boldsymbol{\tau}_{iso}$ is defined in terms of the Eulerian deviator of the fictitious Kirchhoff stress tensor $\overline{\boldsymbol{\tau}}$ as

$$\boldsymbol{\tau}_{iso} = \mathrm{dev}\left(\overline{\boldsymbol{\tau}}\right) \tag{4.13}$$

The fictitious Kirchhoff stress tensor is defined in terms of the same scalar coefficients as previous, a_1 and a_2, by

$$\overline{\boldsymbol{\tau}} = a_1\overline{\mathbf{b}} - a_2\overline{\mathbf{b}}^2 \tag{4.14}$$

This is then used in the Eulerian deviatoric operator $\mathrm{dev}\left(\mathbf{a}\right)$, which is defined in terms of a generic second-order spatial tensor $\mathbf{a}$ as

$$\mathrm{dev}\left(\mathbf{a}\right) = \left(\mathbf{a}\right) - \frac{1}{3}\mathrm{tr}\left(\mathbf{a}\right)\mathbf{1} \tag{4.15}$$

Alternatively, the numerical implementation may use the fully derived form of the isochoric Kirchhoff stress tensor. This is defined by

$$\boldsymbol{\tau}_{iso} = a_1\left(\overline{\mathbf{b}} - \frac{1}{3}\overline{I}_1\mathbf{1}\right) + a_2\left(\overline{\mathbf{b}}^2 - \frac{1}{3}\mathrm{tr}\left(\overline{\mathbf{b}}^2\right)\mathbf{1}\right) \tag{4.16}$$

The spatial Cauchy stress tensor $\boldsymbol{\sigma}$ is required for implementation into Abaqus. By summation of the isochoric and volumetric Kirchhoff stress tensors, defined in equations (4.16) and (4.12), the Cauchy stress tensor is calculated from the total Kirchhoff stress tensor as

$$\boldsymbol{\sigma} = J^{-1}\boldsymbol{\tau} \tag{4.17}$$

Material Elasticity Tensor The material elasticity tensor may be obtained by connection of the rate form of the stress and deformation tensors, $\dot{\mathbf{S}}$ and $\dot{\mathbf{C}}$ respectively (151). These quantities are connected to the material elasticity tensor $\mathbb{C}$ by

$$\dot{\mathbf{S}} = \mathbb{C} : \dot{\mathbf{C}}/2 \tag{4.18}$$

Due to the rate-independence of hyperelasticity and the objective nature of the material elasticity tensor, $\mathbb{C}$ may be defined equivalently by differentiation of the second

Piola-Kirchhoff stress tensor with respect to the right Cauchy-Green deformation tensor

$$\mathbb{C} = 2\frac{\partial \mathbf{S}}{\partial \mathbf{C}} \tag{4.19}$$

The fourth-order material elasticity tensor $\mathbb{C}$ is additively split into isochoric $\mathbb{C}_{iso}$ and volumetric components $\mathbb{C}_{vol}$ by

$$\mathbb{C} = \mathbb{C}_{iso} + \mathbb{C}_{vol} \tag{4.20}$$

The volumetric elasticity tensor is defined in both implementations in terms of a chain rule. The volumetric second Piola-Kirchhoff stress, defined in equation (4.4), is differentiated with respect to the right Cauchy-Green tensor. This is given as

$$\mathbb{C}_{vol} = 2\frac{\partial \mathbf{S}_{vol}}{\partial \mathbf{C}} = 4\left[\frac{\partial U}{\partial J}\left(\frac{\partial^2 J}{\partial \mathbf{C}\partial \mathbf{C}}\right) + \frac{\partial^2 U}{\partial J^2}\left(\frac{\partial J}{\partial \mathbf{C}} \otimes \frac{\partial J}{\partial \mathbf{C}}\right)\right] \tag{4.21}$$

Using various identities, see Holzapfel (5) for full derivation, this leads to the expression

$$\mathbb{C}_{vol} = J\left(\frac{\partial U}{\partial J} + \frac{\partial^2 U}{\partial J^2} J\right)\left(\mathbf{C}^{-1} \otimes \mathbf{C}^{-1}\right) - 2\frac{\partial U}{\partial J} J\left(\mathbf{C}^{-1} \odot \mathbf{C}^{-1}\right) \tag{4.22}$$

The symmetric fourth-order dyadic product, notated by $\odot$, has been introduced for convenience, as in the work of Holzapfel (5). It is defined as

$$(\mathbf{A} \odot \mathbf{B})_{IJKL} = \frac{1}{2}\left(A_{IK}B_{JL} + A_{IL}B_{JK}\right) \tag{4.23}$$

To obtain the isochoric contribution to the material elasticity tensor, the derivative in equation (4.19) can be applied to the fully derived and expanded form of the isochoric second Piola-Kirchhoff stress tensor in equation (4.10) or to the earlier form in equation (4.5). In the implementation of the fully derived and expanded variables, either approach may be used. The implementation using the fictitious stress tensor and matrix operations requires differentiation of equation (4.5). This results in the following definition for the isochoric material elasticity tensor

$$\mathbb{C}_{iso} = \mathrm{Dev}\left(\overline{\mathbb{C}}\right) + \frac{2}{3}J^{-\frac{2}{3}}\left(\overline{\mathbf{S}} : \mathbf{C}\right)\overline{\mathbb{P}} - \frac{2}{3}J^{-\frac{2}{3}}\left(\mathbf{S}_{iso} \otimes \mathbf{C}^{-1} + \mathbf{C}^{-1} \otimes \mathbf{S}_{iso}\right) \tag{4.24}$$

The material elasticity tensor requires definition of the modified projection tensor $\overline{\mathbb{P}}$ and the fictitious elasticity tensor $\overline{\mathbb{C}}$, which uses the fourth-order Lagrangian deviatoric operator $\mathrm{Dev}\left(\mathbb{A}\right)$. These are defined by

$$\overline{\mathbb{P}} = \left[\left(\mathbf{C}^{-1} \odot \mathbf{C}^{-1}\right) - \frac{1}{3}\left(\mathbf{C}^{-1} \otimes \mathbf{C}^{-1}\right)\right] \tag{4.25}$$

$$\overline{\mathbb{C}} = J^{-\frac{4}{3}}\left[b_1\left(\mathbf{1} \otimes \mathbf{1}\right) - b_2\left(\mathbf{1} \otimes \overline{\mathbf{C}} + \overline{\mathbf{C}} \otimes \mathbf{1}\right) + b_3\left(\overline{\mathbf{C}} \otimes \overline{\mathbf{C}}\right) - b_4\mathbb{I}\right] \tag{4.26}$$

$$\mathrm{Dev}\left(\mathbb{A}\right) = \mathbb{A} - \frac{1}{3}\left[\mathbf{C}^{-1} \otimes \left(\mathbb{A} : \mathbf{C}\right)\right] - \frac{1}{3}\left[\left(\mathbb{A} : \mathbf{C}\right) \otimes \mathbf{C}^{-1}\right] + \frac{1}{9}\left(\mathbf{C} : \mathbb{A} : \mathbf{C}\right)\left(\mathbf{C}^{-1} \otimes \mathbf{C}^{-1}\right) \tag{4.27}$$

The constitutive model dependent scalar coefficients b_1, b_2, b_3 and b_4 are defined by

$$b_1 = 4\left(\frac{\partial^2 W}{\partial \bar{I}_1{}^2} + \frac{\partial W}{\partial \bar{I}_2} + \bar{I}_1{}^2\frac{\partial^2 W}{\partial \bar{I}_2{}^2} + 2\bar{I}_1\frac{\partial^2 W}{\partial \bar{I}_1 \partial \bar{I}_2}\right) \tag{4.28}$$

$$b_2 = 4\left(\bar{I}_1\frac{\partial^2 W}{\partial \bar{I}_2{}^2} + \frac{\partial^2 W}{\partial \bar{I}_1 \partial \bar{I}_2}\right) \tag{4.29}$$

$$b_3 = 4\left(\frac{\partial^2 W}{\partial \bar{I}_2{}^2}\right) \tag{4.30}$$

$$b_4 = 4\left(\frac{\partial W}{\partial \bar{I}_2}\right) \tag{4.31}$$

These variables are sufficient for numerical implementation with coded tensor operations. With further derivation for the alterative implementation, the material elasticity tensor may be given as

$$\begin{aligned}\mathbb{C}_{iso} = {} & \Delta_1\left(\mathbf{1}\otimes\mathbf{1}\right) + \Delta_2\left[\left(\mathbf{1}\otimes\mathbf{C}\right) + \left(\mathbf{C}\otimes\mathbf{1}\right)\right] + \Delta_3\left[\left(\mathbf{1}\otimes\mathbf{C}^{-1}\right) + \left(\mathbf{C}^{-1}\otimes\mathbf{1}\right)\right] \\ & + \Delta_4\left(\mathbf{C}\otimes\mathbf{C}\right) + \Delta_5\left[\left(\mathbf{C}^{-1}\otimes\mathbf{C}\right) + \left(\mathbf{C}\otimes\mathbf{C}^{-1}\right)\right] + \Delta_6\left(\mathbf{C}^{-1}\otimes\mathbf{C}^{-1}\right) \\ & + \Delta_7\left(\mathbf{C}^{-1}\odot\mathbf{C}^{-1}\right) + \Delta_8\left(\mathbf{1}\odot\mathbf{1}\right)\end{aligned} \tag{4.32}$$

The eight Δ_n coefficients of the material elasticity tensor are defined as

$$\Delta_1 = b_1 J^{-\frac{4}{3}} \tag{4.33}$$

$$\Delta_2 = -b_2 J^{-2} \tag{4.34}$$

$$\Delta_3 = \frac{1}{3}\left(2a_1 J^{-\frac{2}{3}} - b_1 I_1 J^{-\frac{4}{3}} + b_2 \mathrm{tr}\left(\mathbf{C}^2\right) J^{-2}\right) \tag{4.35}$$

$$\Delta_4 = b_3 J^{-\frac{8}{3}} \tag{4.36}$$

$$\Delta_5 = \left(2a_2 J^{-\frac{4}{3}} + b_2 I_1 J^{-2} - b_3 \mathrm{tr}\left(\mathbf{C}^2\right) J^{-\frac{8}{3}} + b_4 J^{-\frac{4}{3}}\right) \tag{4.37}$$

$$\begin{aligned}\Delta_6 = {} & \frac{1}{9}\left(2a_1 I_1 J^{-\frac{2}{3}} - 2a_2 \mathrm{tr}\left(\mathbf{C}^2\right) J^{-\frac{4}{3}} + b_1 {I_1}^2 J^{-\frac{4}{3}}\right) \\ & + \frac{1}{9}\left(-2b_2 I_1 \mathrm{tr}\left(\mathbf{C}^2\right) J^{-2} + b_3 \mathrm{tr}\left(\mathbf{C}^2\right)^2 J^{-\frac{8}{3}} - b_4 \mathrm{tr}\left(\mathbf{C}^2\right) J^{-\frac{4}{3}}\right)\end{aligned} \tag{4.38}$$

$$\Delta_7 = \frac{2}{3}\left(a_1 I_1 J^{-\frac{2}{3}} - a_2 \mathrm{tr}\left(\mathbf{C}^2\right) J^{-\frac{4}{3}}\right) \tag{4.39}$$

$$\Delta_8 = -b_4 J^{-\frac{4}{3}} \tag{4.40}$$

Spatial Elasticity Tensor While the material elasticity tensor is naturally objective (182), the spatial elasticity tensor exists in several forms to enable objectivity (198). The form required by Abaqus/Standard is the Jaumann-rate of Cauchy stress $\mathbb{c}_{ABQ}$. For convenience, the spatial elasticity tensor $\mathbb{c}$ defined as the Oldroyd-rate of the Kirchhoff stress was initially derived. Its fourth-order spatial tensors are obtained by

push-forward of the equivalent material elasticity variables. The Jaumann-rate of the Cauchy-Stress may then be found using the relationship between these two variations of the spatial elasticity tensor.

In index notation, the total fourth-order material elasticity tensor $\mathbb{C}$ is related to the total spatial elasticity tensor $\mathbb{c}$ by

$$\mathbb{c}_{ijkl} = J^{-1} F_{iI} F_{jJ} F_{kK} F_{lL} \mathbb{C}_{IJKL} \tag{4.41}$$

Using this relationship the volumetric spatial elasticity tensor $\mathbb{c}_{vol}$ is defined as

$$\mathbb{c}_{vol} = J \left(\frac{\partial U}{\partial J} + \frac{\partial^2 U}{\partial J^2} J \right) (\mathbf{1} \otimes \mathbf{1}) - 2 \frac{\partial U}{\partial J} J (\mathbf{1} \odot \mathbf{1}) \tag{4.42}$$

The isochoric contribution $\mathbb{c}_{iso}$ is obtained by push-forward of equation (4.24) to give

$$\mathbb{c}_{iso} = \operatorname{dev}(\overline{\mathbb{c}}) + \frac{2}{3} \operatorname{tr}(\overline{\boldsymbol{\tau}}) \overline{\mathbb{p}} - \frac{2}{3} (\boldsymbol{\tau}_{iso} \otimes \mathbf{1} + \mathbf{1} \otimes \boldsymbol{\tau}_{iso}) \tag{4.43}$$

The equivalent spatial fourth-order tensors require definition. These are the spatial projection tensor $\overline{\mathbb{p}}$ and the fictitious spatial elasticity tensor $\overline{\mathbb{c}}$, for which the Eulerian deviatoric operator of a fourth-order tensor $\operatorname{dev}(\mathbb{a})$ is used. These are obtained by push forward operations and defined as

$$\overline{\mathbb{p}} = \left[(\mathbf{1} \odot \mathbf{1}) - \frac{1}{3} (\mathbf{1} \otimes \mathbf{1}) \right] \tag{4.44}$$

$$\overline{\mathbb{c}} = \left[b_1 \left(\overline{\mathbf{b}} \otimes \overline{\mathbf{b}} \right) - b_2 \left(\overline{\mathbf{b}} \otimes \overline{\mathbf{b}}^2 + \overline{\mathbf{b}}^2 \otimes \overline{\mathbf{b}} \right) + b_3 \left(\overline{\mathbf{b}}^2 \otimes \overline{\mathbf{b}}^2 \right) - b_4 \left(\overline{\mathbf{b}} \odot \overline{\mathbf{b}} \right) \right] \tag{4.45}$$

$$\operatorname{dev}(\mathbb{a}) = \mathbb{a} - \frac{1}{3} [\mathbf{1} \otimes (\mathbb{a} : \mathbf{1})] - \frac{1}{3} [(\mathbb{a} : \mathbf{1}) \otimes \mathbf{1}] + \frac{1}{9} (\mathbf{1} : \mathbb{a} : \mathbf{1}) (\mathbf{1} \otimes \mathbf{1}) \tag{4.46}$$

These variables are sufficient for the computation of $\mathbb{c}$ if the numerical implementation performs the required tensor operations within the subroutine. The alternative form of the isochoric component $\mathbb{c}_{iso}$ can be further derived from the above or by push forward of equation (4.32). This is defined as

$$\begin{aligned} \mathbb{c}_{iso} = {} & \delta_1 \left(\overline{\mathbf{b}} \otimes \overline{\mathbf{b}} \right) + \delta_2 \left[\left(\overline{\mathbf{b}} \otimes \overline{\mathbf{b}}^2 \right) + \left(\overline{\mathbf{b}}^2 \otimes \overline{\mathbf{b}} \right) \right] + \delta_3 \left[\left(\overline{\mathbf{b}} \otimes \mathbf{1} \right) + \left(\mathbf{1} \otimes \overline{\mathbf{b}} \right) \right] \\ & + \delta_4 \left(\overline{\mathbf{b}}^2 \otimes \overline{\mathbf{b}}^2 \right) + \delta_5 \left[\left(\mathbf{1} \otimes \overline{\mathbf{b}}^2 \right) + \left(\overline{\mathbf{b}}^2 \otimes \mathbf{1} \right) \right] + \delta_6 (\mathbf{1} \otimes \mathbf{1}) \\ & + \delta_7 (\mathbf{1} \odot \mathbf{1}) + \delta_8 \left(\overline{\mathbf{b}} \odot \overline{\mathbf{b}} \right) \end{aligned} \tag{4.47}$$

With the eight δ_n coefficients defined by

$$\delta_1 = b_1 \tag{4.48}$$

$$\delta_2 = -b_2 \tag{4.49}$$

$$\delta_3 = \frac{1}{3}\left(2a_1 - b_1 I_1 + b_2 \mathrm{tr}\left(\mathbf{b}^2\right)\right) \tag{4.50}$$

$$\delta_4 = b_3 \tag{4.51}$$

$$\delta_5 = \left(2a_2 + b_2 I_1 - b_3 \mathrm{tr}\left(\mathbf{b}^2\right) + b_4\right) \tag{4.52}$$

$$\begin{aligned}\delta_6 = &\frac{1}{9}\left(2a_1 I_1 - 2a_2 \mathrm{tr}\left(\mathbf{b}^2\right) + b_1 {I_1}^2\right) \\ &+ \frac{1}{9}\left(-2b_2 I_1 \mathrm{tr}\left(\mathbf{b}^2\right) + b_3 \mathrm{tr}\left(\mathbf{b}^2\right)^2 - b_4 \mathrm{tr}\left(\mathbf{b}^2\right)\right)\end{aligned} \tag{4.53}$$

$$\delta_7 = \frac{2}{3}\left(a_1 I_1 - a_2 \mathrm{tr}\left(\mathbf{b}^2\right)\right) \tag{4.54}$$

$$\delta_8 = -b_4 \tag{4.55}$$

The total spatial elasticity tensor $\mathbb{c}$, defined in terms of the Oldroyd-rate of the Kirchhoff stress, is then transformed in both implementation methods using the relationship to the Jaumann-rate of the Cauchy stress $\mathbb{c}_{ABQ}$. This is the form required by UMAT subroutines in Abaqus/Standard and it is computed as follows (156)

$$\mathbb{c}_{ABQ} = J^{-1}\left(\mathbb{c}_{iso} + \mathbb{c}_{vol}\right) + \left(\boldsymbol{\sigma} \odot \mathbf{1}\right) + \left(\mathbf{1} \odot \boldsymbol{\sigma}\right) \tag{4.56}$$

4.1.2 Aspects of FEM Implementation

With the definition of the second-order Cauchy stress tensor $\boldsymbol{\sigma}$ and the fourth-order elasticity tensor in terms of the Jaumann-rate of the Cauchy stress $\mathbb{c}_{ABQ}$, some further considerations are required for the two methods of numerical implementation. The following discussion is based on the use of the input of a UMAT subroutine in Abaqus/Standard using the standardised format for a Fortran ".for" code provided in the Abaqus documentation (3). The method for developing the implementations initially used self-contained Fortran programs with a manually prescribed deformation gradient. These programs were then adapted to an additional subroutine to be called within the standardised UMAT formatted codes. The stand-alone programs and UMAT subroutines for the developed implementations are available in the dataset (4).

An aim for the developed FEM implementations was to reduce the user input. For an isochoric material in either configuration, the user is required only to provide the derivatives $\frac{\partial W}{\partial \bar{I}_1}$ and $\frac{\partial W}{\partial \bar{I}_2}$ to compute the stress tensors. For computing the tangent

moduli, the derivatives $\frac{\partial^2 W}{\partial \bar{I}_1{}^2}$, $\frac{\partial^2 W}{\partial \bar{I}_2{}^2}$ and $\frac{\partial^2 W}{\partial \bar{I}_1 \partial \bar{I}_2}$ require definition. Then with the declaration of the constitutive model parameters and any additional values as variables, the derivatives may be computed. Optionally, the elastic strain energy density may be defined and computed. The codes were annotated to highlight where user input is required. The remainder of the UMAT codes remains independent for Cauchy-Green invariant constitutive models. The amount of user input was therefore considered to be minimised and of similar difficulty as that of an Abaqus/Standard UHYPER subroutine.

The stress and tangent moduli components are predefined in UMAT by the arrays STRESS(6) and DDSDDE(6,6), or STRESS(4) and DDSDDE(4,4) for 2D plane strain or axisymmetric FE models. The bracketed terms represent the dimensions of the arrays. However, the second-order Cauchy stress tensor $\boldsymbol{\sigma}$ has nine components and the spatial elasticity tensor $\mathbb{c}_{ABQ}$ has eighty-one components. The difference is due to the use of Voigt notation. The symmetric second-order tensor σ_{ij}, where $i, j = 1, 2, 3$, may be represented in Voigt notation as σ_a, where $a = 1, 2, 3, 4, 5, 6$. This is because symmetric second-order tensors have three pairs of equal components, for example $\sigma_{12} = \sigma_{21}$, $\sigma_{13} = \sigma_{31}$ and $\sigma_{23} = \sigma_{32}$. In the notation used by Abaqus, the indices (1, 2, 3, 4, 5, 6) representing (11, 22, 33, 12, 13, 23), respectively. Similarly, the eighty-one components of the elasticity tensor $\mathbb{c}_{ABQ_{ijkl}}$ where $i, j, k, l = 1, 2, 3$ may be represented by thirty-six components in Voigt notation. This is due to the minor symmetries $\mathbb{c}_{ABQ_{ijkl}} = \mathbb{c}_{ABQ_{jikl}}$ and $\mathbb{c}_{ABQ_{ijkl}} = \mathbb{c}_{ABQ_{ijlk}}$. Hence, the elasticity tensor is defined in Voigt notation as $\mathbb{c}_{ABQ_{ab}}$, where $a, b = 1, 2, 3, 4, 5, 6$ with the same definitions of the indices as previous. For isotropic materials, the elasticity may be further reduced to twenty-one components as it also has major symmetry, $\mathbb{c}_{ABQ_{ijkl}} = \mathbb{c}_{ABQ_{klij}}$ or in Voigt notation $\mathbb{c}_{ABQ_{ab}} = \mathbb{c}_{ABQ_{ba}}$. In 2D problems, the user subroutines are adapted to reduce the STRESS and DDSDDE matrices to the required dimensions. For the stress components only the first four components are used and for the elasticity tensor the matrix is reduced to the first four by four components. The codes are otherwise unaltered.

The deformation gradient alone is sufficient to compute the stress tensor and tangent moduli for a hyperelastic constitutive model. In UMAT, the deformation gradient $\mathbf{F}$ is input to the Fortran subroutine at each integration point of the FE model as the variable DFGRD1(3,3). As this tensor is not symmetric, it may not be stored in Voigt notation. However, the required strain tensor $\mathbf{b}$, and its isochoric variants, are symmetric and are therefore computed and stored in Voigt notation throughout. Within the developed codes, utility subroutines were used to perform repeat operations for computing the determinant of arrays, the fourth-order tensor products, and the fourth-order symmetric tensor products. The UMAT user subroutines then coded

the expressions defined in Section 4.1.1 within the two developed numerical implementation methods for comparison with built-in and UHYPER implementations of hyperelasticity.

4.1.3 Finite Element Investigation of Cauchy-Green Invariant Implementations

The investigation of the two UMAT implementations, UHYPER implementation and a built-in model for hyperelasticity in Cauchy-Green invariants used Finite Element models created in the Abaqus/CAE interface and solved using Abaqus/Standard. For a built-in constitutive model, the user is required only to select the constitutive model and define the magnitude of its parameters. If the material is incompressible, the user specifies incompressibility by equating the volumetric parameters to zero. In UHYPER, a user-defined hyperelastic material is selected and the parameters are assigned by modifying the ".inp" input file. Also, the user must assign a Fortran file with definition of the number of parameters and the strain energy density derivatives with respect to $\overline{I}_1$, $\overline{I}_2$ and J. The UHYPER interface provides a checkbox to specify whether compressible effects are considered and included in the Fortran file. With UMAT the user enters the parameter values and the number of parameters are implied by the number of values entered in the provided interface. The UMAT Fortran file is specified within the interface and requires definition of the stress components and tangent moduli as discussed in Sections 4.1.1 and 4.1.2. The input file is modified to specify that the solution requires the use of a fully incompressible hybrid formulation if no volumetric behaviour is defined. Otherwise, the volumetric strain energy and its derivatives must be defined in the UMAT Fortran code with non-zero compressibility parameters.

The chosen geometry, shown in 4.1, for the FE investigations was a three-dimensional rectangular plate of 4mm in length, 2mm in height and 1mm thick, with a hole of 0.5mm diameter through its centre. The 3D geometry was discritized using linear, quadrilateral, hybrid C3D8H elements. The hybrid element is a mixed displacement-pressure element used to maintain constant volume (3). The models were solved using five meshes with an increasing number of elements to compare the computation time of the different implementations when computational costs vary. Due to symmetry, only an eighth of the model was used. The Haines-Wilson (190) constitutive model, as defined in Table A.1, was used throughout. Its parameters were obtained from identification from Section 3.4.1 using the complete data set of Treloar (127). The plate was loaded in its longitudinal direction by an applied displacement of 2mm in ten fixed increments of 0.2mm.

All FE models by the four different implementations achieved converged solutions. The total iterations to gain a converged solution was approximately equal. When there were differences in the total iterations, there was no general conclusion that a particular implementation required fewer total iterations. The two UMAT implementations were identical in this respect for all levels of mesh refinement. The physical results of the simulation showed the two UMAT variations were identical for all observed values. Comparing the physical results for UHYPER and UMAT to the built-in constitutive behaviour, only small differences were found which decreased with mesh refinement. The largest percentage difference was in the first mesh of 112 elements for the von Mises stresses σ_{vM}; the built in model calculated the stress as $\sigma_{vM} = 2.47$MPa, while the UHYPER and UMAT results were both approximately 1.65% higher at $\sigma_{vM} = 2.51$MPa. For the fifth mesh, all output physical results for UHYPER and UMAT were within 0.20% of the built-in constitutive model. The von Mises stresses are shown on the deformed shape of the third mesh in Figure 4.1.

The only significant differences in the four implementations were found in their computational efficiencies. The relative solve times of the UHYPER and two UMAT implementations were computed with respect to the built-in constitutive model's solve times. These are shown in Figure 4.2, where the fully derived UMAT implementation is referred to as "Derived" and the matrix operation UMAT implementation is referred to as "Matrices". The UHYPER implementation required less computational effort than either of the UMAT implementations. Compared to the built-in model it also generally had lower computational cost. Both UMAT implementations required as much as 46% additional solution time than the built-in model. With increased model complexity this difference decreased. For the numerically converged fifth mesh with 76640 elements, the difference was within 10% of the built-in and UHYPER solve times. The fully derived UMAT implementation was generally more computationally efficient than the implementation with matrix operations.

4.1.4 Discussion of Cauchy-Green Invariant Implementations

The two developed FE implementations for hyperelasticity in terms of Cauchy-Green invariants by UMAT were proven to be numerically accurate and converged appropriately. The practical differences in the built-in, UHYPER and UMAT implementations have already been discussed in the introduction to Section 4.1. In terms of computation time, the UMAT methods have higher computation times when compared with built-in and UHYPER implemented models. The "Derived" implementation has a lower solve time than the "Matrices" implementation, and should be preferred for UMAT implementation of Cauchy-Green invariant models. However, the "Matrices"

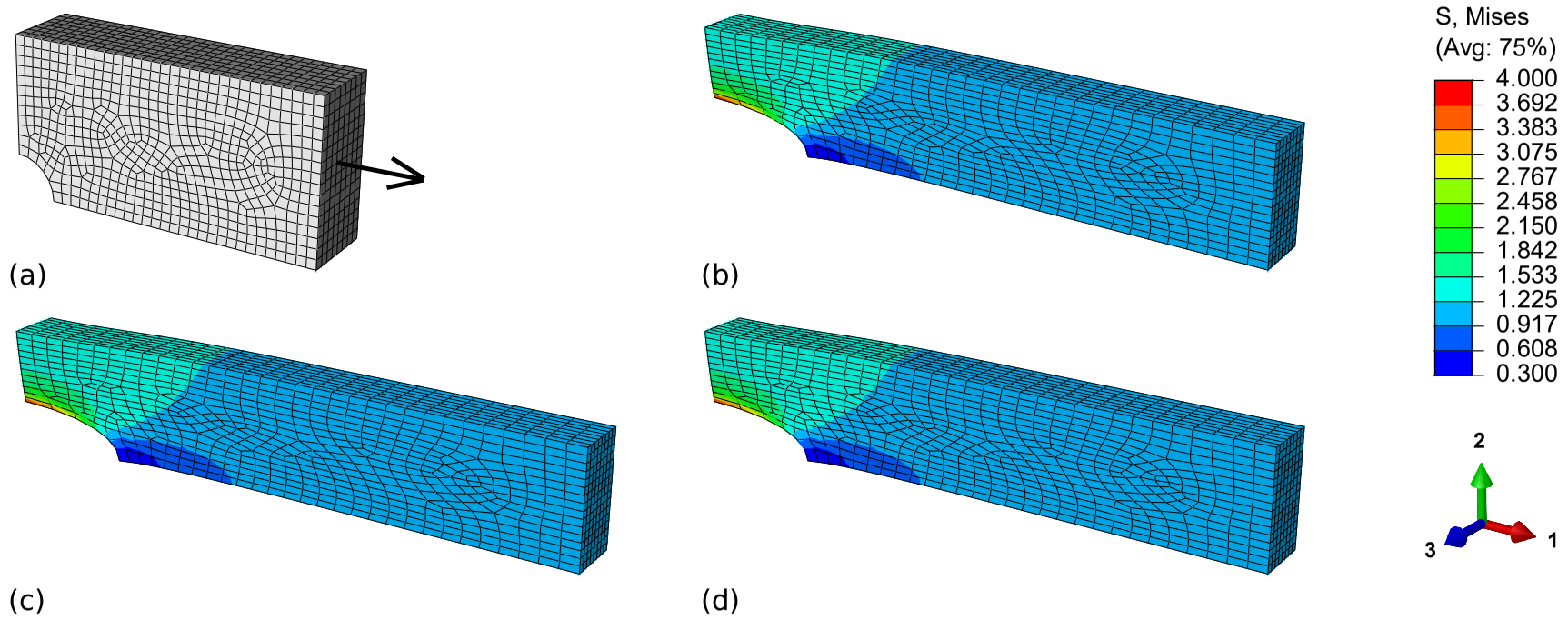

Figure 4.1: Finite Element model of a hole-plate (a) eighth geometry and loading direction (b) built-in, von Mises stress, (c) UHYPER, von Mises stress and (d) UMAT, von Mises stress

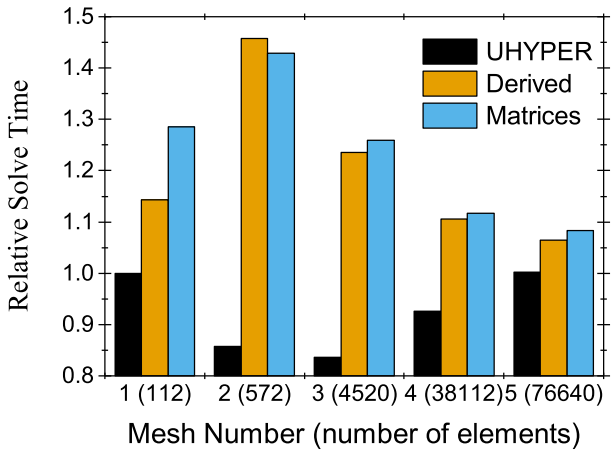

Figure 4.2: Solve times of the two user subroutine implementations and the UHYPER relative to a built-in model for increasing mesh density of a hole-plate test

implementation makes it possible to implement the non-affine micro-sphere model (11), or any model defined in terms of fictitious stress and elasticity tensors.

4.2 Numerical Approximations of Elasticity Moduli

The ambiguous nature of the elasticity tensors for hyperelasticity in principal stretches led to an investigation into alternative differentiation methods, discussed in Section 2.5.3. These methods obtain the tangent moduli by automating the derivative of the stress tensor with respect to the strain tensor. Due to the use of fixed format Fortran code in UMAT for Abaqus/Standard, the methods of interest used only numerical approximations in the real domain. These methods are advantageous as they do not require the redefinition of preprogrammed mathematical functions. From the studied literature presented in Section 2.5.3, two complimentary methods of numerical approximation were identified. These have not otherwise been developed or investigated within the context of approximating finite strain tangent moduli. The methods are higher-order and higher floating-point precision numerical approximations.

The aim of these investigations was to develop a real-domain approximation method for elasticity moduli with comparable accuracy and computational effort to the analytical fully derived implementation developed in Section 4.1. The formulae are first outlined for n^{th}-order approximations in Lagrangian and Eulerian configurations and the procedure to enable higher-order approximations is subsequently derived. Additionally, the procedure to incorporate higher floating-point precision is described. The numerical accuracy of the proposed methods was investigated using Fortran programs wherein the approximated elasticity moduli were quantitatively compared to the analytical elasticity moduli from Section 4.1. The computation time was in-

vestigated, as previous, by solving a benchmark FE problem in Abaqus/Standard. The Fortran programs and subroutines for the higher-order and higher floating-point precision methods are available in the dataset (4).

4.2.1 Approximated Material Elasticity Tensor

The first-order approximated material elasticity tensor is defined. For proof, see Miehe (169) and the references therein. The second Piola-Kirchhoff stress $\mathbf{S}$ is taken as a function of the right Cauchy-Green tensor $\mathbf{C}$. Alternatively to Section 4.1.1, the material elasticity is expressed as a linear relationship of the stress increment $\mathbf{\Delta S}$ and the strain increment $\mathbf{\Delta C}$ and defined as

$$\mathbf{\Delta S} = 2\frac{\partial \mathbf{S}}{\partial \mathbf{C}} \ : \frac{1}{2}\mathbf{\Delta C} \tag{4.57}$$

This implies that $\mathbb{C}$ may also be defined by numerical differentiation of $\mathbf{S}$ with respect to $\mathbf{C}$. Here, only the first-order forward approximation is shown. The general formula of a first-order forward difference approximation is given by

$$f'(x) = \frac{f(x+\eta) - f(x)}{\eta} + \mathcal{O}(\eta) \tag{4.58}$$

where η is a small perturbation magnitude, $\mathcal{O}(\eta)$ is the truncation error and $\mathcal{O}$ is the big $\mathcal{O}$ Landau symbol. Adapting this to compute the material elasticity moduli in the form proposed by Miehe (169)

$$\mathbb{C}_{IJ(KL)} \approx \frac{1}{\eta}\left[\hat{S}_{IJ}\left(\hat{\mathbf{F}}_{(KL)}\right) - S_{IJ}\right] \tag{4.59}$$

$\hat{S}_{IJ}$ represents the perturbed stress tensors which are each a function of the perturbed right Cauchy-Green tensors and may therefore be defined as an argument of the perturbed deformation gradient $\hat{\mathbf{F}}_{(KL)}$. The indices IJ are the components of the second Piola-Kirchhoff stress tensors and KL indicate the direction and orientation of the applied perturbations. To compute the forward perturbed strains, and subsequently the perturbed stresses, the perturbed deformation gradients are calculated by

$$\hat{\mathbf{F}}_{(KL)} = \mathbf{F} + \mathbf{\Delta}\hat{\mathbf{F}}_{(KL)} \tag{4.60}$$

The applied perturbation, denoted as $\mathbf{\Delta}\hat{\mathbf{F}}_{(KL)}$, is defined as

$$\mathbf{\Delta}\hat{\mathbf{F}}_{(KL)} = \frac{\eta}{2}\left(\mathbf{F}^{-\mathrm{T}}E_K \otimes E_L + \mathbf{F}^{-\mathrm{T}}E_L \otimes E_K\right) \tag{4.61}$$

Including the indices of the deformation gradient in equation (4.60) and using the Kronecker delta δ_{ij}, the perturbed deformation gradients are calculated using

$$\left(\hat{F}_{(KL)}\right)_{iJ} = F_{iJ} + \frac{\eta}{2}\left(F_{iK}{}^{-\mathrm{T}}\delta_{LJ} + F_{iL}{}^{-\mathrm{T}}\delta_{KJ}\right) \tag{4.62}$$

The perturbed stresses are calculated, allowing calculation of the approximated material elasticity moduli using equation (4.59).

As the elasticity tensor has both minor symmetries, it may therefore be computed using only six approximations, or four if the problem is reduced to assume 2D plane strain or axisymmetric conditions. Voigt notation is employed with the same definition of indices as in Section 4.1.2. Using the indices $A = IJ$ and $B = KL$ (in 3D A and B = 1, 2, 3, 4, 5, 6; in 2D A and B = 1, 2, 3, 4) the approximated material elasticity tensor from equation (4.59) is given in the convenient form

$$\mathbb{C}_{A(B)} \approx \frac{1}{\eta}\left[\hat{S}_A\left(\hat{\mathbf{F}}_{(B)}\right) - S_A\right] \tag{4.63}$$

4.2.2 Approximated Spatial Elasticity Tensor

For computation of the approximate spatial elasticity tensor $\mathbb{c}$, the Kirchhoff stress tensor $\boldsymbol{\tau}$ and the left Cauchy-Green tensor $\mathbf{b}$ were used initially. The spatial elasticity tensor as required by Abaqus/Standard $\mathbb{c}_{ABQ}$ was obtained as previous using equation (4.56). Proofs are omitted and only the first-order forward approximation is given.

Expanding the increment of the strain tensor $\boldsymbol{\Delta}\mathbf{C} = \left(\mathbf{F}^{\mathrm{T}}\boldsymbol{\Delta}\mathbf{F} + \boldsymbol{\Delta}\mathbf{F}^{\mathrm{T}}\mathbf{F}\right)$ followed by a push-forward operation, the spatial equivalent of equation (4.57) is given as

$$\boldsymbol{\Delta\tau} - \boldsymbol{\tau}\left(\boldsymbol{\Delta}\mathbf{F}\mathbf{F}^{-1}\right) - \boldsymbol{\tau}\left(\boldsymbol{\Delta}\mathbf{F}\mathbf{F}^{-1}\right)^{\mathrm{T}} = \mathbb{c} : \frac{1}{2}\left[\left(\boldsymbol{\Delta}\mathbf{F}\mathbf{F}^{-1}\right) + \left(\boldsymbol{\Delta}\mathbf{F}\mathbf{F}^{-1}\right)^{\mathrm{T}}\right] \tag{4.64}$$

$\mathbb{c}$ may also be defined in terms of the Lie time derivative of the Kirchhoff stress $\mathcal{L}_v(\boldsymbol{\tau})$ and the rate of deformation tensor $\mathbf{d}$ as $\mathcal{L}_v(\boldsymbol{\tau}) = \mathbb{c} : \mathbf{d}$. The rate of deformation has its usual definition in terms of the spatial velocity tensor $\mathbf{L}$, which in turn is defined in terms of the rate of the deformation gradient, as follows $\mathbf{d} = \frac{1}{2}\left(\mathbf{L} - \mathbf{L}^{\mathrm{T}}\right) = \frac{1}{2}\left(\dot{\mathbf{F}}\mathbf{F}^{-1} - \left(\dot{\mathbf{F}}\mathbf{F}^{-1}\right)^{\mathrm{T}}\right)$. The derivatives may be linearized (5) and can therefore also be numerically approximated. However, unlike the material tensor, geometric contributions are present to preserve objectivity. The first-order forward approximation of the spatial elasticity tensor is therefore defined as

$$\mathbb{c}_{ij(kl)} \approx \frac{1}{\eta}\left[\hat{\tau}_{ij}\left(\hat{\mathbf{F}}_{(kl)}\right) - \tau_{ij}\right] - \left(\mathbf{1} \odot \boldsymbol{\tau} + \boldsymbol{\tau} \odot \mathbf{1}\right)_{ij(kl)} \tag{4.65}$$

where $\hat{\tau}_{ij}$ represents the perturbed Kirchhoff stress tensors, which are a function of the spatial perturbed deformation gradients $\hat{\mathbf{F}}_{(kl)}$. The other symbols have their usual meanings.

Equivalent to the material implementation, the spatial perturbed deformation gradient is given by

$$\hat{\mathbf{F}}_{(kl)} = \mathbf{F} + \boldsymbol{\Delta}\hat{\mathbf{F}}_{(kl)} \tag{4.66}$$

However, the spatial perturbed deformation gradients are calculated using

$$\boldsymbol{\Delta}\hat{\mathbf{F}}_{(kl)} = \frac{\eta}{2}\left(e_k \otimes e_l\mathbf{F} + e_l \otimes e_k\mathbf{F}\right) \tag{4.67}$$

Then, including the indices and the Kronecker delta in equation (4.66), the perturbed deformation gradients are calculated by

$$\left(\hat{F}_{(kl)}\right)_{iJ} = F_{iJ} + \frac{\eta}{2}\left(\delta_{ik}F_{lJ} + \delta_{il}F_{kJ}\right) \tag{4.68}$$

In Voigt notation, with the same interpretations as in the material tensor, the spatial elasticity tensor defined in terms of the Oldroyd-rate of the Kirchhoff stress is simplified to

$$\mathbb{c}_{a(b)} \approx \frac{1}{\eta}\left[\hat{\tau}_a\left(\hat{\mathbf{F}}_{(b)}\right) - \tau_a\right] - \left(\mathbf{1}\odot\boldsymbol{\tau} + \boldsymbol{\tau}\odot\mathbf{1}\right)_{a(b)} \tag{4.69}$$

By substitution of this equation (4.69) in the conversion of the Oldroyd-rate of the Kirchhoff stress to the Jaumann-rate of the Cauchy stress, given in equation (4.56), the required spatial elasticity tensor $\mathbb{c}_{ABQ}$ is defined by

$$\mathbb{c}_{ABQ_{ij(kl)}} \approx \frac{1}{J\eta}\left[\hat{\tau}_{ij}\left(\hat{\mathbf{F}}_{(kl)}\right) - \tau_{ij}\right] \tag{4.70}$$

In Voigt notation it is given as

$$\mathbb{c}_{ABQ_{a(b)}} \approx \frac{1}{J\eta}\left[\hat{\tau}_a\left(\hat{\mathbf{F}}_{(b)}\right) - \tau_a\right] \tag{4.71}$$

4.2.3 Higher-order Numerical Approximation

General equations are derived for higher-order approximations of both the material and spatial elasticity moduli. While higher-order approximations of forward and backward difference methods are possible, only central difference methods were investigated in detail, as they are generally of higher numerical accuracy (199). Furthermore, central difference methods are more convenient for investigation as their truncation error exponentially decreases twofold compared with forward and backward methods, $\mathcal{O}\left(\eta^{2n}\right)$ compared with $\mathcal{O}\left(\eta^{n}\right)$. For clarity, central difference schemes are referred to by their order of approximation. For example, the first central difference is a second-order approximation and so is referred to as the second-order central difference approximation.

For a fixed perturbation magnitude, increasing the order of the approximation will, in theory, reduce the truncation error. For this, the higher-order approximations require more forward and backward perturbed points. In the central difference approximations applied here, an equal number of equidistant forward and backward

perturbations are used. Weighted coefficients are assigned to ensure that the approximation is found at the centre point. The general formula for a central difference of n^{th}-order, where n is an even number, from Li (200), is given as

$$f'(x) = \left(\frac{1}{\eta} \sum_{2m=-n_{even}}^{n_{even}} (c_m) f(x_m) \right) + \mathcal{O}\left(\eta^{2\text{n}}\right) \tag{4.72}$$

Here, m refers to the position of the approximation as if it were to lie on a linear grid, such that $m = -2$ is a twice backward perturbed point, which is non-zero for central difference schemes of fourth-order and greater. Then the argument $(x_m) = (x + m\eta)$ is calculated. For forward and backward perturbed points, the coefficients c_m are calculated by the equation

$$c_m = \frac{(-1)^{m+1}\left[\left(\frac{n}{2}\right)!\right]^2}{m\left(\frac{n}{2}-m\right)!\left(\frac{n}{2}+m\right)!} \tag{4.73}$$

Manual calculation of the required coefficients can be tedious and so an algorithm similar to that of Fornberg (201) may be used to obtain them. The coefficients for the central difference schemes used in this study, up to twelfth-order, are given in Table C.1 in Appendix C.

Higher-order Approximations of Material Elasticity Moduli Higher-order approximations of the material elasticity moduli require calculation of additional perturbed second Piola-Kirchhoff stresses. The stresses are a function of the perturbed deformation gradients, which are calculated using a modification of equation (4.60)

$$\overbrace{\left(\hat{\mathbf{F}}_{(KL)}\right)}^{m} = \mathbf{F} + m\left(\boldsymbol{\Delta}\hat{\mathbf{F}}_{(KL)}\right) \tag{4.74}$$

The notation $\overbrace{(\cdot)}^{m}$ is introduced to identify the position, m, of the approximation, with m defined as previous. In 3D the $6n$ ($4n$ for 2D) perturbed second Piola-Kirchhoff stresses are then calculated. The general formula for central difference approximate elasticity moduli is found by combining equations (4.59) and (4.72) to give

$$\mathbb{C}_{IJ(KL)} \approx \left[\frac{1}{\eta} \left(\sum_{2m=-n_{even}}^{n_{even}} (c_m) \hat{S}_{IJ}\overbrace{\left(\hat{\mathbf{F}}_{(KL)}\right)}^{m} \right) \right] + \mathcal{O}\left(\eta^{2n}\right) \tag{4.75}$$

In Voigt notation, where A and B are as previously defined, this is defined as

$$\mathbb{C}_{A(B)} \approx \left[\frac{1}{\eta} \left(\sum_{2m=-n_{even}}^{n_{even}} (c_m) \hat{S}_{A}\overbrace{\left(\hat{\mathbf{F}}_{(B)}\right)}^{m} \right) \right] + \mathcal{O}\left(\eta^{2n}\right) \tag{4.76}$$

Higher-order Approximations of Spatial Elasticity Moduli The higher-order approximations are then modified equivalently to give the corresponding equations for the spatial elasticity tensor. In the spatial configuration, the perturbed deformation gradients are calculated using

$$\overbrace{\left(\hat{\mathbf{F}}_{(kl)}\right)}^{m} = \mathbf{F} + m\left(\boldsymbol{\Delta}\hat{\mathbf{F}}_{(kl)}\right) \tag{4.77}$$

The general equation for the spatial elasticity tensor in terms of the Oldroyd-rate of the Kirchhoff stress is given by

$$\mathbb{c}_{ij(kl)} \approx \left[\frac{1}{\eta}\left(\sum_{2m=-n_{even}}^{n_{even}} (c_m)\,\hat{\tau}_{ij}\overbrace{\left(\hat{\mathbf{F}}_{(kl)}\right)}^{m}\right) - (\mathbf{1}\odot\boldsymbol{\tau}+\boldsymbol{\tau}\odot\mathbf{1})_{ij(kl)}\right] + \mathcal{O}\left(\eta^{2n}\right) \tag{4.78}$$

Then in Voigt notation this is defined as

$$\mathbb{c}_{a(b)} \approx \left[\frac{1}{\eta}\left(\sum_{2m=-n_{even}}^{n_{even}} (c_m)\,\hat{\tau}_{a}\overbrace{\left(\hat{\mathbf{F}}_{(kl)}\right)}^{m}\right) - (\mathbf{1}\odot\boldsymbol{\tau}+\boldsymbol{\tau}\odot\mathbf{1})_{a(b)}\right] + \mathcal{O}\left(\eta^{2n}\right) \tag{4.79}$$

As in equation (4.70), the geometric contributions cancel to give the general formula for the spatial elasticity tensor in terms of the Jaumann-rate of the Cauchy stress as

$$\mathbb{c}_{ABQ_{ij(kl)}} \approx \left[\frac{1}{J\eta}\left(\sum_{2m=-n_{even}}^{n_{even}} (c_m)\,\hat{\tau}_{ij}\overbrace{\left(\hat{\mathbf{F}}_{(kl)}\right)}^{m}\right)\right] + \mathcal{O}\left(\eta^{2n}\right) \tag{4.80}$$

Furthermore, in Voigt notation, it is given by

$$\mathbb{c}_{ABQ_{a(b)}} \approx \left[\frac{1}{J\eta}\left(\sum_{2m=-n_{even}}^{n_{even}} (c_m)\,\hat{\tau}_{a}\overbrace{\left(\hat{\mathbf{F}}_{(b)}\right)}^{m}\right)\right] + \mathcal{O}\left(\eta^{2n}\right) \tag{4.81}$$

4.2.4 Higher Floating-point Precision

While higher-order approximations increase the exponential decay of the truncation error, by $\mathcal{O}\left(\eta^{2n}\right)$ for increasing n, the benefit of this is well-known to be restricted by the conflicting round-off errors (171, 202). However, with higher floating-point precision, the range of perturbation magnitudes for which round-off error is negligible may increase. Due to its availability within current Fortran compilers, quadruple precision was used. In Fortran, all arrays, variables and constants are initially defined in quadruple precision. The variables and arrays required by the FE solver are also defined equivalently in double precision. After computation of the quadruple precision arrays, the values are returned to double precision by equating these arrays to

their double precision counterparts. This truncates the higher precision values to approximately 16 significant figures. The method has not previously been implemented or investigated in this context. For all orders of approximation, quadruple precision enables twice the number of significant figures allowing smaller perturbation magnitudes. This was expected to result in lower truncation error and more accurate approximations of the elasticity moduli.

4.2.5 Optimal Perturbation Magnitude

The optimal perturbation magnitude is that which exactly minimises the impact of both truncation and round-off errors. As these are known to vary for even a scalar function of an independent scalar variable, determining the exact optimal perturbation magnitude is generally not possible. An approximation of the optimal perturbation can be obtained by optimisation (172), which, in this context, would require a minimisation in which all tensor components are considered. A simpler approach by Miehe (169) concludes that for a first-order approximation of the first derivative, the optimal perturbation η^{opt} may be approximated as

$$\eta^{opt} \approx \sqrt{\texttt{macheps}} \tag{4.82}$$

The machine epsilon, `macheps` is the smallest computable η for $1 + \eta > 1$ to hold true. The approximation in equation (4.82) can be seen to hold true graphically in log-log plots of relative error vs perturbation magnitude from later studies (149, 173, 175, 176, 180). Based on equation (4.82) and the observations of Pérez-Foguet et al (173), a simple general equation for higher-order derivatives and higher-order approximations is proposed here as

$$\eta^{opt} \approx (\texttt{macheps})^{\frac{1}{n+d}} \tag{4.83}$$

The superscripts n and d are the orders of the approximation and of the derivative, respectively. The equation draws on the observation that the total error corresponds to the truncation error: $\texttt{Error} \approx \gamma\eta^n$, where γ is a constant, until it intercepts the round-off errors. The round-off errors then increase the total error by $\texttt{Error} \approx \omega\eta^{-d}$, where ω is a constant. Therefore, by assuming the minimum error occurs when truncation and round-off errors are equal, as in Pérez-Foguet et al (173), and that the constants are a function of `macheps` such that equation (4.82) is satisfied, the optimal perturbation magnitude may be approximated by equation (4.83).

This equation permits an approximation of the optimal perturbation magnitude, which can be seen to hold true to the error plots of previous studies and is in agreement with equation (4.82). Comparisons with previous studies (149, 173, 175, 176,

180) is not a complete validation as these approximations only investigated up to second-order approximations and second-order derivatives. The validity for first-order derivatives and approximations of up to the twelfth-order is assessed in Section 4.3.3.

The proposed equation (4.83) predicts that for increasingly higher-order approximations the optimal perturbation size exponentially increases due to conflicting round-off error. It also predicts that the use of quadruple precision lowers the optimal perturbation magnitude. For example, a first-order forward approximation in double precision ($\texttt{macheps} = 1\text{E}{-16}$, $n = 1$ and $d = 1$) the optimal perturbation magnitude is calculated as $\eta^{opt} \approx 1\text{E}{-8}$. With the same approximation scheme in quadruple precision ($\texttt{macheps} = 1\text{E}{-32}$, $n = 1$ and $d = 1$) the optimal perturbation magnitude is predicted as $\eta^{opt} \approx 1\text{E}{-16}$. In terms of the truncation error $\mathcal{O}(\eta^n)$, the use of quadruple precision reduces the error by a squared power. Given that double precision numbers are stored with $1\text{E}{-16}$ significant figures, a first-order approximation using quadruple precision is predicted to obtain solutions with error approximately equal to the finite precision limit. Following the investigation into higher-order approximations in double and quadruple precision, the optimal perturbation magnitude and the validity of equation (4.83) is discussed in further detail in Section 4.3.5.

4.3 Numerical Investigation of Approximated Elasticity Moduli

The use of higher-order numerical approximation methods was investigated in standard double precision and with the proposed quadruple precision method. The methods were assessed in terms of their numerical accuracy through comparison with analytical solutions for both material and spatial configurations. Two hyperelastic constitutive models were used throughout: the neo-Hookean (69) and Gent (18) models. These were chosen due to their differences in stability and function smoothness. The neo-Hookean model is unconditionally stable and a smooth function. The Gent model has a clearly defined numerical stability limit, where the stiffness increases asymptotically as the strain tends towards the finite extensibility limit of the material. Stability here refers to the positive definiteness of stress and strain increments, as discussed by Hartmann (145) for hyperelastic parameter estimation.

4.3.1 Hyperelastic Constitutive Models

The neo-Hookean and Gent strain energy functions were defined only in terms of an isochoric energy contribution. An incompressible hybrid formulation and the use

of hybrid elements later enforced incompressibility in the FE investigations. The volumetric contributions to the total energy, stress and elasticity moduli were disregarded. The isochoric energy of the two models was defined as in Section 3.2.2, see equation (3.13) for the neo-Hookean model and equation (3.14) for the Gent model. The parameters were defined as $C_{10} = 0.1\text{MPa}$, $\mu = 1\text{MPa}$ and $J_m = 22.5$ throughout the initial purely numerical investigations and the latter FE investigations.

4.3.2 Investigation of Approximate Elasticity Moduli

The accuracy of the approximate elasticity moduli was investigated by comparison to the analytical solutions outlined in Section 4.1. The average relative error was calculated for all (Voigt notation) tensor components using five unique deformation gradients. The deformation gradients were input to a Fortran program to calculate the stress tensor and elasticity moduli. These programs are also available in the dataset (4). The five deformation gradients may be respectively described as follows: undeformed, uniaxial tension, uniaxial compression, shear without dilation and shear with dilation. In matrix form, they are given as

$$\begin{aligned}\mathbf{F}_1 &= \begin{pmatrix} 1 & 0 & 0 \\ 0 & 1 & 0 \\ 0 & 0 & 1 \end{pmatrix}; \mathbf{F}_2 = \begin{pmatrix} 4.5 & 0 & 0 \\ 0 & \frac{1}{\sqrt{4.5}} & 0 \\ 0 & 0 & \frac{1}{\sqrt{4.5}} \end{pmatrix}; \mathbf{F}_3 = \begin{pmatrix} 0.2 & 0 & 0 \\ 0 & \frac{1}{\sqrt{0.2}} & 0 \\ 0 & 0 & \frac{1}{\sqrt{0.2}} \end{pmatrix}; \\ \mathbf{F}_4 &= \begin{pmatrix} 3 & 1 & 0 \\ 1 & 1 & 0 \\ 0 & 0 & 0.5 \end{pmatrix}; \mathbf{F}_5 = \begin{pmatrix} 1.1 & 0.2 & 0.2 \\ 0 & 0.9535 & 0.2 \\ 0 & 0 & 0.9535 \end{pmatrix}\end{aligned} \tag{4.84}$$

The relative error was calculated for each approximation method using a range of perturbation magnitudes η. The investigations used perturbations of $1\text{E}x$ and $3\text{E}x$, where x is an integer, to provide a good insight into the range of suitable perturbation magnitudes and to find an approximate value of the optimal perturbation magnitude. For double precision, perturbation magnitudes from $1\text{E}0$ down to $1\text{E}{-}18$ were used. For quadruple precision, the range was extended from $1\text{E}0$ to $1\text{E}{-}36$. Perturbation magnitudes smaller than these ranges were much lower than `macheps` and thus resulted in an unperturbed deformation gradient for real domain approximations, which implies $1 + \eta > 1$ is false. The relative error was calculated by comparison of the approximate moduli, $\mathbb{C}_{App.}$ and $\mathbb{c}_{App.}$, to the quadruple precision analytical elasticity moduli, $\mathbb{C}_{A16}$ and $\mathbb{c}_{A16}$, for the material and spatial configurations respectively. This also allowed for the double precision analytical elasticity moduli, denoted A(8), to be included in the comparison. The error between the double and quadruple precision analytical moduli is a result of the truncation and rounding errors throughout its calculation. The relative error E_R was calculated and averaged for each index of

the elasticity tensor in Voigt notation by the following equation

$$E_R = \left[\sum_{a,b=1}^{6} \left(\mathbb{C}_{A16ab} - \mathbb{C}_{App.ab} \right)^2 \right]^{\frac{1}{2}} / \left[\sum_{a,b=1}^{6} \left(\mathbb{C}_{A16ab} \right)^2 \right]^{\frac{1}{2}} \tag{4.85}$$

To independently investigate the effect of higher-order approximations and higher floating-point precision, approximated material and spatial moduli were compared for both constitutive models using double and quadruple precision for approximations up to the twelfth-order. The results are plotted using log-log graphs of perturbation magnitude vs relative error. These plots also reveal the approximate optimal perturbation magnitude. In the following numerical investigations, the first two letters indicate the type of approximation scheme used (FD and CD are the forward and central differences respectively), the number in brackets is the precision used (double precision is (8) and quadruple precision is (16)), and the number following the hyphen indicates the order of the approximation.

4.3.3 Numerical Validation of Material Elasticity Moduli

The result of the comparison between the approximated and analytical material elasticity moduli is shown for double precision in Figures 4.3a and 4.3b. These plots show there was little difference between the neo-Hookean and Gent models for all approximations, suggesting that the approximation methods are not affected by differences in function stability or smoothness. For both constitutive models, lower relative error was obtained with an increased order of approximation but with diminishing returns. Once round-off errors were significant, as the perturbation magnitude decreased, all orders of approximation converged to the same error as the first-order approximation.

With quadruple precision, shown in Figures 4.3c & 4.3d, the approximated elasticity moduli reached higher accuracy than the double precision analytical solution for all orders of approximation. When truncated to double precision, these quadruple precision approximations of the material elasticity moduli were generally identical to the double precision analytical solutions. This was true for all non-zero terms; otherwise, values close to zero were found to have a residual value of around $1\text{E}{-16}$ since these were not lost in truncation. However, given their magnitude, these errors are physically negligible.

At larger perturbation magnitudes, greater than $1\text{E}{-2}$, it was found that the relative error of the approximations does not follow the expected logarithmic gradient equal to the order of the approximation. Since this was present in both double and quadruple precision, this error was not due to truncation or rounding errors. Also, as it was

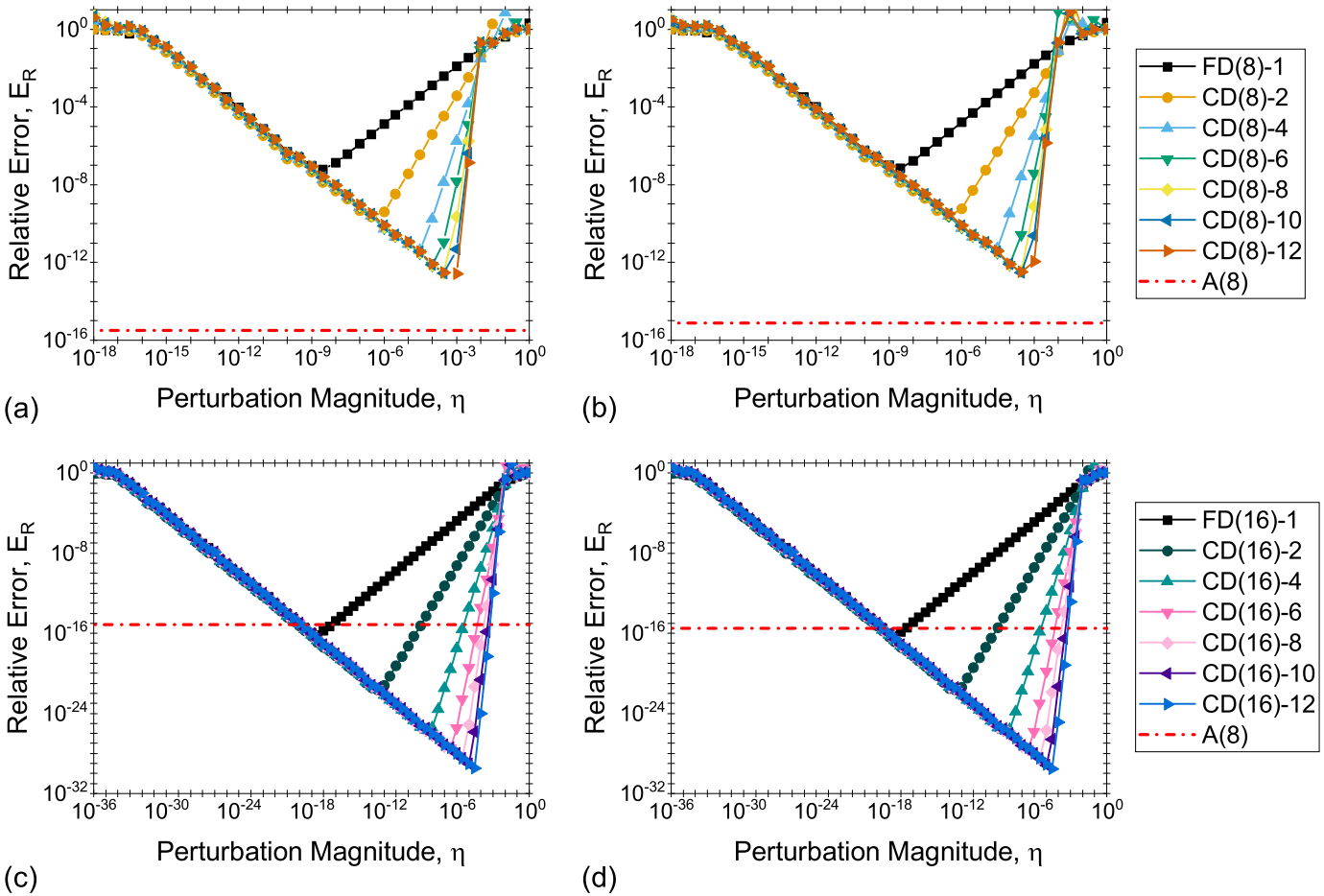

Figure 4.3: Relative error of material elasticity moduli approximations (a) neo-Hookean, double precision, (b) Gent, double precision, (c) neo-Hookean, quadruple precision, (d) Gent, quadruple precision. CD, central difference; FD, forward difference

present in both neo-Hookean and Gent constitutive models, it was not due to stability or smoothness. The error was therefore due to invalid truncation errors (172). Approximations greater than first-order resulted in an invalid perturbation, which restricted the accuracy of higher-order approximations whose optimal perturbation would be expected within this range.

4.3.4 Numerical Validation of Spatial Elasticity Moduli

The results for the spatial approximated elasticity moduli are shown in Figure 4.4 for both neo-Hookean and Gent constitutive models. These results were similar to those of the material elasticity moduli but the spatial approximations were less affected by invalid perturbation error. In double precision, the increased order of approximation generally achieved lower error. However, approximations of greater than the eighth-order showed diminishing increases in accuracy. The quadruple precision results were similar to those of the material elasticity moduli, though their error continued to decrease for higher-order approximations since the optimal perturbation occured at lower (valid) perturbation magnitudes. As with the material elasticity moduli, the use of higher floating-point precision obtained more accurate elasticity moduli than the double precision analytical solution for all orders of approximation.

4.3.5 Optimal Perturbation Magnitude

The approximate optimal perturbation magnitudes were calculated using equation (4.83) for both double and quadruple precision and all orders of approximations used in the numerical investigations. The calculated approximations were compared to the measured spatial neo-Hookean optimal perturbation magnitudes, with measured values taken to the nearest exponent, as shown in Table 4.1. The approximate values of equation (4.83) were generally reasonable for lower orders of approximation; but the optimal perturbation magnitudes were not in agreement for double precision higher-order approximations due to the invalid perturbation errors.

The nature of truncation and round-off errors were examined further using more perturbation magnitudes around the minimum error. The neo-Hookean spatial elasticity moduli were approximated using fourth- and eighth-order central difference approximations in quadruple precision with 450 linear steps of the perturbation magnitude for each order of magnitude, as shown in Figure 4.5. Using more points revealed that the truncation errors steadily decreased at a logarithmic gradient equal to the order of the approximation. However, when approaching the optimal perturbation magnitude, the round-off errors fluctuated, as highlighted in Figure 4.5. Following the optimal perturbation, they continued to fluctuate but then tended towards an

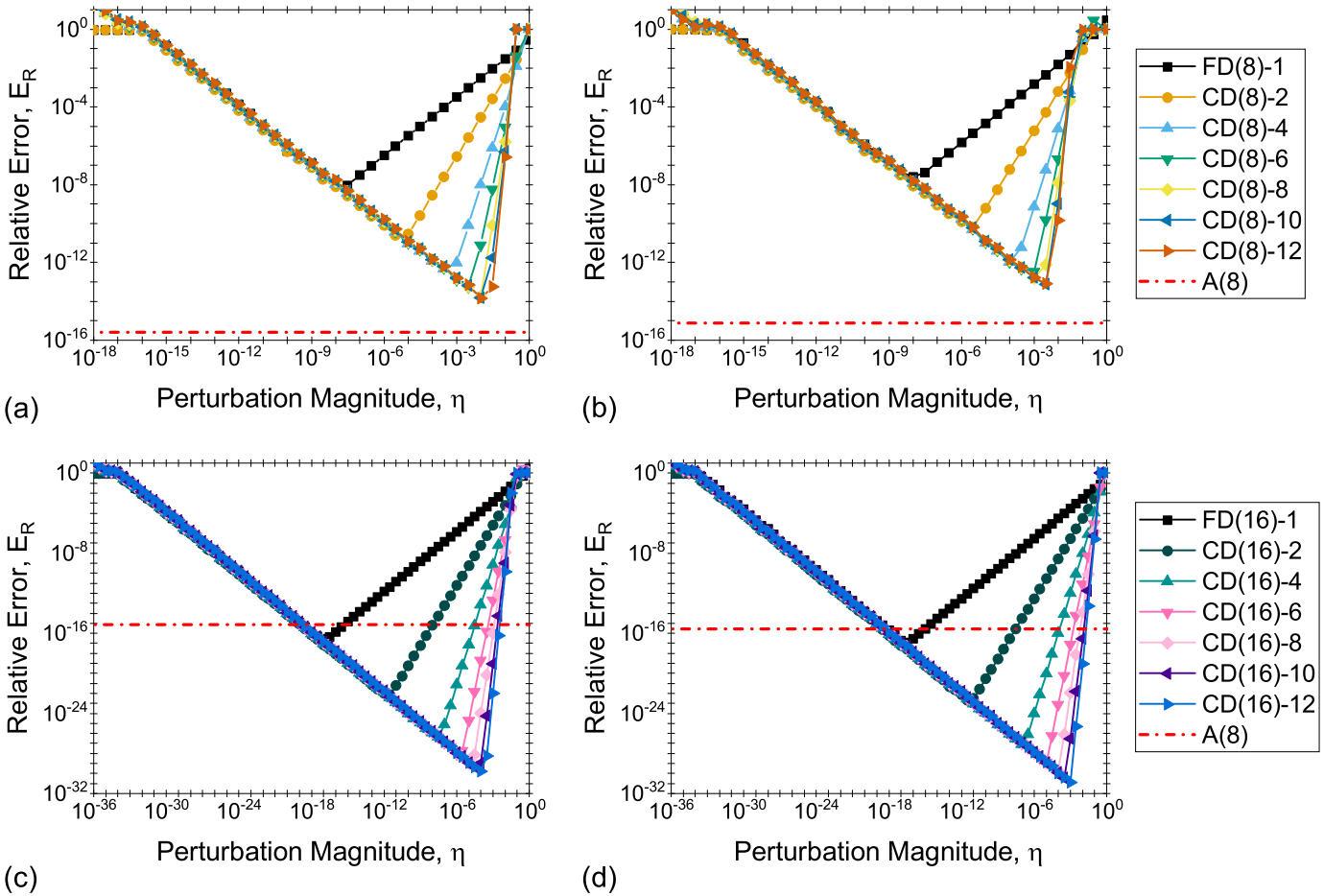

Figure 4.4: Relative error of spatial elasticity moduli approximations (a) neo-Hookean, double precision, (b) Gent, double precision, (c) neo-Hookean, quadruple precision, (d) Gent, quadruple precision. CD, central difference; FD, forward difference

Table 4.1: Approximate optimal perturbation magnitudes, from equation (4.83) and Figures 4.4a and 4.4c

	FD-1	CD-2	CD-4	CD-6	CD-8	CD-10	CD-12
DP: calculated	1.0E−8	4.6E−6	6.3E−4	5.2E−3	1.7E−2	3.5E−2	5.9E−2
DP: measured	1.0E−8	1.0E−5	1.0E−3	1.0E−3	1.0E−2	1.0E−2	1.0E−2
QP: calculated	1.0E−16	2.2E−11	4.1E−7	2.7E−5	2.8E−4	1.2E−3	3.5E−3
QP: measured	1.0E−17	1.0E−11	1.0E−7	1.0E−5	1.0E−4	1.0E−4	1.0E−3

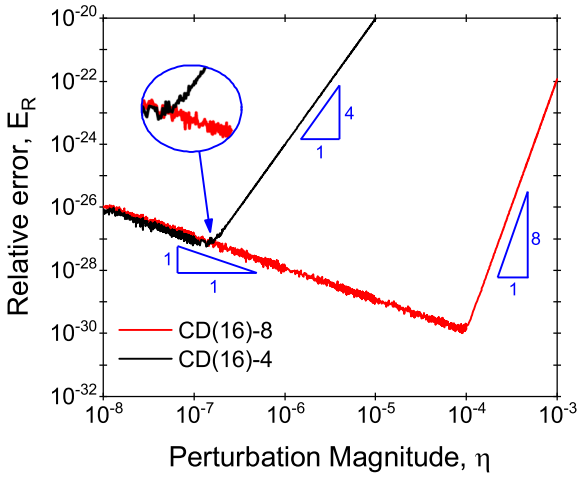

Figure 4.5: Relative error of fourth- and eighth-order approximations of neo-Hookean spatial elasticity moduli

indirectly proportional relationship between the perturbation magnitude and the error. These results showed further agreement with equation (4.83) and the related discussion of Section 4.2.5.

4.3.6 Discussion of Numerical Investigation

The numerical investigations show that higher-order and higher floating-point precision approximations both improve the accuracy of approximated elasticity moduli, in the material and spatial configurations. With increasing order of approximation, the accuracy of the approximated elasticity moduli was generally increased but with diminishing returns. The diminishing returns were due to the requirement for a larger perturbation, which resulted in invalid perturbation errors and was also likely to be influenced by the rounding errors from the additional coefficients. The use of quadruple precision numerical approximations, novel in this context, is the more significant development. Due to round-off errors in the computation of the double precision analytical solutions, the quadruple precision approximated elasticity moduli are more accurate than these analytical solutions for even a first-order approximation. This level of accuracy with real-domain approximations is not known to have otherwise

been accomplished in this context.

It was shown that the higher-order and higher floating-point precision approximation methods are complementary. Utilising both of these methods, approximated elasticity moduli tend towards the quadruple precision analytical moduli. However, current FE solvers use only double precision and hence any improvement in accuracy beyond the double precision limit is inconsequential due to truncation. Therefore, a first-order quadruple precision approximation is at present a satisfactory means of obtaining precise elasticity moduli. Though another important factor is the associated computational costs of these methods. This was investigated in the context of the FEM and is presented in the following section.

4.4 Finite Element Investigation of Approximated Elasticity Moduli

The performance of the approximation methods in FE simulation was investigated in terms of numerical convergence and computation time. For double precision UMAT subroutines, the Cauchy stress was computed and stored in the STRESS(6) array, as in the previous subroutines in Section 4.1. The spatial elasticity tensor in terms of the Jaumann-rate of the Cauchy stress was obtained by numerical approximation and stored in the DDSDDE(6,6) tangent moduli array. For quadruple precision codes, the stress and tangent moduli arrays were first calculated using independently defined quadruple precision arrays. These were then truncated to double precision by equating them to the pre-defined arrays STRESS(6) and DDSDDE(6,6).

Higher-order approximations, with standard double precision and the novel quadruple precision method, were investigated by solving the well-known Cook's membrane problem. The measured approximate optimal perturbation magnitudes from Table 4.1 were used throughout. The convergence and computation time of the approximation methods were compared to a solution obtained using the analytically fully derived elasticity tensor from Section 4.1 over seven levels of mesh refinement. The UMAT subroutines used here are available in the dataset (4).

4.4.1 Cook's Membrane

The Cook's membrane problem is commonly used in the assessment of FE procedures. The model is shown with dimensions for the third level of mesh refinement with 2048 elements in Figure 4.6a. It consists of a tapered membrane where one face is fully fixed and a shearing load is applied at the opposite face. The model was simulated in 3D using plane strain boundary conditions such that its thickness

was constant. The body was meshed using hybrid C3D8H elements to enforce incompressibility. For all approximation methods, the model was simulated with a shearing load of 15 N for both neo-Hookean and Gent constitutive models, with the parameters defined in Section 4.3.1.

4.4.2 Convergence with Optimal Perturbation Magnitudes

All approximation methods with optimal perturbation magnitudes were found to attain convergence. The deformed contour plot showing the shear stress in the 1-2 plane is shown in Figures 4.6b and 4.6c for the neo-Hookean and Gent constitutive models respectively. Given that the stress was computed equivalently for the analytical and approximation methods, the same values were computed for all output quantities. Within Abaqus/Standard, the convergence behaviour may be observed by inspection of the maximum residuals in each iteration. The maximum force residuals were plotted for both neo-Hookean and Gent simulations, as shown in Figures 4.7(a) and 4.7(b). Both double and quadruple precision analytical elasticity moduli are included, denoted as A(8) and A(16) respectively. Quadratic convergence in five iterations was reliably obtained for all methods, despite minor differences in their residuals.

4.4.3 Computation times

Where available, evaluating the analytical elasticity moduli was found to be more computationally efficient than using numerical approximation. This is due to analytical solutions typically requiring fewer computations and quadratic convergence is generally guaranteed. While the numerical approximations implemented here with optimal perturbation magnitude show quadratic convergence, it was known from the first implementation by Miehe (169) that approximation methods have higher computation times. However, previous studies (149, 169, 177, 180) have shown that with increased mesh refinement the difference between analytical and approximate methods' solve times are decreased. This is due to the increased solution time required for the global matrix iterations in a more complex model, such that the computational effort of the stress and tangent components becomes less significant.

Using seven levels of mesh refinement, the computation time of higher-order approximations, with standard double precision and the novel quadruple precision method, was investigated using the neo-Hookean constitutive model. Mesh refinement was controlled using a constant two elements through the thickness, since stress was constant in this direction. Then, starting with an 8×8 mesh, the elements were doubled on each side, increasing the total elements by a factor of four for each subsequent

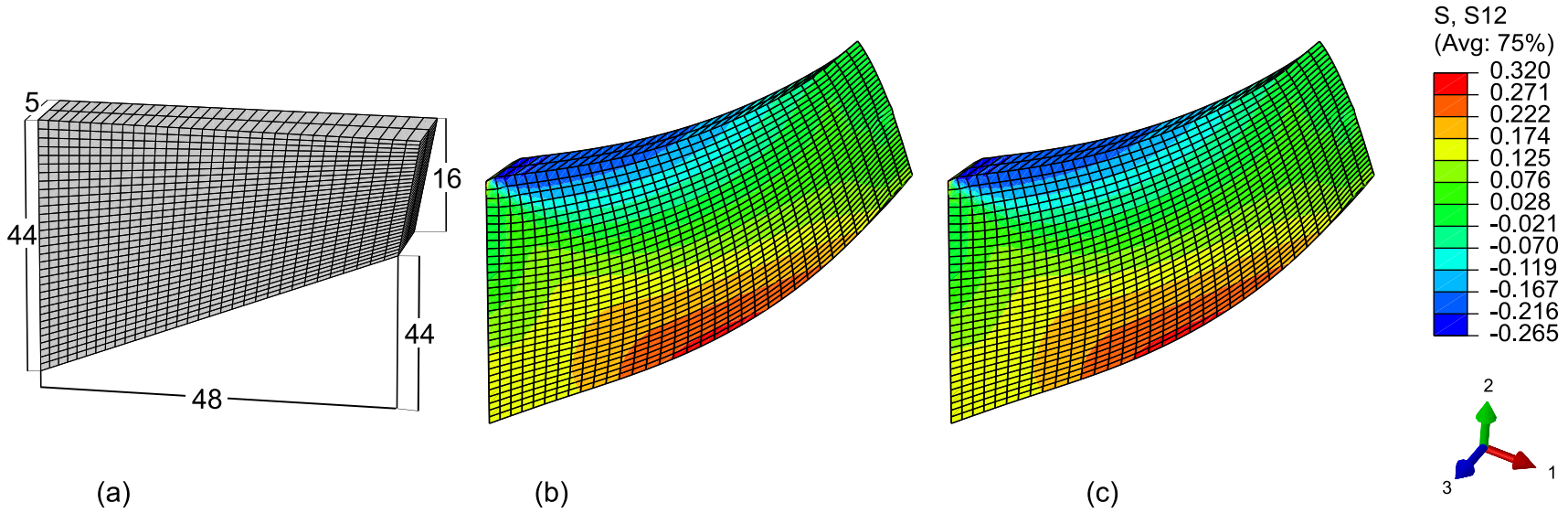

Figure 4.6: (a) Cook's membrane, dimensions in mm, (b) neo-Hookean, shear stress (MPa), (c) Gent, shear stress (MPa)

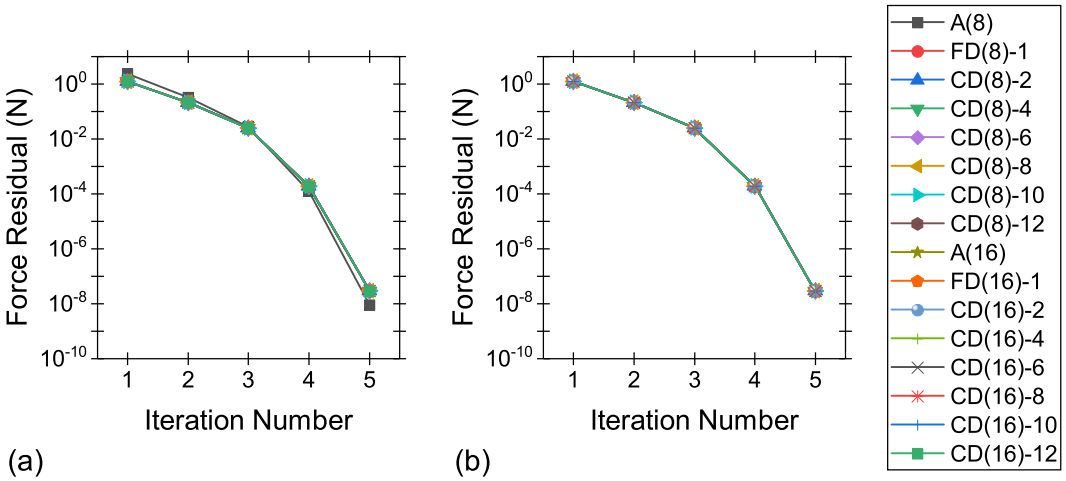

Figure 4.7: Maximum force residuals during convergence for (a) neo-Hookean and (b) Gent simulations. CD, central difference; FD, forward difference

mesh. In a finite elasticity problem, the elasticity moduli require recalculation at each iteration for all integration points. Therefore the total CPU times were compared.

The results are given in Figure 4.8 where double and quadruple precision results are separated due to their considerable difference. To demonstrate the disparity, and for improved clarity, the quadruple precision first-order forward difference approximation (FD(16)-1) result is included in both plots. The plots show that even the first-order forward difference in quadruple precision required significantly higher CPU times than all orders of double precision approximation. In contrast, the double precision first- and second-order approximations show CPU times similar and even lower than the analytical implementation. Using a greater number of mesh refinements than previous studies (149, 169, 177, 180), the relative CPU times were found here to generally increase as the mesh was refined until it reached a maximum before then decreasing with further refinements. The quadruple precision approximations require more than twice the CPU time for all meshes.

4.5 Summary of Analytical and Numerical Implementation Studies of Cauchy-Green Invariant Hyperelasticity

Hyperelastic constitutive models defined in terms of Cauchy-Green invariants allowed the development, validation and investigation of four methods of FE implementation of hyperelasticity. The use of their known elasticity tensors enabled validation of two developed analytical implementations. Both methods were identical in their numerical accuracy. Fully derived terms were found to be more computationally efficient than using the matrix implementations. However, the latter method enables implementations of constitutive models defined in terms of fictitious tensors. These

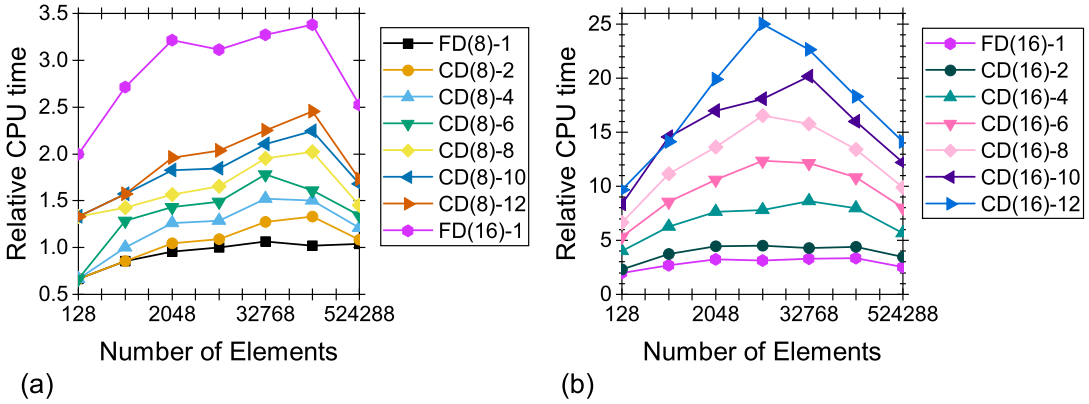

Figure 4.8: Relative CPU time for (a) double and (b) quadruple precision approximations. CD, central difference; FD, forward difference

implementations were compared to built-in and UHYPER implemented constitutive models. No general differences were found in their convergence behaviour and all output physical results were found to be within 1.65%. However, the solution times of both UMAT implementations were found to be consistently higher. In implementing user-defined hyperelastic constitutive models defined in terms of Cauchy-Green invariants, UHYPER subroutines are the recommended method. If more complex behaviour is required, the equilibrium hyperelastic behaviour should be implemented using the developed fully derived method.

With the validated UMAT implementation, two numerical approximation methods were developed and investigated. These two real-domain approximation methods, higher-order and higher floating-point precision, were confirmed to be complimentary and found to be capable of attaining accuracy comparable to analytical solutions. Using higher-order approximations, accuracy that tended towards the analytical values was found but with diminishing returns as the order of the approximation increased. However, in terms of numerical accuracy, higher floating-point precision was shown to be the more effective method.

For all orders of approximation, the increase to quadruple precision obtained elasticity moduli more accurate than the double precision analytical solution. This was due to the higher floating-point precision tangent moduli having reduced round-off errors throughout their computation. In current FE solvers, quadruple precision approximations higher than first-order are not required as the additional accuracy is negated upon truncation. The first-order quadruple precision approximation therefore guarantees equivalent convergence to an analytical solution with a simpler implementation. If computational effort is an important consideration, analytical tangent moduli should be preferred, if they are available.

When analytical tangent moduli are complicated or intractable, the proposed first-

order quadruple precision approximation method is an accurate and effective means of implementation. This approximation method did not achieve the complete aim of approximating elasticity moduli with comparable accuracy *and* computational effort of an analytical implementation. However, it permits a simpler implementation requiring only the definition of the stress tensor. Approximating tangent moduli therefore remains a useful aid to confirm derived analytical tangent moduli and for debugging their implementation. Though it was determined that an analytical implementation of principal stretch hyperelasticity should be developed. This is presented subsequently in Chapter 5.

Chapter 5

Finite Element Implementation of Principal Stretch Hyperelasticity

Various forms of the elasticity tensor for hyperelasticity in terms of principal stretches were known from literature, as discussed in Section 2.5. A Finite Element implementation for principal stretch hyperelasticity was therefore developed using analytically derived elasticity tensors. These required explicit computation of the principal stretches and principal directions for which an efficient, open-source Jacobi method algorithm was employed, from Kopp (203). The aim was to develop a numerically stable and accurate implementation of principal stretch hyperelastic constitutive models using analytically derived stress and elasticity tensors with minimised user input and comparable computation time to a built-in constitutive model. The developed implementation has some novel features: the stress and elasticity coefficients are efficiently implemented, symmetric dyadic products of the principal directions are utilised, and the numerical instabilities associated with equal and similar principal stretches are resolved by derived approximations with L'Hôpital's rule.

The implementation was numerically validated by evaluating the stress and elasticity tensors for constitutive models typically described in terms of Cauchy-Green invariants. By expressing these constitutive models in terms of principal invariants, this enabled a comparison to the implementations of Cauchy-Green invariants developed in Section 4.1. These were known to be free from numerical instabilities for deformations with equal and similar principal stretches. This form of validation was not otherwise known from literature. The implementation was further validated and its computation time was investigated using Finite Element simulations in Abaqus/Standard, where the developed implementation was programmed as a UMAT subroutine. This investigation used all previous implementations from Chapter 4, with approximated implementations in terms of Cauchy-Green invariants and principal stretches, and an implementation based on Simo and Taylor (155).

For implementations with approximated tangent moduli, only first-order double and quadruple precision approximations were used.

5.1 Isotropic Hyperelasticity in Principal Stretches

The stress and elasticity tensors for isotropic hyperelasticity in principal stretches were derived based on the explicit computation of principal stretches and principal directions (19, 153, 154). The strain, stress and elasticity tensors were defined with respect to the framework outlined in Section 2.1. In the following, the complete derivation is omitted but is referenced where required. Some additional aspects of the developed numerical implementation are also detailed, including the treatment of numerically similar and equal eigenvalues.

The material tensors were defined with respect to the reference configuration, then transformed to their spatial equivalent form in the current configuration by push-forward operation. The push-forward operations, were defined previously in equation (4.11) for the material second Piola-Kirchhoff stress tensor pushed-forward to the spatial Kirchhoff stress tensor and in equation (4.41) for the material elasticity tensor pushed-forward to the spatial elasticity tensor defined in terms of the Oldroyd-rate of the Kirchhoff stress.

For stress and elasticity tensors defined in terms of principal stretches and principal directions, the push forward operations used a form of the deformation gradient based on spectral decomposition. The deformation gradient is not generally symmetric, and cannot therefore be represented using spectral decomposition as in equations (2.4) and (2.5) for the Cauchy-Green strain tensors. However, it can be described in terms of the same real eigenvalues and orthogonal eigenvectors by

$$\mathbf{F} = \mathbf{R}\mathbf{U} = \sum_{a=1}^{3} \lambda_a \left(\mathbf{R}\mathbf{N}_a \otimes \mathbf{N}_a\right) = \sum_{a=1}^{3} \lambda_a \left(\mathbf{n}_a \otimes \mathbf{N}_a\right) \tag{5.1}$$

The material principal directions $\mathbf{N}_a$ are related to the spatial principal directions $\mathbf{n}_a$ by $\mathbf{n}_a = \mathbf{R}\mathbf{N}_a$. As they are of unit length, this implies $|\mathbf{N}_a| = |\mathbf{n}_a| = 1$, which is equivalent to the identity

$$\mathbf{N}_a \cdot \mathbf{N}_a = 1; \quad a = 1, 2, 3 \tag{5.2}$$

Equations (5.1) and (5.2) enable convenient push-forward operations of the material stress and elasticity tensors to their equivalent spatial tensors.

5.1.1 Definition of Stress Tensors

As in Chapter 4, the definition of the stress and elasticity tensors is derived from the split of the total strain energy ψ into isochoric W and volumetric components U (6). For hyperelasticity in terms of principal stretches the additive split is defined as the sum

$$\psi = W\left(\overline{\lambda}_1, \overline{\lambda}_2, \overline{\lambda}_3\right) + U\left(J\right) \tag{5.3}$$

The isochoric contribution to the energy is computed using isochoric principal stretches defined in equation (2.13). The volumetric strain energy contribution is identical to hyperelasticity in terms of Cauchy-Green invariants defined in Section 4.1. Hence, the volumetric stress and elasticity tensors in material and spatial configurations were omitted as they are as previously defined.

Material Stress Tensor In the reference configuration, as in Section 4.1, the second Piola-Kirchhoff stress tensor $\mathbf{S}$ is defined as the derivative of the total strain energy ψ with respect to the right Cauchy-Green deformation tensor $\mathbf{C}$. Its isochoric contribution is defined equivalently where the strain energy density is a function of the isochoric principal stretches $\overline{\lambda}_a$ defined by

$$\mathbf{S}_{iso} = 2\frac{\partial W\left(\overline{\lambda}_1, \overline{\lambda}_2, \overline{\lambda}_3\right)}{\partial \mathbf{C}} \tag{5.4}$$

The derivative is found using well-known identities and the chain rule, see Simo and Taylor (155) and the references therein for a complete derivation. This results in the following expression for the isochoric stress tensor

$$\mathbf{S}_{iso} = 2\sum_{a,b=1}^{3}\frac{\partial W}{\partial \overline{\lambda}_a}\frac{\partial \overline{\lambda}_a}{\partial \lambda_b}\frac{\partial \lambda_b}{\partial \mathbf{C}} = \sum_{a=1}^{3}\beta_a {\lambda_a}^{-2}\mathbf{N}_a \otimes \mathbf{N}_a \tag{5.5}$$

In this expression the principal directions $\mathbf{N}_a$ and squared principal stretches ${\lambda_a}^2$ are found from the right Cauchy-Green deformation tensor $\mathbf{C}$ defined in equation (2.4), using the iterative Jacobi algorithm from Kopp (203). The stress coefficients β_a are defined as

$$\beta_a = \overline{\lambda}_a\frac{\partial W}{\partial \overline{\lambda}_a} - \frac{1}{3}\sum_{b=1}^{3}\overline{\lambda}_b\frac{\partial W}{\partial \overline{\lambda}_b} \tag{5.6}$$

Spatial Stress Tensors The spatial stress tensor was defined initially in terms of the Kirchhoff stress, $\boldsymbol{\tau}$. This was found using the push-forward operation from the second Piola-Kirchhoff stress tensor, defined previously in equation (4.11), $\boldsymbol{\tau} = \mathbf{F}\mathbf{S}\mathbf{F}^{\mathrm{T}}$. The isochoric Kirchhoff stress tensor was found using the identities defined in equations (5.1) and (5.2) in equation (5.5) to give

$$\boldsymbol{\tau}_{iso} = \sum_{a=1}^{3}\beta_a\left(\mathbf{n}_a \otimes \mathbf{n}_a\right) \tag{5.7}$$

The stress coefficients β_a are as previously defined. The principal directions $\mathbf{n}_a$ and the squared principal stretches ${\lambda_a}^2$ for the current metric are found from the left Cauchy-Green deformation tensor $\mathbf{b}$, defined in equation (2.5). Here, the Jacobi method from Kopp (203) was used.

As previous, the spatial Cauchy stress tensor $\boldsymbol{\sigma}$ is required by Abaqus. It was obtained using its relationship to the total spatial Kirchhoff stress tensor $\boldsymbol{\tau}$, as was previously defined in equation (4.17), $\boldsymbol{\sigma} = J^{-1}\boldsymbol{\tau}$.

5.1.2 Definition of Elasticity Tensors

Unlike the stress tensor, the elasticity tensor appears in different forms throughout the literature. This is due to differences in the calculation of the principal directions. Here, the elasticity tensor was defined explicitly in terms of the principal directions, which were calculated from the relevant Cauchy-Green tensor by the Jacobi algorithm. As mentioned in Section 4.1.1, the derivation of the elasticity tensor may have its foundations in either the rate-forms, using $\dot{\mathbf{S}}$ and $\dot{\mathbf{C}}$, or by differentiation of $\mathbf{S}$ with respect to $\mathbf{C}$. In other definitions of the elasticity tensor with explicit calculation of the principal directions (5, 153, 154), the derivation is based on the use of the rate form. The developed implementation derived the material elasticity tensor $\mathbb{C}$ by differentiation, as defined in equation (4.19). The spatial elasticity tensors were then obtained by a push-forward operation with the inclusion of additional terms for objectivity where required.

Material Elasticity Tensor The isochoric component of the material elasticity tensor was obtained by differentiation of the isochoric second Piola-Kirchhoff stress defined in equation (5.5) with respect to the right Cauchy-Green tensor. Using the chain rule, this may be represented by three components as follows

$$\begin{aligned}\mathbb{C}_{iso} = 2\frac{\partial \mathbf{S}_{iso}}{\partial \mathbf{C}} &= 2\left(\sum_{a=1}^{3}\frac{\partial \beta_a}{\partial \mathbf{C}}{\lambda_a}^{-2}\left(\mathbf{N}_a \otimes \mathbf{N}_a\right)\right) \\ &+ 2\left(\sum_{a=1}^{3}\beta_a\frac{\partial {\lambda_a}^{-2}}{\partial \mathbf{C}}\left(\mathbf{N}_a \otimes \mathbf{N}_a\right)\right) \\ &+ 2\left(\sum_{a=1}^{3}\beta_a{\lambda_a}^{-2}\frac{\partial}{\partial \mathbf{C}}\left(\mathbf{N}_a \otimes \mathbf{N}_a\right)\right)\end{aligned} \tag{5.8}$$

The first and second terms were derived with reference to Simo and Taylor (155). The third term appears in explicit derivations where the rate form is used (5, 19, 153). It may otherwise be derived using linear perturbation theory (204). The combined

derived terms give the following definition of the isochoric elasticity tensor

$$\begin{aligned}\mathbb{C}_{iso} = &\sum_{a,b=1}^{3} \left(\gamma_{ab}\lambda_a^{-2}\lambda_b^{-2} - 2\delta_{ab}\beta_a\lambda_a^{-4}\right)(\mathbf{N}_a \otimes \mathbf{N}_a \otimes \mathbf{N}_b \otimes \mathbf{N}_b) \\ &+ \sum_{a,b=1;a\neq b}^{3} \frac{\beta_b\lambda_b^{-2} - \beta_a\lambda_a^{-2}}{\lambda_b^2 - \lambda_a^2}\left[(\mathbf{N}_a \otimes \mathbf{N}_b) \otimes (\mathbf{N}_a \otimes \mathbf{N}_b + \mathbf{N}_b \otimes \mathbf{N}_a)\right]\end{aligned} \tag{5.9}$$

The isochoric elasticity coefficients γ_{ab} are defined as

$$\begin{aligned}\gamma_{ab} = &\left[\overline{\lambda}_b\left(\overline{\lambda}_a\frac{\partial W}{\partial \overline{\lambda}_a}\right)\frac{\partial W}{\partial \overline{\lambda}_b}\right] + \frac{1}{9}\sum_{c,d=1}^{3}\left[\overline{\lambda}_d\left(\overline{\lambda}_c\frac{\partial W}{\partial \overline{\lambda}_c}\right)\frac{\partial W}{\partial \overline{\lambda}_d}\right] \\ &-\frac{1}{3}\sum_{c=1}^{3}\left[\overline{\lambda}_c\left(\overline{\lambda}_a\frac{\partial W}{\partial \overline{\lambda}_a}\right)\frac{\partial W}{\partial \overline{\lambda}_c} + \overline{\lambda}_b\left(\overline{\lambda}_c\frac{\partial W}{\partial \overline{\lambda}_c}\right)\frac{\partial W}{\partial \overline{\lambda}_b}\right]\end{aligned} \tag{5.10}$$

When the squared principal stretches are equal in equation (5.9) a numerical divide by zero error will occur, due to its second term. In general, a numerical treatment such as eigenvalue perturbation (159) may be used. However, for the explicitly defined elasticity tensor, an analytical solution is obtained by applying L'Hôpital's rule (5, 19). As the squared principal stretches tend towards one another, this rule enables the second term in equation (5.9) to be approximated by

$$\lim_{\lambda_a\to\lambda_b}\frac{\beta_b{\lambda_b}^{-2} - \beta_a{\lambda_a}^{-2}}{{\lambda_b}^2 - {\lambda_a}^2} = \frac{\partial\left(\beta_b{\lambda_b}^{-2}\right)}{\partial{\lambda_b}^2} - \frac{\partial\left(\beta_a{\lambda_a}^{-2}\right)}{\partial{\lambda_b}^2} \tag{5.11}$$

This equation was further developed to be approximated in terms of the stress and elasticity coefficients as follows

$$\lim_{\lambda_a\to\lambda_b}\frac{\beta_b{\lambda_b}^{-2} - \beta_a{\lambda_a}^{-2}}{{\lambda_b}^2 - {\lambda_a}^2} = {\lambda_b}^{-4}\left(\frac{1}{2}\gamma_{bb} - \beta_b\right) - \frac{1}{2}{\lambda_a}^{-2}{\lambda_b}^{-2}\gamma_{ab} \tag{5.12}$$

The numerical implementation of this required consideration of a means of detecting the numerical similarity of the squared principal stretches with an associated numerical tolerance. This is discussed further in Section 5.1.3.

Spatial Elasticity Tensors The isochoric elasticity tensor defined in terms of the Oldroyd-rate of the Kirchhoff stress $\mathbb{c}_{iso}$ was obtained from the equation for the material elasticity tensor $\mathbb{C}_{iso}$, defined in equation (5.9). The push-forward relationship defined in equation (4.41), with the identities defined in equations (5.1) and (5.2), was applied to define $\mathbb{c}_{iso}$ as

$$\begin{aligned}\mathbb{c}_{iso} = &\sum_{a,b=1}^{3}\left(\gamma_{ab} - 2\delta_{ab}\beta_a\right)(\mathbf{n}_a \otimes \mathbf{n}_a \otimes \mathbf{n}_b \otimes \mathbf{n}_b) \\ &+ \sum_{a,b=1;a\neq b}^{3}\frac{\beta_b\lambda_a^2 - \beta_a\lambda_b^2}{\lambda_b^2 - \lambda_a^2}\left[(\mathbf{n}_a \otimes \mathbf{n}_b) \otimes (\mathbf{n}_a \otimes \mathbf{n}_b + \mathbf{n}_b \otimes \mathbf{n}_a)\right]\end{aligned} \tag{5.13}$$

The elasticity coefficients γ_{ab} are defined as previous in equation (5.10). This elasticity tensor is also subjected to divide by zero errors if two or more principal stretches are equal. The expression obtained from the use of L'Hôpital's rule in the reference configuration, in equation (5.12), was pushed-forward to give the spatial equivalent form as

$$\lim_{\lambda_a \to \lambda_b} \frac{\beta_b {\lambda_a}^2 - \beta_a {\lambda_b}^2}{{\lambda_b}^2 - {\lambda_a}^2} = {\lambda_a}^2 {\lambda_b}^{-2} \left(\frac{1}{2}\gamma_{bb} - \beta_b \right) - \frac{1}{2}\gamma_{ab} \tag{5.14}$$

The implementation of this approximation also required consideration of detecting numerical similarity with definition of a numerical tolerance, discussed in Section 5.1.3.

To obtain the spatial elasticity tensor in terms of the Jaumann-rate of the Cauchy stress $\mathbb{c}_{ABQ}$, as required by Abaqus/Standard, the transformation defined in equation (4.56) was used $\left(\mathbb{c}_{ABQ} = J^{-1}\mathbb{c} + (\boldsymbol{\sigma} \odot \mathbf{1}) + (\mathbf{1} \odot \boldsymbol{\sigma})\right)$.

5.1.3 Aspects of Numerical Implementation

With the stress and elasticity tensors defined in reference and current configurations, these terms may be implemented in numerical methods. Some additional considerations are now discussed regarding particular aspects of the developed numerical implementation for any hyperelastic constitutive model defined in terms of principal stretches. The first consideration is the simplified implementation of the isochoric stress and elasticity coefficients β_a and γ_{ab}. The next is the use of symmetric dyadic products of the principal directions, which enables Voigt notation and reduces the computational cost. The final consideration is the required algorithm for detection of numerical similarity in the squared principal stretches and employment of the L'Hôpital's rule approximations to avoid numerical instability. These features are discussed in reference to the developed programs and subroutines in the associated dataset (4).

Implementation of Isochoric Stress and Elasticity Coefficients In the proposed implementation, the required user input was minimised. In other implementations (22, 132, 155), the stress coefficients β_a are required. Here it is noted from equation (5.6) that the use of a generic expression for $\frac{\partial W}{\partial \overline{\lambda}_a}$ may be defined by considering a specified principal stretch e.g. $\frac{\partial W}{\partial \overline{\lambda}_1}$. As, due to isotropy, this derivative is symbolically equivalent to $\frac{\partial W}{\partial \overline{\lambda}_2}$ and $\frac{\partial W}{\partial \overline{\lambda}_3}$, a general expression is therefore defined to compute all three derivatives. The stress coefficients β_a are then computed using these derivatives, as defined in equation (5.6).

Similarly, in other implementations the elasticity coefficients γ_{ab} are defined in full. It is observed here that in the definition of γ_{ab} in equation (5.10), the derivatives expand

to the same form

$$\overline{\lambda}_b \left(\overline{\lambda}_a \frac{\partial W}{\partial \overline{\lambda}_a} \right) \frac{\partial}{\partial \overline{\lambda}_b} = \left(\frac{\partial^2 W}{\partial \overline{\lambda}_a \partial \overline{\lambda}_b} \overline{\lambda}_a \overline{\lambda}_b + \frac{\partial W}{\partial \overline{\lambda}_a} \delta_{ab} \overline{\lambda}_b \right) \tag{5.15}$$

Only the second derivatives of the isochoric energy function $\frac{\partial^2 W}{\partial \overline{\lambda}_a \partial \overline{\lambda}_b}$ require definition, which may be defined for the two possibilities: $a = b$ and $a \neq b$. As in the definition of the stress coefficients, the derivatives may be obtained by considering specific principal stretches (e.g. $\frac{\partial^2 W}{\partial \overline{\lambda}_1 \partial \overline{\lambda}_1}$ and $\frac{\partial^2 W}{\partial \overline{\lambda}_1 \partial \overline{\lambda}_2}$) before generalising. The elasticity coefficients were therefore implemented using the expanded expression

$$\begin{aligned} \gamma_{ab} \; = & \left(\frac{\partial^2 W}{\partial \overline{\lambda}_a \partial \overline{\lambda}_b} \overline{\lambda}_a \overline{\lambda}_b + \frac{\partial W}{\partial \overline{\lambda}_a} \delta_{ab} \overline{\lambda}_b \right) + \frac{1}{9} \sum_{c,d=1}^{3} \left(\frac{\partial^2 W}{\partial \overline{\lambda}_c \partial \overline{\lambda}_d} \overline{\lambda}_c \overline{\lambda}_d + \frac{\partial W}{\partial \overline{\lambda}_c} \delta_{cd} \overline{\lambda}_d \right) \\ & - \frac{1}{3} \sum_{c=1}^{3} \left(\frac{\partial^2 W}{\partial \overline{\lambda}_a \partial \overline{\lambda}_c} \overline{\lambda}_a \overline{\lambda}_c + \frac{\partial W}{\partial \overline{\lambda}_c} \delta_{ac} \overline{\lambda}_c \right) - \frac{1}{3} \sum_{c=1}^{3} \left(\frac{\partial^2 W}{\partial \overline{\lambda}_b \partial \overline{\lambda}_c} \overline{\lambda}_b \overline{\lambda}_c + \frac{\partial W}{\partial \overline{\lambda}_b} \delta_{bc} \overline{\lambda}_c \right) \end{aligned} \tag{5.16}$$

Using the aforementioned simplifications, an incompressible hyperelastic constitutive response defined in principal stretches may be computed. The user is required to define the isochoric derivatives of the strain energy density function $\frac{\partial W}{\partial \overline{\lambda}_1}$, $\frac{\partial^2 W}{\partial \overline{\lambda}_1 \partial \overline{\lambda}_1}$ and $\frac{\partial^2 W}{\partial \overline{\lambda}_1 \partial \overline{\lambda}_2}$ in general form. To include compressive behaviour, the derivatives $\frac{\partial U}{\partial J}$ and $\frac{\partial^2 U}{\partial J^2}$ require user input.

Symmetric Dyadic Products of Principal Directions For all variations of the elasticity tensors defined in this chapter, the stress and strain tensors used in their derivation are symmetric. This therefore enabled the use of Voigt notation. The convention used by Abaqus/Standard was followed, as defined in Section 4.1.2.

The stress tensors are defined in terms of the stress coefficients and the dyadic products of the relevant principal directions, $\mathbf{n}_a \otimes \mathbf{n}_a$ or $\mathbf{N}_a \otimes \mathbf{N}_a$. These dyadic products are inherently symmetric since they are constructed from the same vectors, as $\mathbf{a} \otimes \mathbf{b} = (\mathbf{a} \otimes \mathbf{b})^{\mathrm{T}}$ if $\mathbf{a} = \mathbf{b}$. These can therefore be represented in Voigt notation. However, the definitions of the elasticity tensors, in equations (5.9) and (5.13), contain several non-symmetric second-order tensors, for example, in equation (5.9), $\mathbf{N}_a \otimes \mathbf{N}_b$ where $a \neq b$ and by the nature of eigenvectors $\mathbf{N}_a \neq \mathbf{N}_b$ for $a \neq b$. In this form, these cannot be represented in Voigt notation and nor can their fourth-order dyadic products, e.g. $\mathbf{N}_a \otimes \mathbf{N}_b \otimes \mathbf{N}_a \otimes \mathbf{N}_b$. A modification was therefore required.

It was known that all elasticity tensors defined previously contain both minor symmetries, such that $\mathbb{c}_{ijkl} = \mathbb{c}_{jikl} = \mathbb{c}_{ijlk}$. Furthermore, due to isotropy, the elasticity tensor also contains major symmetry such that $\mathbb{c}_{ijkl} = \mathbb{c}_{klij}$. Therefore, using the concept that any tensor may be decomposed into a symmetric tensor and a skew symmetric tensor (5), the sum of the components of the isochoric elasticity tensors, in equations (5.9) and (5.13), must result in the cancellation of all skew symmetric

parts. This permits the use of only the symmetric parts of the dyadic products. The symmetric part of a second-order tensor $\mathbf{A}$ is found as the halved sum of itself and its transpose

$$\operatorname{sym}(\mathbf{A}) = \frac{1}{2}\left(\mathbf{A} + \mathbf{A}^{\mathrm{T}}\right) \tag{5.17}$$

This was applied to the dyadic product of the principal directions to give

$$\begin{aligned} \operatorname{sym}(\mathbf{N}_a \otimes \mathbf{N}_b) &= \operatorname{sym}(\mathbf{N}_b \otimes \mathbf{N}_a) \\ &= \frac{1}{2}\left[(\mathbf{N}_a \otimes \mathbf{N}_b) + (\mathbf{N}_b \otimes \mathbf{N}_a)\right] \end{aligned} \tag{5.18}$$

This observation allowed for the symmetric dyadic products of the principal directions to be represented as tensors in Voigt notation. Also, only three of these second-order tensors required calculation, opposed to six. Furthermore, in the calculation of the fourth-order elasticity tensor, in equation (5.9) or equation (5.13), there are only three unique fourth-order dyadic products of the principal directions, opposed to twelve otherwise. This equivalence is shown for the indices 1 and 2 as follows

$$\begin{aligned} \operatorname{sym}(\mathbf{N}_1 \otimes \mathbf{N}_2) \otimes \operatorname{sym}(\mathbf{N}_1 \otimes \mathbf{N}_2) &= \operatorname{sym}(\mathbf{N}_1 \otimes \mathbf{N}_2) \otimes \operatorname{sym}(\mathbf{N}_2 \otimes \mathbf{N}_1) \\ &= \operatorname{sym}(\mathbf{N}_2 \otimes \mathbf{N}_1) \otimes \operatorname{sym}(\mathbf{N}_2 \otimes \mathbf{N}_1) \\ &= \operatorname{sym}(\mathbf{N}_2 \otimes \mathbf{N}_1) \otimes \operatorname{sym}(\mathbf{N}_1 \otimes \mathbf{N}_2) \end{aligned} \tag{5.19}$$

The same can be shown for the other two unique pairs of indices 1 and 3 and 2 and 3. The symmetries used here simplified the implementation significantly by permitting the use of Voigt notation throughout. This approach has not previously been used in literature.

Equal and Similar Principal Stretches When two or three of the squared principal stretches (eigenvalues of the Cauchy-Green deformation tensors) are equal, the elasticity tensors result in a divide by zero error. In a numerical method, the finite floating-point precision limit of the computation means that the solution also encounters numerical inaccuracy when the eigenvalues are numerically similar. With equal eigenvalues, the application of L'Hôpital's rule provides an exact alternative solution, though numerically similar eigenvalues require additional consideration. It was therefore necessary to find an approximate numerical tolerance at which the use of L'Hôpital's rule gives an approximation more accurate than the original function. There was also a requirement for an algorithm to compare the similarity of the eigenvalues.

The proposed algorithm is based on an eigenvalue perturbation algorithm by Miehe (159). Eigenvalue perturbation is an alternative means of avoiding divide by zero errors, but is less accurate and stable (65) than the method used here. The proposed algorithm used a similar method for the detection of equal and similar eigenvalues,

but employed approximations by L'Hôpital's rule if the absolute difference between eigenvalues is found to be less than the defined tolerance value. The developed algorithm includes additional checks for three equal or similar eigenvalues, as it is possible numerically that $(|\lambda_1 - \lambda_2|) \leq tol$ and $(|\lambda_1 - \lambda_3|) \leq tol$ are true but $(|\lambda_2 - \lambda_3|) \leq tol$ is false, repeated for all combinations. The proposed algorithm is defined in Table 5.1 for the spatial elasticity tensor, where *tol* is the magnitude of the numerical tolerance.

An equivalent algorithm was used in the numerical investigations of the isochoric material elasticity tensor defined in equation (5.9). Both can be found in the dataset (4). The algorithm prevents divide by zero errors provided that a suitable tolerance value is selected. Optimisation of the tolerance value was investigated and is discussed in Section 5.2.3.

5.2 Numerical Validation of Principal Stretch Hyperelasticity

The implementation of hyperelasticity in principal stretches defined in Section 5.1 was investigated and validated. Throughout the investigations hyperelastic constitutive models defined in terms of the first and second isochoric Cauchy-Green invariants were used, as defined in Section 4.1. Any constitutive model defined in terms of these isochoric strain invariants may also be defined, and therefore implemented, by isochoric principal stretches using their relationships defined in equations (2.7) and (2.8). A comparison can therefore be made between the implementations, which is otherwise unknown from literature, despite its usefulness; the invariant implementation is unambiguous and is not subjected to numerical difficulties for deformations with equal or similar principal stretches. The invariant implementation therefore provided a stable and accurate solution from which the principal stretch implementation was validated. Additionally these were used to optimise the numerical tolerance of L'Hôpital's rule.

This numerical investigation is divided into three studies, all of which use Fortran programs. These programs allow computation of the stress and elasticity tensors for a user-defined deformation gradient with a chosen constitutive model and definition of its parameters and derivatives. The error is then computed by using an equivalent Cauchy-Green invariant implementation. The proposed implementation was validated for unique eigenvalues, then compared for two and three equal eigenvalues. The tolerance value was optimised using similar eigenvalues. The validated and optimised implementation was then used to create UMAT user subroutines to investigate performance in the FEM using Abaqus/Standard.

Table 5.1: Proposed algorithm for robust computation of the spatial elasticity tensor

- Calculate the common first term

$$\mathbb{c}_{iso} = \sum_{a,b=1}^{3} \left(\gamma_{ab} - 2\delta_{ab}\beta_a\right)\left(\mathbf{n}_a \otimes \mathbf{n}_a \otimes \mathbf{n}_b \otimes \mathbf{n}_b\right)$$

- Define the numerical tolerance, *tol*

$$tol = N$$

- Check numerical similarity and apply L'Hôpital's rule if $\leqslant tol$

If $(|\lambda_1 - \lambda_2|) \leq tol$ then

If $(|\lambda_2 - \lambda_3|) \leq tol$ then

$$\mathbb{c}_{iso} = \mathbb{c}_{iso} + \sum_{a,b=1;a\neq b}^{3} \left[{\lambda_a}^2 {\lambda_b}^{-2}\left(\tfrac{1}{2}\gamma_{bb} - \beta_b\right) - \tfrac{1}{2}\gamma_{ab}\right]$$

Else if $(|\lambda_1 - \lambda_3|) \leq tol$ then

$$\mathbb{c}_{iso} = \mathbb{c}_{iso} + \sum_{a,b=1;a\neq b}^{3} \left[{\lambda_a}^2 {\lambda_b}^{-2}\left(\tfrac{1}{2}\gamma_{bb} - \beta_b\right) - \tfrac{1}{2}\gamma_{ab}\right]$$

Else

$$\mathbb{c}_{iso} = \mathbb{c}_{iso} + \left[{\lambda_a}^2 {\lambda_b}^{-2}\left(\tfrac{1}{2}\gamma_{bb} - \beta_b\right) - \tfrac{1}{2}\gamma_{ab}\right] \text{ [(a,b)=(1,2);(2,1)]}$$
$$+ \left(\frac{\beta_b\lambda_a^2 - \beta_a\lambda_b^2}{\lambda_b^2 - \lambda_a^2}\right) \text{ ((a,b) =(1,3);(3,1);(2,3);(3,2))}$$

End if

Else if $(|\lambda_1 - \lambda_3|) \leq tol$ then

If $(|\lambda_2 - \lambda_3|) \leq tol$ then

$$\mathbb{c}_{iso} = \mathbb{c}_{iso} + \sum_{a,b=1;a\neq b}^{3} \left[{\lambda_a}^2 {\lambda_b}^{-2}\left(\tfrac{1}{2}\gamma_{bb} - \beta_b\right) - \tfrac{1}{2}\gamma_{ab}\right]$$

Else

$$\mathbb{c}_{iso} = \mathbb{c}_{iso} + \left[{\lambda_a}^2 {\lambda_b}^{-2}\left(\tfrac{1}{2}\gamma_{bb} - \beta_b\right) - \tfrac{1}{2}\gamma_{ab}\right] \text{ [(a,b)=(1,3);(3,1)]}$$
$$+ \left(\frac{\beta_b\lambda_a^2 - \beta_a\lambda_b^2}{\lambda_b^2 - \lambda_a^2}\right) \text{ ((a,b)=(1,2);(2,1);(2,3);(3,2))}$$

Else if $(|\lambda_2 - \lambda_3|) \leq tol$ then

$$\mathbb{c}_{iso} = \mathbb{c}_{iso} + \left[{\lambda_a}^2 {\lambda_b}^{-2}\left(\tfrac{1}{2}\gamma_{bb} - \beta_b\right) - \tfrac{1}{2}\gamma_{ab}\right] \text{ [(a,b)=(2,3);(3,2)]}$$
$$+ \left(\frac{\beta_b\lambda_a^2 - \beta_a\lambda_b^2}{\lambda_b^2 - \lambda_a^2}\right) \text{ ((a,b)=(1,2);(2,1);(1,3);(3,1))}$$

Else

$$\mathbb{c}_{iso} = \mathbb{c}_{iso} + \sum_{a,b=1;a\neq b}^{3} \frac{\beta_b\lambda_a^2 - \beta_a\lambda_b^2}{\lambda_b^2 - \lambda_a^2}$$

End if

- *Note: The eigenvector terms* $[(\mathbf{n}_a \otimes \mathbf{n}_b) \otimes (\mathbf{n}_a \otimes \mathbf{n}_b + \mathbf{n}_b \otimes \mathbf{n}_a)]$ *are omitted for brevity.*

The Fortran programs and UMAT user subroutines used in these investigations, as well as templates for a generic implementation of isochoric-volumetric split constitutive models, are provided in the dataset (4).

5.2.1 Unique Eigenvalues

The validity was assessed in the reference configuration, the current configuration defined in terms of the Oldroyd-rate of the Kirchhoff stress and in terms of the Jaumann-rate of the Cauchy stress. To compute the error for the stress tensors calculated in terms of principal stretches, the relative error of each of the 6 components in Voigt notation was calculated by comparison to the invariant implementation. The sum of the error $E_{\mathbf{S}}$ of these components was then computed using an error function equivalent to that used in Section 4.3 defined in equation (4.85). The error function for the stress tensor was defined as

$$E_{\mathbf{S}} = \left[\sum_{I=1}^{6} \left(\mathrm{S}_{\bar{\lambda} I} - \mathrm{S}_{\bar{I}_{12} I} \right)^2 \right]^{\frac{1}{2}} / \left[\sum_{I=1}^{6} \left(\mathrm{S}_{\bar{I}_{12} I} \right)^2 \right]^{\frac{1}{2}} \tag{5.20}$$

Here the components in Voigt notation are denoted by I to represent the indices 1 to 6, as defined previously. The second Piola-Kirchhoff stress tensors $\mathbf{S}_{\bar{\lambda}}$ and $\mathbf{S}_{\bar{I}_{12}}$ represent the components computed in terms of principal stretches and Cauchy-Green invariants respectively. The same method was applied for calculating the error of the spatial Kirchhoff and Cauchy stress tensors, $E_{\boldsymbol{\tau}}$ and $E_{\boldsymbol{\sigma}}$ respectively.

To validate the elasticity tensors, the relative error computation was modified to account for all 36 components of the material elasticity tensor $\mathbb{C}$ in Voigt notation as

$$E_{\mathbb{C}} = \left[\sum_{I,J=1}^{6} \left(\mathbb{C}_{\bar{\lambda} IJ} - \mathbb{C}_{\bar{I}_{12} IJ} \right)^2 \right]^{\frac{1}{2}} / \left[\sum_{I,J=1}^{6} \left(\mathbb{C}_{\bar{I}_{12} IJ} \right)^2 \right]^{\frac{1}{2}} \tag{5.21}$$

The notations are defined analogously to the stress tensor. The error was also calculated equivalently for the spatial Oldroyd-rate and Jaumann-rate tensors, $E_{\mathbb{c}}$ and $E_{\mathbb{c}_{ABQ}}$ respectively.

To validate the developed expressions and their numerical implementation, as defined in Section 5.1, the stress and elasticity tensors were computed for two deformation gradients. These deformation gradients were previously used in Section 4.3 and defined as $\mathbf{F}_4$ and $\mathbf{F}_5$ in equation (4.84). They are redefined here as

$$\mathbf{F}_1 = \begin{pmatrix} 3 & 1 & 0 \\ 1 & 1 & 0 \\ 0 & 0 & 0.5 \end{pmatrix}; \qquad \mathbf{F}_2 = \begin{pmatrix} 1.1 & 0.2 & 0.2 \\ 0 & 0.9535 & 0.2 \\ 0 & 0 & 0.9535 \end{pmatrix} \tag{5.22}$$

To ensure the validity of the use of symmetric dyadic products for the eigenvectors, the deformation gradients were rotated. The method for rotation is equivalent to that

Table 5.2: Error of stress tensors: material (second Piola-Kirchhoff), spatial (Kirchhoff), and spatial (Cauchy)

	E_S	$E_{\boldsymbol{\tau}}$	$E_{\boldsymbol{\sigma}}$
$\mathbf{F}_1$	1.306E-15	3.248E-15	3.248E-15
$\mathbf{F}_2$	3.085E-15	1.145E-15	1.000E-15

of (149, 180). The rotated deformation gradient $\mathbf{F}_{\mathrm{R1}}$ was computed by

$$\mathbf{F}_{\mathrm{R1}} = \mathbf{Q}\mathbf{F}_1 \tag{5.23}$$

The rotation tensor $\mathbf{Q}$ is a product of three rotation matrices

$$\mathbf{Q}= \begin{pmatrix} \cos\frac{\pi}{4} & -\sin\frac{\pi}{4} & 0 \\ \sin\frac{\pi}{4} & \cos\frac{\pi}{4} & 0 \\ 0 & 0 & 1 \end{pmatrix} \begin{pmatrix} \cos\frac{\pi}{3} & 0 & \sin\frac{\pi}{3} \\ 0 & 1 & 0 \\ -\sin\frac{\pi}{3} & 0 & \cos\frac{\pi}{3} \end{pmatrix} \begin{pmatrix} 1 & 0 & 0 \\ 0 & \cos\frac{\pi}{6} & -\sin\frac{\pi}{6} \\ 0 & \sin\frac{\pi}{6} & \cos\frac{\pi}{6} \end{pmatrix} \tag{5.24}$$

The chosen constitutive model for this comparison was the neo-Hookean model (69). This is conventionally represented in terms of the first isochoric Cauchy-Green invariant $\bar{I}_1$ as in equation (3.13) and may also be expressed in terms of the isochoric principal stretches. As the volumetric components were consistent for both implementations, which are mutually defined in terms of the volume ratio J, they were omitted from the comparisons.

The sum of the relative error of the stress tensor is shown in Table 5.2. Given that these were calculated using double precision, their accuracy is close to the finite precision limit $\sim 1\text{E}{-}16$. These low errors are due to rounding. The stress tensors can therefore be said to be consistent and accurate for the principal stretch implementation. There was also no notable difference between the accuracy for isochoric and dilational deformations. As the stress tensors are generally well-agreed upon, this result was anticipated.

The validation of the elasticity tensor and its numerical implementation was of particular interest, as some aspects are novel and had not previously been validated. The error of the elasticity tensors for both deformation gradients and all configurations are given in Table 5.3. The error was of similar scale to the finite precision limit for both isochoric and dilational deformations. This suggested that the developed elasticity tensors and their numerical implementation was consistent with the invariant implementation for deformations with unique eigenvalues.

5.2.2 Equal Eigenvalues

With equal squared principal stretches, the algorithm of Table 5.1 was required to avoid undefined divide by zero errors for all variations of the elasticity tensors. As the

Table 5.3: Error of elasticity tensors: material, spatial (Oldroyd), and spatial (Jaumann)

	$E_{\mathbb{C}}$	$E_{\mathbb{c}}$	$E_{\mathbb{c}_{ABQ}}$
$\mathbf{F}_1$	1.525E-15	5.867E-16	1.449E-15
$\mathbf{F}_2$	1.642E-15	1.243E-15	1.589E-15

eigenvectors are identical, any tolerance value N is acceptable for which $1 + N > 1$ is true. As the stress tensor was found to be accurate and is unaffected by equal or similar principal eigenvalues, it was not considered in the latter investigations. Computation of the eigenvalues and eigenvectors may be problematic when the eigenvalues are equal or similar. However, the Jacobi method algorithm was known to be consistently stable and accurate (203).

With equal eigenvalues, the elasticity tensors were investigated in the same method as previous in Section 5.2.1. The Mooney-Rivlin model was used, as defined in equation (3.12) for the invariant implementation. The identities defined in equations (2.7) and (2.8) were then used to express the model in terms of isochoric principal stretches. The rotation of the deformation gradient defined in equation (5.22) was applied for isochoric and dilational deformations in the case of both two and three equal eigenvalues. The pre-rotation deformation gradients for two equal eigenvalues were the isochoric and dilational uniaxial tension deformations, $\mathbf{F}_3$ and $\mathbf{F}_4$, defined by

$$\mathbf{F}_3 = \begin{pmatrix} 0.25 & 0 & 0 \\ 0 & 2 & 0 \\ 0 & 0 & 2 \end{pmatrix}; \qquad \mathbf{F}_4 = \begin{pmatrix} 4 & 0 & 0 \\ 0 & 0.45 & 0 \\ 0 & 0 & 0.45 \end{pmatrix} \tag{5.25}$$

For three equal eigenvalues, the pre-rotation deformation gradients $\mathbf{F}_5$ and $\mathbf{F}_6$ correspond to an undeformed configuration and a hydrostatic compression. These were respectively defined as

$$\mathbf{F}_5 = \begin{pmatrix} 1 & 0 & 0 \\ 0 & 1 & 0 \\ 0 & 0 & 1 \end{pmatrix}; \qquad \mathbf{F}_6 = \begin{pmatrix} 0.5 & 0 & 0 \\ 0 & 0.5 & 0 \\ 0 & 0 & 0.5 \end{pmatrix} \tag{5.26}$$

The summed errors for the error with two and three equal eigenvalues are respectively given in Tables 5.4 and 5.5. It was found that the error throughout was of a similar order to the finite precision limit. The accuracy was of a similar order for isochoric and dilational deformations in the case of two and three equal eigenvalues. The derived approximations by L'Hôpital's rule and their numerical implementation was therefore assumed to be valid and accurate for the cases of equal eigenvalues.

5.2.3 Eigenvalue Similarity Tolerance

Finding an appropriate tolerance value for numerically similar eigenvalues was required to complete the proposed implementation principal stretch hyperelasticity.

Table 5.4: Error of elasticity tensors with two equal eigenvalues

	$E_{\mathbb{C}}$	$E_{\mathbb{c}}$	$E_{\mathbb{c}_{ABQ}}$
$\mathbf{F}_3$	1.436E-16	5.928E-15	7.398E-16
$\mathbf{F}_4$	1.395E-15	5.478E-15	3.083E-15

Table 5.5: Error of elasticity tensors with three equal eigenvalues

	$E_{\mathbb{C}}$	$E_{\mathbb{c}}$	$E_{\mathbb{c}_{ABQ}}$
$\mathbf{F}_5$	5.617E-16	3.378E-16	3.144E-16
$\mathbf{F}_6$	7.4106E-16	4.798E-16	4.577E-16

The cases of two and three similar eigenvalues were investigated in each configuration. To achieve numerically similar eigenvalues, a perturbation was applied to the deformation gradients. For two similar eigenvalues, a uniaxial tension deformation gradient was used with a perturbation of the two non-zero, equal components prior to rotation. For three similar eigenvalues, the perturbation was applied to two of the non-zero components of the undeformed deformation gradient prior to its rotation. These are defined as $\mathbf{F}_7$, with the perturbation magnitude η, for λ=2 and λ=1 in the equation

$$\mathbf{F}_7 = \begin{pmatrix} \lambda & 0 & 0 \\ 0 & \frac{1}{\sqrt{\lambda}} + \eta & 0 \\ 0 & 0 & \frac{1}{\sqrt{\lambda}} + \eta \end{pmatrix} \tag{5.27}$$

The perturbation magnitude η was decreased exponentially from 1E$-$2 to 1E$-$16 using only integer powers, as perturbations lower than 1E$-$16 result in $1 + \eta \not> 1$ for double precision. The elasticity tensors were calculated with and without L'Hôpital's rule for increasingly similar eigenvalues and compared to the stable solution obtained from a Cauchy-Green invariant implementation. For this investigation, the Gent model (18) was used, as defined as in equation (3.14).

For two and three similar eigenvalues, it was found that as the perturbation magnitude tended towards zero, for all configurations, without L'Hôpital's rule the error increased and with L'Hôpital's rule the error decreased. Both are shown for the spatial elasticity tensor $\mathbb{c}_{ABQ}$ in Figures 5.1a and 5.1b. The optimal tolerance magnitude is therefore that which employs L'Hôpital's rule at the point where these lines intersect. It is seen from Figure 5.1 that the intercept of the lines for these deformation gradients occurs around η=1E$-$6. This was then checked further for what are considered to be the approximate extremes of elastic deformations, with λ=10 and λ=0.05. As shown in Figure 5.1c and 5.1d, the magnitude of the intercept does not diverge significantly in either case from the intercept of η=1E$-$6.

The algorithm presented in Table 5.1 was designed such that the tolerance value

corresponds to the perturbation magnitude. The optimal tolerance magnitude was therefore approximated as $1\text{E}{-6}$, the results for which were also plotted in Figure 5.1. For the four deformation gradients, assumed to be the limits of elastic deformations, and for all configurations, the elasticity tensor was computed accurately, with a maximum error of less than $1\text{E}{-10}$.

5.3 Finite Element Investigations of Principal Stretch Hyperelasticity

The proposed implementation was validated numerically in that it was accurate and consistently stable, even for deformations with equal and similar eigenvalues. Two Finite Element benchmark simulations were performed for further validation and an assessment of computation time. Physical results output by the simulation were compared for further numerical validation. To assess the computation time, solve times relative to the performance of the built-in constitutive model were compared throughout.

The simulated Finite Element models represent an inhomogeneous tensile test and a combined tension-torsion test. These were both created using Abaqus/CAE and solved implicitly using Abaqus/Standard. In the first FE model, a Cauchy-Green invariant hyperelastic constitutive model was used. This enabled a comparison of the developed principal stretch implementation to those from Chapter 4, which included a built-in model, a UHYPER implementation, and first-order forward difference approximations in double and quadruple precision. In addition to these, implementations using the first-order approximated tangent moduli in double and quadruple precision were included where the perturbed stress tensor was defined in terms of principal stretches. Also, an implementation based on that of Simo and Taylor (155) was included in the comparison. The implementation directly computed eigenvalue bases and used eigenvalue perturbation from Miehe (159) to avoid numerical instabilities. For the second FE model, a constitutive model implementable only in terms of principal stretches was applied. This granted an insight into the built-in performance to the developed implementation for this type of model.

5.3.1 Inhomogeneous Tension

The first benchmark simulation was a 3D inhomogeneous tension test of a rubber specimen. The cuboidal specimen had a 1mm by 1mm cross-section and is 1.5mm long. One of the 1mm by 1mm faces of the specimen was fully fixed and a displacement load of 1mm was applied to the opposing face in the longitudinal direction in

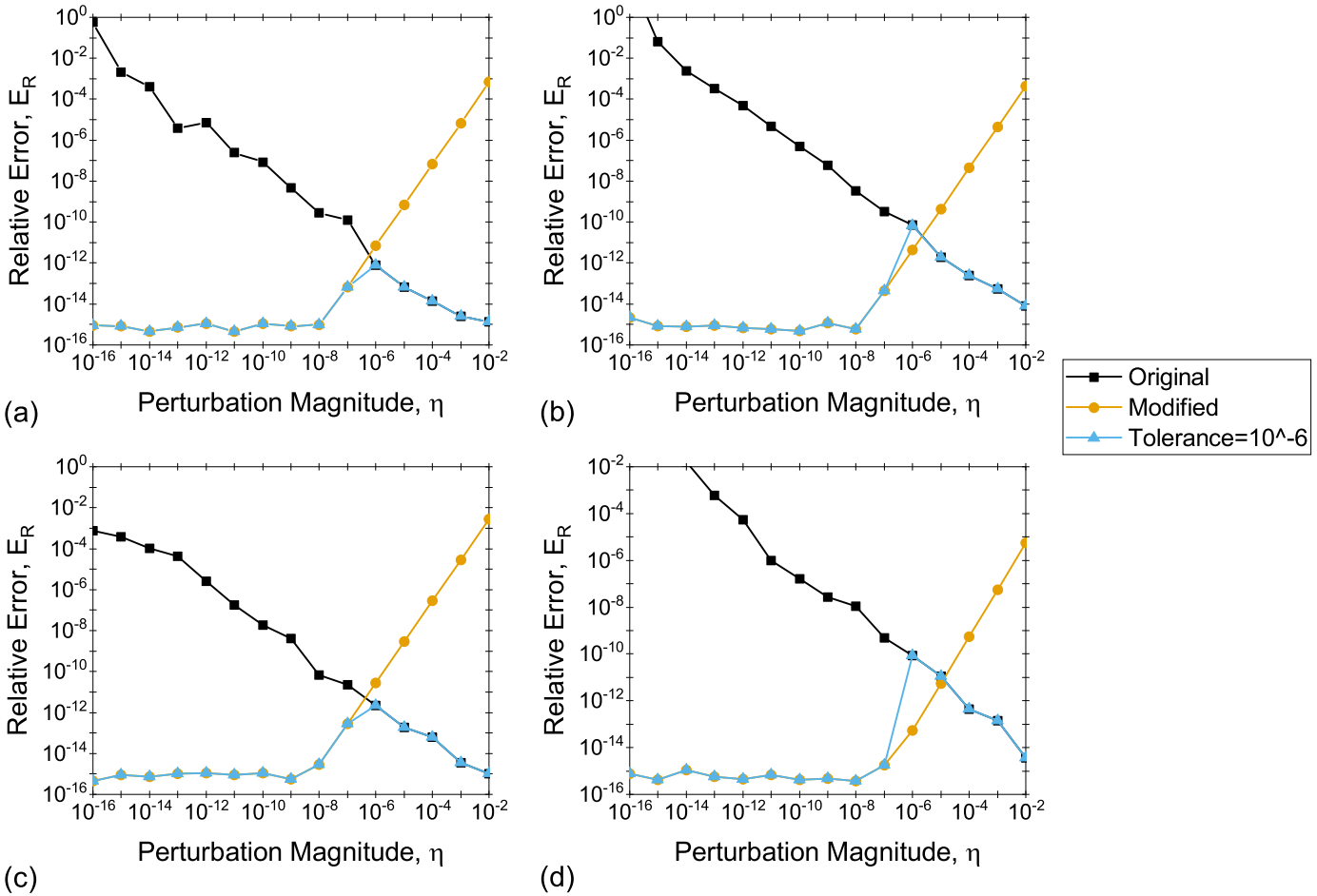

Figure 5.1: Relative error of the proposed implementation in principal stretches to the Cauchy-Green invariant implementation for perturbed uniaxial deformations with varying λ (a) λ=2, (b) λ=1, (c) λ=10, (d) λ=0.05

a minimum of 10 increments using automatic incrementation. The body was meshed by hybrid, higher-order tetrahedral elements (C3D10H). The tetrahedral element was chosen to further ensure that the principal directions were computed appropriately. The model was solved for five levels of mesh refinement, giving additional insight into any differences in computational effort. Incompressibility was assumed such that only the isochoric constitutive model required consideration. The isochoric hyperelastic response used for this was the Yeoh model (189), as defined in equation (3.20). The three model parameters were defined for a fit to Treloar's experimental data (127) and can be found in the dataset (4).

In the incremental solutions of the inhomogeneous tensile test, all implementations, apart from that based on Simo and Taylor (155), achieved convergence in the specified minimum of 10 increments for all levels of mesh refinement, with approximately equal total iterations. The Simo and Taylor (155) implementation achieved convergence in 10 increments for only the simplest mesh, where it required additional iterations in the convergence of the first increment. For an increasingly refined mesh, the Simo and Taylor (155) implementation required additional increments. This was due to the numerical instability in the early increments of the solution. The difference between the implementations was present only in their convergence behaviour. The converged physical results were found to be within 0.1% across all levels of mesh refinement for all implementations.

The von Mises stress results are shown for the third mesh with 5617 elements in Figure 5.2 for solved models using the built-in model and the developed principal stretch implementation. For these results, the maximum residual forces during convergence had a maximum difference of $\Delta F \leq 1\text{E}{-}7\text{N}$ between the presented implementation's model and the built-in model. There were therefore no observable differences between the solved models for all increments.

The computational effort of the implementations were compared by their solve times relative to that of the built-in model. The results for the five levels of mesh refinement are shown in Figure 5.3. In this figure, the analytical Cauchy-Green invariant implementation is labelled as "I_1I_2", the presented implementation is "λ", the Simo and Taylor implementation is "λ S&T", the approximations are forward difference (FD) in double (8) and quadruple (16) precision and their labelling is defined implicitly based on this information.

The built-in model was found to be the most computationally efficient for meshes one through four. Following this, the UHYPER implementation was found to have a maximum relative solve time of 1.214 and was more computationally efficient in the case of the fifth mesh with a relative solve time of 0.995. The developed analytical implementations for Cauchy-Green invariant and principal stretch defined tensors were

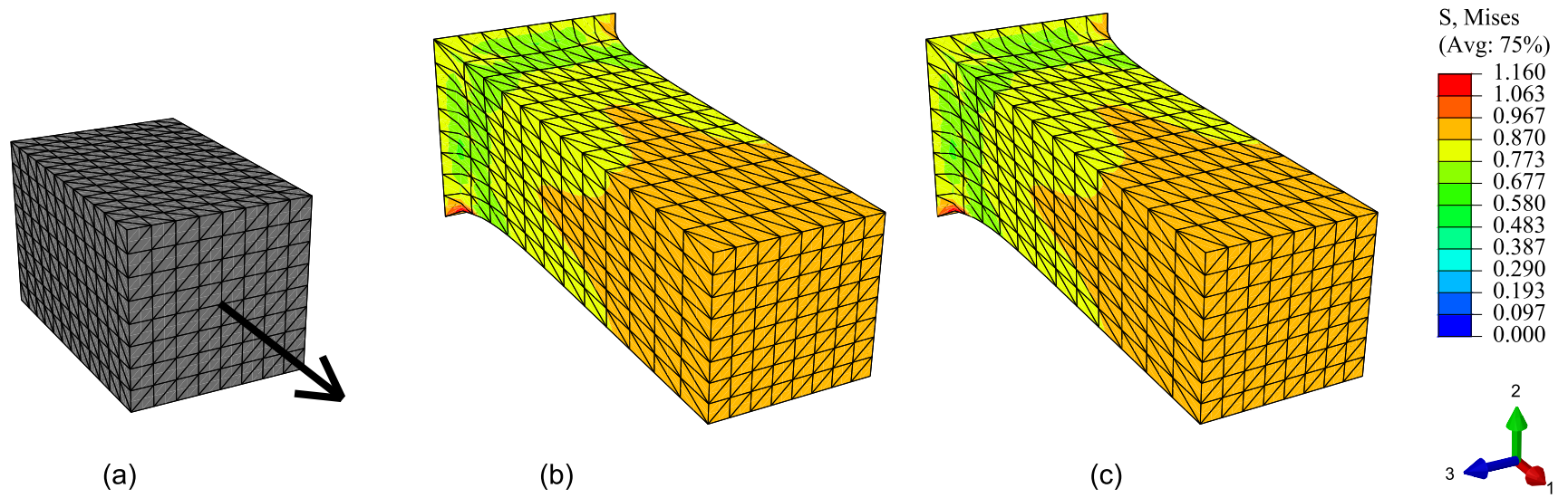

Figure 5.2: Inhomogeneous tension test von Mises stress Finite Element solutions: (a) undeformed mesh 3, (b) built-in model (c) developed principal stretch implementation

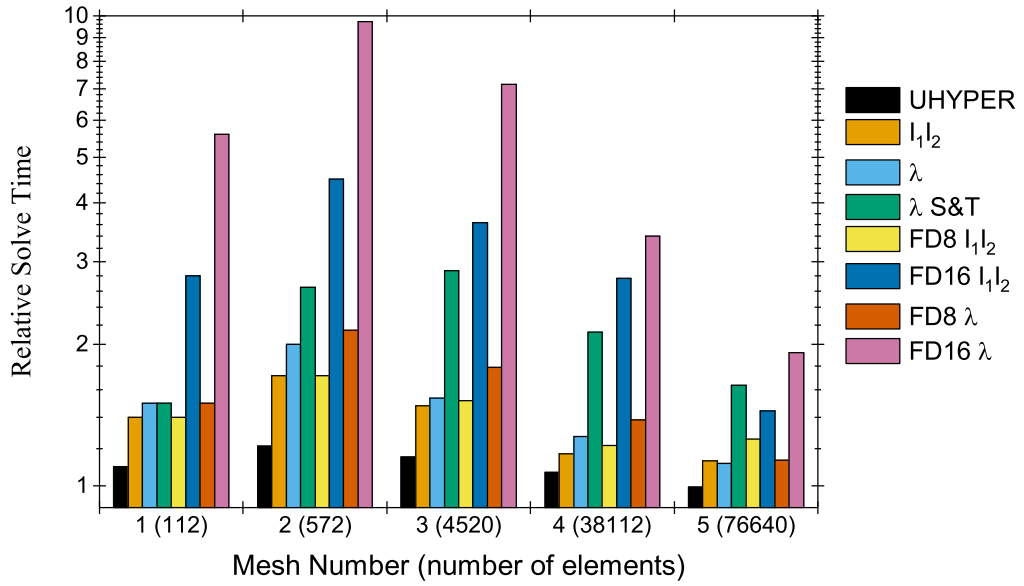

Figure 5.3: Solve times of the three user subroutine implementations relative to a built-in model for increasing mesh density of an inhomogeneous tension test

both of similar computational effort with the former generally requiring less. Compared to the λ S&T implementation, the developed principal stretch implementation was found to be significantly more efficient. The double precision approximation implementations also had lower solve times than the λ S&T implementation. These findings highlight the importance of numerically stable and accurate tangent moduli in implicit FE simulations.

Comparing the two different double precision approximation implementations, the approximated implementation with principal stretches had comparable but generally higher computational effort compared with the approximation with Cauchy-Green invariants. This is due to the additional computation time when computing the eigenvalues and eigenvectors for all perturbed deformation gradients. As found in Section 4.4, the use of quadruple precision significantly increases the solution times. With quadruple precision eigenvalue and eigenvector computation, in the approximated implementation with principal stretches, the solution times further increased. The difference between all implementations was found to decrease with increasing mesh refinement due to the relative increase in solution times of the global matrix iterations, as observed in Section 4.4.3. The implementation by UHYPER subroutine remains the preferred method of implementation for hyperelastic constitutive behaviour in terms of Cauchy-Green invariants.

5.3.2 Combined Tension-torsion

The second Finite Element benchmark model was of a combined tension-torsion test using a specimen geometry defined within Miehe and Göktepe (37). A coupling was used on the top face of the specimen with reference to the centre node. In a minimum of 10 increments using automatic incrementation, the reference node was displaced 10mm in the 2 direction and rotated 90° around the y axis, the top face was otherwise fixed from expanding or contracting. The bottom face of the specimen was fully fixed. The specimen was meshed by hybrid, first-order hexahedral elements (C3D8H) and assumed to be incompressible. As with the previous model, five levels of mesh refinement were used. The third-order Ogden constitutive model was used with parameters fitted to the complete set of Meunier's data (88) from Section 3.4.1. These can be found in the dataset (4).

Based on the results of the first FE study, only the built-in model, the developed implementation and the first-order approximation using principal stretch defined perturbed stress tensors were used. The minimum number of increments were required for the built-in model, the Cauchy-Green invariant implementation and the presented implementation for all levels of mesh refinement, each with approximately the same number of total iterations. As in the previous example, the examined physical results were found to be very similar. The largest difference found was in the case of the first mesh for the minimum principal stress, with an absolute difference of approximately 1.165%. The maximum principal stress results are shown for the third mesh with 5376 elements in Figure 5.4, showing visually inseparable results for the built-in and the proposed implementation FE models.

The computational effort was compared using solve times relative to the built-in model. The results are shown for the five levels of mesh refinement in Figure 5.5 with the same labelling as before. It was found again that increasing mesh density leads to a smaller difference in solve times for all implementations. Compared with the built-in implementation, the developed analytical principal stretch implementation required a minimum of around 35% additional solution time for the fifth mesh and a maximum of around 94% for the third mesh. Although this difference is significant, the developed implementation was consistently more efficient than the alternative implementation by double precision first-order approximated tangent moduli. For implementation of user-defined constitutive models in terms of principal stretches, the developed analytical implementation was shown to be a suitable method.

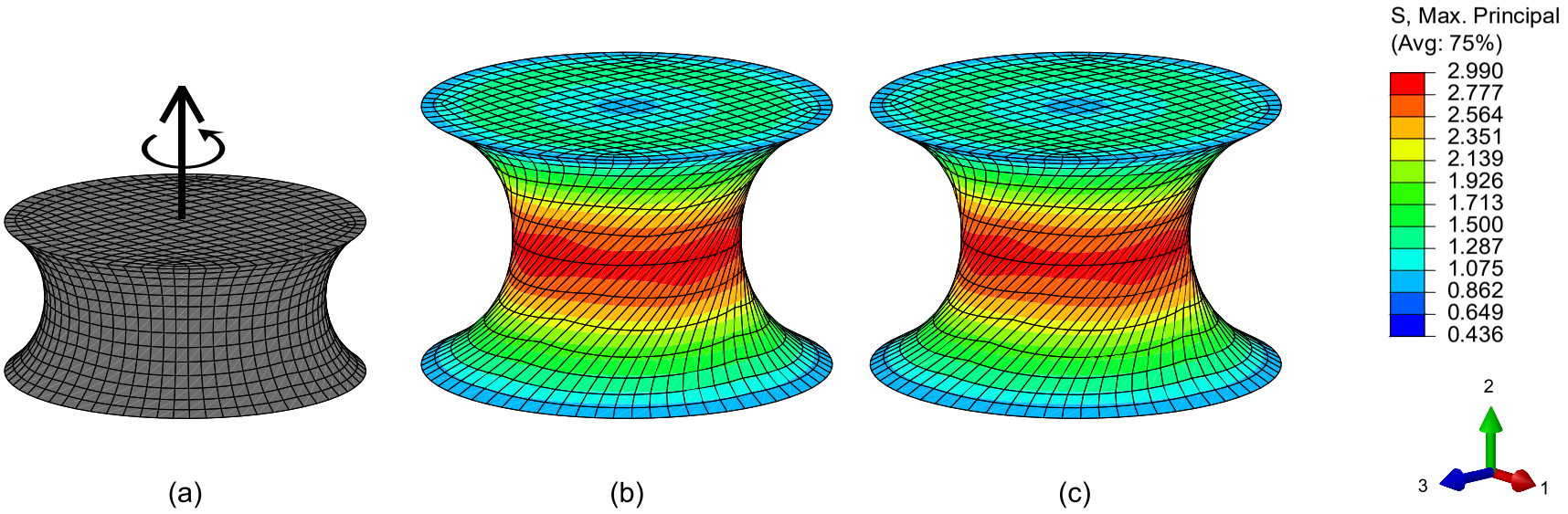

Figure 5.4: Combined tension-torsion test maximum principal stress Finite Element solutions: (a) undeformed mesh 3, (b) built-in model (c) developed principal stretch implementation

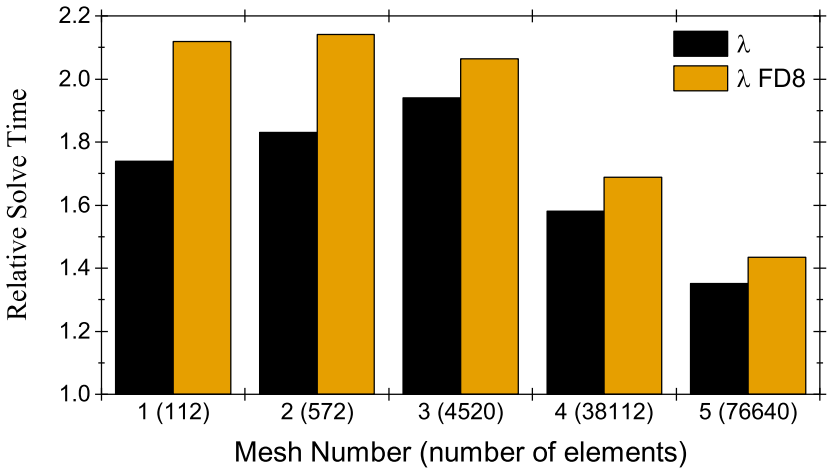

Figure 5.5: Solve times of the two user subroutine implementations relative to a built-in model for increasing mesh density of a combined tension-torsion test

5.3.3 Discussion of Developed Implementation

The numerical validation and Finite Element Method investigation results show that the developed implementation is accurate and of satisfactory computation time. Although it is noted that the proposed implementation was not optimised for computation time. The priority of the developed programs and user subroutines was the ease of user implementation. If all implementations were optimised for computation time then the results may differ.

In the case of equal and similar eigenvalues, it was shown that the approximated terms using L'Hôpital's rule were accurate and valid. It was apparent that in the case of similar eigenvalues that the algorithm and tolerance value could be optimised and improved. However, this would result in imperceptible changes to the output physical results and was not considered to be necessary. The developed algorithm and the approximate tolerance of $1\text{E}{-6}$ is found to produce converging solutions with a maximum error in the order of $1\text{E}{-10}$.

5.4 Summary of Principal Stretch Hyperelasticity Implementation

The proposed implementation of analytically derived principal stretch hyperelasticity involved simple user input while attaining numerical robustness and accuracy. The user input is unchanged in the definition of constitutive models in the reference and current configurations. The user is required only to define the derivatives of the isochoric and volumetric strain energy functions with respect to the isochoric princi-

pal stretches and the volume ratio. The isochoric principal stretches and associated principal directions are computed explicitly using an iterative Jacobi method. Explicit computation requires additional computational effort, compared with a direct method, but was shown to require less total computational effort in the solution of an FE model due to its improved numerical stability and accuracy. Compared with alternative implementations, the computational effort is satisfactory. This is in part due to the novel use of symmetric dyadic products of the principal directions. These enable Voigt notation to be used throughout, reducing the overall number of computations.

The proposed implementation was validated by numerical investigations of hyperelastic constitutive models that are typically defined in terms of the Cauchy-Green invariants. Evaluations were made between the proposed implementation and a conventional Cauchy-Green invariant implementation. The evaluations show that the proposed implementation is accurate and stable. Through an FE simulation, the implementations from Chapter 4 were compared to the developed principal stretch implementation and approximate tangent moduli implementations with perturbed stress tensors defined in terms of principal stretches. It was found that for Cauchy-Green invariant constitutive models, the UHYPER implementation remains the most computationally efficient method for user-defined hyperelastic behaviour in terms of Cauchy-Green invariants. For UMAT subroutines, if more complex behaviour was to be considered, the analytical implementation of Section 4.1 should be preferred for this type of constitutive model. For constitutive models implementable only in terms of principal stretches, the developed analytical implementation is numerically accurate but requires additional solve time compared with a built-in model in Abaqus/Standard. However, it is more computationally efficient than an approximation method and, more importantly, when compared to an implementation based on past approaches.

The developments in chapters 4 and 5 enable the numerical implementation of any user-defined hyperelastic constitutive model in terms of Cauchy-Green invariants, fictitious tensors or principal stretches. The associated programs and subroutines were made available within open-source data sets (205, 206), associated with the related open access publications (207, 208). Thus, all of the constitutive models used in the investigations of Chapter 3 may be implemented within the FEM. The implemented constitutive models enabled the Sufficient data investigation from Section 3.5.3 to be developed for the simulation of industrial rubber components.

Chapter 6

Simulating the Hyperelastic Behaviour of Industrial Rubber Components

It was found in Chapter 3 that accurate prediction of the general mechanical behaviour of a hyperelastic material or component requires a complete set of experimental data and a constitutive model capable of fitting the experimental data. The accuracy in fitting the complete experimental data was shown to be correlated with the ability to predict interpolated behaviour. For predictions of smaller ranges of deformation, it was proposed that it may be more efficient to identify parameters using only a sufficient set of experimental data. It was then shown that constitutive models with parameters fitted to data that encompassed the modified reduced strain regions generally gave more consistent predictions of the interpolated data. The next step was to further develop the proposed method for the analysis of industrial rubber components.

The complex structural behaviour of industrial rubber components may be studied through FEA. In Chapters 4 and 5, numerical implementations were developed to enable hyperelastic constitutive models to be used within the FEM. The approaches revolved around the use of UMAT user subroutines for the implicit FE commercial software Abaqus/Standard. For the investigations in this chapter, the thirteen constitutive models used in Chapter 3 were implemented using analytically derived elasticity tensors. When coding these subroutines, the first-order quadruple precision approximated tangent moduli programs were used for debugging and to ensure that the analytical derivatives were correct for all models. However, the analytical implementations were preferred due to their lower computational costs. Some of the constitutive models were available in the Abaqus/CAE library or could be implemented through UHYPER subroutines. However, the developed UMAT subroutines

were used throughout. This was due to the known differences in formulation, as mentioned in Section 2.5.4 (87, 183, 184, 185, 186), which may affect the simulated results. This would negatively influence the objectivity of the present investigations, as they focus on the parameter identification of constitutive models.

The proposed use of sufficient data was motivated by the desire to improve the performance of industrial rubber components by gaining insight through accurately simulating their structural behaviour. In the present chapter, the methodology developed for the simulation of industrial rubber components with sufficient experimental data is presented. The method was demonstrated for two industrial rubber components under approximated conditions in the FEM using Abaqus/Standard and UMAT subroutines. The FE models' assumptions and variables are outlined with reference to their physical implications. For full definition of the models used in these investigations, their input files are available in the dataset (4). FEA of the two components was used to investigate the consistency and differences of predicting the industrial components' structural behaviour by constitutive models with parameters identified from complete and sufficient experimental data.

6.1 Methodologies for Industrial Component Investigations

In this section the proposed method of using sufficient experimental data for accurate simulation of industrial rubber components is described. Following this the investigation methods are outlined for demonstrating the validity of predicting industrial components' structural behaviour by models fitted to complete and sufficient experimental data.

The proposed methodology for simulation with sufficient data was demonstrated by analysis of two industrial rubber components: an automotive constant velocity (CV) rubber boot and a hydraulic piston radial O-Ring seal. Industrial rubbers are often highly filled causing more complex behaviours to be present. This includes viscoelasticity, the Mullin's effect and permanent set. As discussed in Section 2.2.3, the hyperelastic behaviour represents the equilibrium response in the presence of these complexities. The two components were therefore chosen on the basis that their hyperelastic behaviour is relevant to their performance. Both components also have modes of failure caused by structural phenomena and their design is benefitted by FEA. Furthermore, the nature of their loading differs in that the CV boot is strain-loaded and the O-Ring seal is pressure-loaded. A modification of the proposed method is required depending on whether the component is only strain-loaded or if there are stress loads present.

By either method, initial prototype simulations are utilised. These apply the simple, one-parameter neo-Hookean constitutive model, as defined in equation (3.13). The purpose of the prototype simulations is to reveal a component's approximate strain range such that sufficient experimental data may be identified. The method also has a practical advantage; the neo-Hookean model provides unconditionally stable constitutive behaviour. This is particularly helpful while determining the numerous variables of the often highly nonlinear FE models for industrial rubber components. The importance of the magnitude of the neo-Hookean model's parameter is dependent on whether the component is strain-loaded or stress-loaded.

6.1.1 Sufficient Data for a Strain-loaded Component

A strain-loaded component is considered to be that which is loaded by contacting stiff bodies, often assumed to be rigid. In these cases, the strain will remain constant and the stress will relax over time until it reaches equilibrium. It was hypothesised in Section 3.5.4 that the proposed use of sufficient data for experimental hyperelastic parameter identification is particularly useful for strain-loaded materials or components. In the ideal strain-loaded case, the component could be initially simulated prior to material testing and the strain region would be revealed independently from the constitutive model input.

The proposed method is therefore to first simulate the component using the neo-Hookean constitutive model. The isochoric Cauchy-Green invariants are output by the simulation and plotted within the region of attainable deformations. With the known strain or invariant range, experiments would then be identified to extract the sufficient experimental data. These would ensure that the observed strain region is encompassed, as shown for biaxial predictions in Figure 3.18 of Section 3.5.3. The most accurate model in fitting the sufficient data, with plausibility checks if required, would then be used in FEA of the component for the accurate prediction of the component's stress and stiffness related behaviour.

6.1.2 Sufficient Data for a Stress-loaded Component

A stress-loaded component is one in which the strain will creep until it reaches equilibrium under a constant stress load. This includes force and pressure loading. For stress-loaded components, the magnitude of strain is dependent on the component's material properties; the deformation modes may also be affected by this. A variation on the proposed method was therefore required. For components loaded in this nature, it is proposed that the initial prototype simulation requires initial experimental input. This input is used to configure the single parameter of the neo-Hookean

model. Appropriate testing to configure this parameter may include any single-loading experiment (145) from Chapter 3, a hardness test (209) or an indentation test (131, 132, 145, 210, 211). With this parameter configured, the sufficient data is obtained as with strain loading: the strain region is identified, sufficient experimental data is collected and the component may be efficiently and accurately simulated using a constitutive model fitted to the sufficient data.

6.1.3 Method of Investigating the use of Sufficient Experimental Data

To investigate the validity of the sufficient data method, a study was performed similar to the general biaxial interpolations of Section 3.5.3. Material data from Chapter 3 was applied to each of the two industrial rubber components. Following the initial prototype simulations, the sufficient data set was selected from one of the reduced sets of experimental data from the case studies of Section 3.4. The components were then simulated using the thirteen constitutive models from Section 3.5, using the two sets of parameters. The complete and sufficient fitted parameters were known from the previous investigations.

For both components, the maximum principal stress, maximum principal nominal strain and force reactions from rigid bodies were observed. The principal stress and strain were chosen as they are used in fatigue life calculations (137, 212, 213, 214). The fatigue life could not be computed as this would require additional experimental data from the materials and a post-processing method or fatigue software, which were beyond the scope of the present study. As the principal stress and strain quantities consider the maximum values from a single nodal value, the force reactions were studied as they provided an insight into the components' macroscopic behaviour. The simulated deformed components were also compared visually to ensure their macroscopic behaviour was similar.

The consistency of FE results by complete and sufficient data fitted models was studied using the observed physical measures. The average output quantities of the thirteen constitutive models fitted to complete and sufficient data were compared. An error function was computed with the assumption that the most accurate fit to each of the complete or sufficient data sets represented synthetic data of the component. In addition to this, the relative standard deviation of each quantity was also computed. This gave a quantitative value for the variance of each output quantity as a percentage such that the consistency of their predictions could be compared. As a relative value, it enabled the computation of an average percentage of the variance across all observed outputs.

It is noted that both FE models used a simple representation of rubber friction. A Coulomb frictional coefficient was used throughout to model the tangential contact

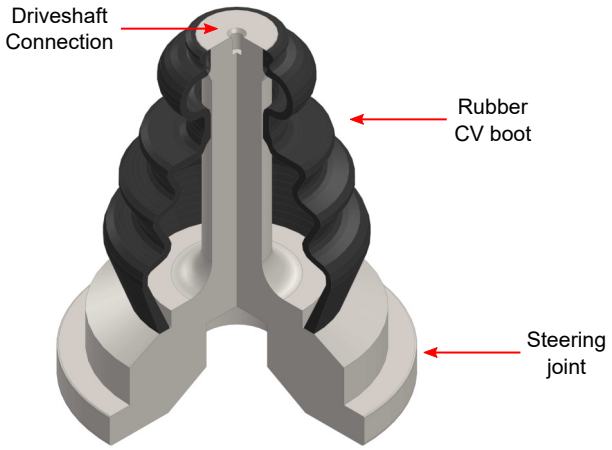

Figure 6.1: Simplified assembly of outer CV joint and rubber CV boot

behaviour. It was known that realistic modelling of rubber friction would require a more complex model or a different approach, such as multi-scale modelling (215, 216). However, this was beyond the scope of the present investigation. In both cases, the coefficient was chosen based on some trial-and-error analysis between a range of values assumed to be representative of approximate values for rubber-to-steel and rubber-to-rubber interfaces ranging from 0 to 0.6 (217). The chosen value was that which provided the most stable model in terms of numerical convergence. A coefficient of zero, which assumes fully frictionless behaviour, was found to be the least stable for both components.

6.2 Automotive Rubber CV Boot

In automotive applications, a constant-velocity (CV) axle connects the drive shaft to the steering joint of front-wheel drive vehicles to enable power transmission through a required range of steering angles. CV axles consist of a pair of CV joints, termed as inner and outer CV joints. To ensure smooth operation and prevent corrosive and erosive wear, a rubber CV boot is used, as shown in the assembly in Figure 6.1 for an outer CV joint. The CV joint is initially greased, the boot is then fitted over both ends, the drive shaft connection and the steering joint, and fastening rings are applied to each. This effectively encloses the CV joint from the surrounding environment, preventing damage by external contaminants such as dust, dirt, water and oil. Rubber is chosen for this component due to its flexibility and low stiffness. This ensures continuous protection of the joint through a wide range of motion with a negligible increase in the operating forces of the joint.

During operation, the outer CV boot is loaded by axial and bending displacement loads from the steering joint. The axial displacements are due to the suspension system and may be tensile or compressive. Angular displacements occur during

steering. Due to the nature of these loads, it was assumed that the strain region during operation would be independent of the constitutive behaviour of the material. However, upon bending of the boot during steering, both its inner and outer surfaces come into contact with themselves and the material is compressed. During these interactions, the contact forces are dependent on the material's stiffness characteristics. It was found that the small amount of compression due to self-contact did not significantly affect the component's predicted strain range. The CV boot was therefore considered to be a suitable strain-loaded component for demonstration of the method.

A correctly fitted CV boot is expected to have an operating lifespan of tens of thousands of miles (218). Towards the end of its productive lifespan, a CV boot's failure is due to ageing of the rubber. Ageing leads to embrittlement of the material which causes a loss of elasticity and fracture may occur. The ageing of natural rubber is well-understood to be accelerated by stress magnitude (219). FEA of the CV boot is therefore relevant in that areas of increased stress magnitude may be identified. From this the fatigue life may be computed and the design may be optimised to reduce the stress in these areas and increase its lifespan. It was found that the largest stresses occurred during simultaneous compression and bending of the steering joint. This loading scenario was therefore used for the investigation of the complete and sufficient experimental data simulations.

6.2.1 Finite Element Model of a CV Boot

The CV boot assembly was created in Abaqus/CAE. To simulate a representative FE model of this component, several variables required consideration. This included the geometry, displacement constraints, contact interactions and meshing. These are subsequently outlined. The material properties are discussed independently with reference to the prototype simulations in the following subsection.

The geometry for the CV boot assembly is shown in Figure 6.4a. The component was created in 3D, utilising symmetry in the out-of-plane 3 axis such that only half of the assembly was modelled. This symmetry plane was valid for the loading scenario used in this investigation. Due to the relative stiffness of the CV joint compared to the CV boot, the CV joint was reduced to a single analytical surface body. This body consists of a revolved cylinder 14mm in radius and 120mm high and a reference point representing the centre of its rotation 25mm below its base. The CV boot geometry was constructed from a two-dimensional surface created in the 1-2 plane and revolved by 180° around the 2 axis. It can be seen from Figure 6.4a that there is an initial overlap of the CV boot over the CV joint. During installation this means that the CV

boot must be stretched over the CV joint. This creates a contact pressure, preventing the entrance of external contaminants and the leakage of internal lubricant.

The boundary conditions were established using displacement constraints applied in three steps. The constraints applied to the CV boot remained constant through all three steps. In the symmetry plane of the CV boot, a symmetric boundary condition was applied to prevent movement in the 3 direction. The remaining two boundary conditions were applied using a cylindrical coordinate system defined with respect to the geometry of the CV joint. The base of the CV boot was constrained in the axial 2 direction. The bottom 5mm of the outer surface of the CV boot was constrained circumferentially, this represented a fastened connection to the steering joint. For the CV joint, displacement constraints were applied at the reference point defined previously. In the first step, the CV joint was fully fixed while contact was established. In the second step, the compressive load was applied by a 10mm axial displacement of the CV joint in the negative 2 direction. In the third step, a steering angle of 20° around the 3 axis was applied at the reference point.

As mentioned, simple Coulomb friction was used to define the tangential contact behaviour. The CV boot assembly contained three contact pairs. Due to the CV boot's smaller radius, an interference fit of the contact between the inner surface of the CV boot and the outer surface of the CV joint was solved in the first step. The remaining two contact pairs were due to self-contact of the CV boot's inner and outer surfaces. These were modelled using surface-to-surface contact, as this was found to be more computationally efficient than establishing both surfaces as "general contact" groups. For all contact pairs, a friction coefficient of 0.2 was found to be stable.

The CV boot was then meshed. As the CV joint was represented by an analytically rigid surface, it did not require meshing. The CV boot was assumed to be incompressible due to it not being highly confined. A swept mesh of C3D8H hybrid elements was applied. The number of elements was determined by a mesh sensitivity study. It was found that a mesh of 17,613 elements produced stable results. While a more refined mesh would give higher numerical accuracy, the investigations of this chapter revolved around the constitutive material behaviour using complete and sufficient data for the thirteen constitutive models.

6.2.2 Prototype Simulation of CV Boot Assembly

The prototype simulations of the CV boot required only the definition of the neo-Hookean model's isochoric parameter, C_{10}, and modification of the input file to enable a fully incompressible hybrid formulation. As the component was primarily strain-loaded, the magnitude of C_{10} was arbitrarily defined as $C_{10} = 0.16$MPa. A

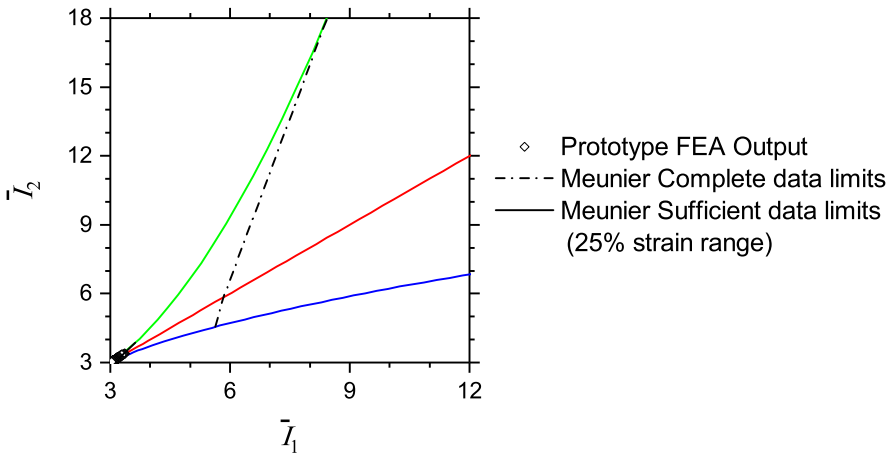

Figure 6.2: CV Boot prototype FEA invariant outputs with plotted Meunier complete and sufficient data limits

UMAT subroutine of the neo-Hookean model was created with user-defined variables to output the first and second isochoric Cauchy-Green invariants $\bar{I}_1$ and $\bar{I}_2$ as field variables. The nodal results for these were plotted on an invariant plane to view the strain region of the deformed component.

As shown in Figure 6.2, the strain range of the CV boot is comparatively small when plotted with the limits of the experimental data of Meunier et al (88). As this data set had the lowest strain range of those investigated in Chapter 3, it was chosen to represent the material of the CV boot. Based on this plotted data, the most appropriate choice for the sufficient data, from the reduced experimental data sets, was a 25% strain range of Meunier's experimental data. The component was then simulated using the most accurate fitting models to the complete and sufficient data, which were the Ogden and Haines-Wilson models respectively. The $\bar{I}_1$ and $\bar{I}_2$ outputs were plotted and compared for the prototype neo-Hookean model, the Ogden complete data fitted model and the Haines-Wilson sufficient data fitted models, shown in respective order in Figures 6.3a, 6.3b and 6.3c. These show that most output values are contained within the interpolated limits of the 25% Meunier data and this is therefore an appropriate choice of sufficient experimental data.

The plotted invariants revealed that the strain region for all input data variations remains similar and appears to be independent of the constitutive model input. This was assessed further by comparison of their maximum principal nominal strains. The deformed FE models with contours for this output are shown for the CV boot with the prototype, complete data and sufficient data input in Figures 6.4c, 6.4d and 6.4e, respectively. The maximum principal nominal strain for the prototype simulation was computed as 0.333. The average value of the maximum principal nominal strain for the thirteen constitutive models fitted to complete data was also computed as 0.333. For the sufficient data fitted models this was computed as 0.344. It could therefore

be assumed that the strain region of this component may be accurately predicted by a prototype simulation.

To ensure that the validity was not the result of an appropriately chosen value for the neo-Hookean C_{10} parameter, the maximum principal stresses were observed. The prototype simulation computed a maximum principal stress of 2.508MPa, the average value for the complete fitted models was 2.710MPa and for the sufficient fitted models was 2.715MPa. As the prototype simulation stress value was somewhat similar, the prototype simulation was repeated with the parameter $C_{10} = 160$MPa. The maximum principal stress in the repeated simulation was computed as 250.735MPa, while the maximum principal nominal strain remained very similar to previous, it was computed as 0.331. The use of strain-loaded prototype simulations was therefore shown to be valid for this component.

6.2.3 Complete and Sufficient Data Predictions of CV Boot

The CV boot was simulated with the thirteen constitutive models fitted to complete and sufficient experimental data. The numerical results of the maximum principal stress, maximum principal nominal strain, force reaction in the 1 direction and force reaction in the 2 direction are given in Tables D.1 and D.2. The results are presented in order of the constitutive models' error in fitting the prescribed complete or sufficient experimental data. The average values and standard deviation (SD) were then computed, from which the relative standard deviation (RSD) was found. Additionally, average errors were computed with respect to the most accurate model for each data set, using equation (3.33).

The average values for the maximum principal stress and maximum principal nominal strain have already been stated. These were found to be similar for the complete data and sufficient data fitted models. The average stress was predicted within a 0.19% difference and the average strain was within 3.25%. The average force reaction in the 1 direction and 2 directions were also found to be similar, 5.79N and -3.57N for the complete data fitted models and 5.82N and -3.62N for the sufficient data fitted models, respectively. This is a difference of less than 0.52% for the 1 direction and 1.40% for the 2 direction.

The error across all measured values was low; with the highest error computed as 5.13% for the maximum principal nominal strain with the Diani and Rey model fitted to complete data. The average error was computed with respect to the most accurate model for each data set. On average it was found that the percentage error was lower for the sufficient data fitted models than the complete data fitted models, 0.98% compared with 1.22%. In terms of the computed RSD, the variance for models fitted to either of the input experimental data sets was low. The sufficient data fitted models

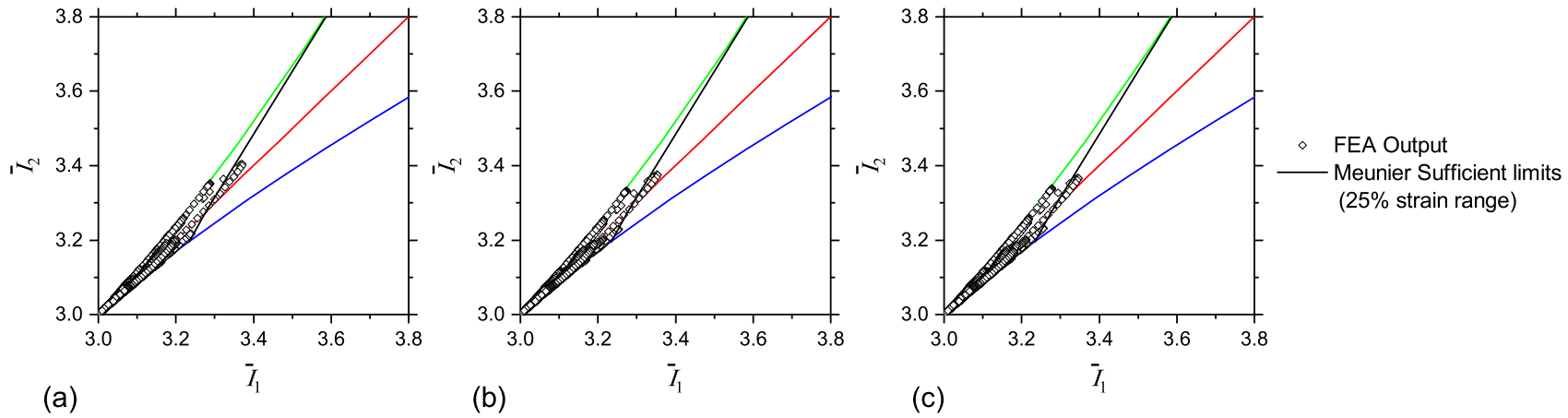

Figure 6.3: Invariant FEA outputs for CV Boot with (a) the prototype neo-Hookean model, (b) the Ogden model fitted to complete experimental data and (c) the Haines-Wilson model fitted to sufficient experimental data

were found to have a lower average variance, 1.21% compared with 1.48% of the complete data fitted models.

6.2.4 Discussion of Strain-loaded CV Boot Results

Across all simulated results using the complete and sufficient data fitted models, the observed outputs were found to be similar. The low statistical variance within each data variation showed that the CV boot's behaviour may be predicted with high consistency, with an RSD of less than 1.25%. These results are in agreement with the biaxial study of Section 3.5.3. These suggest that the use of sufficient data gives a more reliable prediction than fitting to a larger complete experimental data set. The method of attaining the sufficient data strain region by prototype simulation was shown to be effective for a strain-loaded component. Only a small difference was found in their computed isochoric Cauchy-Green invariants between the prototype simulation and the complete and sufficient data fitted simulations. This method was therefore assumed to be valid for strain-loaded components under the present assumptions.

6.3 Hydraulic Cylinder: Radial O-ring Seal

A common application of rubber in engineering components is for the purpose of fluid sealing. An application where rubber seals are applied is in hydraulic cylinders. A hydraulic cylinder is a linear actuation device used to apply a pushing or pulling force. In its simplest form, the device consists of a piston and a cylinder. The piston is inserted into the cylinder, sealing one or two fluid chambers. Either one or both sides of the piston may be pressurised, and often also depressurised. A linear force is created by the pressurised and expanding fluid volume. To achieve this force, the pressurised fluid medium must maintain a complete seal of the fluid chamber. Hydraulic cylinders require multiple seals to prevent fluid leakage.

A rubber O-Ring seal within a single acting hydraulic cylinder was studied. A simplified model of the hydraulic cylinder assembly is shown in Figure 6.5. The chosen design used a two-part piston, consisting of a piston-rod and piston-head, in which an O-Ring is installed radially to prevent leakage. Prior to assembling the two-part piston, the radial O-Ring seal is lubricated and installed into a gland in the piston-rod's outer surface. The diameter of this gland should be larger than the inner diameter of the O-Ring. This initial "stretch" phase induces a hoop stress in the O-Ring to provide a sealing pressure at the O-Ring and piston-rod interface. The piston-head is then installed over the tapered and threaded end of the piston-rod. The inner diameter of the piston-head must be larger than the outer diameter of the piston-rod

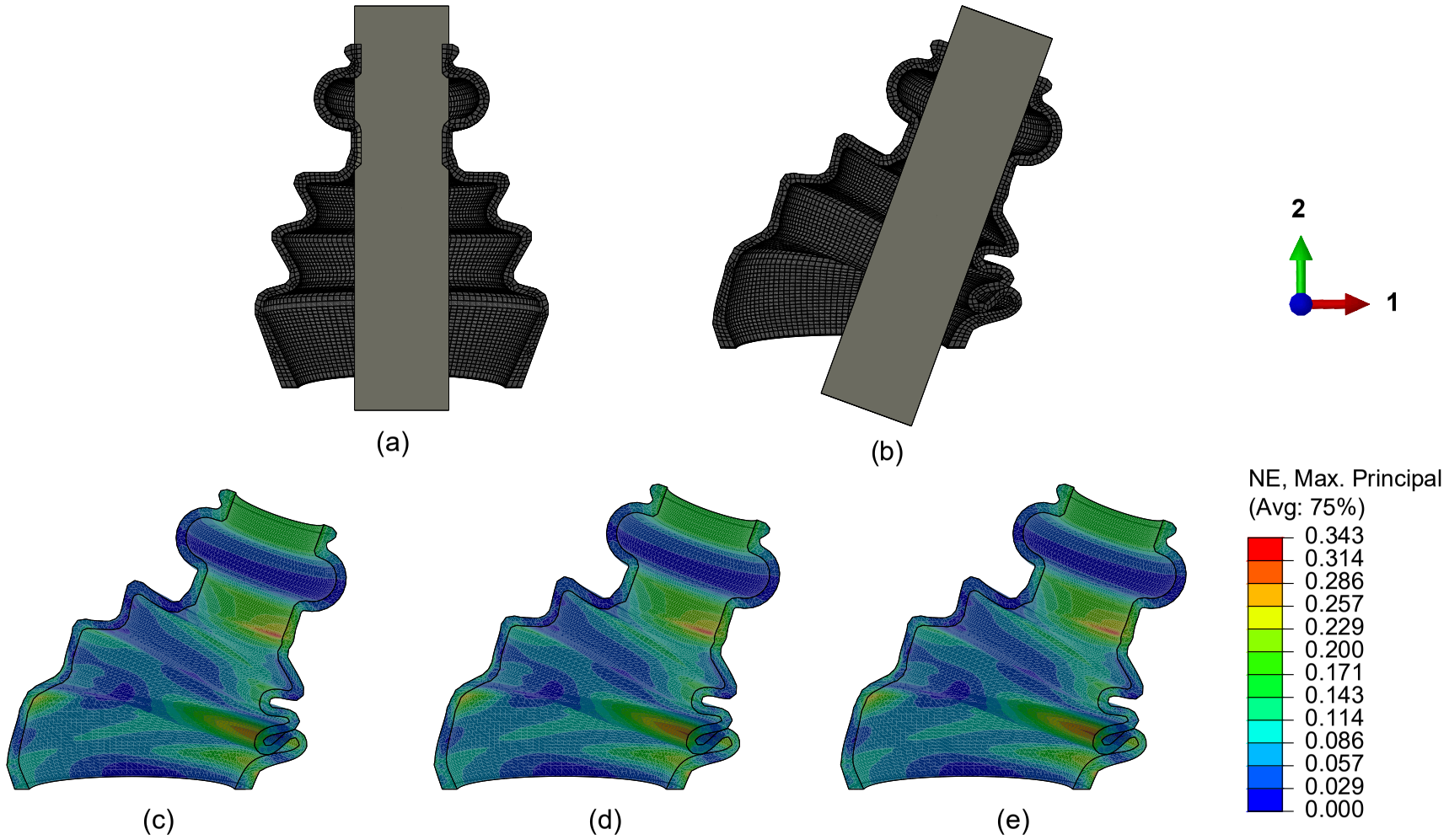

Figure 6.4: Finite Element model for a simplified automotive outer CV joint assembly (a) undeformed meshed assembly and (b) deformed meshed assembly. Deformed maximum principal nominal strain plots for (c) the prototype neo-Hookean model, (d) the Ogden model fitted to complete experimental data and (e) the Haines-Wilson model fitted to sufficient experimental data

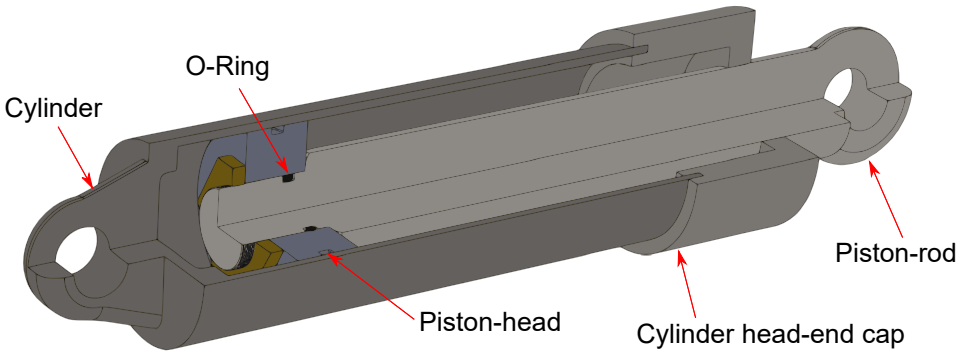

Figure 6.5: Simplified and sectioned assembly of hydraulic cylinder with static radial O-ring seal

to allow clearance during assembly. To prevent fluid leakage through this clearance gap, the O-Ring cross-sectional diameter must be larger than the gland depth. The installation of the piston-head therefore induces radial compressive stress of the O-Ring's cross-section. During assembly of the cylinder, this "squeeze" phase creates a sealing pressure between the O-Ring and the piston-head while further increasing the sealing pressure between the O-Ring and the piston-rod.

The clearance gap between the piston-head and piston-rod is required such that these parts may be assembled without damage. However, once the system is pressurised, the O-Ring may extrude into the clearance gap. As the O-Ring extrudes into the small clearance gap, a large stress concentration occurs at the corner of the gland closest to the gap. For this reason, a small fillet radius is applied at the corner of the gland to reduce this stress. Excessive pressure or incorrect design may still lead to extrusion damage, known as fretting (220). This damage may cause leakage, or in the worst case scenario the seal may fail catastrophically. In the event of the hydraulic cylinder O-Ring's failure, the pressurised fluid would leak into the opposing end and cause pressure loss and loss of function. To replace this O-Ring, disassembly of the cylinder and two-piece piston is required.

Industry guides for O-Ring selection (221) can provide reliable recommendations for the appropriate O-Ring material and dimensions for standardised component geometries. For these components, FEA of the assembled O-Ring provides confidence and additional insights into the design. For non-standard geometries, the use of FEA or a similar design tool is essential. In either case, FEA can be used to predict the amount of extrusion that will occur under operating pressures and surging pressures. As previous, the stresses and strains may also be observed for the computation of fatigue life. These results could then be used to determine if the seal is fit for purpose or if the design could be improved. These engineering design decisions rely on accurate modelling of the O-Ring's constitutive behaviour.

6.3.1 Finite Element Model of Static Radial O-ring Seal Assembly

The piston-rod and piston-head move relative to one another during operation. The O-Ring seal assembly was therefore assumed to be static and the equilibrium hyperelastic behaviour of the industrial rubber would appropriately represent the constitutive material behaviour. The geometry of the radial O-Ring allows reduction to a 2D axisymmetric model, created in Abaqus/CAE. As previous, the FE variables are described prior to the prototype simulation and sufficient data investigation.

The chosen geometry for the hydraulic piston assembly is shown in Figure 6.5. The dimensions of the assembly revolved around the recommended dimensions for an O-Ring with a 5.33mm cross-sectional diameter fitted to a standardised piston bore diameter of 40.25mm, using Parker's O-Ring Handbook (221). The recommended O-Ring size for this piston has an inner diameter of 32.69mm. The gland depth was 4.02mm, which gives a diameter for the gland of 33.81mm. These dimensions determine the initial amount of stretch of the O-Ring, which is computed by the following

$$Stretch\,(\%) = \left(\frac{d_{gland}}{d_{O-Ring}} - 1\right) \times 100 \tag{6.1}$$

From this it was found that the O-Ring's stretch is around 3.43%, which lies in the typical range from 0-6%. Based on these established dimensions, the maximum amount of squeeze of the O-Ring cross-section may be computed by the equation

$$Squeeze\,(\%) = \left[1 - \left(\frac{d_{bore} - d_{gland}}{2CS_{O-Ring}}\right)\right] \times 100 \tag{6.2}$$

This gives a maximum squeeze of approximately 24.58%. However, a clearance is required between the piston-rod and piston-head during installation to avoid damage to either of these surfaces. The inner diameter for the piston head was chosen to give a 20% squeeze of the O-Ring cross-section. This lies in the recommended range of squeeze of 12-28%. Assuming that the stretch during installation causes a negligible difference to the O-Ring cross-section, equation (6.2) was used to compute the piston-head inner diameter as 42.339mm. During assembly, the piston-head slides over the O-Ring, inducing the compressive force. To avoid damage to the O-Ring during sliding, the leading edge of the piston-head should be chamfered to $15 - 20^{\circ}$; a chamfer of 20° was used.

The remaining dimensions to be defined are that of the O-Ring seal gland. The width of a gland is designed based on the desired percentage amount of "fill", recommended between 60-90%. From a 2D axisymmetric view, the fill is computed as a

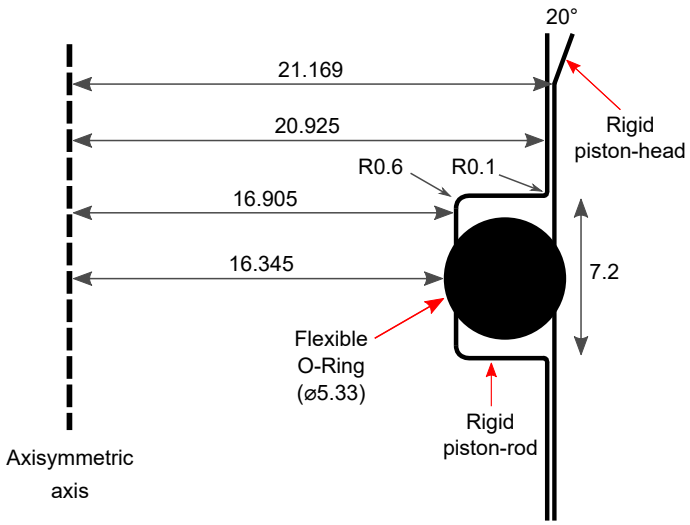

Figure 6.6: Radial O-Ring and piston geometry (dimensions in millimetres)

ratio of the cross-sectional area of the O-Ring and the gland area including the clearance gap. Neglecting the area of the gland's filleted radii, a gland width of 7.2mm was chosen, which gives a fill of approximately 72.68%. The inner fillet radius of the gland was chosen as 0.6mm based on the Parker O-Ring Handbook (221) for this geometry. A fillet radius of 0.1mm was applied to the corners of the clearance interface to reduce stress concentrations during extrusion.

The O-Ring FE model established boundary conditions over three steps. These were representative of the stages in assembling the O-Ring seal and its operating conditions. In all three steps, the piston-rod was assumed to be fully fixed and the O-Ring was unconstrained in terms of applied displacements. The first step simulated the "stretch" of the O-Ring over the gland. This involved solving the interference fit of the contact between the O-Ring and the piston-rod's outer surface. In the second step, the "squeeze" was applied by installation of the chamfered piston-head with a displacement in the positive 2 direction. The piston-head was otherwise fully constrained. In the third step, pressure was applied to the O-Ring through a "pressure penetration" boundary condition available in Abaqus/CAE. This boundary condition applies a normal pressure across an existing contact group in all locations that are not considered to be in closed contact (72). The pressure was initiated in the centre of the exposed surface of the O-Ring and propagated bi-directionally until the elements that were in contact with the piston-head and piston-rod. It was therefore considered to be a reasonable approximation of fluid pressure, avoiding the complexity of modelling the fluid itself (222). The pressure magnitude was chosen as 2.5 MPa. For the chosen material, this magnitude allowed for stable convergence and did not produce excessive element distortion in the extruded region.

Three contact groups were created; two contact groups simulated the connection be-

tween the O-Ring and the two piston surfaces, the third contact group applied the pressure penetration. A contact group was created between all outer surfaces of the piston-rod and select outer surfaces of the partitioned O-Ring. The partitions were required as this contact was used to initiate the pressure penetration boundary condition, which does not allow closed-loop contact surfaces. A break in the outer surface of the O-Ring was therefore created in a location that could not come into contact with the piston-rod throughout the analysis. In the first step, this contact group solved the initial interference fit of these bodies, with standard Coulomb frictional contact behaviour continued in the second and third steps. The second contact group was created with Coulomb friction between the inner surfaces of the piston-head and the outer surfaces of the O-Ring. For these two groups, a Coulomb friction coefficient of 0.3 was found to give stable convergence and was used throughout. The third contact group was activated in the third step to apply fluid pressure. A central point on the surface of the O-Ring was selected as an initiation point. The pressure was ramped up linearly throughout the load step. This allowed for the location of the pressure to update with the changing contact status at higher pressures.

For a highly confined component, such as the O-Ring in the current investigation, the effect of compressibility should be considered. As well as improving the prediction of the true material behaviour, including a small amount of compressibility improves the numerical stability and convergence for highly confined FE models of nearly incompressible components. The thirteen constitutive models were therefore considered to be the isochoric contributions of the overall strain energy by using an isochoric-volumetric split, as defined in equation (4.1). A one parameter volumetric constitutive model was included for all constitutive models. This was defined as

$$U = \frac{1}{D_1}(J-1)^2 \tag{6.3}$$

As no material data for the compressibility of the materials was known, the chosen magnitude for the compressibility parameter, D_1, was that which provided stable convergence with negligible total change in the volume of the body. To check this, the volume ratio J of each element was output by a user-defined variable in the UMAT subroutine. The chosen value was $D_1 = 0.001\text{MPa}^{-1}$. This was the most stable in terms of convergence and was found to have a maximum dilatational change in volume of 0.08% and a minimum change of -0.35%.

The piston-head and piston-rod were assumed to be rigid in comparison with the O-Ring seal. They were therefore each represented as 2D analytical rigid line bodies with an assigned reference point and did not require meshing. The O-Ring was modelled as nearly incompressible using axisymmetric CAX4H hybrid elements. As the component was not modelled as fully incompressible, the solver formulation was

not updated to a fully incompressible hybrid formulation. The inclusion of a small amount of compressibility may therefore be seen as a penalty parameter (223). In terms of the mesh density, the partitioning of the O-Ring allowed higher refinement at the surface of the O-Ring, with further refinement of the extruding elements. A lower mesh density was applied to the centre of the O-Ring. A mesh of 13374 elements was found to be stable in terms of numerical convergence and it was assumed to be accurate in terms of mesh sensitivity.

6.3.2 Prototype Simulation of Radial O-Ring Seal

As a stress-loaded component, the prototype simulation of the O-Ring seal required the initial selection of a material. The experimental data of Heuillet and Dugautier (193) from Chapter 3 was selected to represent the O-Ring material. The neo-Hookean C_{10} parameter was then approximately fitted manually to the uniaxial tension data for the H&D material. This test was chosen as tensile testing of a cut ring specimen is simple to perform and well-defined in tensile testing standards for rubber, BS ISO 37 (104) and ASTM D412-16 (105). A value of $C_{10} = 0.21$MPa fitted the low strain range for this material and was therefore used in the prototype simulation. The UMAT subroutine for the neo-Hookean model was modified to include the volumetric behaviour defined in equation (6.3); a value of $D_1 = 0.001\text{MPa}^{-1}$ was used throughout.

The prototype simulation of the O-Ring was solved with $\overline{I}_1$ and $\overline{I}_2$ outputs. These were plotted on the invariant plane with the interpolated limits of the H&D complete experimental data. As shown in Figure 6.7, the strain range of the O-Ring is much lower than that of the complete H&D experimental data. The highest range of deformation of the plotted $\overline{I}_1$ and $\overline{I}_2$ values were found to lie close to the pure shear line. From the reduced data of the Case Studies in Section 3.4, it was determined that the most appropriate choice of sufficient experimental data was a 50% strain range. For the initial prototype simulation, it was found that the chosen sufficient data fully encompassed the prototype $\overline{I}_1$ and $\overline{I}_2$ values.

The model was then solved using the thirteen constitutive models with parameters fitted to the complete and sufficient experimental data. The output $\overline{I}_1$ and $\overline{I}_2$ values were plotted for the best fitting models to the complete and sufficient data, which were the micro-sphere and Alexander models. This is shown with the prototype outputs in Figure 6.8. It was found that the models fitted accurately to the complete and sufficient data similarly predicted the O-Ring's strain region. The output maximum $\overline{I}_1$ and $\overline{I}_2$ points were found to be lower for the complete and sufficient data compared with the prototype simulation. This was due to the neo-Hookean model with $C_{10} = 0.21$MPa predicting a softer response for planar tension at moderate strains.

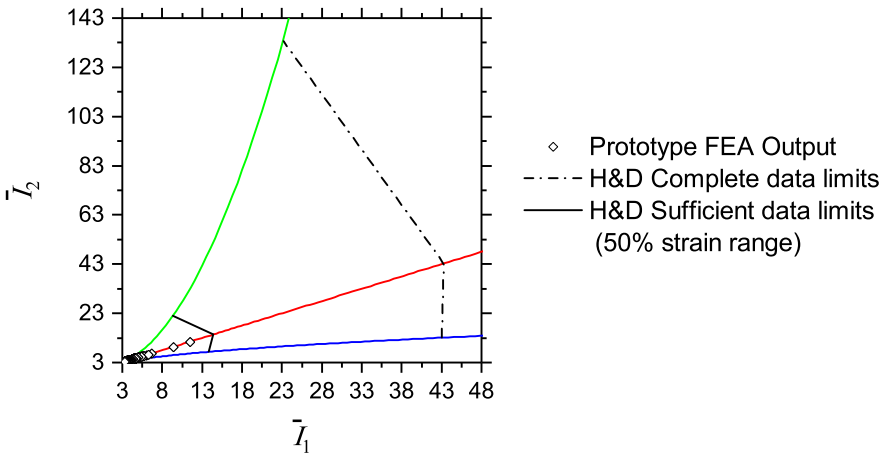

Figure 6.7: O-Ring prototype FEA invariant outputs with H&D complete and sufficient data

However, their predicted strain regions are generally similar and encompassed by the interpolated strain range limits of the chosen sufficient data.

Comparing the deformed and contoured results for the maximum principal nominal strains of the O-Rings further demonstrates the macroscopic similarity of the prototype simulation to the complete and sufficient data fitted simulations, as shown in Figures 6.9a, 6.9b and 6.9c. In terms of their output maximum principal values, the differences are more significant. The prototype simulation had a maximum principal nominal strain of 2.285, whereas the complete data fitted micro-sphere model computed a value of 1.768 and the sufficient data fitted Alexander model computed a value of 1.724. In terms of the maximum principal stress, the prototype model computed a value of 2.358MPa, the complete fit stress was computed as 1.626MPa and the sufficient fit computed a value of 1.524MPa. Overall, these results demonstrate that the modified prototype simulation provides a good approximation of the strain range. It may therefore be used to obtain sufficient experimental data.

6.3.3 Complete and Sufficient Data Predictions of an O-Ring Seal

The O-Ring simulations were investigated on a nodal level by comparison of their maximum principal stresses and nominal strains and on a macroscopic level by their force reactions in the 1 and 2 directions. An extruded length was also considered. This was manually measured as the furthest point in the 2 direction from the upper surface of the gland to the outermost point of the O-Ring. These results are given in Tables D.3 and D.4 in order of the constitutive models' error in fitting their fitted experimental data.

The measured values for complete and sufficient data fitted models were generally found to be predicted consistently. The average maximum principal stresses for the

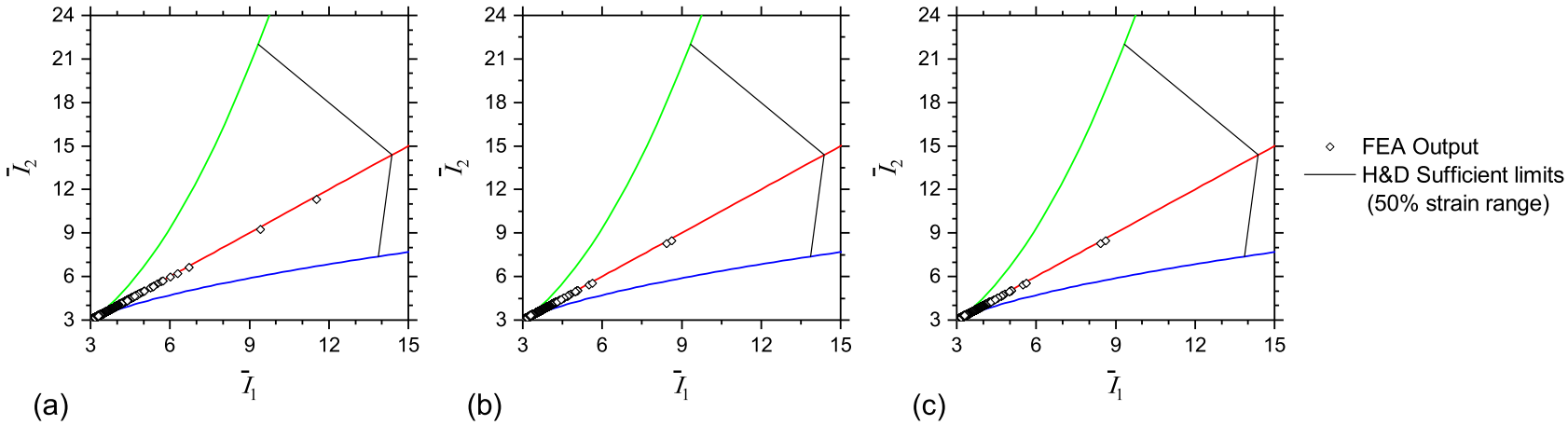

Figure 6.8: Invariant FEA outputs for O-Ring with (a) the prototype neo-Hookean model, (b) the micro-sphere model fitted to complete experimental data and (c) the Alexander model fitted to sufficient experimental data

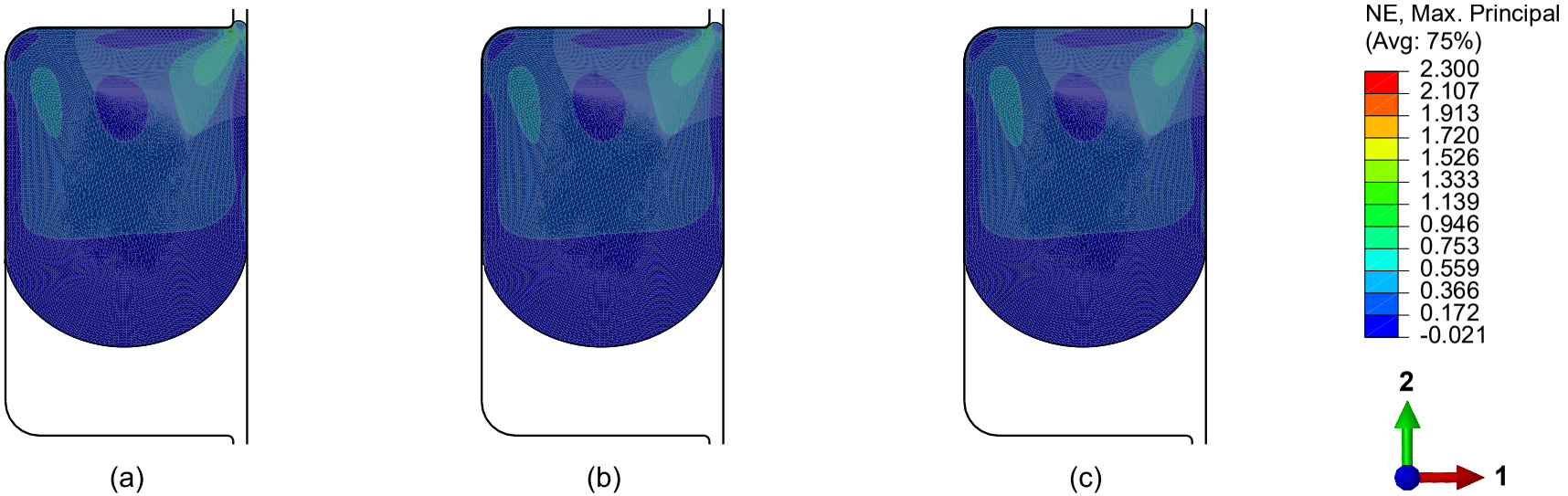

Figure 6.9: Deformed maximum principal nominal strain plots for a Finite Element model of a hydraulic cylinder radial O-Ring seal with (a) the prototype neo-Hookean model, (b) the micro-sphere model fitted to complete experimental data and (c) the Alexander model fitted to sufficient experimental data

complete and sufficient data fitted models were computed as 1.58MPa and 1.52MPa, which is a difference of 3.48%. The average maximum principal nominal strains were both approximately found as 1.78, with a percentage difference of 0.14% between their exact values. The force reactions in the 1 and 2 directions were also very similar; for the complete data these were computed as 1249.36N and -1274.73N, and 1253.37N and -1275.53N for the sufficient data. This gives a percentage difference of only 0.32% and 0.06% for the average force reactions in the 1 and 2 directions. The average extrusion amount had the largest difference between complete and sufficient data fitted models' predictions of 4.12%. The extrusion for the complete data fitted models was computed as $10.06\text{E}{-2}$mm and for the sufficient fitted models it was predicted as $9.65\text{E}{-2}$mm.

In terms of the overall averages, it was found that the complete data fitted models had a lower average error but the sufficient data gave the lower average RSD. In both cases, the error and relative standard deviation are small values. The overall average errors were computed as 1.83% for the complete data fitted models and 2.26% for the sufficient data fitted models. The average RSD was computed as 2.29% for the complete data fitted models 1.92% for the sufficient data fitted models.

6.3.4 Discussion of Stress-loaded Radial O-Ring Seal Results

It was found that the predicted strain range with the fitted neo-Hookean parameter was similar to that of the complete and sufficient data fitted models. To account for the differences in the prototype data, it is recommended that the encompassing boundaries of sufficient data should be extended. The low variance of all observed outputs further confirms the ability to consistently predict interpolated behaviour between single-loading experiments. Using sufficient data was found again to provide more consistent predictions of an industrial rubber component's structural behaviour.

The modified method for finding the strain region by prototype simulation of stress-loaded components was implied to be valid. The requirement of initial experimental input means that the approach is less time and resource efficient than with strain-loaded components. However, for a stress-loaded component, the initial prototype simulations may reveal that the chosen material is not appropriate for the application based on the simulation with minimal input experimental data. For instance, a chosen O-Ring material may be found to extrude excessively under the design pressure. The design may then require consideration of one or more backup rings (221) or the use of a stiffer material. The proposed method can therefore be more economical, as complete material testing would not be required for each possible material or design.

6.4 Summary of Industrial Component Investigations

Based on the conclusion from Chapter 3, the hyperelastic behaviour of two industrial rubber components was studied with the aim of demonstrating the use of sufficient experimental data for parameter identification in a practical context. The developed implementations of Chapters 4 and 5 allowed the thirteen constitutive models to be utilised for FEA of the industrial components. The use of sufficient data was developed into an approach of using prototype simulations. This was demonstrated to effectively reveal the approximate strain range of the studied components. In both cases, the rubber components deformed inhomogeneously such that predicting their behaviour requires the input of experimental data from across the invariant plane. In practice, the use of prototype simulations may be affected by frictional behaviour if candidate materials for a component are diverse in this regard. In this case, frictional experimental data would be required along with a more accurate numerical model for rubber friction.

The results of this chapter extend the earlier conclusion, that predictions encompassed within a fitted strain range are consistent, to the case of predicting rubber industrial components' hyperelastic behaviour by FEA. It has been shown that the hyperelastic behaviour of industrial rubber components may be consistently predicted by FEA with hyperelastic constitutive models fitted to complete and sufficient experimental data. The predictions by sufficient data were found to have lower variance for two investigated industrial rubber components. This was computed in terms of relative standard deviation using FE computed values of interest for engineering design of rubber components and force reactions to ensure consistent macroscopic behaviour.

Though the average error for the complete data was found to be lower in the case of the O-Ring simulation, the RSD value was lower for both components. As the strain range of the simulated components do not output evenly distributed points, the ability to predict these results is less correlated with the error in fitting the experimental data. The RSD value was therefore considered to the more meaningful result. This value provides a measure of the statistical variance of predictions from the fitted constitutive models independent of the fitted data error. Therefore, a lower RSD value computed for the sufficient data fitted models implies that inhomogeneous predictions are predicted with higher consistency by this input data.

Chapter 7

Conclusions

This thesis and the associated research aimed to contribute to the understanding of the numerical modelling of rubber hyperelasticity. This focused on homogeneous experimental parameter identification for hyperelastic constitutive models, implementations of hyperelasticity in the FEM and simulating the hyperelastic behaviour of industrial rubber components. Contributions were made to each of these three areas. The contributions are presented by summarising the findings from each research chapter.

Chapter 2. The isothermal behaviour of rubber was discussed with a review of the equilibrium hyperelastic behaviour. The complete hyperelastic response was identified to consist of three behaviours, a low strain decrease in stiffness, an asymptotic finite extensibility and a distinct deformation state dependence. Hyperelastic constitutive modelling approaches were discussed. The selection of constitutive models and the extent of experimental data to identify their parameters were discussed and suspected to affect one another. Postulates and criteria to ensure the physical plausibility of constitutive models and their identified parameters were outlined. Studies of inhomogeneous parameter identification methods in the FEM revealed that parameters may be identified using only sufficient experimental data. To enable the use of most known hyperelastic constitutive models in the FEM, numerical implementations of hyperelasticity were reviewed in terms of analytically derived hyperelasticity and alternative numerical implementation methods.

Chapter 3. Homogeneous parameter identification of hyperelastic constitutive models were studied. Postulates were proposed to ensure the physical behaviour of homogeneous experimental data and their validity was demonstrated by case studies of published data sets. With physically plausible experimental data and a developed parameter identification method, parameter identification of hyperelastic constitutive models by single loading experiments was studied. It was found that no constitutive model has a general ability to predict behaviour outside of the experimentally

measured strain range. The prediction of the general hyperelastic behaviour requires complete experimental data and a constitutive model capable of fitting this behaviour. Through investigations of synthetic general biaxial experiments, the accuracy of fitting a complete set of single loading experimental data was found to be correlated with the consistency of interpolated predictions. This implies validity of the use of a complete set of single loading experiments. This consists of at least uniaxial tension and equibiaxial tension, or equivalent experiments. The inclusion of pure shear data improves the accuracy of interpolated predictions. Smaller strain ranges were found to be more accurately predicted by parameters identified using only sufficient experimental data. The sufficient experimental data consists of single loading experiments that encompass the interpolated strain region.

Chapter 4. In this chapter, UMAT and UHYPER user subroutines were initially developed and compared to a built-in model for hyperelasticity in terms of Cauchy-Green invariants. Two variations of the UMAT implementation were investigated. The fully derived implementation was more computationally efficient but the matrix method allows models defined in terms of fictitious stress and elasticity tensors. With validated UMAT implementations, two complimentary real-domain numerical approximation methods were developed, using higher floating-point precision and higher-orders of approximation. It was found that as the order of approximation increased, the numerical error tended towards a limit greater than the tolerance for floating-point precision. The numerical accuracy of all orders of quadruple floating-point precision approximation was found to be greater than analytical terms in double precision. However, quadruple precision approximations have higher computational costs, with a minimum of double the computation time compared with an analytical implementation. Implementation of analytically derived tangent moduli should therefore be preferred unless they are intractable.

Chapter 5. Analytical implementations were developed for hyperelasticity in terms of principal stretches. These used explicitly derived stress and elasticity tensors and utilised current algorithms to compute the necessary eigenvalues and eigenvectors. When principal stretches were equal or similar, an algorithm was developed to employ L'Hôpital's rule and avoid numerical instability. Implementations were validated by expressing Cauchy-Green invariant models in terms of principal stretches, a simple and novel approach. The developed implementations were demonstrated to be highly accurate, including when principal stretches were equal or similar. This enabled a comparison of all developed implementations and a previous implementation of principal stretch hyperelasticity. The developed implementation had higher computational costs than Cauchy-Green invariant constitutive models, however, it was more efficient than the alternative implementation.

Chapter 6. Methodologies were developed for efficient simulation of the hyperelastic behaviour of industrial rubber components. The approach considered the use of constitutive models with parameters identified using only sufficient experimental data. Prototype simulations were used effectively to determine the expected strain region of the component. The simulation methodology was adapted to ensure the method of obtaining sufficient experimental data was effective for both strain-loaded and stress-loaded components. Through simulation of two industrial rubber components, the method was demonstrated to predict their hyperelastic behaviour with improved consistency when compared with predictions by constitutive models with parameters identified using complete experimental data.

Recommendations for Future Work

The research presented here contributes to the understanding of numerical modelling of the behaviour of rubber in terms of hyperelasticity. The conclusions drawn from the use of physically plausible experimental data in Chapter 3 are generally considered to be validated. An exception to this is the use of synthetic general biaxial interpolated data. Though using synthetic data for these removed the influence of experimental errors, experimental validation with a biaxial experiment would further strengthen the conclusions regarding interpolated predictions by single loading experiments.

The extent of experimental data to characterise the complete hyperelastic behaviour is now better understood in terms of using homogeneous data. This could be developed for inhomogeneous parameter identification methods. Component-oriented parameter identification achieves this to some degree. However, complex geometries and loading conditions are not feasible. Using the strain region identified from prototype simulations, the suggested method would use the specimen geometry and apply easily attained experimental boundary conditions to provide data that encompasses the expected deformations. The extension of this simulation methodology and the existing methods proposed in Chapter 6 should also be validated experimentally.

Another extension of this work is to consider the more complex behaviours of rubber. As in the study of homogeneous parameter identification methods for hyperelasticity, this would require some consideration of the use of sufficient data. For example, viscoelastic behaviour has an almost infinite experiment range, restricted by the maximum applied strain rates. With a parameter identification procedure for more complex models, the development of open-source user subroutines considering one or more of the complex behaviours would be a valuable contribution. The simulation methodology using sufficient data for simulation of the complex behaviour of rubber industrial components could also be further developed.

List of References

[1] J. T. Bauman. *Fatigue, Stress, and Strain of Rubber Components*. Carl Hanser Verlag GmbH & Co. KG, München, 2008. 1

[2] A. N. Gent. *Engineering with Rubber*. Carl Hanser Verlag GmbH & Co. KG, 2012. 1, 7, 8, 10, 11, 46

[3] Dassault Systemes. *Abaqus 2016 Documentation*. Dassault Systemes Simulia Corporation, 2016. 2, 27, 79, 87, 89

[4] S. J. Connolly and D. Mackenzie. **Data for: Numerical modelling of rubber hyperelasticity: parameter identification and finite element implementations**, 2020. 2, 57, 72, 87, 93, 100, 106, 117, 120, 122, 128, 131, 136

[5] G. A. Holzapfel. *Nonlinear Solid Mechanics: A Continuum Approach for Engineering*. Wiley & Sons, Ltd., Chichester, UK, 2000. 4, 13, 28, 29, 54, 81, 82, 84, 94, 115, 116, 118

[6] P. J. Flory. **Thermodynamic relations for high elastic materials**. *Transactions of the Faraday Society*, **57**:829–838, 1961. 6, 13, 81, 114

[7] L. R. G. Treloar. *The Physics of Rubber Elasticity (Third Edition)*. Oxford University Press, third edition edition, 1975. 7, 8, 9, 11, 14, 15, 16, 18, 22, 25

[8] Z. Fei, B. Weina, and Z. Shugao. **Influence of Crosslink Density on Mechanical Properties of Natural Rubber Vulcanizates**. *Journal of Macromolecular Science, Part B*, **50**(7):1460–1469, 2011. 7

[9] K. Roy, S. C. Debnath, and P. Potiyaraj. **A critical review on the utilization of various reinforcement modifiers in filled rubber composites**. *Journal of Elastomers and Plastics*, **52**(2):167–193, 2020. 7

[10] B. Meissner and L. Matějka. **A Langevin-elasticity-theory-based constitutive equation for rubberlike networks and its comparison with biaxial stress–strain data. Part I**. *Polymer*, **44**(16):4599–4610, 2003. 7, 8, 17, 18, 70

[11] C. Miehe, S. Göktepe, and F. Lulei. **A micro-macro approach to rubber-like materials-Part I: the non-affine micro-sphere model of rubber elasticity**. *Journal of the Mechanics and Physics of Solids*, **52**(11):2617–2660, 2004. 7, 8, 14, 18, 26, 28, 52, 54, 55, 81, 92, 177

[12] J. D. Davidson and N. C. Goulbourne. **A nonaffine network model for elastomers undergoing finite deformations**. *Journal of the Mechanics and Physics of Solids*, **61**(8):1784–1797, 2013. 7, 16, 17

[13] M. R. Mansouri and H. Darijani. **Constitutive modeling of isotropic hyperelastic materials in an exponential framework using a self-contained approach**. *International Journal of Solids and Structures*, **51**(25-26):4316–4326, 2014. 7, 17

[14] Y. Xiang, D. Zhong, P. Wang, G. Mao, H. Yu, and S. Qu. **A general constitutive model of soft elastomers**. *Journal of the Mechanics and Physics of Solids*, **117**:110–122, 2018. 7, 16, 17

[15] E. M. Arruda and M. C. Boyce. **A three-dimensional constitutive model for the large stretch behavior of rubber elastic materials**. *Journal of the Mechanics and Physics of Solids*, **41**(2):389–412, 1993. 7, 8, 16, 18, 39, 70

[16] M. M. Attard and G. W. Hunt. **Hyperelastic constitutive modeling under finite strain**. *International Journal of Solids and Structures*, **41**(18-19):5327–5350, 2004. 7, 15, 45

[17] P. Flory. **Molecular Theory of Rubber Elasticity**. *Polymer Journal*, **17**:1–12, 1985. 8

[18] A. N. Gent. **A New Constitutive Relation for Rubber**. *Rubber Chemistry and Technology*, **69**(1):59–61, 1996. 8, 15, 16, 39, 99, 125

[19] R. W. Ogden. *Non-linear elastic deformations*. Dover Publications, 1997. 8, 14, 29, 113, 115, 116

[20] A. Elías-Zúñiga. **A non-Gaussian network model for rubber elasticity**. *Polymer*, **47**(3):907–914, 2006. 8

[21] S. F. Edwards and T. A. Vilgis. **The effect of entanglements in rubber elasticity**. *Polymer*, **27**(4):483–492, 1986. 8

[22] M. Kaliske and G. Heinrich. **An Extended Tube-Model for Rubber Elasticity: Statistical-Mechanical Theory and Finite Element Implementation**. *Rubber Chemistry and Technology*, **72**(4):602–632, 1999. 8, 15, 16, 17, 29, 45, 52, 54, 70, 117, 177, 178

[23] T. C. B. McLeish. **Tube theory of entangled polymer dynamics**. *Advances in Physics*, **51**(6):1379–1527, 2002. 8

[24] A. Lion. **A constitutive model for carbon black filled rubber: Experimental investigations and mathematical representation**. *Continuum Mechanics and Thermodynamics*, **8**(3):153–169, 1996. 9, 10

[25] A. Dorfmann and R. W. Ogden. **A constitutive model for the Mullins effect with permanent set in particle-reinforced rubber**. *International Journal of Solids and Structures*, **41**(7):1855–1878, 2004. 9, 11

[26] J. S. Bergström. *Large strain time-dependent behavior of elastomeric materials*. Ph.d. thesis, Massachusetts Institute of Technology, 1999. 9, 10, 21

[27] J. S. Bergström and M. C. Boyce. **Large strain time-dependent behavior of filled elastomers**. *Mechanics of Materials*, **32**(11):627–644, 2000. 9

[28] C. Miehe and J. Keck. **Superimposed finite elastic-viscoelastic-plastoelastic stress response with damage in filled rubbery polymers. Experiments, modelling and algorithmic implementation**. *Journal of the Mechanics and Physics of Solids*, **48**(2):323–365, 2000. 9

[29] L. M. Yang, V. P. W. Shim, and C. T. Lim. **A visco-hyperelastic approach to modelling the constitutive behaviour of rubber**. *International Journal of Impact Engineering*, **24**:545–560, 2000. 9, 10

[30] M. Kaliske, L. Nasdala, and H. Rothert. **On damage modelling for elastic and viscoelastic materials at large strain**. *Computers & Structures*, **79**(22):2133–2141, 2001. 9, 11

[31] B. N. J. Persson. **Theory of rubber friction and contact mechanics**. *Journal of Chemical Physics*, **115**(8):3840–3861, 2001. 9

[32] G. Fortunato, V. Ciaravola, A. Furno, M. Scaraggi, B. Lorenz, and B. N. J. Persson. **Dependency of Rubber Friction on Normal Force or Load: Theory and Experiment**. *Tire Science and Technology*, **45**(1):25–54, 2017. 9

[33] J. D. Ferry. *Viscoelastic Properties of Polymers*. John Wiley & Sons, Ltd, 1980. 10

[34] C. M. Roland. **Viscoelastic Behavior of Rubbery Materials**. *Viscoelastic Behavior of Rubbery Materials*, pages 1–344, 2011. 10

[35] J. S. Bergström and M. C. Boyce. **Constitutive modeling of the large strain time-dependent behavior of elastomers**. *Journal of the Mechanics and Physics of Solids*, **46**(5):931–954, 1998. 10, 21

[36] T. Rey, G. Chagnon, D. Favier, and J. B. Le Cam. **Hyperelasticity with rate-independent microsphere hysteresis model for rubberlike materials**. *Computational Materials Science*, **90**:89–98, 2014. 10

[37] C. Miehe and S. Göktepe. **A micro-macro approach to rubber-like materials. Part II: The micro-sphere model of finite rubber viscoelasticity**. *Journal of the Mechanics and Physics of Solids*, **53**(10):2231–2258, 2005. 10, 11, 131

[38] T. Scheffer, H. Seibert, and S. Diebels. **Optimisation of a pretreatment method to reach the basic elasticity of filled rubber materials**. *Archive of Applied Mechanics*, **83**(11):1659–1678, 2013. 10

[39] M. Johlitz and S. Diebels. **Characterisation of a polymer using biaxial tension tests. Part I: Hyperelasticity**. *Archive of Applied Mechanics*, **81**(10):1333–1349, 2011. 10, 23, 26

[40] A. H. Muhr. **Modeling the Stress-Strain Behavior of Rubber**. *Rubber Chemistry and Technology*, **78**(3):391–425, 2005. 10, 18

[41] L. Mullins. **Effect of Stretching on the Properties of Rubber**. *Rubber Chemistry and Technology*, **21**(2):281–300, 1948. 10

[42] J. Diani, B. Fayolle, and P. Gilormini. **A review on the Mullins effect**. *European Polymer Journal*, **45**(3):601–612, 2009. 10

[43] L. Mullins. **Softening of Rubber by Deformation**. *Rubber Chemistry and Technology*, **42**(1):339–362, 1969. 10

[44] R. W. Ogden and D. G. Roxburgh. **A pseudo-elastic model for the Mullins effect in filled rubber**. *Proceedings of the Royal Society A: Mathematical, Physical and Engineering Sciences*, **455**(1988):2861–2877, 1999. 11

[45] L. Mullins. **Permanent Set in Vulcanized Rubber**. *Rubber Chemistry and Technology*, **22**(4):1036–1044, 1949. 11

[46] J. Diani, M. Brieu, and J. M. Vacherand. **A damage directional constitutive model for Mullins effect with permanent set and induced anisotropy**. *European Journal of Mechanics, A/Solids*, **25**(3):483–496, 2006. 11

[47] R. Dargazany and M. Itskov. **A network evolution model for the anisotropic Mullins effect in carbon black filled rubbers**. *International Journal of Solids and Structures*, **46**(16):2967–2977, 2009. 11

[48] K. Loos, A. B. Aydogdu, A. Lion, M. Johlitz, and J. Calipel. **Strain-induced crystallisation in natural rubber: a thermodynamically consistent model of the material behaviour using a multiphase approach**. *Continuum Mechanics and Thermodynamics*, **32**(2):501–526, 2020. 11

[49] N. Candau, R. Laghmach, L. Chazeau, J. Chenal, C. Gauthier, T. Biben, and E. Munch. **Influence of strain rate and temperature on the onset of strain induced crystallization in natural rubber**. *European Polymer Journal*, **64**:244–252, 2015. 11

[50] H. Donner, L. Kanzenbach, J. Ihlemann, and C. Naumann. **Efficiency of rubber material modelling and characterisation**. In A. Lion and M. Johlitz, editors, *Constitutive Models for Rubber X*, pages 19–29. CRC Press, Munich, Germany, 2017. 11, 62

[51] S. Wang and S. A. Chester. **Experimental characterization and continuum modeling of inelasticity in filled rubber-like materials**. *International Journal of Solids and Structures*, **136-137**:125–136, 2018. 11

[52] M. Hossain, G. Possart, and P. Steinmann. **A finite strain framework for the simulation of polymer curing. Part I: elasticity**. *Computational Mechanics*, **44**:621–630, 2009. 11

[53] M. Hossain, G. Possart, and P. Steinmann. **A finite strain framework for the simulation of polymer curing. Part I. Viscoelasticity and shrinkage**. *Computational Mechanics*, **46**:363–375, 2010. 11

[54] R. Landgraf, M. Rudolph, R. Scherzer, and J. Ihlemann. **Modelling and simulation of adhesive curing processes in bonded piezo metal composites**. *Computational Mechanics*, **54**:547–565, 2014. 11

[55] S. Wang and S. A. Chester. **Modeling thermal recovery of the Mullins effect**. *Mechanics of Materials*, **126**:88–98, 2018. 11

[56] J. Lambert-Diani and C. Rey. **New phenomenological behavior laws for rubbers and thermoplastic elastomers**. *European Journal of Mechanics, A/Solids*, **18**(6):1027–1043, 1999. 13, 15, 16, 45, 54, 177, 178

[57] P. Steinmann, M. Hossain, and G. Possart. **Hyperelastic models for rubber-like materials: Consistent tangent operators and suitability for Treloar's data**. *Archive of Applied Mechanics*, **82**(9):1183–1217, 2012. 14, 26, 45, 66

[58] M. Hossain and P. Steinmann. **More hyperelastic models for rubber-like materials: consistent tangent operators and comparative study**. *Journal of the Mechanical Behavior of Materials*, **22**(1-2):27–50, 2013. 14, 26, 45, 66

[59] V. N. Khiêm and M. Itskov. **Analytical network-averaging of the tube model: Rubber elasticity**. *Journal of the Mechanics and Physics of Solids*, **95**:254–269, 2016. 14, 16, 45, 70, 179

[60] M. M. Attard. **Finite strain - isotropic hyperelasticity**. *International Journal of Solids and Structures*, **40**(17):4353–4378, 2003. 14, 17

[61] H. Darijani and R. Naghdabadi. **Hyperelastic materials behavior modeling using consistent strain energy density functions**. *Acta Mechanica*, **213**(3-4):235–254, 2010. 14, 15, 16, 45

[62] P. A. Przybylo and E. M. Arruda. **Experimental Investigations and Numerical Modeling of Incompressible Elastomers during Non-Homogeneous Deformations**. *Rubber Chemistry and Technology*, **71**(4):730–749, 1998. 15, 17, 19, 38

[63] S. Hartmann. **Parameter estimation of hyperelasticity relations of generalized polynomial-type with constraint conditions**. *International Journal of Solids and Structures*, **38**(44-45):7999–8018, 2001. 15, 38, 42

[64] M. H. B. M. Shariff. **Strain Energy Function for Filled and Unfilled Rubberlike Material**. *Rubber Chemistry and Technology*, **73**(1):1–18, 2000. 15, 17, 54, 177, 178

[65] S. Hartmann and P. Neff. **Polyconvexity of generalized polynomial-type hyperelastic strain energy functions for near-incompressibility**. *International Journal of Solids and Structures*, **40**(11):2767–2791, 2003. 15, 38, 40, 119

[66] M. Mooney. **A theory of large elastic deformation**. *Journal of Applied Physics*, **11**(9):582–592, 1940. 15, 38

[67] R. S. Rivlin. **Large elastic deformations of isotropic materials IV. further developments of the general theory**. *Philosophical Transactions of the Royal Society of London. Series A, Mathematical and Physical Sciences*, **241**(835):379–397, 1948. 15

[68] R. S. Rivlin and D. W. Saunders. **Large elastic deformations of isotropic materials VII. Experiments on the deformation of rubber**. *Philosophical Transactions of the Royal Society of London. Series A, Mathematical and Physical Sciences*, **243**(865):251–288, 1951. 15

[69] R. S. Rivlin. **Large Elastic Deformations of Isotropic Materials. I. Fundamental Concepts**. *Philosophical Transactions of the Royal Society A: Mathematical, Physical and Engineering Sciences*, **240**(822):459–490, 1948. 15, 17, 38, 99, 123

[70] O. H. Yeoh and P. D. Fleming. **A new attempt to reconcile the statistical and phenomenological theories of rubber elasticity**. *Journal of Polymer Science Part B: Polymer Physics*, **35**(12):1919–1931, 1997. 16, 46

[71] O. Lopez-Pamies. **A new I1-based hyperelastic model for rubber elastic materials**. *Comptes Rendus - Mecanique*, **338**(1):3–11, 2010. 16, 45

[72] T. Hohenberger, J. Busfield, and N. Pugno. **Numerical leak prediction of elastomeric seals**. In *26th International Conference on Fluid Sealing*, 2020. 16, 149

[73] T. Beda. **Modeling hyperelastic behavior of rubber: A novel invariant-based and a review of constitutive models**. *Journal of Polymer Science Part B: Polymer Physics*, **45**(13):1713–1732, 2007. 16

[74] H. Alexander. **A constitutive relation for rubber-like materials**. *International Journal of Engineering Science*, **6**(9):549–563, 1968. 16, 54, 70, 177, 178, 179

[75] H. G. Kilian. **Equation of state of real networks**. *Polymer*, **22**(2):209–217, 1981. 16

[76] M. M. Carroll. **A strain energy function for vulcanized rubbers**. *Journal of Elasticity*, **103**(2):173–187, 2011. 16, 54, 177, 178

[77] L. J. Hart-Smith. **Elasticity parameters for finite deformations of rubber-like materials**. *Zeitschrift für angewandte Mathematik und Physik ZAMP*, **17**(5):608–626, 1966. 16, 17, 40, 70, 179

[78] G. Chagnon, G. Marckmann, and E. Verron. **A comparison of the Hart-Smith model with Arruda-Boyce and Gent formulations for rubber elasticity**. *Rubber chemistry and technology*, **77**(4):724–735, 2004. 16, 40

[79] S. F. Edwards and T. A. Vilgis. **The tube model theory of rubber elasticity**. *Reports on Progress in Physics*, **51**(2):243–297, 1988. 16, 17, 70, 179

[80] C. O. Horgan and M. G. Smayda. **The importance of the second strain invariant in the constitutive modeling of elastomers and soft biomaterials**. *Mechanics of Materials*, **51**:43–52, 2012. 16

[81] R. W. Ogden, G. Saccomandi, and I. Sgura. **Fitting hyperelastic models to experimental data**. *Computational Mechanics*, **34**(6):484–502, 2004. 17

[82] C. O. Horgan. **The remarkable Gent constitutive model for hyperelastic materials**. *International Journal of Non-Linear Mechanics*, **68**:9–16, 2015. 17, 39

[83] K. C. Valanis and R. F. Landel. **The Strain-Energy Function of a Hyperelastic Material in Terms of the Extension Ratios**. *Journal of Applied Physics*, **38**(7):2997–3002, 1967. 17

[84] R. W. Ogden. **Large Deformation Isotropic Elasticity - On the Correlation of Theory and Experiment for Incompressible Rubberlike Solids**. *Proceedings of the Royal Society A: Mathematical, Physical and Engineering Sciences*, **326**(1567):565–584, 1972. 17, 25, 42, 45, 49, 54, 177, 178

[85] Y. Basar and M. Itskov. **Finite element formulation of the Ogden material model with application to ruber-like shells**. *International Journal for Numerical Methods in Engineering*, **42**(7):1279–1305, 1998. 17

[86] C. O. Horgan and J. G. Murphy. **Limiting chain extensibility constitutive models of Valanis-Landel type**. *Journal of Elasticity*, **86**(2):101–111, 2007. 17

[87] B. Nedjar, H. Baaser, R. J. Martin, and P. Neff. **A finite element implementation of the isotropic exponentiated Hencky-logarithmic model and simulation of the eversion of elastic tubes**. *Computational Mechanics*, **62**(4):635–654, 2018. 17, 31, 136

[88] L. Meunier, G. Chagnon, D. Favier, L. Orgéas, and P. Vacher. **Mechanical experimental characterisation and numerical modelling of an unfilled silicone rubber**. *Polymer Testing*, **27**(6):765–777, 2008. 17, 46, 51, 52, 131, 142

[89] C. O. Horgan and J. G. Murphy. **Compression tests and constitutive models for the slight compressibility of elastic rubber-like materials**. *International Journal of Engineering Science*, **47**(11-12):1232–1239, 2009. 17, 51

[90] M. C. Boyce and E. M. Arruda. **Constitutive Models of Rubber Elasticity: A Review**. *Rubber Chemistry and Technology*, **73**(3):504–523, 2000. 18

[91] M. C. Wang and E. Guth. **Statistical Theory of Networks of Non-Gaussian Flexible Chains**. *The Journal of Chemical Physics*, **20**(7):1144–1157, 1952. 18

[92] M. Kroon. **An 8-chain model for rubber-like materials accounting for non-affine chain deformations and topological constraints**. *Journal of Elasticity*, **102**(2):99–116, 2011. 18

[93] M. Dalémat, M. Coret, A. Leygue, and E. Verron. **Measuring stress field without constitutive equation**. *Mechanics of Materials*, **136**(March):103087, 2019. 18, 19

[94] R. S. Marlow. **A general first-invariant hyperelastic constitutive model**. In James J. C. Busfield and Alan Muhr, editors, *Constitutive Models for Rubber III*, pages 157–160, London, 2003. CRC Press. 18

[95] R. S. Marlow. **A Second-Invariant Extension of the Marlow Model : Representing Tension and Compression Data Exactly**. *ABAQUS Users' Conference*, pages 1–7, 2008. 18

[96] T. Sussman and K. J. Bathe. **A model of incompressible isotropic hyperelastic material behavior using spline interpolations of tension-compression test data**. *Communications in Numerical Methods in Engineering*, **25**(1):53–63, 2009. 19

[97] M. Latorre and F. J. Montáns. **Extension of the Sussman-Bathe spline-based hyperelastic model to incompressible transversely isotropic materials**. *Computers and Structures*, **122**:13–26, 2013. 19

[98] M. Latorre and F. J. Montáns. **What-You-Prescribe-Is-What-You-Get orthotropic hyperelasticity**. *Computational Mechanics*, **53**(6):1279–1298, 2014. 19

[99] J. Crespo, M. Latorre, and F. J. Montáns. **WYPIWYG hyperelasticity for isotropic, compressible materials**. *Computational Mechanics*, **59**(1):73–92, 2017. 19

[100] M. Latorre and F. J. Montáns. **Experimental data reduction for hyperelasticity**. *Computers & Structures*, 2018. 19

[101] C. K. L. Davies, D. K. De, and A. G. Thomas. **Characterization of the Behavior of Rubber for Engineering Design Purposes. 1. Stress-Strain Relations**. *Rubber Chemistry and Technology*, **67**(4):716–728, 1994. 19

[102] D. Schellenberg, D. Juhre, and J. Ihlemann. **Parameter identification based on multiple inhomogeneous experiments of practical relevance**. In *Constitutive Models for Rubber VII*, pages 33–38. CRC Press, 2012. 19, 25

[103] P. K. Currie. **The Attainable Region of strain-invariant space for elastic materials**. *International Journal of Non-Linear Mechanics*, **39**(5):833–842, 2004. 19

[104] British Standards Institution. **Rubber, vulcanized or thermoplastic — Determination of tensile stress-strain properties**, 2017. 20, 151

[105] ASTM International. **Standard Test Methods for Vulcanized Rubber and Thermoplastic Elastomers—Tension**, 2016. 20, 151

[106] M. Sasso, G. Palmieri, G. Chiappini, and D. Amodio. **Characterization of hyperelastic rubber-like materials by biaxial and uniaxial stretching tests based on optical methods**. *Polymer Testing*, **27**(8):995–1004, 2008. 21, 24

[107] G. Palmieri, M. Sasso, G. Chiappini, and D. Amodio. **Virtual fields method on planar tension tests for hyperelastic materials characterisation**. *Strain*, **47**(SUPPL. 2):196–209, 2011. 21, 51

[108] British Standards Institution. **Rubber , vulcanized or thermoplastic — Determination of shear modulus and adhesion to rigid plates — Quadruple- shear methods**, 2011. 22

[109] ASTM International. **Standard Test Methods for Rubber Property — Adhesion to Rigid Substrate**, 2003. 22

[110] A. N. Gent, J. B. Suh, and S. G. Kelly. **Mechanics of rubber shear springs**. *International Journal of Non-Linear Mechanics*, **42**(2):241–249, 2007. 22

[111] L. C. S. Nunes. **Mechanical characterization of hyperelastic polydimethylsiloxane by simple shear test**. *Materials Science and Engineering A*, **528**(3):1799–1804, 2011. 22

[112] L. C. S. Nunes and D. C. Moreira. **Simple shear under large deformation: Experimental and theoretical analyses**. *European Journal of Mechanics, A/Solids*, **42**:315–322, 2013. 22

[113] M. Destrade, J. G. Murphy, and G. Saccomandi. **Simple shear is not so simple**. *International Journal of Non-Linear Mechanics*, **47**(2):210–214, 2012. 22, 51

[114] C. O. Horgan and J. G. Murphy. **Simple shearing of incompressible and slightly compressible isotropic nonlinearly elastic materials**. *Journal of Elasticity*, **98**(2):205–221, 2010. 22, 44, 51

[115] ASTM International. **Standard Test Methods for Rubber Properties in Compression**, 2012. 23

[116] British Standards Institution. **Rubber, vulcanized or thermoplastic — Determination of compression stress-strain properties**, 2017. 23

[117] G. L. Bradley, P. C. Chang, and G. B. Mckenna. **Rubber modeling using uniaxial test data**. *Journal of Applied Polymer Science*, **81**(4):837–848, 2001. 23, 26, 46, 49, 62

[118] R. L. Spilker, J. K. Suh, and V. C. Mow. **Effects of friction on the unconfined compressive response of articular cartilage: A finite element analysis**. *Journal of Biomechanical Engineering*, **112**(2):138–146, 1990. 23

[119] M. Brieu, J. Diani, and N Bhatnagar. **A New Biaxial Tension Test Fixture for Uniaxial Testing Machine—A Validation for Hyperelastic Behavior of Rubber-like Materials**. *Journal of Testing and Evaluation*, **35**(4):100688, 2007. 23

[120] M. Fujikawa, N. Maeda, J. Yamabe, Y. Kodama, and M. Koishi. **Determining Stress–Strain in Rubber with In-Plane Biaxial Tensile Tester**. *Experimental Mechanics*, **54**(9):1639–1649, 2014. 23

[121] H. Hariharaputhiran and U. Saravanan. **A new set of biaxial and uniaxial experiments on vulcanized rubber and attempts at modeling it using classical hyperelastic models**. *Mechanics of Materials*, **92**:211–222, 2016. 23

[122] B. Pan, K. Qian, H. Xie, and A. Asundi. **Two-dimensional digital image correlation for in-plane displacement and strain measurement: a review**. *Measurement Science and Technology*, **20**(6):062001, 2009. 23

[123] J. J. Hu, G. W. Chen, Y. C. Liu, and S. S. Hsu. **Influence of Specimen Geometry on the Estimation of the Planar Biaxial Mechanical Properties of Cruciform Specimens**. *Experimental Mechanics*, **54**(4):615–631, 2014. 23

[124] H. Seibert, T. Scheffer, and S. Diebels. **Biaxial testing of elastomers - Experimental setup, measurement and experimental optimisation of specimen's shape**. *Technische Mechanik*, **34**(2):72–89, 2014. 23

[125] G. Machado, D. Favier, and G. Chagnon. **Membrane Curvatures and Stress-strain Full Fields of Axisymmetric Bulge Tests from 3D-DIC Measurements. Theory and Validation on Virtual and Experimental results**. *Experimental Mechanics*, **52**(7):865–880, 2012. 24, 25

[126] R. Österlöf, H. Wentzel, and L. Kari. **An efficient method for obtaining the hyperelastic properties of filled elastomers in finite strain applications**. *Polymer Testing*, **41**:44–54, 2015. 24

[127] L. R. G. Treloar. **Stress-Strain Data for Vulcanized Rubber under Various Types of Deformation**. *Rubber Chemistry and Technology*, **17**(4):813–825, 1944. 24, 25, 26, 27, 45, 51, 89, 128

[128] D. F. Jones and L. R. G. Treloar. **The properties of rubber in pure homogeneous strain**. *Journal of Physics D: Applied Physics*, **8**(11):1285–1304, 1975. 24, 25, 45

[129] S. Kawabata, M. Matsuda, K. Tei, and H. Kawai. **Experimental survey of the strain energy density function of isoprene rubber vulcanizate**. *Macromolecules*, **14**(1):154–162, 1981. 24, 25, 27, 45

[130] T. Guélon, E. Toussaint, J. B. Le Cam, N. Promma, and M. Grédiac. **A new characterisation method for rubber**. *Polymer Testing*, **28**(7):715–723, 2009. 25

[131] A. E. Giannakopoulos and D. I. Panagiotopoulos. **Conical indentation of incompressible rubber-like materials**. *International Journal of Solids and Structures*, **46**(6):1436–1447, 2009. 25, 138

[132] V. Le Saux, Y. Marco, G. Bles, S. Calloch, S. Moyne, S. Plessis, and P. Charrier. **Identification of constitutive model for rubber elasticity from micro-indentation tests on natural rubber and validation by macroscopic tests**. *Mechanics of Materials*, **43**(12):775–786, 2011. 25, 26, 29, 49, 70, 117, 138

[133] R. Mahnken and E. Stein. **A unified approach for parameter identification of inelastic material models in the frame of the finite element method**. *Computer Methods in Applied Mechanics and Engineering*, **136**(3-4):225–258, 1996. 25

[134] R. Mahnken and E Stein. **Parameter identification for finite deformation elasto-plasticity in principal directions**. *Comput. Methods Appl. Mech. Engrg.*, **147**(97):17–39, 1997. 25

[135] D. Schellenberg, D. Juhre, and J. Ihlemann. **Identification of inelastic material parameters using component-oriented specimen**. In *Constitutive Models for Rubber VIII*, **17**, pages 191–196. CRC Press, 2013. 25

[136] B. Chouchaoui. **Optimizing rubber products for the automotive industry via characterization of compounds and computer modeling**. *SAE Technical Papers*, **2001**(724), 2001. 25

[137] W. V. Mars and A. Fatemi. **Multiaxial stress effects on fatigue behavior of filled natural rubber**. *International Journal of Fatigue*, **28**(5-6):521–529, 2006. 25, 138

[138] G. Marckmann and E. Verron. **Comparison of Hyperelastic Models for Rubber-Like Materials**. *Rubber Chemistry and Technology*, **79**(5):835–858, 2006. 25, 26, 27, 45, 52, 58, 59, 70

[139] M. R. Mansouri, H. Darijani, and M. Baghani. **On the Correlation of FEM and Experiments for Hyperelastic Elastomers**. *Experimental Mechanics*, **57**(2):195–206, 2017. 26, 62, 66

[140] M. Latorre, E. D. Rosa, and F. J. Montáns. **Understanding the need of the compression branch to characterize hyperelastic materials**. *International Journal of Non-Linear Mechanics*, **89**(August 2016):14–24, 2017. 26, 62

[141] D. J. Seibert and N. Schöche. **Direct Comparison of Some Recent Rubber Elasticity Models**. *Rubber Chemistry and Technology*, **73**(2):366–384, 2000. 26

[142] K. Urayama. **An experimentalist's view of the physics of rubber elasticity**. *Journal of Polymer Science Part B: Polymer Physics*, **44**(24):3440–3444, 2006. 26

[143] S. Hartmann. **Numerical studies on the identification of the material parameters of Rivlin's hyperelasticity using tension-torsion tests**. *Acta Mechanica*, **148**(1-4):129–155, 2001. 26, 42

[144] A. P. S. Selvadurai and M. Shi. **Fluid pressure loading of a hyperelastic membrane**. *International Journal of Non-Linear Mechanics*, **47**(2):228–239, 2012. 26

[145] S. Hartmann and R. R. Gilbert. **Identifiability of material parameters in solid mechanics**. *Archive of Applied Mechanics*, **88**(1):1–24, 2017. 26, 49, 55, 99, 138

[146] Y. Pan, Y. Zhan, H. Ji, X. Niu, and Z. Zhong. **Can hyperelastic material parameters be uniquely determined from indentation experiments?** *RSC Advances*, **6**(85):81958–81964, 2016. 26, 55

[147] H. Dal, Y. Badienia, K. Açıkgöz, and F. A. Denlï. **A comparative study on hyperelastic constitutive models on rubber: State of the art after 2006**. In *Constitutive Models for Rubber XI*, pages 239–244. CRC Press, 2019. 27, 45, 52, 54, 58, 59, 70

[148] Chennakesava Kadapa and Mokarram Hossain. **A linearized consistent mixed displacement-pressure formulation for hyperelasticity**. *Mechanics of Advanced Materials and Structures*, pages 1–18, may 2020. 27

[149] M. Tanaka, M. Fujikawa, D. Balzani, and J. Schröder. **Robust numerical calculation of tangent moduli at finite strains based on complex-step derivative approximation and its application to localization analysis**. *Computer Methods in Applied Mechanics and Engineering*, **269**:454–470, 2014. 28, 30, 98, 107, 109, 123

[150] C. H. Liu, G. Hofstetter, and H. A. Mang. **3D finite element analysis of rubber-like materials at finite strains**. *Engineering computations*, **11**(2):111–128, 1994. 29, 81

[151] C. Miehe. **Aspects of the formulation and finite element implementation of large strain isotropic elasticity**. *International Journal for Numerical Methods in Engineering*, **37**(12):1981–2004, 1994. 29, 81, 82, 83

[152] M. Kaliske and H. Rothert. **On the finite element implementation of rubber-like materials at finite strains**. *Engineering Computations*, **14**(2):216–232, 1997. 29, 81, 82

[153] P. Chadwick and R. W. Ogden. **A theorem of tensor calculus and its application to isotropic elasticity**. *Archive for Rational Mechanics and Analysis*, **44**(1):54–68, 1971. 29, 113, 115

[154] P. Chadwick and R. W. Ogden. **On the definition of elastic moduli**. *Archive for Rational Mechanics and Analysis*, **44**(1):41–53, 1971. 29, 113, 115

[155] J. C. Simo and R. L. Taylor. **Quasi-incompressible finite elasticity in principal stretches. continuum basis and numerical algorithms**. *Computer Methods in Applied Mechanics and Engineering*, **85**(3):273–310, 1991. 29, 112, 114, 115, 117, 126, 128

[156] J. C. Simo. **Numerical analysis and simulation of plasticity**. In *Handbook of Numerical Analysis*, **Numerical Methods for Solids (Part 3)**, pages 183–499. Elsevier, 1998. 29, 87

[157] S. Govindjee. **Numerical Issues in Finite Elasticity and Viscoelasticity**. In Giuseppe Saccomandi and Raymond W. Ogden, editors, *Mechanics and Thermomechanics of Rubberlike Solids*, pages 187–232. Springer Vienna, 2004. 29

[158] B. Jeremić and Z. Cheng. **Significance of equal principal stretches in computational hyperelasticity**. *Communications in Numerical Methods in Engineering*, **21**(9):477–486, 2005. 29

[159] C. Miehe. **Computation of isotropic tensor functions**. *Communications in Numerical Methods in Engineering*, **9**(11):889–896, 1993. 29, 116, 119, 126

[160] Y. Chen and G. Dui. **The Derivative of Isotropic Tensor Functions, Elastic Moduli and Stress Rate: I. Eigenvalue Formulation**. *Mathematics and Mechanics of Solids*, **9**(5):493–511, 2004. 29

[161] E. A. de Souza Neto. **On general isotropic tensor functions of one tensor**. *International Journal for Numerical Methods in Engineering*, **61**(6):880–895, 2004. 29

[162] G. Dui, Z. Wang, and Q. Ren. **Explicit formulations of tangent stiffness tensors for isotropic materials**. *International Journal for Numerical Methods in Engineering*, **69**(4):665–675, 2007. 29

[163] F. Peyraut, Z. Q. Feng, Q. C. He, and N. Labed. **Robust numerical analysis of homogeneous and non-homogeneous deformations**. *Applied Numerical Mathematics*, **59**(7):1499–1514, 2009. 29

[164] J. M. Young, J. Yao, A. Ramasubramanian, L. A. Taber, and R. Perucchio. **Automatic Generation of User Material Subroutines for Biomechanical Growth Analysis**. *Journal of Biomechanical Engineering*, **132**(10):104505–1–104505–5, 2010. 29

[165] J. Korelc. **Multi-language and multi-environment generation of nonlinear finite element codes**. *Engineering with Computers*, **18**(4):312–327, 2002. 30

[166] J. Korelc. **Automation of primal and sensitivity analysis of transient coupled problems**. *Computational Mechanics*, **44**(5):631–649, 2009. 30

[167] S. Rothe and S. Hartmann. **Automatic differentiation for stress and consistent tangent computation**. *Archive of Applied Mechanics*, **85**(8):1103–1125, 2015. 30

[168] P. Wriggers. *Nonlinear Finite Element Methods*. Springer Berlin Heidelberg, Berlin, Heidelberg, 2008. 30

[169] C. Miehe. **Numerical computation of algorithmic (consistent) tangent moduli in large-strain computational inelasticity**. *Computer Methods in Applied Mechanics and Engineering*, **134**(96):223–240, 1996. 30, 93, 98, 107, 109

[170] W. Sun, E. L. Chaikof, and M. E. Levenston. **Numerical Approximation of Tangent Moduli for Finite Element Implementations of Nonlinear Hyperelastic Material Models**. *Journal of Biomechanical Engineering*, **130**(6):061003, 2008. 30

[171] J. E. Dennis and R. B. Schnabel. *Numerical Methods for Unconstrained Optimization and Nonlinear Equations*, **16**. Society for Industrial and Applied Mathematics, 1996. 30, 97

[172] R. Mathur. *An analytical approach to computing step sizes for finite-difference derivatives*. Phd thesis, The University of Texas at Austin, 2012. 30, 98, 103

[173] A. Pérez-Foguet, A. Rodríguez-Ferran, and A. Huerta. **Numerical differentiation for local and global tangent operators in computational plasticity**. *Computer Methods in Applied Mechanics and Engineering*, **189**(1):277–296, 2000. 30, 31, 98

[174] A. Pérez-Foguet, A. Rodríguez-Ferran, and A. Huerta. **Numerical differentiation for non-trivial consistent tangent matrices: an application to the MRS-Lade model**. *International Journal for Numerical Methods in Engineering*, **48**(2):159–184, 2000. 30

[175] R. Kiran and K. Khandelwal. **Complex step derivative approximation for numerical evaluation of tangent moduli**. *Computers and Structures*, **140**:1–13, 2014. 30, 98

[176] R. Kiran and K. Khandelwal. **Numerically approximated Cauchy integral (NACI) for implementation of constitutive models**. *Finite Elements in Analysis and Design*, **89**:33–51, 2014. 30, 31, 98

[177] H. Liu and W. Sun. **Computational efficiency of numerical approximations of tangent moduli for finite element implementation of a fiber-reinforced hyperelastic material model**. *Computer Methods in Biomechanics and Biomedical Engineering*, **19**(11):1171–1180, 2016. 30, 107, 109

[178] J. R. R. A. Martins and J. T. Hwang. **Review and Unification of Methods for Computing Derivatives of Multidisciplinary Computational Models**. *AIAA Journal*, **51**(11):2582–2599, 2013. 30

[179] J. Fike and J. Alonso. **The Development of Hyper-Dual Numbers for Exact Second-Derivative Calculations**. In *49th AIAA Aerospace Sciences Meeting including the New Horizons Forum and Aerospace Exposition*, page 124, Reston, Virigina, 2011. American Institute of Aeronautics and Astronautics. 31

[180] M. Tanaka, T. Sasagawa, R. Omote, M. Fujikawa, D. Balzani, and J. Schröder. **A highly accurate 1st- and 2nd-order differentiation scheme for hyperelastic material models based on hyper-dual numbers**. *Computer Methods in Applied Mechanics and Engineering*, **283**:22–45, 2015. 31, 98, 99, 107, 109, 123

[181] D. H. Bailey, R. Barrio, and J. M. Borwein. **High-precision computation: Mathematical physics and dynamics**. *Applied Mathematics and Computation*, **218**(20):10106–10121, 2012. 31

[182] J. C. Simo. **On a fully three-dimensional finite-strain viscoelastic damage model: Formulation and computational aspects**. *Computer Methods in Applied Mechanics and Engineering*, **60**(2):153–173, 1987. 31, 85

[183] Z. P. Bažant. **A Correlation Study of Formulations of Incremental Deformation and Stability of Continuous Bodies**. *Journal of Applied Mechanics*, **38**(4):919, 1971. 31, 136

[184] Z. P. Bažant, M. Gattu, and J. Vorel. **Work conjugacy error in commercial finite-element codes: Its magnitude and how to compensate for it**. *Proceedings of the Royal Society A: Mathematical, Physical and Engineering Sciences*, **468**(2146):3047–3058, 2012. 31, 136

[185] W. Ji, A. M. Waas, and Z. P. Bažant. **On the Importance of Work-Conjugacy and Objective Stress Rates in Finite Deformation Incremental Finite Element Analysis**. *Journal of Applied Mechanics*, **80**(4):041024, 2013. 31, 136

[186] J. Vorel and Z. P. Bažant. **Review of energy conservation errors in finite element softwares caused by using energy-inconsistent objective stress rates**. *Advances in Engineering Software*, **72**:3–7, 2014. 31, 136

[187] L. Zanelli, A. Montanaro, E. L. Carniel, P. G. Pavan, and A. N. Natali. **The study of equivalent material parameters in a hyperelastic model**. *International Journal of Non-Linear Mechanics*, **89**(March 2016):142–150, 2017. 38, 42

[188] G. Puglisi and G. Saccomandi. **The Gent model for rubber-like materials: An appraisal for an ingenious and simple idea**. *International Journal of Non-Linear Mechanics*, **68**:17–27, 2015. 39

[189] O. H. Yeoh. **Characterization of Elastic Properties of Carbon-Black-Filled Rubber Vulcanizates**. *Rubber Chemistry and Technology*, **63**(5):792–805, 1990. 40, 128

[190] D. W. Haines and W. D. Wilson. **Strain-energy density function for rubberlike materials**. *Journal of the Mechanics and Physics of Solids*, **27**(4):345–360, 1979. 40, 45, 54, 89, 177, 178

[191] O. H. Yeoh. **On the Ogden Strain-Energy Function**. *Rubber Chemistry and Technology*, **70**(2):175–182, 1997. 42

[192] R. S. Rivlin. **Large Elastic Deformations of Isotropic Materials. VI. Further Results in the Theory of Torsion, Shear and Flexure**. *Philosophical Transactions of the Royal Society A: Mathematical, Physical and Engineering Sciences*, **242**(845):173–195, 1949. 44

[193] P. Heuillet and L. Dugautier. **Modélisation du comportement hyperélastique des caoutchoucs et élastoméres thermoplastiques, compacts on cellulaires**. In *Génie mécanique des caoutchoucs : Et des élastomères thermoplastiques*, pages 67–103. Apollor, 1997. 45, 51, 52, 151

[194] H. Bechir, L. Chevalier, M. Chaouche, and K. Boufala. **Hyperelastic constitutive model for rubber-like materials based on the first Seth strain measures invariant**. *European Journal of Mechanics, A/Solids*, **25**(1):110–124, 2006. 45

[195] D. C. Moreira and L. C. S. Nunes. **Comparison of simple and pure shear for an incompressible isotropic hyperelastic material under large deformation**. *Polymer Testing*, **32**(2):240–248, 2013. 49

[196] L. Chevalier and Y. Marco. **Tools for multiaxial validation of behavior laws chosen for modeling hyper-elasticity of rubber-like materials**. *Polymer Engineering and Science*, **42**(2):280–298, 2002. 51

[197] L. Chevalier, S. Calloch, F. Hild, and Y. Marco. **Digital image correlation used to analyze the multiaxial behavior of rubber-like materials**. *European Journal of Mechanics, A/Solids*, **20**(2):169–187, 2001. 51

[198] J. C. Simo and T. J. R. Hughes. *Computational Inelasticity*, **7** of *Interdisciplinary Applied Mathematics*. Springer-Verlag, New York, 1998. 85

[199] I. R. Khan and R. Ohba. **New finite difference formulas for numerical differentiation**. *Journal of Computational and Applied Mathematics*, **126**(1-2):269–276, 2000. 95

[200] J. Li. **General explicit difference formulas for numerical differentiation**. *Journal of Computational and Applied Mathematics*, **183**(1):29–52, 2005. 96

[201] B. Fornberg. **Generation of finite difference formulas on arbitrarily spaced grids**. *Mathematics of Computation*, **51**(184):699–699, 1988. 96

[202] E. Isaacson and H. B. Keller. *Analysis of numerical methods*. Courier Corporation, 1994. 97

[203] J. Kopp. **Efficient numerical diagonalization of hermitian 3 x 3 matrices**. *International Journal of Modern Physics C*, **19**(03):523–548, 2008. 112, 114, 115, 124

[204] T. Kato. *Perturbation theory for linear operators*, **132**. Springer-Verlag Berlin Heidelberg, 1995. 115

[205] S. J. Connolly. **Fortran programs and Abaqus subroutines: Higher-order and higher precision numerical approximations of finite strain elasticity moduli**, 2018. 134

[206] S. J. Connolly. **Isotropic hyperelasticity in principal stretches: Fortran programs and subroutines**, 2019. 134

[207] S. J. Connolly, D. Mackenzie, and Y. Gorash. **Isotropic hyperelasticity in principal stretches: explicit elasticity tensors and numerical implementation**. *Computational Mechanics*, **64**(5):1273–1288, 2019. 134

[208] S. J. Connolly, D. Mackenzie, and Y. Gorash. **Higher-order and higher floating-point precision numerical approximations of finite strain elasticity moduli**. *International Journal for Numerical Methods in Engineering*, **120**(10):1184–1201, 2019. 134

[209] H. J. Qi, K. Joyce, and M. C. Boyce. **Durometer Hardness and the Stress-Strain Behavior of Elastomeric Materials**. *Rubber Chemistry and Technology*, **76**(2):419–435, 2003. 138

[210] G. Rauchs, J. Bardon, and D. Georges. **Identification of the material parameters of a viscous hyperelastic constitutive law from spherical indentation tests of rubber and validation by tensile tests**. *Mechanics of Materials*, **42**(11):961–973, 2010. 138

[211] M. Bäker and A. Shrot. **Inverse parameter identification with finite element simulations using knowledge-based descriptors**. *Computational Materials Science*, **69**:128–136, 2013. 138

[212] A. Ali, M. Hosseini, and B. B. Sahari. **Fatigue life modeling for elastomeric materials: A review**. *International Review of Mechanical Engineering*, **3**(3):332–338, 2009. 138

[213] G. Ayoub, M. Naït-Abdelaziz, and F. Zaïri. **Multiaxial fatigue life predictors for rubbers: Application of recent developments to a carbon-filled SBR**. *International Journal of Fatigue*, **66**:168–176, 2014. 138

[214] J. Suter, B. Beutler, W. Mars, B. Beutler, and B. Young. **Analyzing elastomeric CV boot performance**. Technical report, Endurica L.L.C., 2014. 138

[215] P. Wriggers and J. Reinelt. **Multi-scale approach for frictional contact of elastomers on rough rigid surfaces**. *Computer Methods in Applied Mechanics and Engineering*, **198**(21-26):1996–2008, 2009. 139

[216] K. Matsuda, D. Hashimoto, and K. Nakamura. **Real contact area and friction property of rubber with two-dimensional regular wavy surface**. *Tribology International*, **93**:523–529, 2016. 139

[217] P. Wriggers and G. Zavarise. **Computational Contact Mechanics**. In *Encyclopedia of Computational Mechanics*. John Wiley & Sons, Ltd, Chichester, UK, 2004. 139

[218] J. Erjavec. *Automotive technology: a systems approach*. Thomson Delmar Learning, fifth edition edition, 2004. 140

[219] S. M. Clarke, F. Elias, and E. M. Terentjev. **Ageing of natural rubber under stress**. *The European Physical Journal E*, **2**(2):335–341, 2000. 140

[220] H. Müller and B. S. Nau. *Fluid Sealing Technology: Principles and Applications*. Marcel Dekker, Inc, New York, 1998. 147

[221] Parker O-Ring Division. *Parker O-Ring Handbook*. Parker Hannifin Corporation, Cleveland, OH, USA, 2018. 147, 148, 149, 155

[222] Y. Gorash, A. Bickley, and F. Gozalo. **Assessment of leak tightness for swellable elastomeric seals considering fluid-structure interaction with the CEL approach**. In *24th International Conference on Fluid Sealing*, 2018. 149

[223] J. C. Simo and R. L. Taylor. **Penalty function formulations for incompressible nonlinear elastostatics**. *Computer Methods in Applied Mechanics and Engineering*, **35**(1):107–118, 1982. 151

Appendix A

Hyperelastic Constitutive Models: Strain Energy Density Functions

Table A.1: Strain energy density functions for studied hyperelastic constitutive models

	Strain energy density, W	Parameters
Extended-tube (22)	$W_{e-t} = \frac{G_c}{2}\left[\frac{\left(1-\delta^2\right)\left(I_1-3\right)}{1-\delta^2\left(I_1-3\right)}\right] + \frac{G_e}{\beta^2}\sum_{a=1}^{3}\left({\lambda_a}^{-\beta}-1\right)$	G_c, G_e, β, δ
Shariff (64)	(-)	$E, \alpha_1, \alpha_2, \alpha_3, \alpha_4$
Micro-sphere (11)	see (11)	μ, N, p, U, q
3-term Ogden (84)	$W_{Og} = \sum_{i=1}^{3}\frac{2\mu_i}{{\alpha_i}^2}\left({\lambda_1}^{\alpha_i}+{\lambda_2}^{\alpha_i}+{\lambda_3}^{\alpha_i}-3\right)$	$\mu_1, \alpha_1, \mu_2, \alpha_2, \mu_3, \alpha_3$
Haines-Wilson (190)	$W_{HW} = C_{10}\left(I_1-3\right)+C_{01}\left(I_2-3\right)+C_{11}\left(I_1-3\right)\left(I_2-3\right)+C_{20}\left(I_1-3\right)^2+C_{02}\left(I_2-3\right)^2+C_{30}\left(I_1-3\right)^3$	$C_{01}, C_{10}, C_{11}, C_{20}, C_{02}, C_{30}$
Alexander (74)	$W_{Alex.} = C_1\int \mathrm{e}^{k\left(I_1-3\right)^2}\mathrm{d}I_1 + C_2\ln\left(\frac{\left(I_2-3\right)+\gamma}{\gamma}\right)+C_3\left(I_2-3\right)$	C_1, C_2, C_3, γ, k
Diani-Rey (56)	$W_{D\&R} = \int \mathrm{e}^{a_0+a_1\left(I_1-3\right)^{a_2}}\mathrm{d}I_1 + \frac{1}{b_1+1}\left(\mathrm{e}^{b_0}{I_2}^{b_1+1}\right)$	a_0, a_1, a_2, b_0, b_1
Carroll (76)	$W_{Carroll} = \int\left(A+4B^{{I_1}^3}\right)\mathrm{d}I_1 + C\sqrt{I_2}$	A, B, C

Table A.2: Derivative of strain energy density functions in terms of principal stretches λ_a

	First derivatives of W with respect to λ_a, $\frac{\partial W}{\partial \lambda_a}$
Extended-tube (22)	$\frac{\partial W_{e-t}}{\partial \lambda_a} = \frac{G_c \left(1 + (I_1 - 3)\,\delta^4 - 2\,\delta^2\right)\lambda_a}{\left(1 - \delta^2\,(I_1 - 3)\right)^2} - 2\,\frac{G_e}{\beta}\lambda_a{}^{-\beta-1}$
Ogden (84)	$\frac{W_{Og}}{\partial \lambda_a} = \frac{2}{\lambda_a}\sum_{i=1}^{3}\frac{\mu_i}{\alpha_i}\lambda_a{}^{\alpha_i}$
Shariff (64)	$\frac{W_{Shariff}}{\partial \lambda_a} = \frac{1}{\lambda_a}E\left[\frac{2\ln\lambda_a}{3} + \alpha_1\left(e^{1-\lambda_a} + \lambda_a - 2\right) + \alpha_2\left(e^{\lambda_a - 1} - \lambda_a\right) + \alpha_3\frac{(\lambda_a - 1)^3}{\lambda_a{}^{3.6}} + \alpha_4\,(\lambda_a - 1)^3\right]$

Table A.3: Derivatives of strain energy density functions in terms of strain invariants I_1 and I_2

	First derivatives of W with respect to I_1, $\frac{\partial W}{\partial I_1}$	First derivatives of W with respect to I_2, $\frac{\partial W}{\partial I_2}$
Haines-Wilson (190)	$\frac{\partial W_{HW}}{\partial I_1} = C_{10} + C_{11}\,(I_2 - 3) + C_{20}\,(I_1 - 3)^2 + C_{30}\,(I_1 - 3)^3$	$\frac{\partial W_{HW}}{\partial I_2} = C_{01}\,(I_2 - 3) + C_{11}\,(I_1 - 3) + C_{02}\,(I_2 - 3)^2$
Alexander (74)	$\frac{\partial W_{Alex.}}{\partial I_1} = C_1 e^{k(I_1-3)^2}$	$\frac{\partial W_{Alex.}}{\partial I_2} = \left(\frac{C_2}{(I_2 - 3) + \gamma}\right) + C_3$
Diani-Rey (56)	$\frac{\partial W_{D\&R}}{\partial I_1} = e^{a_0 + a_1 (I_1-3)^{a_2}}$	$\frac{\partial W_{D\&R}}{\partial I_2} = e^{b_0}{I_2}^{b_1+1}$
Carroll (76)	$\frac{\partial W_{Carroll}}{\partial I_1} = A + 4B{I_1}^3$	$\frac{\partial W_{Carroll}}{\partial I_2} = \frac{C}{2\sqrt{I_2}}$

Table A.4: Strain energy density functions for additional hyperelastic constitutive models used in general biaxial investigations

	Strain energy density, W	Parameters
Bid. (74)	$W_{Bid.} = C_{10}\left(I_1 - 3\right) + C_{01}\left(I_2 - 3\right) + C_{20}\left(I_1 - 3\right)^2 + C_{30}\left(I_1 - 3\right)^3$	$C_{10}, C_{01}, C_{20}, C_{30}$
H-S (77)	$W_{H-S} = \int A\mathrm{e}^{C\left(I_1-3\right)^2}\mathrm{d}I_1 + AB\ln I_2$	A, B, C
NA-t (59)	$W_{NA-t} = \mu_c \kappa n \ln\left(\dfrac{\sin\left(\left(\frac{\pi}{\sqrt{n}}\right)\left(\frac{I_1}{3}\right)^{\frac{q}{2}}\right)}{\sin\left(\frac{\pi}{\sqrt{n}}\left(\frac{I_1}{3}\right)^{\frac{q}{2}}\right)}\right) + \mu_t\left[\left(\dfrac{I_2}{3}\right)^{\frac{1}{2}} - 1\right]$	$\mu_c\kappa, n, q, \mu_t$
E-V (79)	$W_{E-V} = \dfrac{N_c}{2}\left[\dfrac{\left(1-\alpha^2\right)I_1}{1-\alpha^2 I_1} + + \ln\left(1-\alpha^2 I_1\right)\right] + \dfrac{N_s}{2}\left[\dfrac{\left(1-\alpha^2\right)\left(1+\eta\right)}{1-\alpha^2 I_1}\sum_{a=1}^{3}\dfrac{{\lambda_a}^2}{1+\eta{\lambda_a}^2}\right] + \dfrac{N_s}{2}\left[\ln\left(1-\alpha^2 I_1\right) + \sum_{a=1}^{3}\ln\left(1+\eta{\lambda_a}^2\right)\right]$	N_c, N_s, α, η
8c-t	$W_{8c-t} = \mu\left[\dfrac{1}{2}\left(I_1 - 3\right) + \dfrac{1}{20N}\left(I_1^2 - 9\right) + \dfrac{11}{1050N^2}\left(I_1^3 - 27\right) + \dfrac{19}{7000N^3}\left(I_1^4 - 81\right) + \dfrac{519}{673750N^4}\left(I_1^5 - 243\right)\right] + \dfrac{2G_e}{\eta^2}\sum_{a=1}^{3}\left({\lambda_a}^{\eta} - 1\right)$	μ, N, G_e, η

Appendix B

Tabular Results from Chapter 3

Table B.1: Case study 2: tabulated results for parameters identified using reduced strain ranges of Treloar data

	75% strain range					50% strain range					25% strain range					Overall	
	$E_{F\%}$	R_F	$E_{P\%}$	R_P	Dif.	$E_{F\%}$	R_F	$E_{P\%}$	R_P	Dif.	$E_{F\%}$	R_F	$E_{P\%}$	R_P	Dif.	R_F	R_P
e-t	1.97%	3	2.22%	2	0.34%	1.93%	2	8.11%	4	6.23%	1.86%	6	13.01%	3	11.13%	4	2
Shariff	1.87%	2	4.31%	4	2.24%	2.03%	6	6.80%	2	4.73%	2.04%	8	14.95%	4	12.88%	6	4
m-s	2.24%	5	5.12%	8	2.66%	1.95%	3	4.80%	1	2.35%	1.56%	2	7.76%	1	5.31%	3	3
Ogden	1.10%	1	1.43%	1	0.16%	1.34%	1	7.65%	3	6.38%	1.80%	5	10.03%	2	8.76%	1	1
HW	3.28%	7	4.40%	5	0.41%	1.98%	5	26.62%	7	22.63%	1.66%	3	180.59%	7	176.60%	5	7
Alex.	2.82%	6	4.95%	7	1.78%	2.09%	7	10.35%	5	7.18%	1.69%	4	24.87%	5	21.70%	7	6
D&R	2.12%	4	3.26%	3	1.28%	1.95%	4	11.14%	6	9.16%	1.47%	1	29.09%	6	27.10%	2	5
Carroll	4.37%	8	4.80%	6	0.99%	3.70%	8	32.53%	8	28.71%	1.92%	7	412.32%	8	408.50%	8	8
Average	2.47%		3.81%		1.23%	2.12%		13.50%		10.92%	1.75%		86.58%		84.00%		

Table B.2: Case study 2: tabulated results for parameters identified using reduced strain ranges of H&D data

	75% strain range					50% strain range					25% strain range					Overall	
	$E_{F\%}$	R_F	$E_{P\%}$	R_P	Dif.	$E_{F\%}$	R_F	$E_{P\%}$	R_P	Dif.	$E_{F\%}$	R_F	$E_{P\%}$	R_P	Dif.	R_F	R_P
e-t	4.03%	7	5.63%	6	1.25%	3.60%	5	6.48%	2	2.10%	4.07%	7	8.57%	2	4.19%	7	3
Shariff	3.62%	6	4.54%	3	0.96%	3.67%	6	12.67%	6	9.10%	3.55%	3	1.00E3%	7	998.19%	6	6
m-s	3.12%	1	3.12%	1	0.09%	3.09%	2	7.49%	3	4.46%	4.60%	8	6.94%	1	3.91%	3	1
Ogden	3.60%	3	4.84%	4	1.44%	3.59%	4	6.15%	1	2.75%	3.57%	4	93.43%	4	90.03%	2	2
HW	3.62%	5	8.42%	8	4.35%	3.46%	3	53.93%	8	49.86%	3.62%	5	449.35%	6	445.28%	4	8
Alex.	3.45%	2	4.42%	2	1.23%	3.08%	1	11.71%	5	8.52%	3.52%	2	5.06E6%	8	5.06E6%	1	5
D&R	3.61%	4	4.98%	5	0.79%	4.76%	8	10.02%	4	5.83%	3.23%	1	11.00%	3	6.81%	5	4
Carroll	4.13%	8	6.01%	7	1.86%	4.22%	7	34.25%	7	30.10%	4.07%	6	380.53%	5	376.38%	8	7
Average	3.64%		5.24%		1.50%	3.68%		17.84%		14.09%	3.78%		6.33E5%		6.33E5%		

Table B.3: Case study 2: tabulated results for parameters identified using reduced strain ranges of Meunier data

	75% strain range					50% strain range					25% strain range					Overall	
	$E_{F\%}$	R_F	$E_{P\%}$	R_P	Dif.	$E_{F\%}$	R_F	$E_{P\%}$	R_P	Dif.	$E_{F\%}$	R_F	$E_{P\%}$	R_P	Dif.	R_F	R_P
e-t	3.08%	8	5.70%	7	1.45%	2.65%	7	9.86%	4	5.61%	2.93%	8	9.97%	1	5.72%	8	3
Shariff	2.53%	6	2.77%	2	0.05%	2.51%	5	4.90%	1	2.17%	2.29%	4	17.40%	2	14.67%	5	1
m-s	2.26%	3	7.82%	8	5.44%	2.62%	6	9.31%	3	6.93%	2.50%	7	17.67%	3	15.28%	6	4
Ogden	2.34%	4	3.02%	3	0.88%	2.28%	4	32.38%	7	30.24%	2.31%	5	28.12%	5	25.98%	4	5
HW	1.95%	2	4.23%	5	2.05%	1.66%	1	30.10%	6	27.92%	1.74%	1	605.59%	7	603.41%	1	8
Alex.	2.40%	5	4.20%	4	1.02%	2.12%	3	97.47%	8	94.29%	2.08%	2	21.30%	4	18.11%	3	6
D&R	1.94%	1	2.42%	1	0.19%	1.99%	2	7.32%	2	5.09%	2.24%	3	1E99%	8	1E99%	2	2
Carroll	3.03%	7	5.32%	6	1.37%	2.71%	8	12.88%	5	8.92%	2.35%	6	59.66%	6	55.71%	7	7
Average	2.44%		4.44%		1.55%	2.32%		25.53%		22.65%	2.30%		1E99%		1E99%		

Table B.4: Case study 3: tabulated results for parameters identified using two single loading experiments from Treloar data

	UT&PT					PT&ET					UT&ET					Average	Overall	
	$E_{F\%}$	R_F	$E_{P\%}$	R_P	Dif.	$E_{F\%}$	R_F	$E_{P\%}$	R_P	Dif.	$E_{F\%}$	R_F	$E_{P\%}$	R_P	Dif.	Dif.	R_F	R_P
e-t	2.02%	4	1.93%	1	0.05%	1.43%	2	2.21%	3	0.33%	1.86%	3	2.16%	2	0.28%	0.22%	3	1
Shariff	1.84%	3	4.41%	3	2.34%	1.58%	3	5.19%	6	3.12%	1.96%	4	2.20%	4	0.13%	1.86%	4	4
m-s	2.49%	6	7.34%	5	4.88%	1.68%	5	3.98%	4	1.52%	2.03%	5	2.75%	5	0.29%	2.23%	5	5
Ogden	1.46%	1	69.23%	7	67.96%	0.58%	1	1.41%	1	0.13%	1.66%	2	1.60%	1	0.32%	22.80%	1	3
HW	3.73%	8	1.68E4%	8	1.68E4%	3.18%	7	6.75%	8	2.76%	3.92%	8	4.04%	8	0.05%	5.59E4%	8	8
Alex.	2.26%	5	8.45%	6	5.28%	2.52%	6	5.81%	7	2.65%	3.83%	7	3.43%	6	0.26%	2.73%	6	7
D&R	1.72%	2	4.12%	2	2.14%	1.60%	4	2.12%	2	0.13%	1.64%	1	2.20%	3	0.21%	0.83%	2	2
Carroll	3.64%	7	5.94%	4	2.13%	3.73%	8	4.32%	5	0.50%	3.35%	6	3.92%	7	0.10%	0.91%	7	6
Average	2.39%		2.11E3%		2.11E3%	2.04%		3.97%		1.39%	2.53%		2.79%		0.21%			

Table B.5: Case study 3:tabulated results for parameters identified using two single loading experiments from H&D data

	UT&PT					PT&ET					UT&ET					Average	Overall	
	$E_{F\%}$	R_F	$E_{P\%}$	R_P	Dif.	$E_{F\%}$	R_F	$E_{P\%}$	R_P	Dif.	$E_{F\%}$	R_F	$E_{P\%}$	R_P	Dif.	Dif.	R_F	R_P
e-t	1.48%	4	7.84%	3	3.46%	3.85%	7	4.78%	5	0.39%	4.93%	8	4.89%	7	0.51%	1.46%	7	6
Shariff	1.53%	5	24.02%	7	20.44%	2.82%	3	4.15%	3	0.57%	2.79%	2	3.70%	4	0.13%	7.04%	4	5
m-s	1.03%	1	6.25%	2	3.21%	3.32%	4	3.63%	2	0.60%	3.24%	4	3.39%	2	0.36%	1.39%	3	1
Ogden	1.08%	2	10.73%	5	7.33%	2.64%	2	4.51%	4	1.11%	2.24%	1	3.47%	3	0.07%	2.84%	1	4
HW	1.71%	6	303.31%	8	299.24%	3.51%	6	6.69%	8	2.62%	3.62%	5	7.70%	8	3.63%	101.83%	5	8
Alex.	1.42%	3	9.79%	4	6.60%	2.00%	1	3.49%	1	0.30%	2.91%	3	3.33%	1	0.14%	2.35%	2	2
D&R	2.51%	8	22.94%	6	18.75%	3.38%	5	4.81%	7	0.62%	3.74%	6	4.87%	6	0.68%	6.68%	6	7
Carroll	1.78%	7	4.76%	1	0.61%	4.20%	8	4.79%	6	0.64%	4.73%	7	4.41%	5	0.26%	0.50%	8	3
Average	1.57%		48.71%		44.96%	3.22%		4.60%		0.86%	3.52%		4.47%		0.72%			

Table B.6: Case study 3: tabulated results for parameters identified using two single loading experiments from Meunier data

	UT&PT					**PT&ET**					**UT&ET**					**Average**	**Overall**	
	$E_{F\%}$	R_F	$E_{P\%}$	R_P	Dif.	$E_{F\%}$	R_F	$E_{P\%}$	R_P	Dif.	$E_{F\%}$	R_F	$E_{P\%}$	R_P	Dif.	Dif.	R_F	R_P
e-t	1.96%	7	11.52%	5	7.27%	3.66%	8	5.14%	7	0.89%	3.68%	8	4.96%	8	0.71%	2.96%	8	8
Shariff	1.17%	3	4.98%	2	2.26%	1.09%	2	3.79%	5	1.07%	1.39%	4	2.85%	5	0.13%	1.15%	3	4
m-s	1.66%	5	22.62%	6	20.23%	1.20%	4	2.84%	1	0.46%	2.27%	5	2.80%	4	0.42%	7.04%	4	3
Ogden	1.14%	2	5.00%	3	2.86%	0.99%	1	3.02%	2	0.88%	0.79%	1	2.31%	1	0.17%	1.30%	1	1
HW	1.10%	1	92.25%	8	90.07%	1.10%	3	3.38%	3	1.20%	0.83%	2	2.80%	3	0.62%	30.63%	2	5
Alex.	1.44%	4	43.60%	7	40.42%	1.67%	5	3.54%	4	0.36%	2.43%	6	3.68%	6	0.49%	13.76%	6	7
D&R	1.87%	6	3.74%	1	1.50%	2.59%	6	6.06%	8	3.82%	1.38%	3	2.60%	2	0.36%	1.90%	5	2
Carroll	2.25%	8	9.43%	4	5.48%	2.73%	7	4.40%	6	0.45%	3.48%	7	4.65%	7	0.69%	2.21%	7	6
Average	1.57%		24.14%		21.26%	1.88%		4.02%		1.14%	2.03%		3.33%		0.45%			

Table B.7: Case study 4: tabulated results for parameters identified using one single loading experiment from Treloar data

	UT					PT					ET					Average	Overall	
	$E_{F\%}$	R_F	$E_{P\%}$	R_P	Dif.	$E_{F\%}$	R_F	$E_{P\%}$	R_P	Dif.	$E_{F\%}$	R_F	$E_{P\%}$	R_P	Dif.	Dif.	R_F	R_P
e-t	2.24%	4	2.07%	1	0.20%	0.39%	3	6.58%	1	4.70%	1.07%	5	2.99%	1	1.11%	2.00%	5	1
Shariff	2.12%	3	1.19E3%	5	1.18E3%	0.34%	1	201.67%	5	199.60%	1.39%	6	20.12%	5	18.05%	467.39%	3	5
m-s	2.54%	6	2.34E12%	8	2.34E12%	0.39%	4	35.90%	3	33.45%	0.55%	2	12.16%	4	9.71%	7.80E11%	4	6
Ogden	1.46%	1	8.30E8%	7	8.30E8%	0.40%	5	697.56%	7	696.29%	0.66%	3	106.02%	7	104.75%	2.77E8%	2	7
HW	1.46%	2	6.87E4%	6	6.87E4%	2.04%	8	2.63E4%	8	2.63E4%	0.83%	4	1.75E4%	8	1.75E4%	1.16E5%	6	8
Alex.	2.76%	7	87.85%	3	84.68%	1.11%	7	257.91%	6	254.74%	2.55%	8	5.82%	3	2.65%	114.03%	8	4
D&R	2.42%	5	1.09E3%	4	1.09E3%	0.34%	2	52.39%	4	50.40%	0.49%	1	3.14%	2	1.16%	378.85%	1	3
Carroll	3.11%	8	6.24%	2	2.42%	0.73%	6	21.88%	2	18.06%	1.58%	7	42.16%	6	38.35%	19.61%	7	2
Average	2.27%		2.92E11%		2.92E11%	0.72%		3.30E4%		3.30E4%	1.14%		2.22E3%		2.21E3%	9.75E10%		

Table B.8: Case study 4: tabulated results for parameters identified using one single loading experiment from H&D data

	UT					PT					ET					Average	Overall	
	$E_{F\%}$	R_F	$E_{P\%}$	R_P	Dif.	$E_{F\%}$	R_F	$E_{P\%}$	R_P	Dif.	$E_{F\%}$	R_F	$E_{P\%}$	R_P	Dif.	Dif.	R_F	R_P
e-t	0.60%	4	6.48%	2	2.10%	0.89%	5	8.58%	3	4.19%	3.94%	8	37.38%	2	33.00%	13.10%	6	1
Shariff	0.51%	3	1.69E4%	7	1.69E4%	0.80%	1	159.15%	7	155.58%	2.02%	6	5.02E3%	7	5.02E3%	7.73E3%	2	6
m-s	0.60%	5	3.88%	1	0.84%	0.84%	3	6.76%	2	3.73%	1.48%	4	190.68%	6	187.65%	64.07%	4	4
Ogden	0.48%	2	6.81E5%	8	6.81E5%	0.82%	2	118.64%	5	115.24%	0.90%	2	53.20%	4	49.81%	2.27E5%	1	7
HW	0.45%	1	1.21E4%	6	1.21E4%	1.76%	8	3.89E4%	8	3.89E4%	0.66%	1	4.55E5%	8	4.55E5%	2.05E5%	3	8
Alex.	0.61%	6	84.29%	5	81.10%	0.86%	4	119.29%	6	116.10%	1.51%	5	46.98%	3	43.79%	80.33%	5	2
D&R	1.55%	8	59.09%	4	54.90%	1.34%	7	22.25%	4	18.06%	0.93%	3	31.52%	1	27.33%	33.43%	7	2
Carroll	0.63%	7	8.38%	3	4.23%	1.23%	6	5.02%	1	0.87%	2.12%	7	117.73%	5	113.58%	39.56%	8	3
Average	0.68%		8.87E5%		8.87E5%	1.07%		540.67%		536.92%	1.69%		6.38E3%		6.37E3%	3.19E4%		

Table B.9: Case study 4: tabulated results for parameters identified using one single loading experiment from Meunier data

	UT					**PT**					**ET**					**Average**	**Overall**	
	$E_{F\%}$	R_F	$E_{P\%}$	R_P	Dif.	$E_{F\%}$	R_F	$E_{P\%}$	R_P	Dif.	$E_{F\%}$	R_F	$E_{P\%}$	R_P	Dif.	Dif.	R_F	R_P
e-t	0.70%	7	22.67%	3	18.42%	1.36%	8	20.27%	2	16.02%	3.55%	8	7.60%	4	3.35%	12.60%	8	2
Shariff	0.40%	5	2.94E3%	8	2.94E3%	1.34%	6	251.84%	6	249.12%	0.59%	6	3.46%	1	0.74%	1.06E3%	6	7
m-s	0.19%	2	285.25%	4	282.86%	0.65%	3	21.54%	3	19.16%	0.15%	3	7.89%	5	5.50%	102.51%	1	3
Ogden	0.78%	8	3.63%	1	1.48%	1.32%	4	4.38%	1	2.24%	0.08%	2	8.12%	6	5.98%	3.24%	5	1
HW	0.03%	1	1.29E3%	7	1.29E3%	1.35%	7	392.04%	8	389.86%	0.08%	1	161.30%	8	159.12%	612.37%	3	8
Alex.	0.24%	4	472.68%	6	469.50%	0.43%	1	22.88%	4	19.70%	0.40%	5	4.38%	2	1.20%	163.47%	4	4
D&R	0.22%	3	448.00%	5	445.76%	0.62%	2	258.67%	7	256.44%	0.26%	4	6.12%	3	3.88%	235.36%	2	6
Carroll	0.67%	6	18.89%	2	14.94%	1.32%	5	37.17%	5	33.22%	1.29%	7	10.69%	7	6.74%	18.30%	7	5
Average	0.40%		685.46%		682.58%	1.05%		126.10%		123.22%	0.80%		26.20%		23.31%	276.37%		

Table B.10: Average percentage error values for Treloar and H&D synthetic general biaxial data

	Treloar						**H&D**					
	$UT+PT+ET$			$UT+ET$			$UT+PT+ET$			$UT+ET$		
	$E_{F\%}$	$UT\rightarrow PT\rightarrow ET$	$UT\rightarrow ET$	$E_{F\%}$	$UT\rightarrow PT\rightarrow ET$	$UT\rightarrow ET$	$E_{F\%}$	$UT\rightarrow PT\rightarrow ET$	$UT\rightarrow ET$	$E_{F\%}$	$UT\rightarrow PT\rightarrow ET$	$UT\rightarrow ET$
e-t	1.88%	1.96%	2.05%	1.86%	1.22%	1.25%	4.38%	2.45%	2.62%	4.93%	3.03%	3.08%
Shariff	2.07%	2.30%	2.39%	1.96%	1.49%	2.16%	3.58%	4.09%	4.29%	2.79%	1.07%	1.18%
m-s	2.46%	4.01%	3.89%	2.03%	3.27%	2.68%	3.03%	0.00%	0.00%	3.24%	7.58%	7.75%
Ogden	1.27%	0.00%	0.00%	1.66%	3.42%	3.79%	3.40%	4.18%	4.34%	2.24%	0.00%	0.00%
HW	3.99%	4.13%	4.72%	3.92%	5.72%	9.50%	4.07%	3.50%	3.01%	3.62%	10.97%	11.65%
Alex.	3.17%	2.47%	2.32%	3.83%	3.56%	3.05%	3.19%	2.73%	2.91%	2.91%	2.31%	2.39%
D&R	1.98%	2.32%	2.53%	1.64%	0.00%	0.00%	4.19%	3.05%	2.92%	3.74%	2.98%	2.29%
Carroll	3.82%	4.19%	3.92%	3.35%	2.72%	2.25%	4.15%	2.47%	2.68%	4.73%	2.99%	3.19%
Bid.	5.75%	4.75%	4.18%	6.77%	4.96%	4.19%	4.61%	4.36%	4.09%	4.59%	2.78%	2.57%
H-S	4.99%	3.83%	3.54%	6.19%	5.04%	4.51%	8.64%	7.67%	9.40%	9.09%	5.33%	6.84%
E-V	3.22%	2.32%	2.36%	3.51%	1.73%	1.42%	7.88%	7.85%	8.36%	8.63%	4.95%	6.01%
Khiem	3.13%	3.35%	3.72%	3.19%	3.08%	3.07%	3.82%	3.26%	3.52%	3.97%	2.76%	2.99%
8c-t	2.11%	2.15%	2.33%	1.97%	1.28%	1.19%	4.37%	2.47%	2.65%	4.89%	2.84%	3.04%
Average	3.06%	2.91%	2.92%	3.22%	2.88%	3.00%	4.56%	3.70%	3.91%	4.57%	3.82%	4.08%
PCC	–	0.808	0.724	–	0.732	0.474	–	0.865	0.898	–	0.230	0.341

Table B.11: Average percentage error values for Meunier synthetic general biaxial data and overall averages considering all material data

	Meunier						**All**				
	$UT{+}PT{+}ET$			$UT{+}ET$			**Materials**				
	$E_{F\%}$	$UT{\rightarrow}PT{\rightarrow}ET$	$UT{\rightarrow}ET$	$E_{F\%}$	$UT{\rightarrow}PT{\rightarrow}ET$	$UT{\rightarrow}ET$	$UT{+}PT{+}ET$	$UT{+}ET$	$UT{\rightarrow}PT{\rightarrow}ET$	$UT{\rightarrow}ET$	**Overall**
e-t	4.25%	3.42%	3.33%	3.68%	3.89%	4.08%	2.64%	2.76%	2.66%	3.17%	2.70%
Shariff	2.72%	1.06%	1.04%	1.39%	1.41%	1.73%	2.53%	1.51%	1.90%	3.20%	2.02%
m-s	2.38%	3.67%	4.02%	2.27%	2.85%	3.29%	2.60%	4.57%	3.56%	3.29%	3.58%
Ogden	2.14%	0.00%	0.00%	0.79%	0.00%	0.00%	1.42%	1.20%	1.27%	3.27%	1.31%
HW	2.18%	1.92%	2.46%	0.83%	1.64%	2.21%	3.29%	6.95%	4.65%	3.46%	5.12%
Alex.	3.18%	2.67%	1.68%	2.43%	2.57%	1.75%	2.46%	2.61%	2.72%	3.22%	2.53%
D&R	2.24%	1.74%	1.73%	1.38%	1.26%	1.15%	2.38%	1.28%	1.89%	3.33%	1.83%
Carroll	3.95%	3.19%	2.72%	3.48%	2.84%	2.68%	3.20%	2.78%	3.07%	3.55%	2.99%
Bid.	4.29%	3.33%	2.50%	4.09%	3.33%	2.69%	3.87%	3.42%	3.92%	3.66%	3.64%
H-S	6.43%	6.08%	6.04%	7.28%	6.66%	6.93%	6.09%	5.88%	5.77%	3.71%	5.99%
E-V	3.99%	3.21%	3.00%	3.34%	2.85%	2.77%	4.52%	3.29%	3.82%	3.09%	3.90%
NA-t	3.63%	3.17%	2.11%	3.01%	3.66%	2.61%	3.19%	3.03%	3.22%	2.79%	3.11%
8c-t	3.70%	3.09%	2.03%	3.00%	2.82%	1.96%	2.46%	2.19%	2.44%	2.69%	2.32%
Average	3.47%	2.81%	2.51%	2.84%	2.75%	2.60%	**3.13%**	**3.19%**	**3.15%**	**3.17%**	**3.16%**
PCC	–	0.841	0.723	–	0.947	0.885	**0.822**	**0.540**	**0.659**	**0.634**	**0.644**

Table B.12: Overall averaged data rearranged in terms of complete single loading experiment variations

	Treloar		**H&D**		**Meunier**		
	$UT{\rightarrow}PT{\rightarrow}ET$	$UT{\rightarrow}ET$	$UT{\rightarrow}PT{\rightarrow}ET$	$UT{\rightarrow}ET$	$UT{\rightarrow}PT{\rightarrow}ET$	$UT{\rightarrow}ET$	**Average**
Error							
$UT{+}PT{+}ET$	2.91%	2.92%	3.70%	3.91%	2.81%	2.51%	3.13%
$UT{+}ET$	2.88%	3.00%	3.82%	4.08%	2.75%	2.60%	3.19%
Difference	0.02%	-0.08%	-0.12%	-0.17%	0.06%	-0.09%	-0.06%
PCC							
$UT{+}PT{+}ET$	0.808	0.724	0.865	0.898	0.841	0.723	0.810
$UT{+}ET$	0.732	0.474	0.230	0.341	0.947	0.885	0.601
Difference	0.076	0.250	0.636	0.557	-0.106	-0.162	0.209

Table B.13: Overall averaged data rearranged in terms of interpolation method variations

	Treloar		**H&D**		**Meunier**		
	$UT{+}PT{+}ET$	$UT{+}ET$	$UT{+}PT{+}ET$	$UT{+}ET$	$UT{+}PT{+}ET$	$UT{+}ET$	**Average**
Error							
$UT{\rightarrow}PT{\rightarrow}ET$	2.91%	2.88%	3.70%	3.82%	2.81%	2.75%	3.15%
$UT{\rightarrow}ET$	2.92%	3.00%	3.91%	4.08%	2.51%	2.60%	3.17%
Difference	-0.01%	-0.12%	-0.21%	-0.26%	0.30%	0.15%	-0.03%
PCC							
$UT{\rightarrow}PT{\rightarrow}ET$	0.808	0.732	0.865	0.230	0.841	0.947	0.737
$UT{\rightarrow}ET$	0.724	0.474	0.898	0.341	0.723	0.885	0.674
Difference	0.084	0.258	-0.033	-0.111	0.118	0.062	0.063

Table B.14: Comparison of fitted and predicted errors for synthetic general biaxial data generated by $UT{+}PT{+}ET$ fits

	Treloar			**H&D**			**Meunier**		
UT+PT+ET	$E_{GB\%}$	$E_{FB\%}$	Dif.	$E_{GB\%}$	$E_{FB\%}$	Dif.	$E_{GB\%}$	$E_{FB\%}$	Dif.
e-t	1.96%	1.86%	0.11%	2.45%	1.89%	0.56%	3.42%	3.12%	0.31%
Shariff	2.30%	2.14%	0.15%	4.09%	2.88%	1.20%	1.06%	0.70%	0.37%
m-s	4.01%	3.76%	0.26%	0.00%	0.00%	0.00%	3.67%	1.45%	2.22%
Ogden	0.00%	0.00%	0.00%	4.18%	1.76%	2.42%	0.00%	0.00%	0.00%
HW	4.13%	3.53%	0.60%	3.50%	2.56%	0.94%	1.92%	0.44%	1.48%
Alex.	2.47%	2.02%	0.45%	2.73%	2.17%	0.55%	2.67%	2.26%	0.41%
D&R	2.32%	1.80%	0.53%	3.05%	2.09%	0.96%	1.74%	1.16%	0.58%
Carroll	4.19%	4.08%	0.11%	2.47%	2.37%	0.10%	3.19%	2.86%	0.34%
Bid.	4.75%	4.44%	0.31%	4.36%	3.10%	1.25%	3.33%	2.94%	0.39%
H-S	3.83%	3.52%	0.31%	7.67%	6.17%	1.50%	6.08%	5.81%	0.27%
E-V	2.32%	1.90%	0.42%	7.85%	4.64%	3.21%	3.21%	2.75%	0.46%
NA-t	3.35%	3.17%	0.19%	3.26%	2.08%	1.18%	3.17%	2.63%	0.54%
8c-t	2.15%	1.71%	0.44%	2.47%	1.87%	0.61%	3.09%	2.46%	0.63%
Average	2.91%	2.61%	0.30%	3.70%	2.58%	1.11%	2.81%	2.20%	0.61%

Table B.15: Comparison of fitted and predicted errors for synthetic general biaxial data generated by $UT+ET$ fits

	Treloar			**H&D**			**Meunier**		
UT+ET	$E_{GB\%}$	$E_{FB\%}$	Dif.	$E_{GB\%}$	$E_{FB\%}$	Dif.	$E_{GB\%}$	$E_{FB\%}$	Dif.
e-t	1.22%	0.66%	0.55%	3.03%	1.99%	1.04%	3.89%	3.07%	0.82%
Shariff	1.49%	0.73%	0.76%	1.07%	0.62%	0.45%	1.41%	0.62%	0.79%
m-s	3.27%	2.56%	0.71%	7.58%	3.86%	3.72%	2.85%	1.39%	1.46%
Ogden	3.42%	1.40%	2.02%	0.00%	0.00%	0.00%	0.00%	0.00%	0.00%
HW	5.72%	3.26%	2.46%	10.97%	2.01%	8.97%	1.64%	0.37%	1.27%
Alex.	3.56%	2.08%	1.48%	2.31%	1.23%	1.08%	2.57%	2.16%	0.40%
D&R	0.00%	0.00%	0.00%	2.98%	2.52%	0.46%	1.26%	1.10%	0.16%
Carroll	2.72%	2.60%	0.12%	2.99%	2.97%	0.02%	2.84%	2.74%	0.09%
Bid.	4.96%	4.28%	0.68%	2.78%	2.07%	0.71%	3.33%	2.75%	0.58%
H-S	5.04%	4.49%	0.55%	5.33%	4.40%	0.92%	6.66%	5.89%	0.77%
E-V	1.73%	1.41%	0.32%	4.95%	3.73%	1.22%	2.85%	2.71%	0.14%
Khiem	3.08%	2.50%	0.59%	2.76%	1.40%	1.36%	3.66%	2.52%	1.14%
8c-t	1.28%	1.05%	0.23%	2.84%	1.89%	0.94%	2.82%	2.33%	0.49%
Average	2.88%	2.08%	0.81%	3.82%	2.21%	1.61%	2.75%	2.13%	0.62%

Appendix C

Coefficients for Central Difference Approximations

Table C.1: Weighted coefficients c_m for central difference approximations up to twelfth-order

	m											
n_{even}	-6	-5	-4	-3	-2	-1	1	2	3	4	5	6
2						$-\frac{1}{2}$	$\frac{1}{2}$					
4					$\frac{1}{12}$	$-\frac{2}{3}$	$\frac{2}{3}$	$-\frac{1}{12}$				
6				$-\frac{1}{60}$	$\frac{3}{20}$	$-\frac{3}{4}$	$\frac{3}{4}$	$-\frac{3}{20}$	$\frac{1}{60}$			
8			$\frac{1}{280}$	$-\frac{4}{105}$	$\frac{1}{5}$	$-\frac{4}{5}$	$\frac{4}{5}$	$-\frac{1}{5}$	$\frac{4}{105}$	$-\frac{1}{280}$		
10		$-\frac{1}{1260}$	$\frac{5}{504}$	$-\frac{5}{84}$	$\frac{5}{21}$	$-\frac{5}{6}$	$\frac{5}{6}$	$-\frac{5}{21}$	$\frac{5}{84}$	$-\frac{5}{504}$	$\frac{1}{1260}$	
12	$\frac{1}{5544}$	$-\frac{1}{385}$	$\frac{1}{56}$	$-\frac{5}{63}$	$\frac{15}{56}$	$-\frac{6}{7}$	$\frac{6}{7}$	$-\frac{15}{56}$	$\frac{5}{63}$	$-\frac{1}{56}$	$\frac{1}{385}$	$\frac{1}{5544}$

Appendix D

Tabular Results from Chapter 6

Table D.1: Complete data fitted models: results and percentage error for CV boot simulation

	Stress: Max. Principal		Strain: Max. Principal		Force Reaction (1)		Force Reaction (2)	
	(MPa)	(%)	(-)	(%)	(N)	(%)	(N)	(%)
Ogden	2.68E-1	0.00%	3.31E-1	0.00%	5.71	0.00%	-3.54	0.00%
HW	2.74E-1	2.28%	3.33E-1	0.77%	5.88	2.80%	-3.63	2.44%
D&R	2.73E-1	1.89%	3.49E-1	5.13%	5.79	1.28%	-3.62	2.11%
m-s	2.74E-1	2.17%	3.36E-1	1.46%	5.92	3.52%	-3.62	2.10%
Shariff	2.69E-1	0.36%	3.32E-1	0.44%	5.76	0.73%	-3.55	0.18%
Alex.	2.73E-1	1.97%	3.31E-1	0.15%	5.83	2.03%	-3.59	1.40%
NA-t	2.73E-1	1.80%	3.32E-1	0.33%	5.83	2.01%	-3.58	1.05%
8c-t	2.72E-1	1.49%	3.32E-1	0.26%	5.81	1.65%	-3.57	0.73%
Carroll	2.66E-1	0.58%	3.30E-1	0.07%	5.68	0.63%	-3.49	1.63%
E-V	2.66E-1	0.60%	3.30E-1	0.24%	5.67	0.78%	-3.49	1.51%
e-t	2.65E-1	1.28%	3.30E-1	0.32%	5.63	1.51%	-3.46	2.30%
Bid.	2.70E-1	0.78%	3.32E-1	0.47%	5.78	1.07%	-3.54	0.21%
H-S	2.78E-1	3.75%	3.32E-1	0.35%	5.95	3.94%	-3.66	3.02%
Averages	2.71E-1	1.46%	3.33E-1	0.77%	5.79	1.69%	-3.57	1.44%
SD	3.79E-3		4.74E-3		9.38E-2		5.75E-2	
RSD (%)	1.40%		1.42%		1.62%		1.61%	
Average % error	1.22%							
Average RSD (%)	1.48%							

Table D.2: Sufficient data fitted models: results and percentage error for CV boot simulation

	Stress: Max. Principal		Strain: Max. Principal		Force Reaction (1)		Force Reaction (2)	
	(MPa)	(%)	(-)	(%)	(N)	(%)	(N)	(%)
HW	2.71E-1	0.00%	3.43E-1	0.00%	5.83	0.00%	-3.64	0.00%
Alex.	2.72E-1	0.06%	3.52E-1	2.52%	5.86	0.44%	-3.65	0.40%
Bid.	2.71E-1	0.02%	3.52E-1	2.59%	5.84	0.08%	-3.63	0.31%
D&R	2.73E-1	0.64%	3.53E-1	2.80%	5.85	0.32%	-3.65	0.40%
Shariff	2.71E-1	0.08%	3.52E-1	2.53%	5.82	0.20%	-3.62	0.53%
Ogden	2.72E-1	0.14%	3.52E-1	2.59%	5.83	0.07%	-3.63	0.31%
NA-t	2.71E-1	0.03%	3.50E-1	2.03%	5.82	0.19%	-3.62	0.53%
Carroll	2.72E-1	0.14%	3.52E-1	2.65%	5.83	0.10%	-3.62	0.33%
E-V	2.72E-1	0.05%	3.35E-1	2.41%	5.82	0.14%	-3.62	0.56%
m-s	2.74E-1	0.89%	3.37E-1	1.67%	5.90	1.14%	-3.64	0.09%
8c-t	2.72E-1	0.10%	3.33E-1	3.10%	5.81	0.31%	-3.60	1.10%
H-S	2.73E-1	0.44%	3.31E-1	3.45%	5.82	0.26%	-3.59	1.17%
e-t	2.66E-1	1.93%	3.31E-1	3.51%	5.69	2.58%	-3.52	3.23%
Averages	2.72E-1	0.35%	3.44E-1	2.45%	5.82	0.45%	-3.62	0.69%
SD	1.69E-3		8.82E-3		4.56E-2		3.19E-2	
RSD (%)	0.62%		2.56%		0.78%		0.88%	
Average % error	0.98%							
Average RSD (%)	1.21%							

Table D.3: Complete data fitted models: results and percentage error for O-Ring simulation

	Stress: Max. Principal		Strain: Max. Principal		Force Reaction (1)		Force Reaction (2)		Extrusion	
	(MPa)	(%)	(-)	(%)	(N)	(%)	(N)	(%)	(mm)	(%)
m-s	1.63	0.00%	1.77	0.00%	1248.77	0.00%	-1274.81	0.00%	1.01E-1	0.00%
Alex.	1.54	5.51%	1.80	1.55%	1250.45	0.13%	-1274.74	0.01%	9.98E-2	0.81%
Ogden	1.59	2.51%	1.81	2.14%	1248.33	0.04%	-1274.58	0.02%	1.01E-1	0.27%
Shariff	1.54	5.92%	1.78	0.54%	1251.71	0.23%	-1275.31	0.04%	9.74E-2	3.32%
NA-t	1.51	7.98%	1.77	0.32%	1252.46	0.29%	-1275.38	0.04%	9.68E-2	3.91%
HW	1.65	1.39%	1.81	2.04%	1242.31	0.52%	-1273.72	0.09%	1.04E-1	3.26%
Carroll	1.63	0.17%	1.79	0.94%	1246.74	0.16%	-1273.94	0.07%	1.03E-1	2.23%
D&R	1.70	4.18%	1.79	1.43%	1249.22	0.04%	-1274.27	0.04%	1.03E-1	2.21%
8c-t	1.59	2.10%	1.79	1.41%	1247.21	0.13%	-1274.19	0.05%	1.10E-1	8.49%
e-t	1.59	2.08%	1.79	1.38%	1247.24	0.12%	-1274.20	0.05%	1.02E-1	1.32%
Bid.	1.57	3.38%	1.77	0.36%	1245.12	0.29%	-1274.51	0.02%	1.01E-1	0.12%
E-V	1.58	3.17%	1.79	1.03%	1246.58	0.18%	-1274.01	0.06%	1.02E-1	1.25%
H-S	1.38	18.20%	1.71	3.40%	1265.58	1.33%	-1277.88	0.24%	8.77E-2	14.76%
Averages	1.58	4.35%	1.78	1.27%	1249.36	0.27%	-1274.73	0.06%	1.01E-1	3.23%
SD	7.54E-2		2.37E-2		5.35		1.03		4.85E-3	
RSD (%)	4.78%		1.33%		0.43%		0.08%		4.82%	
Average % error	1.83%									
Average RSD (%)	2.29%									

Table D.4: Sufficient data fitted models: results and percentage error for O-Ring simulation

	Stress: Max. Principal		Strain: Max. Principal		Force Reaction (1)		Force Reaction (2)		Extrusion	
	(MPa)	(%)	(-)	(%)	(N)	(%)	(N)	(%)	(mm)	(%)
Alex.	1.52	0.00%	1.72	0.00%	1263.79	0.00%	-1276.78	0.00%	9.22E-2	0.00%
m-s	1.54	1.24%	1.79	3.50%	1247.83	1.28%	-1274.94	0.14%	9.88E-2	6.68%
NA-t	1.51	0.65%	1.80	3.99%	1254.36	0.75%	-1275.64	0.09%	9.64E-2	4.32%
HW	1.50	1.29%	1.81	4.92%	1247.75	1.29%	-1274.83	0.15%	9.51E-2	2.98%
Ogden	1.51	0.91%	1.78	3.22%	1253.88	0.79%	-1275.61	0.09%	9.69E-2	4.78%
8c-t	1.51	1.09%	1.78	3.04%	1253.23	0.84%	-1275.55	0.10%	9.69E-2	4.86%
e-t	1.54	0.88%	1.77	2.83%	1252.99	0.86%	-1275.50	0.10%	9.68E-2	4.71%
Shariff	1.54	0.76%	1.79	3.44%	1251.72	0.96%	-1275.30	0.12%	9.76E-2	5.45%
H-S	1.45	4.92%	1.75	1.68%	1260.36	0.27%	-1276.65	0.01%	9.22E-2	0.04%
E-V	1.57	3.25%	1.73	0.25%	1254.52	0.74%	-1275.57	0.09%	9.60E-2	3.88%
Carroll	1.64	6.95%	1.80	3.99%	1245.10	1.50%	-1273.89	0.23%	1.03E-1	10.64%
Bid.	1.56	2.46%	1.84	6.30%	1247.24	1.33%	-1274.47	0.18%	1.02E-1	9.36%
D&R	1.38	10.48%	1.78	3.18%	1261.03	0.22%	-1277.22	0.03%	9.08E-2	1.56%
Averages	1.52	2.68%	1.78	3.10%	1253.37	0.83%	-1275.53	0.10%	9.65E-2	4.56%
SD	5.86E-2		3.01E-2		5.48		8.94E-1		3.41E-3	
RSD (%)	3.85%		1.69%		0.44%		0.07%		3.53%	
Average % error	2.26%									
Average RSD (%)	1.92%									